

**Pool-riffle dynamics in mountain streams: implications for  
maintenance, formation and equilibrium**

by

Shawn M. Chartrand

BA, Environmental Geology, Case Western Reserve University, 1995

MS, Geological Sciences, Case Western Reserve University, 1997

A THESIS SUBMITTED IN PARTIAL FULFILLMENT  
OF THE REQUIREMENTS FOR THE DEGREE OF

**Doctor of Philosophy**

in

THE FACULTY OF GRADUATE AND POSTDOCTORAL STUDIES  
(Geography)

The University of British Columbia  
(Vancouver)

July 2017

© Shawn M. Chartrand, 2017

# Abstract

It is common for mountain riverbeds to exhibit a repetitive pattern of topographic lows and highs known respectively as pools and riffles. Pool-riffle structures are ecologically important because salmon rely on them for birth, growth and regeneration, and they are physically important because pool-riffles are observed across diverse landscape settings. A common physical characteristic of pool-riffles is that pool spacing is proportional to channel width, for longitudinal bed slopes that vary by two-orders of magnitude. Furthermore, field, numerical and laboratory based studies observe that pools are colocated with points of channel narrowing, and riffles with points of widening. What is not known, however, is how downstream changes of channel width give rise to, and maintain pool-riffles. The goal of my thesis is to address this knowledge gap, and to specifically build physical understanding for the observed spatial correlation between channel width and pool-riffle architecture. I use field work, laboratory experiments and theory to address this goal. In Chapter 2 I apply non-parametric statistics and self-organizing maps to understand the spatial and temporal character of riffle bed surface texture spanning 11 different sediment mobilizing floods, and conclude that frequent texture adjustment is part of the maintenance process for pool-riffles which exhibit topographic stationarity. I build from this finding in Chapters 3, 4 and 5 with laboratory experiments designed to investigate how pool-riffles form and evolve along variable width channel reaches. In Chapter 4 I conclude that pool-riffle formation is physically driven by two competing timescales which reflect the tendency to build riverbed topography through sediment deposition, vs. the tendency to destroy topography through net particle entrainment. I capture these timescales in a mathematical model I develop using theory with physical scaling. In Chapter 5 I show that the (dis)equilibrium state of pool-riffle evolution is quantitatively described by a competition between two rates which reflect the temporal adjustment of riverbed topography and riverbed surface texture. I conclude that equilibrium, or comparability between the rates of topographic and sediment texture adjustment, is most likely to occur when overall sediment mobility and grain size sorting are relatively high.

# Lay Summary

Mountain streams commonly display a riverbed shape that has a repetitive pattern of topographic lows and highs known respectively as pools and riffles. Visually, pools appear as relatively deep portions of a river, with slow water velocities, and riffles appear as comparatively shallow portions, with more rapid water velocities. Pool-riffles are ecologically important because salmon rely on them for birth, growth and regeneration, and they are physically important because pool-riffles are observed across diverse landscape settings. Despite their importance, the scientific community lacks a clear explanation for pool-riffle formation. This research shows that pool-riffles develop in response to how channel width and water velocity change moving in the downstream direction, reflecting a tendency to either build or destroy riverbed topography. We demonstrate our finding with a mathematical model motivated by experimental observations, and built using a combination of theory and physical scaling.

# Preface

This thesis is original work completed by Shawn Chartrand. Guidance was given by the supervisory committee, and laboratory assistance was provided by Rick Ketler, Carles Ferrer-Boix, and Ryan Buchanan.

This thesis includes one manuscript, and three complementary Chapters that will be submitted for publication as two or more manuscripts. The published manuscript is presented in Chapter 2. Chapter 3, Chapter 4 and Chapter 5 are the complementary Chapters.

A version of the work in Chapter 2 is published in *Water Resources Research Chartrand et al.* (2015). The co-authors are Marwan Hassan and Valentina Radić. I am responsible for developing the field sampling program, implementation, and analysis of all field data presented in Chapter 2, except use of self-organizing maps (SOMs), which was completed by Valentina Radić. I completed a majority of the writing presented in Chapter 2. Marwan Hassan and Valentina Radić provided editorial review of the manuscript prior to publication.

Chartrand, S. M., M. A. Hassan, and V. Radić (2015), Pool-riffle sedimentation and surface texture trends in a gravel bed stream, *Water Resources Research*, 51, 9127-9140.

# Table of Contents

<b>Abstract</b> . . . . .	<b>ii</b>
<b>Lay Summary</b> . . . . .	<b>iii</b>
<b>Preface</b> . . . . .	<b>iv</b>
<b>Table of Contents</b> . . . . .	<b>v</b>
<b>List of Tables</b> . . . . .	<b>ix</b>
<b>List of Figures</b> . . . . .	<b>x</b>
<b>List of Symbols and Acronyms</b> . . . . .	<b>xii</b>
<b>Acknowledgments</b> . . . . .	<b>xxiii</b>
<b>Dedication</b> . . . . .	<b>xxvi</b>
<b>1 Introduction and motivation</b> . . . . .	<b>1</b>
1.1 Overview . . . . .	2
1.2 Motivation . . . . .	3
1.2.1 River size at the local scale . . . . .	3
1.2.2 Evidence and knowledge gaps of the physical connection between chan- nel width variation and pool-riffle architecture . . . . .	4
1.3 Making sense of coupling between channel width and bed architecture . . . . .	6
<b>2 Pool-riffle sedimentation and surface texture trends in a gravel bed stream</b> . . . . .	<b>10</b>
2.1 Summary . . . . .	10
2.2 Introduction . . . . .	10
2.3 Study site . . . . .	12
2.4 Data collection and analysis . . . . .	15
2.4.1 Riffle texture . . . . .	16
2.4.2 $V^*$ and pool cross-section surveys . . . . .	23

2.4.3	Bedload transport measurements and modeling . . . . .	24
2.4.4	Bed surface sampling . . . . .	27
2.5	Results . . . . .	27
2.5.1	Riffle texture adjustment . . . . .	27
2.5.2	$V^*$ and cross-section surveys . . . . .	32
2.5.3	Sediment transport and bed surface sampling . . . . .	33
2.6	Discussion . . . . .	34
2.6.1	Riffle texture dynamics and spatial organization . . . . .	34
2.6.2	Pool-riffle sedimentation coupling . . . . .	37
2.7	Concluding remarks and next steps . . . . .	38
2.8	Details of SOM methods . . . . .	39
<b>3</b>	<b>Experimental setup and measurements . . . . .</b>	<b>41</b>
3.1	Introduction . . . . .	41
3.2	Laboratory experiment and methods . . . . .	42
3.2.1	Setup and construction . . . . .	42
3.2.2	Experimental design . . . . .	43
3.2.3	Experimental procedure . . . . .	47
3.2.4	Experimental measurements and processing . . . . .	49
3.2.5	Bed surface grain size distributions . . . . .	53
3.2.6	Manual water and bed surface profiles . . . . .	54
3.2.7	Flow depth, flow area and average streamwise velocity . . . . .	55
<b>4</b>	<b>Morphodynamics of a width-variable gravel-bed stream: new insights on pool-riffle formation . . . . .</b>	<b>56</b>
4.1	Summary . . . . .	56
4.2	Introduction . . . . .	57
4.3	Results . . . . .	59
4.3.1	Identifying general response regimes with sediment flux, mean bed topography and bed sediment texture . . . . .	59
4.3.2	Topographic response: channel-wide and longitudinal profile development . . . . .	62
4.3.3	Effects of initial conditions on topographic responses . . . . .	70
4.3.4	Summary of main results . . . . .	71
4.4	Physically linking channel width changes to topographic response . . . . .	71
4.4.1	Downstream changes in flow speed and mobility . . . . .	71
4.4.2	Downstream changes in channel width and bed slope . . . . .	73
4.4.3	Theory for the local channel profile . . . . .	76
4.5	Discussion . . . . .	79
4.5.1	Predicting local channel slope along variable-width channels . . . . .	80

4.5.2	Maintenance of bed topography along variable-width channels: support for an emerging view . . . . .	84
4.5.3	Development of pool-riffles along variable width channels . . . . .	85
4.5.4	General implications of unique profiles for sediment transport theory . . . . .	86
4.6	Conclusions and next steps . . . . .	87
<b>5</b>	<b>Morphodynamic evolution of a width-variable gravel-bed stream: a battle between local topography and grain size texture . . . . .</b>	<b>89</b>
5.1	Summary . . . . .	89
5.2	Introduction . . . . .	90
5.3	Morphodynamic evolution metrics at the scale of a channel width . . . . .	92
5.3.1	Problem set-up . . . . .	92
5.3.2	Mass conservation . . . . .	95
5.3.3	Nondimensional Exner and Hirano equations . . . . .	97
5.3.4	Dimensionless channel response number: $N_e$ . . . . .	99
5.3.5	Calculations of $\delta_2$ , $U_b$ , $U_p$ and $N_e$ . . . . .	100
5.4	Results . . . . .	104
5.4.1	Topographic and sediment texture response numbers: $N_t$ and $N_p$ . . . . .	105
5.4.2	Sediment texture $\delta_2$ . . . . .	105
5.4.3	Channel response number: $N_e$ . . . . .	107
5.4.4	Results summary . . . . .	107
5.5	Discussion . . . . .	108
5.5.1	Local contributions to equilibrium conditions during pool-riffle and roughened channel development and maintenance . . . . .	108
5.5.2	Local and channel response numbers: a new view of fluvial equilibrium . . . . .	109
5.6	Conclusions . . . . .	110
<b>6</b>	<b>Concluding remarks . . . . .</b>	<b>112</b>
6.1	Summary . . . . .	112
6.2	Future directions . . . . .	113
	<b>Bibliography . . . . .</b>	<b>118</b>
<b>A</b>	<b>Numerical channel evolution model description . . . . .</b>	<b>131</b>
A.1	Summary . . . . .	131
A.2	1D nonuniform hydrodynamic model . . . . .	132
A.3	Mixed grain sediment transport model . . . . .	133
A.4	Channel evolution model . . . . .	135
A.5	Grain sorting model . . . . .	135
A.6	Model set-up and boundary conditions . . . . .	136
A.7	Model application to experiment PRE1 . . . . .	137

<b>B</b>	<b>Probabilistic friction angle model of particle mobility . . . . .</b>	<b>138</b>
B.1	Motivation . . . . .	138
B.2	Simplifying assumption of the present model . . . . .	139
B.3	Solution for $\tau_c$ with the $p$ simplification . . . . .	140
B.4	Sample simulation inputs and results . . . . .	142
B.5	Friction angle model availability and citation . . . . .	144
<b>C</b>	<b>Sediment transport as a rarefied phenomenon . . . . .</b>	<b>145</b>

# List of Tables

Table 2.1	Characteristics of the sampling program . . . . .	14
Table 2.2	McNemar sequential event transect test results . . . . .	19
Table 3.1	Experimental details for PRE1 . . . . .	46
Table 4.1	Experimental details for PRE1 . . . . .	63
Table 4.2	Values of downstream width change between subsampling locations . . . . .	65
Table 4.3	Values of average channel bed slope for initial and steady-state conditions . . . . .	67
Table 4.4	Mean values of $U_x/\bar{U}_x$ and $\tau^*/\tau_{ref}^*$ for subsampling locations . . . . .	74
Table 6.1	Mean values of normalized residual depth $\bar{\eta}_x$ for subsampling locations . . . . .	115

# List of Figures

Figure 1.1	Overview of links between watershed scale processes and channel morphology. . . . .	1
Figure 1.2	Aerial photograph of a mountain river segment in Southwest Iceland. . . .	3
Figure 1.3	Graphic of East Creek showing pool-riffle pairs and sequences with a photograph of one pair. . . . .	5
Figure 2.1	Majors Creek project site. . . . .	13
Figure 2.2	Majors Creek grain size distribution curves. . . . .	15
Figure 2.3	Record of mean daily flow for the study period. . . . .	16
Figure 2.4	Riffle sediment texture data organization for non-parametric tests. . . . .	20
Figure 2.5	Schematic illustration of SOM implementation. . . . .	22
Figure 2.6	Dimensionless bed load transport rates for Majors Creek. . . . .	25
Figure 2.7	Riffle texture point count results. . . . .	28
Figure 2.8	Spatial observations of riffle texture. . . . .	29
Figure 2.9	Spatial observations of riffle texture change. . . . .	30
Figure 2.10	SOM grid of characteristic temporal patterns of riffle texture. . . . .	31
Figure 2.11	Spatial distribution of the three characteristic riffle texture temporal patterns. . . . .	31
Figure 2.12	$V^*$ and residual pool and sediment volume change of the pool. . . . .	32
Figure 2.13	Repeat cross-sectional surveys at the riffle head. . . . .	33
Figure 2.14	Cumulative exceedence curves for streamflow and bedload sediment. . . . .	34
Figure 2.15	Test of the <i>Buffington and Montgomery (1999a)</i> shear stress-grain size model. . . . .	35
Figure 2.16	$V^*$ and fine sediment fraction change in the pool. . . . .	37
Figure 3.1	Overview graphic of the experimental setup and field stream reach. . . . .	43
Figure 3.2	PRE1 cumulative grain size distributions. . . . .	44
Figure 3.3	PRE1 initial bed topography conditions. . . . .	48
Figure 3.4	PRE1 details of water and sediment supply. . . . .	49
Figure 3.5	Example sub-sampled DEM and photograph pair for station 10000 mm, elapsed time 2150 minutes. . . . .	53
Figure 4.1	Downstream pool spacing as a function of the local channel width. . . . .	58

Figure 4.2	PRE1 morphodynamics summary: water and sediment supply, sediment flux, longitudinal mean bed topography, and geometric mean and characteristic coarse grain sizes. . . . .	60
Figure 4.3	Summary panel of PRE1 topographic responses illustrated with DEMs. . .	64
Figure 4.4	Summary panel of longitudinal profiles with zero-crossing residuals. . . .	66
Figure 4.5	Summary panel of SS box-and-whiskers plots. . . . .	68
Figure 4.6	Profile traces of average topographic response for two steady-state cases. .	69
Figure 4.7	Normalized topographic profiles of the six steady-state cases. . . . .	70
Figure 4.8	Average steady-state topography with downstream changes in flow speed and particle mobility. . . . .	73
Figure 4.9	Average channel bed slope as a function of the downstream change in channel width and flow speed. . . . .	75
Figure 4.10	Downstream changes in local mean flow speed for associated changes in channel width . . . . .	79
Figure 4.11	Prediction of local SS channel slope across the range of channel width conditions. . . . .	81
Figure 4.12	Summary of $\Lambda$ of Equation 4.11 vs. $\Gamma$ for PRE1. . . . .	83
Figure 5.1	Conceptual illustration of how topographic and sediment texture filters work.	93
Figure 5.2	Example values of $\delta_2$ of Equation 5.14 for differing values of $f_{us}$ , $f_b$ , and $f_{es}$ .	99
Figure 5.3	Example bed sediment texture data used to build stratigraphic column at station 10000 mm for $t_e = 19, 50$ and 110 minutes. . . . .	102
Figure 5.4	Summary of $Q_{sf}$ , $N_t$ , $N_p$ , $\delta_2$ and $N_e$ for PRE1. . . . .	106
Figure 6.1	Observations of residual depths for PRE1 determined from zero-crossing profiles. . . . .	114
Figure 6.2	Concept mountain streambed architecture regime diagram. . . . .	115
Figure 6.3	Photograph of an inverted pool-riffle channel segment along the Bridge River, near Camoo Creek Road, BC, Canada. . . . .	116
Figure A.1	Profile comparison of experimental and simulation outcomes for $t_e = 2150$ minutes. . . . .	137
Figure B.1	Schematic view of friction angle based mobilization problem as defined by <i>Kirchner et al. (1990)</i> . . . . .	139
Figure B.2	Sample grain size distribution for the friction angle model. . . . .	142
Figure B.3	Simulated grain mobility conditions using the friction angle model. . . . .	143
Figure C.1	Measured sediment flux from the flume. . . . .	145

# List of Symbols and Acronyms

## Roman Symbols

Symbol	Definition	Units
$[A_p]_{HSV}$	HSV color of a sampled pixel based on 1 of 12 colors used to paint sediment for experiments	(-)
$[A_p]_{RGB}$	RGB color of a sampled pixel based on 1 of 12 colors used to paint sediment for experiments	(-)
$A$	flow area	$L^2$
$b_w$	Wilcock-Crowe sediment transport function fitting exponent	1
$C_f$	dimensionless bed resistance coefficient	1
$C_n$	Courant stability number	1
$c_1$	image scale factor in the streamwise direction	(-)
$c_2$	image scale factor in the cross stream direction	(-)
$D_c$	characteristic grain size	L
$D_g$	geometric mean grain size	L

$D_{gf}$	geometric mean grain size of the sediment flux at the outlet	L
$D_{gs}$	geometric mean grain size of the sediment supply	L
$D_i$	grain size of percentile i	L
$D_{sm}$	mean grain size of the bed surface	L; mm
$D_{g'}$	ratio of $D_{gs}/D_{gf}$	1
$D_{90f}$	90 <sup>th</sup> percentile grain size of the sediment flux at the outlet	L
$D_{90s}$	90 <sup>th</sup> percentile grain size of the sediment supply	L
$D_{90'}$	ratio of $D_{90s}/D_{90f}$	1
DEM	digital elevation model; topographic map	(-)
$\bar{d}$	cross-sectionally average water depth	L
$F_i$	proportion of grain size class i of the bed surface used in Equation 2.10	1
$F_s$	total proportion of sand-sized sediments of the bed surface used in Equation 2.9	1
$F(x)$	step function for SOM Equation 2.8C	(-)
$Fr$	Froude number: $\bar{U}_x^2/gL_c$	1

$Fr_r$	Froude number ratio	1
$f_a$	volume probability density of grain size class $\psi$ on the bed surface, or of the active layer	1
$f_a^*$	normalized volume probability density of grain size class $\psi$ on the bed surface, or of the active layer	1
$f_b$	volume probability density of grain size class $\psi$ in the local bedload supply	1
$f_c$	characteristic volume probability density of grain size class $\psi$	1
$f_{es}$	volume probability density of grain size class $\psi$ of the exchange surface at the lower boundary of the active layer	(-)
$f_s$	volume probability density of grain size class $\psi$ in the local bed substrate, which contributes to $f_{es}$	1
$f_{us}$	volume probability density of grain size class $\psi$ in the long term average sediment supply	1
$g$	acceleration due to gravity on Earth	$L \cdot t^{-2}$
$g'$	measure of the relative bed strength: $g[(\rho_s/\rho_w) - 1]$	1
$h$	neighborhood or kernel function used in SOM Equation 2.8A	(-)

HSV	image hue, saturation and value (brightness) color values	(-)
$i_j$	grid points of the mapping domain for SOM Equation 2.8A	(-)
$i_k$	grid point of interest with application of the learning rate parameter for SOM Equation 2.8A	(-)
$K$	total number of grain size fractions used in Equation 5.19	(-)
$k$	constant between 1 and 2, here taken to have a value of 2, used to determine active layer length scale	(-)
$k_s$	measure of local bed roughness: $n_k D_{90}$	1
$L$	forward difference length scale used in Equation 4.1	L
$L_a$	active layer length scale: $kD_{90}$	L
$L_r$	length scale ratio	1
$N_e$	dimensionless channel response number	1
$N_p$	dimensionless bed sediment particle number	1
$N_t$	dimensionless bed topography number	1
$n$	learning rate parameter used in SOM Equation 2.8A	(-)

$n_k$	roughness scaling factor	1
$px$	pixel	(-)
$Q$	Cochran non-parametric test statistic	1
$Q_r$	flow rate ratio	1
$Q_{sf}$	sediment flux per unit channel width	$L^2 \cdot t^{-1}$
$Q_{ss}$	sediment supply per unit channel width	$L^2 \cdot t^{-1}$
$Q_w$	water supply per unit channel width	$L^2 \cdot t^{-1}$
$q_b^*$	dimensionless sediment flux for grain size class $i$	1
$q_b$	total sediment flux per unit channel width	$L^2 \cdot t^{-1}$
$q_{bi}$	sediment flux for grain size class $i$ per unit channel width	$L^2 \cdot t^{-1}$
$q_w$	unit flow rate: $Q_w/w$	$L^2 \cdot t^{-1}$
$q_\psi$	sediment flux for grain size class $\psi$ per unit channel width	$L^2 \cdot t^{-1}$
$R$	relative density: $R = [(\rho_s/\rho_w) - 1]$	1
RGB	image red, blue and green color values	(-)
$S$	elevation gradient	1

$S_{local}$	local elevation gradient determined between subsampling locations	1
SS	steady-state	(-)
Sinuosity	ratio of channel length to valley length	1
$s_b$	grain size fraction sample standard deviation of the local bedload supply	1
$s_{es}$	grain size fraction sample standard deviation of the local exchange surface	1
$s_{us}$	grain size fraction sample standard deviation of the upstream bedload supply	1
$t$	time	t
$t_a$	activation time	t
$t_e$	experimental elapse time	t
$t_o$	dimensionless experimental time	1
$t_r$	bed response to steady-state period	(-)
$t_t$	bed response to developing flow period	(-)
$t^*$	dimensionless time	1
$U_b$	bed speed: rate of channel topography change	$L \cdot t^{-1}$

$U_c$	characteristic velocity	$L \cdot t^{-1}$
$U_p$	particle speed: rate of sediment particle size change	$L \cdot t^{-1}$
$\bar{U}_x$	Cross-sectionally averaged downstream flow velocity	$L \cdot t^{-1}$
$\bar{U}_{xr}$	Cross-sectionally averaged downstream flow velocity ratio	1
$u(z)$	vertical velocity	$L \cdot t^{-1}$
$u^*$	shear velocity	$L \cdot t^{-1}$
$V^*$	dimensionless pool sediment storage	1
$w$	channel width: measured from top of bank to top of bank	L
$w_o$	normalized channel width: $w/w'$	1
$w'$	reach average channel width: average of widths measured over a lengthscale of many channel widths	L
$\bar{w}$	average channel width: average of widths measured over a subsampling region with lengthscale of 320 mm	L
$W_i^*$	Wilcock-Crowe dimensionless sediment transport function	1
$X$	real world coordinate in the streamwise direction	L

$X_o$	real world coordinate of the origin	L
$x$	streamwise location	L
$x^*$	dimensionless streamwise location	L
$\hat{x}$	image coordinate in streamwise distance	L
$x_o$	image center coordinate	L
$Y$	real world coordinate in the cross stream direction	L
$Y_o$	real world coordinate of the origin	L
$\hat{y}$	image coordinate in cross stream distance	L
$y_o$	image center coordinate	L
$z$	elevation of grain top used in the friction angle based mobility model	L
$z_o$	elevation of the lowest grain elevation exposed to the oncoming flow used in the friction angle based mobility model	L
$z_j$	initial data vectors used in SOM	(-)

## Greek Symbols

$\alpha$	width to depth ratio: $w/d$	1
$\alpha_r$	dimensionless sediment transport coefficient	1

$\beta$	partitioning coefficient that ranges from 0 to 1	1
$\Gamma$	downstream change in channel width	1
$\Delta$	denotes a difference of some variable or quantity	(-)
$\frac{\Delta w(x)}{\Delta L}$	forward difference equation where L is the differencing length scale, and $w$ is differencing quantity	1
$\delta_1$	$(f_b - f_{es})/\varepsilon$ expresses the dissimilarity between the fractional composition of the local bedload supply and the local exchange surface	(-)
$\delta_2$	expresses the dissimilarity between the fractional composition of the three grain size populations which contribute to bed sediment texture: $f_{us}/(f_b - f_{es})$	(-)
$\varepsilon$	solid fraction in the bed: $1 - \phi$	(-)
$\eta$	channel bed elevation	L
$\eta^*$	dimensionless channel bed elevation	1
$\kappa$	van Karmen's constant, here assumed to have a value of 0.407	1
$\Lambda$	$\frac{(g')^{0.5} D_c^{1.5}}{\varepsilon U_c L_c}$	1
$\rho'$	relative density: $(\rho_s/\rho_w) - 1$	1

$\rho_s$	sediment density	$m \cdot L^{-3}$
$\rho_w$	water density	$m \cdot L^{-3}$
$\sigma_g$	geometric standard deviation	L
$\sigma_v$	$\delta_1/L_a$	(-)
$T$	time scale of local bed elevation adjustment	t
$\tau$	shear stress	$m \cdot L^{-1} \cdot t^{-2}$
$\tau^*$	dimensionless Shields stress condition	1
$\tau_c^*$	critical or threshold dimensionless Shields stress	1
$\hat{\tau}^*$	normalized dimensionless Shields stress	1
$\tau_{ref}^*$	reference dimensionless Shields stress	1
$\tau_{c50}$	threshold shear stress for the 50 <sup>th</sup> percentile grain size	$m \cdot L^{-1} \cdot t^{-2}$
$\tau_{c50}^*$	dimensionless threshold shear stress for the 50 <sup>th</sup> percentile grain size	1
$\tau_{ri}$	reference threshold shear stress for grain size $i$	$m \cdot L^{-1} \cdot t^{-2}$
$\tau_{rm}$	reference threshold shear stress for the mean grain size of the bed surface $i$	$m \cdot L^{-1} \cdot t^{-2}$

$\tau_{rs50}$	reference threshold shear stress for 50 <sup>th</sup> percentile grain size of the bed surface	$m \cdot L^{-1} \cdot t^{-2}$
$\phi$	porosity of bed sediments determined as volume of the voids and taken here as a constant: 0.40	(1)
$X$	length scale of local bed slope adjustment	L
$\chi$	numerical constant	(-)
$\psi$	$\log_2$ grain size scale: $\log_2 D = D_{psi}$	(-)

---

# Acknowledgments

Seven years ago, Emma and I hatched a plan to move to Vancouver. A new adventure, aimed at providing me the privilege of sitting around and thinking all day, about problems that maybe only a handful of other people in the world care about. This move was an attempt to get back in touch with my curiosity for how planet Earth works. In the end, this has been an utterly life changing journey, touched by many people. Here I endeavor to thank all of you.

In the Fall 2010, I met Marwan Hassan outside his flume lab of the old Ponderosa Building. I was prepared to beg, plead really, for a chance to work with him and learn about his experimental craft. Instead, I was met with an immediate openness and acceptance, which in my experience, is a rare trait amongst us humans, let alone academic researchers. We took this journey together, as world citizens, and in the process you have taught me to stand on my own two feet, and chart my own path through the world of learning. More importantly, there were times when you stood back and let me make mistakes, no matter how much time you knew it would cost me, because you knew it was the only way I would learn. And learning, for us, is what matters. Thank you does not begin to express how lucky I feel to have your mentorship and support over the last 5 years, and friendship. Here's to many more years of fun together, venturing into questions which at present, may only be a faint glimmer of thought.

In 1999, I met Mark Jellinek when I was working at Marmot Mountain Works, in Berkeley, CA. Mark has a mass to his personality that makes our own sun jealous. As a result, I immediately went into orbit. We have shared much together over the years, but to the present point, you have shaped me for the scientist I am. I have pile, upon pile of papers, with comments scribbled in red, blue, black, green, really all the colors (guess you got bored with just one), which together, is testament to the craft and precision you have opened to, and taught me. Many of my thoughts and ideas live in my head. Thanks to your untraining, and then retraining, that will change. To all the late nights, and early mornings reading my half-baked, poorly communicated ideas - thanks for your unwavering support, mentorship and acceptance of this challenge. Despite all of this, I still will not share the maple-peacan scone I saved from yesterday (ever!). And since the first time you crushed my hand in the Marmot entrance, the initial orbiting response has grown into something more a kin to a binary star system. But, I will always stand in awe.

In the Fall 2012 I had the privilege to meet Carles Ferrer-Boix. Your friendship and support through my work have been absolutely invaluable. You have taught me much, and have

played an instrumental role in development of all my seemingly crazy ideas, and I assure you, Marwan and Mark thank you. Your patience and supportive teaching in working through difficult ideas is something I will strive to carry forward. Sometime soon, may we enjoy a nice Catalonian Cava on the southern beaches of Spain, and chart a path to venture into some new, and exciting problem. Here's to the road ahead Carles.

To my lab mates from both Marwan's lab, and the mjcj-research group. Carles, Leo, David, Katie, Ashley, Elli, Maria, Tobias (thanks for the hours working with me trying to figure out the composite photograph!), Matteo, Marco, Emma, Yinlue, Kevin, Alex, Claudia, Ilana; David, Reka, Andreas, Anna G., Anna M, Thomas, Yoshi (thanks for the EOSC 352 night time home-work jams!), Natasha, Georgia, okay, this is getting ridiculous. I am the luckiest person I know to have shared and learned from each of you over the past five years - thanks. The most cherished moments go to David, Reka and Andreas though, for having taught me about the physics of Guinness, the physics of planetary bow shocks (just about the coolest thing ever), and how to plan an asteroid mining mission. To Sir Christian, thanks for teaching me about the ways of the force. You have equipped me to venture into the unknown. To David Furbish, thanks for support over these past two years. You have given me the courage to take the next step. To Olav Slaymaker, you have and always will be my philosophical guru. To John Buffington, thanks for your support and careful review of my PhD research proposal. Your comments and thoughts had a significant role in how I took the proposal forward. And to Tom Dunne, thanks for your careful review of my thesis.

To my Mother, Father and sister Suzanne, thank you for your love and support through it all. You cultivated my curiosity for science and nature, and encouraged me to attend Case and pursue my passions, which among all other things has shaped almost every aspect of my adult life. It all began high up in those trees in the woods, waving in the wind, and with the first chemistry set you bought me, for which the local ant and rock population suffered endlessly. Here's to all the nights sitting around the table drinking tea and eating pinwheel cookies, entertaining all my questions. All my love and thanks.

Many other people have helped and supported me along the way. To Peter Whiting, you gave me a chance and my start as a scientist, nurturing me through those early years. I am forever grateful for your kindness, and setting me on a path that has evolved into an endless curiosity for rivers, and how they work. Thanks Peter. To Barry Hecht, you taught me the value of the big picture, and folding together the many aspects of Earth Science to shape the story of place. You are one of a kind, and I am beyond lucky to have learned from you. Thanks for everything, most of all, room to grow as an Earth Scientist, under your ever watchful eye. To my colleagues at Balance, thanks for the opportunities to venture into the world of reshaping how rivers look. It is one we will learn from for many years to come, and it would not have been possible without your engagement, help and support. Here's to many more sundowns, working with an operator to place that last piece of streamwood. To Dr. A, you were the hook, line and sinker that got me into Earth Science. I will never forget your enthusiasm for teaching

and life. To my SIESD NCED crew, thanks for a wonderful 10 days in 2016! Here's to new friendships and collaborations.

The work presented in this thesis was thankfully funded by the University of British Columbia Four-Year Fellowship, the National Science and Engineering Research Council of Canada Alexander Graham Bell Three-Year Research Fellowship, the Mitacs Accelerate Program Internship, and the Canada Foundation of Innovation. I thank these funding agencies for their generous support of my research, which included painting 6 tons of rock. The unexpected consequence of which, was that the experimental channel looked as if it were filled with peanut M&Ms, explaining why it took so long to complete my work, and why Aidan and Mira visited the lab, frequently. Ever excited to work with me.

To all the rivers that I have gazed upon, measured, prodded and otherwise sat next to. Thanks for sharing some of your secrets...

Rivers and streams, far and wide,  
Change their shape, and their rise,  
Ask why is this so, and you will see,  
It is for how size changes, simple as can be.

# Dedication

This journey is dedicated to the fun-hoggin grissies: Emma, Aidan and Mira. Life is an adventure of many journeys. I could not, and would not have done this one without each of you. Your smiles, giggles, big time wrestling on the bed, walks in the woods for hot chocolate, help shoveling sediment in the Lab, putting up with my late nights running experiments, or writing code, your curiosity for those big math problems that had an unexciting answer of zero, and your absolute love and support saw me through it all. This milestone is as much yours as it is mine. Congratulaton! I can't wait for our next journey. All my love and gratitude.

# Chapter 1

## Introduction and motivation

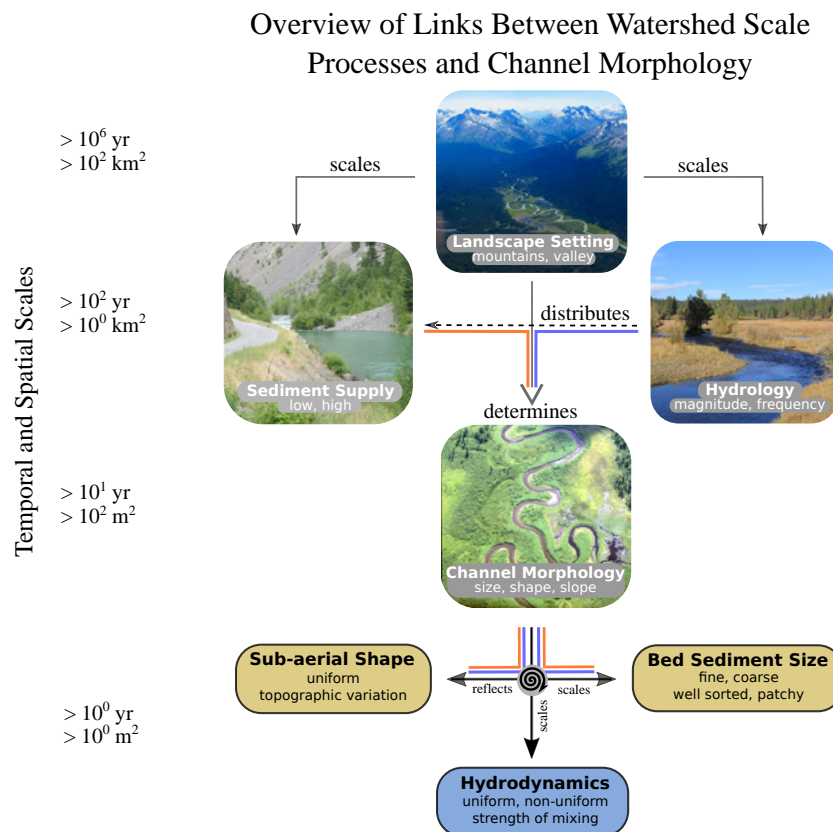


**Figure 1.1:** Overview of links between watershed scale processes and channel morphology. The landscape setting scales basin contributions of water and sediment, which together determines channel morphology as one moves down a river basin. Channel morphology in turn reflects local bed shape, and scales bed sediment texture and hydrodynamics, which evolve in feedbacks which tend to reinforce local responses in the absence of significant disturbances. Approximate temporal and spatial scales of these attributes are provided at the left. Figure motivated by *Church and Jones (1982); Church (2006); Hassan et al. (2008)*

## 1.1 Overview

The landscape setting, its relief, geographic location and diversity scales the supplies of water and sediment delivered to channel networks (Figure 1.1). Streamflow, in turn and over many years distributes and transports the sediment supply throughout the basin. This drives and determines the development of channel morphology, which over length scales of many channel widths comprises a river's overall shape, size, and longitudinal slope. The broad character of channel morphology is described at the local scale of a channel width by the shape of the bed, the spatial distribution of sediment grain sizes on the bed, which we define as bed surface texture, and the flow dynamics, which is characterized by the spatial character of the velocity field. For time scales of many floods, and upstream supplies which vary around some long-term average, the shape of the bed, the bed surface texture and the velocity field interact through feedbacks which lead to local conditions of sediment continuity (*Church and Ferguson, 2015*).

Within this context, we understand that changes to the upstream water and sediment supplies through large floods or landslides can cause changes to channel morphology throughout the downstream basin. When this occurs, four basic morphologic responses are possible (Figure 1.1): a change of channel position, size, steepness, or bed surface roughness. A change of channel position occurs through meandering of the whole channel, or of the primary flow path, called the thalweg, and through complete channel relocation by break out and avulsion. A change of channel size occurs through bank erosion, and through mass movement encroachment, leading to partial channel blockage. A change of river bed steepness occurs through sediment deposition, or net bed material entrainment. A change of bed surface texture occurs through preferential entrainment of particle size fractions present on the bed surface, or through deposition of particle size fractions present within the sediment supply, but which occur in differing concentrations on the bed surface. Predicting how a particular channel reach of many widths in length will respond is difficult, because the four responses are coupled by feedbacks, and these feedbacks trigger additional responses, which occur over differing time scales.

I simplify the problem in two ways. First, we consider rivers within mountain settings, where lateral mobility is constrained by banks and valley walls sufficiently strong to drive development of river reaches that are relatively straight, or which exhibit minor amounts of curvature. Second, we recognize that rivers tend to express sizes which:

1. Reflect the supply of water and sediment delivered by floods of moderate magnitude (*Wolman and Miller, 1960; Leopold and Maddock, 1953; Leopold et al., 1964; Emmett, 1999; Whiting et al., 1999; Emmett and Wolman, 2001*), or a series of moderate floods (*Pickup and Rieger, 1979*), conditioned over times scales of at least  $10^1$  to  $10^2$  years, depending on basin size (*Howard, 1982*); and
2. Are constrained by local conditions such as the occurrence of bedrock outcrops, landslide

deposits, and mature stands of riparian vegetation.

This perspective immediately focuses the problem to one whereby rivers exhibit a downstream variation of size, and given the links shown in Figure 1.1, floods drive adjustments to local channel steepness, bed surface texture, and flow structure, for which the adjustments are modulated by local width conditions (*Bolla Pittaluga et al., 2014*). My interest, therefore, is with river size, and my thesis specifically examines variations of river size at the local scale, and how the properties of size variation mechanically drives riverbed shape, sediment texture and flow character.



**Figure 1.2:** Aerial photograph of a mountain river segment in Southwest Iceland, with flow direction from image right to left. The photograph illustrates channel width variations that range in length from 1 to 5 times the local average width, driven by the occurrence of bedrock, landslide deposits and lateral bar deposits. Image source: Google Earth.

## 1.2 Motivation

### 1.2.1 River size at the local scale

Rivers change size at length scales that range from a few channel widths (Figure 1.2), considered the local scale, to that of the full river. Size change at the largest scale for rivers within non-arid climatic zones reflects increasing downstream contributions of water (*Leopold and Maddock, 1953*), but changes at the scale of a few channel widths are due to local processes and properties, for example the occurrence of bedrock, riparian tree mortality, or landslide deposits (Figure 1.2). We understand that channel width influences the expression of channel bed architecture, which includes bed shape, or topography, and the bed surface texture (*Richards, 1976a; Keller and Melhorn, 1978; Lisle, 1979; Montgomery and Buffington, 1997; Lisle and Hilton, 1999; Chartrand and Whiting, 2000; Chin, 2002; Church, 2006; Church and Zimmermann, 2007; Chin, 2002; Chartrand et al., 2011*). But how and why does width matter for channel bed architecture?

Understanding width-bed coupling at the local scale is important because each are basic

elements of fluvial landscapes, but in particular:

- a. Width scales how much sediment is stored at various points of a river system. Therefore, width regulates the redistribution of sediment down a river, including attenuation of sediment signals from mass movements, earthquakes or forest fires;
- b. Width scales the footprint and diversity of habitats available to aquatic organisms. Therefore, width and its variation sets the foundation of how streams support aquatic organisms, and as a result, width is a key element to the provision of ecosystem services by rivers and streams; and
- c. The periodic character of meanders, pool-riffles and step-pools are each described by channel width *Leopold et al. (1964); Richards (1976a); Keller and Melhorn (1978); Chin (2002)*. Therefore, width is one of the basic properties of rivers which helps to explain their physical character.

Furthermore, the size of rivers reveals information about the local physical character of a river segment, as well as the history of how the physical character has shaped responses driven by upstream conditions.

### **1.2.2 Evidence and knowledge gaps of the physical connection between channel width variation and pool-riffle architecture**

Pool-riffles are perhaps the most common channel architecture of mountain streams, where they occur in pairs (*Carling and Wood, 1994*), and often in sequences of many pairs. The periodic nature of pool-riffles highlights the idea that an underlying, and spatially consistent mechanism is responsible for formation and maintenance (Figure 1.3). A viable explanation stems from the observation and experimental replication of pool collocation with channel and valley segments that are narrowing, or are relatively narrow (*Richards, 1976a; Dolan et al., 1978; Carling, 1991; Clifford, 1993a; Lisle, 1986; Sear, 1996; Montgomery et al., 1995; Montgomery and Buffington, 1997; Thompson et al., 1998, 1999; Repetto et al., 2002; MacWilliams et al., 2006; Harrison and Keller, 2007; Wilkinson et al., 2008; Thompson and McCarrick, 2010; White et al., 2010; de Almeida and Rodríguez, 2012; Venditti et al., 2014; Nelson et al., 2015*), and riffle collocation with segments that are widening, or are relatively wide (*Richards, 1976a; Sear, 1996; Carling, 1991; Montgomery and Buffington, 1997; Repetto et al., 2002; Wilkinson et al., 2008; White et al., 2010; de Almeida and Rodríguez, 2012; Nelson et al., 2015*). One- and multi-dimensional numerical models built to simulate specific field cases also reproduce the spatial association of pools and riffles with relatively narrow and wide channel segments (*Thompson et al., 1998; Booker et al., 2001; Cao et al., 2003; MacWilliams et al., 2006; Harrison and Keller, 2007; de Almeida and Rodríguez, 2011, 2012*) (See Appendix A). Therefore, spatial correlations between width and pool-riffle architecture are suggested by multiple lines of evidence.

*Yalin (1971)* proposes that channel spanning, macroturbulent eddies with overturning length scales comparable to the flow depth are responsible for riffle spacing along straight channel

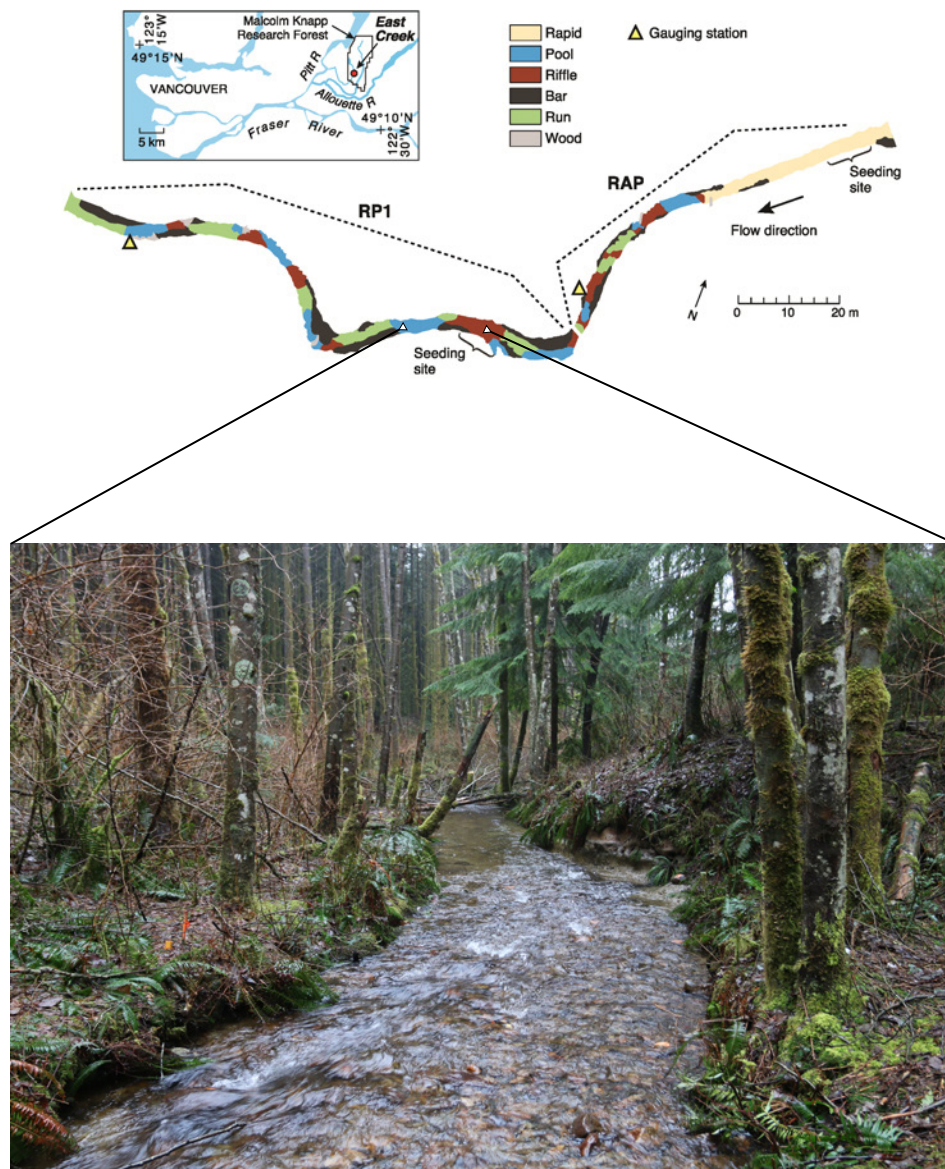


**Figure 1.3:** Graphic of East Creek showing pool-riffle pairs and sequences with a photograph of one pair. The overview map is from *Papangelakis and Hassan (2016)*, and the photograph shows a pool-riffle pair mid-way down RP1 during a relatively low winter flow condition. The photograph perspective is looking downstream. Photograph by Shawn Chartrand.

segments with a meandering thalweg. *Carling and Orr (2000)* interpret Yalin's hypothesis as related to the length scale over which these eddies deliver sufficient momentum to the channel bed to entrain sediment and dig a pool. The theoretical lower limiting case for the eddy length scale is approximately three channel widths (*Yalin, 1971; Carling and Orr, 2000*), or half the average meander wavelength (*Richards, 1976a*); the central tendency of the eddy length scale based on field data is six channel widths (*Richards, 1978; Carling and Orr, 2000*). But pool-

riffle architecture is not necessarily limited to large-scale meanders, or a meandering thalweg. *Lisle* (1986) found that stationary pools and associated riffles were colocated with stream side obstructions and bedrock outcrops, often at channel bends.

*Clifford* (1993a) combines the above works and proposes a systematic 3-step process of pool-riffle formation, that is both probabilistic and autogenic in nature, and consists of a pool digging phase, followed by maturation and autogenic (i.e driven by emergent local conditions) phases. Phase one is probabilistic in nature, and begins with the random occurrence of a local obstruction to the flow, which stimulates pool construction. The obstruction drives lateral flow convergence into the developing pool area due to local width narrowing, which establishes a streamwise or cross-stream gradient in velocity sufficient to entrain bed sediments for pool development. Entrained bed sediments are transported downstream, or away from the pool, and deposited to form a riffle. At the end of phase one, an upstream-downstream pool-riffle pair has formed, and the obstruction which drove development persists. During phase 2, the pool-riffle pair matures, an upstream riffle develops, and the nucleating obstruction either persists, in the case of bedrock, etc., or is removed. The upstream riffle takes shape due to the presence of the pool, and associated development of a streamwise gradient in velocity, and particle drag, which shapes the upstream bed to slope into the pool. At the end of phase 2, a pool-riffle unit consisting of a riffle-pool-riffle morphologic feature emerges. During phase 3, the autogenic process begins and further pool-riffle pair creation occurs due to local flow and sediment transport perturbations driven by the initial pool-riffle unit.

Published field measurements, as well as physical experiments provide constraints on the overall width variation needed to drive pool-riffle development and maintenance. Fieldwork conducted by *Lisle* (1986) suggests that an obstruction extend at least 30% of the channel width to develop a channel-spanning pool. *Wilkinson et al.* (2008) show by contrast that width encroachment as small as 16% may be sufficient to promote pool development in an experimental setting. Yet, flume experiments conducted by *Thompson and McCarrick* (2010) demonstrate pool and downstream riffle development for a width reduction of 40%, and in the most recent case, *Nelson et al.* (2015) produce sequences of pool-riffles along a sinusoidal shaped channel that has a downstream width variation of 40%. Furthermore, 1-D numerical model results of specific field cases suggest that roughly 50% may be necessary (*Carling and Wood*, 1994; *de Almeida and Rodríguez*, 2011, 2012). In summary, the published results show that pool-riffles form and are maintained when downstream total width change varies from 15 to 50%.

### **1.3 Making sense of coupling between channel width and bed architecture**

My primary objective is to examine coupling between local variations of channel width, and channel bed shape and texture. Through this objective I address the questions of how and why width matters, and in the process build understanding of channel bed architecture expression, for the natural conditions of mountain stream settings. I use a combination of field

and experimental work to address my primary objective. The field study addresses next steps motivated by *Nelson et al.* (2009) and *Hodge et al.* (2013), and the experimental study builds directly from *Thompson et al.* (1998); *de Almeida and Rodríguez* (2011, 2012); *MacVicar and Rennie* (2012) and *Nelson et al.* (2015), with the key focus that natural channels exhibit non-uniform changes in downstream channel width (e.g. *Richards*, 1976a; *Thompson et al.*, 1999; *Harrison and Keller*, 2007; *Thompson and McCarrick*, 2010; *de Almeida and Rodríguez*, 2012; *Nelson et al.*, 2015).

I address the primary thesis objective through four specific questions and knowledge gaps:

- A. How variable is riffle surface texture in time and space due to natural variations of water and sediment supply? (Chapter 2)
- B. What mechanisms give rise to, as well as modulate, the spatial organization of pools and riffles along rivers? (Chapter 4)
- C. Are all pool-riffles created by a similar set of processes, and does channel bed constitution predetermine a particular outcome? (Chapter 4)
- D. Which physical processes shape the (dis)equilibrium conditions of gravel-bed streams? (Chapter 5)

In Chapter 2, I address question A through a 3-year field-based study of pool-riffle texture and sedimentation dynamics, along a gravel-bed stream located in coastal California, U.S. I demonstrate that riffle texture change is spatially organized across 11 sediment transporting events, including a 20-year flood, and that the pool-riffle pair responds to the upstream sediment supply in a dissimilar manner for 10 of the 11 transport events. Riffle texture measurements occur through a fixed sampling grid of five transects, where texture is determined at 160–180 locations, depending on riffle footprint. Pool sedimentation measurements occur by quantifying the sediment storage volume relative to the available sediment storage volume of the upstream pool. Cochran's Q and McNemar's tests indicate that riffle sediment surface texture is spatially and temporally varied across each sampling transect, with distinct fining and coarsening trends. This result supports and motivates use of self-organizing maps to characterize the spatial and temporal character of riffle texture. Self-organizing maps (SOM) is a type of machine learning which uses unsupervised learning algorithms. Application of SOM to pool-riffle sediment texture shows that the study riffle responds to sediment supply events in a spatially organized way, with different temporal trends carried preferentially over specific riffle areas. Texture response occurs in a manner that is disconnected from the upstream pool, except for the largest flood, which triggers a fining trend of both pool and riffle. The work demonstrates that riffles in approximate topographic equilibrium with upstream water and sediment supplies, modulate supply changes with texture responses that are spatially organized. This result has implications for pool-riffle maintenance, because organized texture responses are up and till now, an unidentified part of riffle maintenance processes. For a majority of floods, maintenance occurs in pool and riffle along differing trajectories, despite

neighboring proximities. This highlights the localized nature of sediment transport, within continually disturbed gravel-bed river systems.

In Chapter 3, I provide the details of pool-riffle experiment 1 (PRE1), conducted at the University of British Columbia, Canada. I use the experiments to address Questions B–D, with results presented in Chapters 4 and 5. Experiments occurred in an 18-m long flume which re-circulates water but not sediment. Experimental set-up was guided by a gravel-bed stream reach located near Maple Ridge, B.C., Canada. The experiment uses three different flow rates, ranging from an approximate 2-year, to a 10-year flood. Sediment supply is at or near the theoretical capacity. The key characteristic of the experimental channel is downstream varying width, with downstream gradients that range from  $(-0.26)$ – $(+0.18)$ . The experiment uses a poorly-sorted grain size distribution that ranges from 0.5–32 mm, with a geometric mean size of 7.3 mm and a geometric standard deviation of 2.5. The experiment consists of two phases, an initial and repeat phase. During the experiments I collect (a) 1 mm resolution topographic maps (DEM) of the entire channel; (b) composite photographs of the entire channel, mapped to the same coordinate system of the DEMs; (c) 1 Hz sediment flux; and (d) manual measurements of longitudinal bed topography and water surface elevation. This data set facilitates examination of questions B–D. The experiments produce pool, riffle and roughened channel features, which persist across the full range of external supplies.

In Chapter 4, I address questions B and C with PRE1 experimental data, theory and scaling to demonstrate that bed topography expression is systematically organized across the full range of experimental width conditions. Experimental data indicates that pools develop for downstream channel width gradients less than  $-0.10$ , riffles for width gradients  $\Delta w(x) \cdot \Delta L$  greater than  $+0.10$ , and roughened channel features for width gradients in between  $-0.10$  and  $+0.10$ . Topographic diversity is higher when transport conditions are closer to threshold, but topographic relief is higher for increasing transport conditions. This suggests that the effect of channel width variation changes with water and sediment supply, becoming stronger as supplies increase. Results from PRE1 and two other studies demonstrate that the local bed slope  $S_{local}$  exhibits a systematic trend for downstream width gradients that range from  $(-0.30)$ – $(+0.30)$ , and for larger-scale reach averaged bed slopes that vary by 1 order of magnitude. This results motivates development and use of a mathematical model to examine the coupling between the local bed slope, and the downstream channel width gradient. The mathematical model shows that the local bed slope response is driven by  $\Lambda$ , which is a ratio of velocities that represents slope production as a balance between the characteristic spreading time scale of bed sediments, to the forcing time scale that quantifies the magnitude of local momentum flux imparted to the bed surface. Characteristically large spreading time scales drive pool development, small time scales give rise to riffles, and intermediate conditions lead to roughened channel segments. These results are described reasonably well by the mathematical model, which given the range of larger-scale reach average slopes, suggests a scale invariant response, that may be a generalized attribute of river segments governed by downstream changes to channel

width.

In Chapter 5, I address question D with PRE1 experimental data, theory and scaling to demonstrate that fluvial equilibrium conditions  $N_e$  are more readily achieved under increasing supplies of water and sediment, when the rate of local topographic  $N_t$  and bed surface texture  $N_p$  change are comparable. I present a new local view of fluvial equilibrium using statements of mass conservation for the bulk bed, and the particles that compose the bed, scaled to quantities that represent the time, length and dynamical properties of gravel-bed mountain streams. My perspective is motivated by an idea that local bed topography and bed sediment surface texture act as filters to incoming supplies of sediment. The topographic and texture filters change the upstream sediment supply  $Q_{ss}$  through deposition (topographic filter), or via size-preferential entrainment (texture filter), or both. Specifically, and in the simplest case, sediment particles in motion entering a local bed region exhibit 1 of 2 outcomes. The particles can either continue in transport downstream, or come to rest. The outcome is determined by the topographic filter, which scales the average local downstream velocity magnitude  $U_x$ , which in turn scales the average particle drag. Particles resting on the bed surface also exhibit 1 of 2 outcomes. The particles can either remain at rest, or can be entrained by the flow. The outcome is determined by the texture filter, which scales the local bed surface roughness, which in turn scales the mobility of particles resting on the bed surface. The resultant equilibrium statement  $N_e$  quantifies the topographic and texture filters as a ratio of velocities, that represents the rate of change of local bed topography, and bed surface composition. Accordingly, fluvial equilibrium is achieved when the ratio of velocities is  $O(1)$ . The work demonstrates that for the PRE1 conditions, rates of topographic adjustment are dominant and protracted when particle mobility conditions are relatively close to critical, and that  $N_e$  trends toward equilibrium, but does not achieve it. At higher relative mobility conditions, however, rates of topographic and bed surface composition change are rapid, and exhibit comparable values after an initial response period that is relatively short in duration. Hence, fluvial equilibrium is more readily achieved. My view of equilibrium is one of the few attempts to build a formal definition for equilibrium in gravel-bed rivers. It is also flexible in terms of the choices that can be made regarding appropriate scales, and as a result it may be useful beyond the present application.

## Chapter 2

# Pool-riffle sedimentation and surface texture trends in a gravel bed stream

### 2.1 Summary

A 3-year field campaign was completed to investigate spatial and temporal variability of sedimentation trends for a single pool-riffle pair located in the Santa Cruz Mountains, California. Our measurements represent a range of hydrologic conditions over eleven sediment mobilizing events. Two different statistical methods were used to explore riffle sedimentation. Cochran's Q and McNemar's non-parametric tests (one method) indicate that riffle sediment surface texture was spatially and temporally varied at the transect level. For McNemar's test, variation was significant at  $p < 0.05$ , with several trends evident, including strong riffle fining triggered by a 20-year flood event. A nonlinear, empirical orthogonal function method known as Self-organizing maps (SOMs; the second method) shows that riffle sediment surface texture is well described by two characteristic temporal signals, and one transitional signal at the sampling node level. SOM mapping to each sampling node clearly shows riffle sediment surface texture change was spatially organized over the eleven sediment mobilizing events. Observations of pool sediment storage indicate that the pool-riffle pair exhibited a coupled sedimentation response (i.e. similar texture trends between pool and riffle) following the 20-year flood. The coupled response was characterized by a trend toward overall sedimentation conditions that were similar to those measured at the beginning of the study. The reported texture trends may be of interest to salmonid habitat studies that examine factors contributing to successful vs. unsuccessful fry emergence.

### 2.2 Introduction

Mountain streams exhibit a diversity of bed sediment textures that manifest at a range of scales. Bed sediment texture is defined as the general spatial distribution of grain sizes on a streambed (the focus of this study) (Venditti *et al.*, 2012), or the detailed distribution of bed

sediments into patches distinguished by grain size and sorting (Paola and Seal, 1995; Buffington and Montgomery, 1999a). The spatial and temporal character of bed sediment texture is driven by localized patterns of sediment transport, which continually responds to variations of upstream sediment supply (Parker and Klingeman, 1982; Dietrich *et al.*, 1989, 2005; Lisle *et al.*, 1993; Buffington and Montgomery, 1999b; Hassan and Church, 2000; Nelson *et al.*, 2009), spatial patterns of local grain size organization (Paola and Seal, 1995; Church *et al.*, 1998; Hassan and Church, 2000), as well as spatial patterns of local bed topography (Dietrich and Smith, 1984; Dietrich and Whiting, 1989; Clayton and Pitlick, 2007; Nelson *et al.*, 2009, 2010). In sum these works provide for clear process linkages to bed sediment texture development and response. But relatively few field-based studies of bed sediment texture variability over many hydrograph events or field seasons have been completed (Jackson and Beschta, 1982; Lisle and Madej, 1992; Clifford, 1993b; Lisle and Hilton, 1999; Dietrich *et al.*, 2005).

Spatial and temporal variation in bed sediment texture has important implications for the availability of habitats suitable for salmonids (Kondolf and Wolman, 1993; Kondolf, 2000), successful emergence of salmonid fry from streambed sediments and processes that maintain pool-riffles sequences (e.g. Hodge *et al.*, 2013). Since publication of the pool-riffle velocity-reversal maintenance hypothesis (Keller, 1971), subsequent studies have shown that pool-riffle pairs are maintained through a combination of at least several mechanisms that operate and interact over a range of temporal and spatial scales (Lisle, 1979; Clifford and Richards, 1992; Clifford, 1993b; Sear, 1996; Thompson *et al.*, 1999; Carling and Orr, 2000; MacWilliams *et al.*, 2006; Thompson, 2010; White *et al.*, 2010; Sawyer *et al.*, 2010; de Almeida and Rodríguez, 2011; Caamaño *et al.*, 2012; Hodge *et al.*, 2013). Pool-tail and riffle-crest sediment structuring enhances the relative stability of a pool-riffle pair. Structuring occurs through in situ grain vibration and short particle movements (Sear, 1996; MacVicar and Roy, 2011; MacVicar and Best, 2013), and in some cases jetting of fines into pool tail and riffle crest sediments (Hodge *et al.*, 2013), resulting in a mortaring effect. Pool depth and volume is maintained over multi-year and longer timescales via flow convergence into a pool (Thompson and McCarrick, 2010), driven by topographic steering of flow by bars (MacWilliams *et al.*, 2006) or by changes in valley width (Sawyer *et al.*, 2010; White *et al.*, 2010), or due to the effects of drag along pool channel margins (MacVicar and Best, 2013). Pool-riffle form is further maintained during flood hydrographs by riffle crest growth, and an associated upstream pool backwatering, which can limit pool degradation (de Almeida and Rodríguez, 2011), and perhaps promote pool sedimentation. These local interactions however can be disrupted by downstream effects, and shift the balance of response, promoting pool erosion and riffle stability (Pasternack *et al.*, 2008; de Almeida and Rodríguez, 2011). Lastly, the spatial and temporal character of sediment sorting (bed sediment texture) over a pool-riffle pair may play a role in maintenance by limiting or moderating effects of upstream backwatering, or channel bed evolution – hydrodynamic feedbacks in general (Clifford, 1993b; Sear, 1996; de Almeida and Rodríguez, 2011; Hodge *et al.*, 2013). Little regarding the last mechanism, however, is known.

There is a need to explore how pool-riffle texture responds to discrete floods, and how the cumulative texture effect is carried over multiple flood seasons. This study addresses the first need. Our research was guided by two questions: (a) How variable is general riffle surface grain-size texture in time and space as a result of natural variations in sediment supply and streamflow discharge? (b) Does a pool-riffle pair exhibit equivalent sedimentation as a result of a sediment-mobilizing flood? Furthermore, are sedimentation responses consistent through time? Question (b) could be interpreted or conceptualized a few different ways. To be clear, we specifically asked whether the pool filled (an increase of pool sediment storage) and the riffle fined, or the pool scoured (depletion of pool sediment storage) and the riffle coarsened. Either case would qualify as equivalent sedimentation, which we term sedimentation coupling. We note that one could also describe equivalent sedimentation as pool erosion and riffle deposition, with the depositional material comprised of the eroded pool substrate. Whereas the latter description has a process-basis, we use the former description because it is compatible with aggradation or degradation; the latter description is not.

The study research questions were addressed through a combination of field measurements of riffle texture, pool sedimentation ( $V^*$ ), cross-sectional geometry and bedload sediment transport, sediment transport numerical modeling, and statistical analysis, for a sequence of 11 floods that occurred over a 3-year study period. We hypothesized that:

1. The study measurement strategy would be sufficient to characterize spatial and temporal trends of pool-riffle texture adjustment; and
2. The pool-riffle pair would exhibit sedimentation coupling.

## 2.3 Study site

Majors Creek is a mountain stream that drains the western slopes of the Santa Cruz Mountains (Figure 2.1) from a contributing area of 9.2 km<sup>2</sup>, ranging in elevation from 120 to 560 m in its headwaters. Mean annual precipitation ranges from 660 mm (coast) to 1067 mm (headwaters) Rantz (1971). The study site constitutes a pool-riffle pair located in an old-growth redwood (*Sequoia sempervirens* 'Adpressa') forest preserve managed by California State Parks. A 3.5 m dam is located 450 m downstream of the study site. We installed a continuously recording stream gage (gage) within the subject pool (Figure 2.1), 7 years prior to this study.

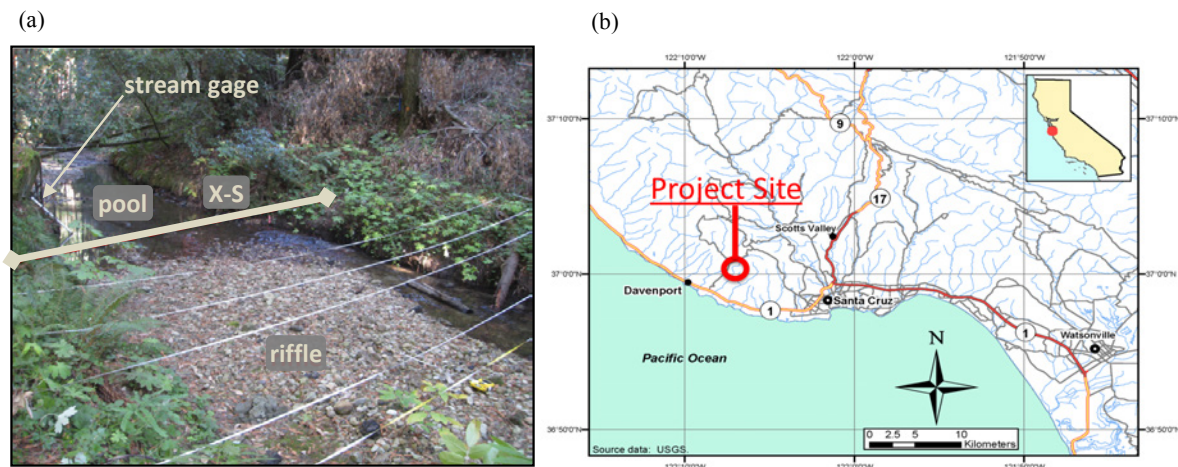


**Figure 2.1:** (A) Photograph shows the pool and riffle pair discussed within this paper, view looking upstream. Solid line indicates location of associated monitoring cross-section. Tape strung over the riffle illustrates the five surface texture sampling transects. Location of stream gage shown in the mid-left part of the image. Photograph taken in October 2012 during low flow. (B) Location map of study site.

Present land uses are mostly rural residential, rangeland and public lands with no major land disturbance in the past 50-years or more. Upstream of the study site the watershed is underlain by two primary geologic units: (1) the southwest-dipping Lompico sandstone of middle Miocene age; and (2) Cretaceous-aged crystalline basement rocks typed as granite and adamellite (Leo, 1961; Clark, 1966; Brabb, 1989). Smaller areas underlain by the upper Miocene Santa Margarita sandstone also occur. The Lompico and Santa Margarita sandstones produce sand-size sediments, whereas the crystalline basement rocks can produce sand- to cobble-size sediments. Sediment contributions from these geologic materials are reflected in the median grain size of the sampled bedload ( $D_{50} = 0.6 \text{ mm}$ ) and streambed substrate ( $D_{50} = 7 \text{ mm}$ ) (Figure 2.2).

Bankfull discharge at the study site is estimated as  $5.70 \text{ m}^3/\text{s}$ . Bankfull channel width varies from 6 to 8 m, and bankfull depth is approximately 0.75 to 1 m. Bankfull discharge has an estimated recurrence interval of 2 years, and is associated with well-defined channel-bank slope breaks within the vicinity of the study site. The recurrence interval estimate is based on a HEC-SSP 2.0 flood-frequency analysis (Log-Pearson Type III distribution) completed with 15 years of available peak flow data (gage records supplemented with USGS Station #11161570). The mean annual flow for the study period was  $0.11 \text{ m}^3/\text{s}$  (Figure 2.3). During the study period several near bankfull flows occurred, an estimated 20-year flood occurred on March 26, 2011 ( $24.64 \text{ m}^3/\text{s}$ ), and a 5-year flood occurred on December 19, 2010 ( $12.03 \text{ m}^3/\text{s}$ ) (Table 2.1; Figure 2.3). Flood recurrence intervals were computed with HEC-SSP 2.0. On March 2, 2011 a relatively small tanoak (*Notholithocarpus densiflorus*) (diameter  $\sim 30 \text{ cm}$ ) fell from the stream right bank (looking downstream) and through the pool longitudinally. The tree was removed

**Table 2.1:** Characteristics of the sampling program

	Mean Daily Flow	Peak Flow	Peak Average Bed Stress	Total Flow Volume	Bedload Discharge	Texture Sampling Events (sampling events)
	$m^3/s$	$m^3/s$	$Pa$	$10^6$ cubic meters	tons	-
<b>Intra-sampling Periods</b>						<i>E1: January 14-15, 2010</i>
January 16-27, 2010	0.29	3.11	7.84	0.30	4.30	
						<i>E2: January 27-28, 2010</i>
January 29-February 10, 2010	0.24	5.07	8.76	0.27	5.51	
						<i>E3: February 10-11, 2010</i>
February 12-March 9, 2010	0.22	4.45	9.81	0.48	9.13	
						<i>E4: March 10, 2010</i>
March 11-December 12, 2010	0.06	1.38	5.47	1.34	1.01	
						<i>E5: December 13 and 15, 2010</i>
December 14, 2010 -January 4, 2011	0.52	12.03	11.22	0.98	36.13	
						<i>E6: January 5-6, 2011</i>
January 6-April 4, 2011	0.40	<b>24.64</b>	<b>14.28</b>	3.10	121.47	
<b>Peak flood of period 3/26/11</b>						<i>E7: April 5-6, 2011</i>
April 6-November 3, 2011	0.09	n/a	5.59	1.57	1.11	
						<i>E8: November 4 and 9, 2011</i>
November 5, 2011-January 30, 2012	0.05	1.53	5.44	0.41	0.65	
						<i>E9: January 30-31, 2012</i>
February 1-April 3, 2012	0.16	9.54	10.16	0.85	22.49	
						<i>E10: April 3-4, 2012</i>
April 5-April 24, 2012	0.14	3.00	7.65	0.25	2.29	
						<i>E11: April 24-25, 2012</i>
<b>Total:</b>					<b>204.09</b>	

## Notes

1. Bedload discharge equals total for the indicated time period, and reflects results of sediment transport modeling. Of the 204.09 tons of bedload computed for the study period, 163.9 tons was sand-sized, and 40.2 tons was gravel-sized up to 32 mm.
2. Peak average bed-stress was computed using the mean daily flow corresponding to the peak flow date.  
Bed-stress was computed in the sediment flux model using a gaging-derived empirical relationship for water depth.  
Bed stress was computed as:  $\rho_w g d' S$ , where  $d'$  is the section-average water depth and  $S$  is the reach-average bed slope.

from the stream in late April 2011 and had minor effects on measured conditions during the study, as evidenced by widespread fine bed texture upstream and downstream of the study site following the March 26<sup>th</sup> flood.

A pronounced eastward bend in the stream is located  $8W_b$  (bankfull widths) upstream of the study site, with another eastward trending bend located more than  $10W_b$  downstream. A tall wood jam was located about  $30W_b$  upstream of the study site. The pool-riffle pair measures about  $2W_b$  longitudinally, along a reach of stream with an average bed slope of 0.4-0.5%, and a bankfull (and higher) water surface slope of roughly 0.3%, based on two field surveys of high-water marks. The reach is relatively confined.

The pool-riffle pair was chosen for study because it occurs along a near straight reach of stream which changed little in character during the 7 years prior to the start of the study.

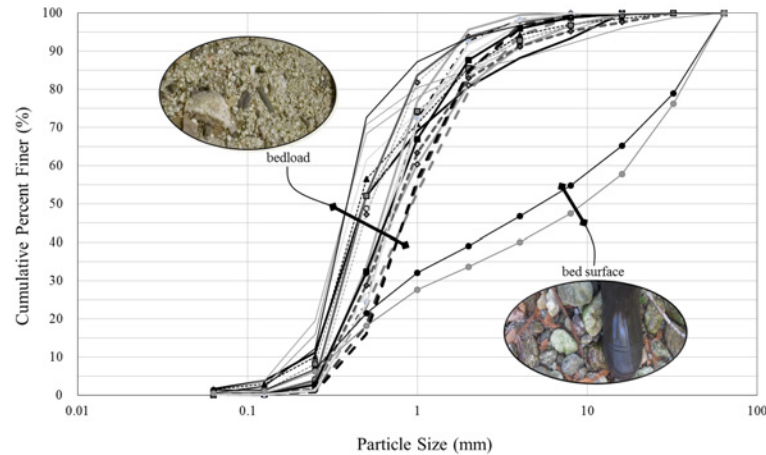


**Figure 2.2:** Cumulative percent finer data for 19 bedload samples collected immediately upstream of the subject riffle, and for 2 bed surface bulk samples collected just downstream of the subject riffle.

As a result it was hypothesized that the pool-riffle pair is a quasi-stable attribute of Majors Creek. We also monitored other pool-riffle pairs. Some of them however were affected by significant wood accumulations during the study period whereas others were influenced by dam operations. The pool-riffle pair was visually identified during low-flow as a backwater feature (pool) of a largely emergent sand-gravel-cobble deposit (riffle).

## 2.4 Data collection and analysis

This section details the data collected during the study, and the analytical methods used to address the research questions. Data collection occurred from January 2010 through April 2012 (Table 2.1). Measurement dates (sampling events) bracket storm periods during which measurable volumes of bedload transport occurred (Table 2.1), and measurement dates were characterized by relatively low winter flows during which little to no bedload transport occurred. As a result it is important to note that our measurements of riffle texture and pool fine sediment storage reflect the net effect of sediment transport during the intra-sampling high-flow periods. Measured data were analyzed with a particularly broad set of analytical methods because we have attempted to explore how event-based riffle textures manifested temporally, and in relation to the magnitude of local sediment transport fluxes and pool sedimentation conditions. As a result, the following discussion is quite detailed. The section is organized by data type, and for each data type proceeds by first discussing data collection methods, followed by how the data were analyzed.

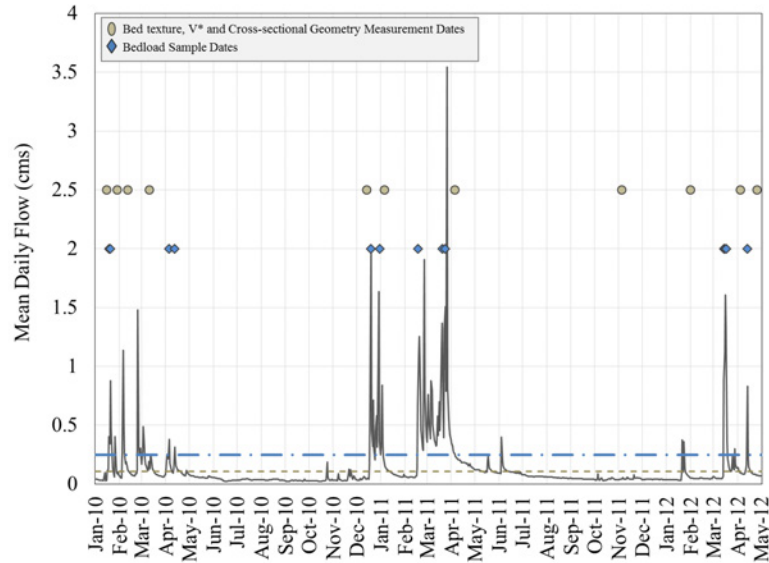


**Figure 2.3:** Record of mean daily streamflow for the study period, Majors Creek immediately upstream of monitored pool-riffle pair, Santa Cruz County, CA. Dates of bed texture,  $V^*$ , cross-sectional geometry and bedload sampling events are indicated by the ovals and diamonds, respectively. Dashed line represents the mean annual flow for the study period ( $0.11 \text{ m}^3/\text{s}$ ), and the dashed-dot line represents the sediment mobilizing flow ( $0.25 \text{ cms}$ ; cf. Figure 2.14 this paper.)

### 2.4.1 Riffle texture

#### Data collection

Riffle surface texture was characterized according to an adaptation of the Sampling Frame and Template (SFT) and Environmental Monitoring and Assessment Program (EMAP) protocols (Bunte *et al.*, 2009). Adaptation of the SFT protocol involved constructing a fixed sampling grid over the subject riffle, coupled with use of grain size classes as specified with the EMAP protocol. The SFT protocol was developed to reduce operator variability and bias from particle selection and size measurement, common to different methodologies, e.g., the more familiar Wolman pebble count (Wolman, 1954). The adapted SFT protocol was suitable for the present study because it permitted bed texture characterization from approximately the same location during each sampling event, deemed necessary in order to compare temporal trends of riffle texture. Grain size calls at each sampling node over the 11 sampling events were generally non-ambiguous, and reflected the local ( $\sim$  several  $\text{cm}^2$ ) texture character.

Riffle extents were established at the start of the study period and a total of five cross-sections were established to construct fixed sampling transects (Figure 2.1). The cross-section endpoints were established with rebar and metal tags, located at what we determined to be the bankfull elevation. One cross-section each was placed at the downstream and upstream extent of the riffle (4.6 m apart), and the remaining three cross-sections were located 0.9 m,

1.8 m and 3.0 m from the downstream-most section. Over the course of the study period the upstream and downstream extents of the riffle varied  $< 1$  m from that observed at the time of cross-section establishment.

Sampling event set-up involved pulling one tape through all cross-section endpoints (Figure 2.1) by fixing the start of the tape to the left end of the downstream most transect, permitting confirmation of general sampling set-up consistency. The sampling grid was defined by a fixed event-based sampling interval along all five transects. The sampling interval for the first sampling event was 18 cm, for the second was 24 cm and for the remaining 9 events was 23 cm. Grid spacing was chosen in order to minimize sampling the largest bed sediment grain more than once (Church *et al.*, 1987). Node zero along each transect was consistently placed at the right-bank margin. Riffle texture characterization was conducted by placement of a fine-tipped rod at each sampling node, and recording whether the grain was organic, sand, gravel, cobble, boulder, or bedrock (a modest adaptation of the EMAP classes), according to a simple grain size score from 0 (organic) to 5 (bedrock), incremented by a value of one.

Quantitative analysis is limited by the texture sample sizes ( $n = 161$  to  $180$ ), associated spatial densities and lack of actual grain lengths. As a result we did not utilize, for example, the statistical methods detailed and used by Nelson *et al.* (2012). We have however used a combination of appropriate statistical analyses to characterize texture trends, and learn how to improve study methods.

### Non-parametric statistics

Two non-parametric tests were used to evaluate similarity and dissimilarity of temporal riffle texture trends for each sampling transect during the study period. Similarity of trends would imply spatially homogeneous texture conditions, for example replacement of a gravel-sized grain with a gravel-sized grain at some specific location (cf. Dietrich *et al.*, 2005), and perhaps consistent sediment supply in terms of grain-size distribution (GSD). Dissimilarity would imply spatially variable texture conditions, and the possibility of either consistent or dynamic sediment supply in terms of GSD, as well as expanding, contracting or migrating sediment patches.

We used non-parametrics to evaluate texture trends at the sampling transect scale, rather than for the entire riffle, for example, because the riffle texture data spatial resolution reported here is best suited for transect consideration. A denser sampling of bed surface sediments lends itself to consideration of texture trends at the entire riffle scale, as reported, for example, by Nelson *et al.* (2012). Non-parametric tests are appropriate because there is no reason to assume residuals normality for riffle texture (Paola and Seal, 1995), and because Aberle and Nikora (2006) previously observed non-Gaussian distributions for armored laboratory gravel beds.

Texture trends along each transect were evaluated using Cochran's test for related observations and the McNemar test for significance of change (Conover, 1980). Cochran's test was

used for each transect for all sampling events ( $r \times 11$  matrix –  $r$  sampling locations and 11 sampling events), and McNemar test was used for each transect for sequential sampling events ( $2 \times 2$  contingency table). Cochran’s test evaluates general transect-based texture trends over the whole study period, whereas McNemar evaluates transect-based trends on an event by event basis, permitting identification of floods which resulted in similar vs. dissimilar texture conditions. Event by event testing with McNemar was predicated on Cochran test results which indicated dissimilar bed texture for any given transect over the 11 sampling events. Both tests assume nominal or binary data types, however, Cochran’s further assumes that sampling locations were randomly selected from the populations of all possible locations, and McNemar that the repeat measurement pairs are mutually independent, consistent in principle with *Wiberg and Smith (1987)*; *Kirchner et al. (1990)* and *Buffington et al. (1992)*, and in spirit with *Schmeeckle and Nelson (2003)* and *Furbish et al. (2012)*. Our texture data set was converted to a nominal scale of two classes by specifying sand and finer grains zeros (fine) and gravel and coarser grains ones (coarse).

The Cochran test statistic is defined as (*Conover, 1980*):

$$Q = c(c-1) \frac{\sum_{j=1}^c (C_j - \frac{N}{c})^2}{\sum_{i=1}^r R_i (c - R_i)} \quad (2.1)$$

The parameter  $c$  is the total number of sampling events (degrees of freedom),  $C_j$  is the total column-wise score for each sampling event (the random variable subject to the Cochran test; simply the sum of zeros and ones for any given sampling event),  $r$  is the total number of sampling locations along each transect (Table 2),  $R_i$  is the total row-wise score for each sampling location and  $N$  is the grand total score across all sampling sites and events (Figure 2.4). The variable  $N/c$  reflects the estimate of  $E(C_j)$ , and the coefficient  $c(c-1)$  and the denominator reflects the estimate of  $Var(C_j)$ ; Equation 2.1 can therefore be seen as approximating the distribution of  $C_j$  with the chi-squared distribution and  $c-1$  degrees of freedom (*Conover, 1980*). The zero-hypothesis,  $H_0$ , is that all floods are equally effective (i.e. generated similar bed textures), and that for each sampling location, the probability of a flood yielding a coarse grain is independent of which flood is considered. The distribution of  $Q$  is set by assuming that the number of sampling locations along all transects is large, for the present study ranging from 29 to 35 locations. If  $Q$  is larger than the  $1-\alpha$  (0.05) quantile of a chi-square random variable with  $(c-1)$  degrees of freedom,  $H_0$  is rejected. The MATLAB `cochraneqtest.m` script was used for the analysis.

The McNemar contingency table is constructed with the four possible pair values for each paired sampling event. If  $X_1$  is the nominal grain size at location  $L_1$  for the first event and  $Y_1$  is the nominal grain size at location  $L_1$  for the second of the paired events, the four possible pair values for  $X_1$  and  $Y_1$  at  $L_1$  are (0,0), (0,1), (1,0), and (1,1) (Figure 2.4). For each paired sampling event (e.g. E2–E3), the number of pairs of  $X_i$  and  $Y_i$  which satisfy each of the four possible pair

**Table 2.2:** McNemar sequential event transect test results

	Transect 1	Transect 2	Transect 3	Transect 4	Transect 5
<b>Paired Texture Sampling Events</b>	n = 31-35	n = 32-35	n = 30-35	n = 32-35	n = 29-35
Event 1 - Event 2	-	-	-	-	-
Event 2 - Event 3			f	f	f
Event 3 - Event 4					
Event 4 - Event 5			c		
Event 5 - Event 6					
Event 6 - Event 7	f	f	f	f	f
Event 7 - Event 8					
Event 8 - Event 9					c
Event 9 - Event 10			c		
Event 10 - Event 11			f		

**Legend**

- Significant change in transect texture ( $p < 0.05$ )
- No significant change in transect texture
- f* indicates more sand and smaller grains counted
- c* indicates more gravel and coarser grains counted

**Notes**

1. See Table 2.1 for the sampling event dates.
2. Event is short for Sampling Event, as presented in the text.
3. McNemar test was not performed for the event 1-event 2 sequence because texture sampling occurred with different sampling intervals.

values is summed and used to build the  $2 \times 2$  contingency table (Conover, 1980):

$$\begin{aligned}
 a_c &= \sum_{i=1}^{i=r} \text{pairs} (X_i = 0, Y_i = 0) & b_c &= \sum_{i=1}^{i=r} \text{pairs} (X_i = 0, Y_i = 1) \\
 c_c &= \sum_{i=1}^{i=r} \text{pairs} (X_i = 1, Y_i = 0) & d_c &= \sum_{i=1}^{i=r} \text{pairs} (X_i = 1, Y_i = 1)
 \end{aligned}
 \tag{2.2}$$

As above,  $r$  is the number of sampling locations along any particular transect for paired sampling events (Table 2). The  $H_0$  specifies that the marginal probability between row and column outcomes is equal (i.e.  $P(a_c) + P(c_c) = P(a_c) + P(b_c)$  or  $P(c_c) + P(d_c) = P(b_c) + P(d_c)$ ), noting that the marginal probabilities associated with  $a_c$  and  $d_c$  cancel and  $H_0$  becomes  $P(c_c) = P(b_c)$  (Conover, 1980). If  $H_0$  is rejected it can be recognized that bed texture along any given transect changed significantly between paired sampling events, and either from finer to coarser, or vice versa (i.e. there is an imbalance between  $c_c$  and  $b_c$  and  $P(c_c) \neq P(b_c)$ ). For the present study, a contingency table, Equation 2.2, was built for each sampling event sequence (e.g. E2–E3), and



### SOM method

Self-organizing maps (SOMs) are a common type of unsupervised artificial neural network particularly adept at pattern recognition and classification, and in many respects SOMs are analogous to more traditional forms of cluster analysis. *Kohonen* (2001) offers an explanation of the development and details of the SOMs algorithm which by now has been used in a wide range of disciplines (e.g. *Kaski et al.*, 1998; *Oja et al.*, 2002). Whereas SOMs method has been commonly used as a clustering tool, it may under perform simpler techniques such as K-means clustering (*Bishop*, 2006). The value of SOMs therefore lies in application as a discrete nonlinear Empirical Orthogonal Function (EOF) method (*Cherkassky and Mulier*, 1998), rather than for clustering. Additional details on the SOMs method are found in Section 2.8, and Figure 2.5 illustrates a conceptual diagram of the SOM's steps. In this section, we introduce the main features of the SOMs method by comparing it with the more commonly known EOF method.

The principles behind SOMs and EOF method are similar in their ability to reduce multi-dimensional data into a smaller set of characteristic modes (spatial and/or temporal patterns). To achieve this goal, the SOMs method performs a nonlinear projection from the input data space to a set of units (neural network nodes) on a 2-D grid (Figure 2.5). Each characteristic pattern identified by the SOMs method can be viewed as an EOF (spatial pattern or eigenvector) of a particular mode. Whereas temporal information in the EOF method is individually expressed for each mode as a time series of principal components (where the components indicate the strength of the particular spatial pattern at a given time), the SOMs patterns are enumerated according to their position in the 2-D grid so the temporal information is given by the time series of the pattern numbers (i.e. time series of the 2-D grid node locations; Figure 2.5). The essential feature of the 2-D grid to which the patterns are mapped is that the neighboring units on the 2-D grid represent similar patterns, while dissimilar patterns are mapped onto units farther apart.

Our goal is to use the SOMs method to identify characteristic temporal patterns (signals) in the classified bed texture data, discussed above. For the present case, a temporal pattern is basically the classified bed texture data (consisting of 2 classes) from any given sampling point  $i$  plotted for each sampling event as a series (Figure 2.5 - result of pre-processing). After removing missing values, our data set generated 154 temporal patterns (154 consistently sampling locations on the subject riffle), or series, of 11 events in length (11 sampling events) (Figure 2.5). These 154 temporal patterns serve as the input data (vectors) to SOMs training (Figure 2.5). SOMs training results in populating the 2-D grid discussed above, which consists of the most characteristic temporal patterns in the bed texture data (Figure 2.5).

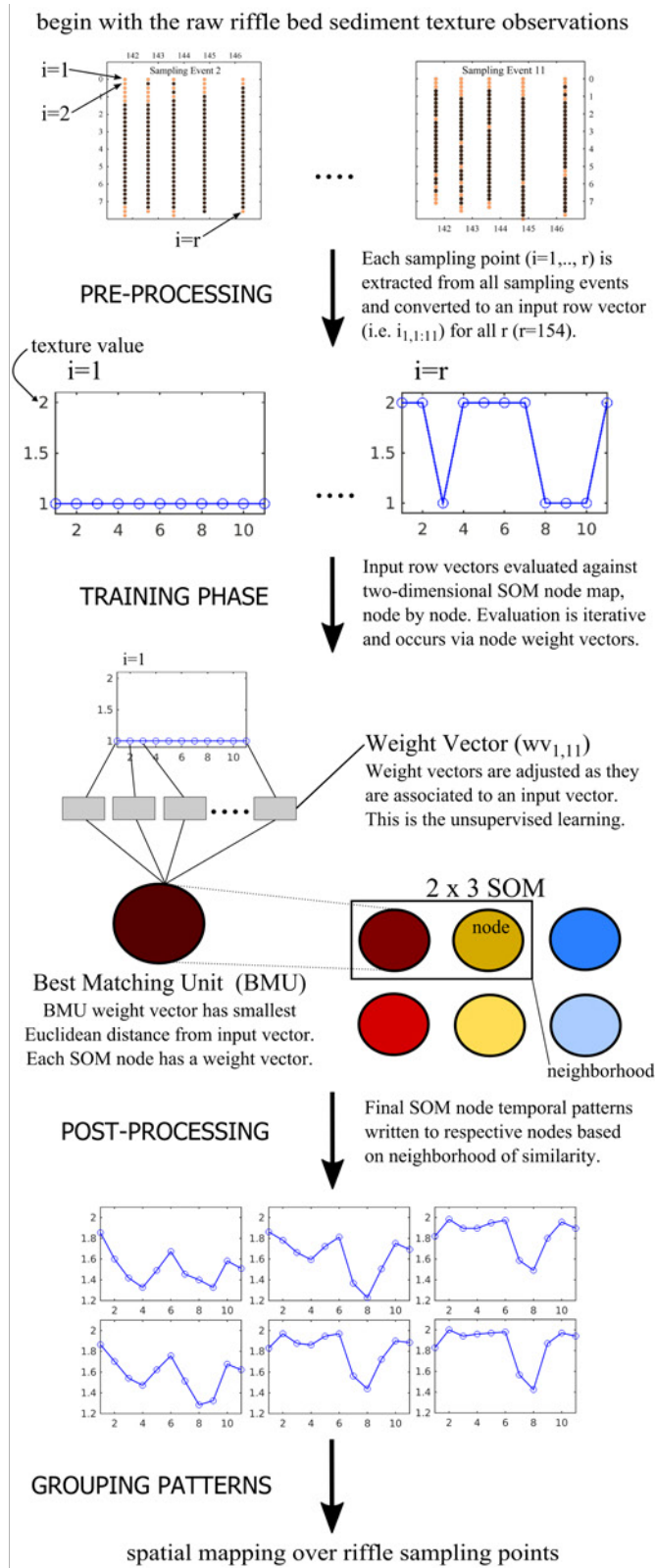


**Figure 2.5:** Schematic illustration of SOMs implementation on our dataset, modified and adapted from Richardson et al. [2003] for the present study. The main steps with SOM implementation are (1) pre-processing, (2) training, and (3) post-processing.

Initial estimates of the SOMs 2-D grid size were identified prior to SOMs analysis by completing Principal Components Analysis (PCA) on the bed texture data. PCA results indicated that a majority of classified bed texture data variance was explained by the first several PCA modes. As a result, the initial SOMs 2-D grid size testing began with several nodes. Furthermore, SOMs training was completed using several different numbers of units in the 2-D grid, with different parameter sets (e.g. neighborhood function and radius, type of training, initialization of weight vectors and number of iterations). As in *Radić and Clarke (2011)*, we find that the sensitivity of pattern recognition in the SOMs training to the choice of the parameters is small (i.e. similar patterns in resulting SOMs are produced with varying parameter values)

### 2.4.2 $V^*$ and pool cross-section surveys

Trends of pool erosion and sedimentation were evaluated within the pool immediately upstream of the riffle (Figure 2.1) using the  $V^*$  methodology developed by *Lisle and Hilton (1992)*, and with repeat elevation surveys conducted along one established cross-section (Figure 2.1). The  $V^*$  methodology uses a repeatable grid-based pattern of depth measurements in a pool to compute the decimal fraction of a pool that is filled with fine sediment (*Lisle and Hilton, 1992*). For example, a  $V^*$  value of 0.63 means that 63% of the residual pool volume is filled with fine sediment, noting that the residual pool volume is an explicit function of the downstream riffle crest elevation. Measurements of  $V^*$  made during this study were not necessarily restricted to measuring volumes of just fine sediment filling the pool. Rod ( $V^*$  rod) penetration was achieved for coarser substrate (the  $V^*$  rod is stainless steel construction of one-half inch in diameter with a hexagonal section, 0.05 feet etched measurement intervals, and an approximately 45-degree tip at one end). Our measurements therefore provide a fuller estimate of total pool fill change through the study period. Repeat  $V^*$  measurements over time permit an objective evaluation of pool sedimentation trends (*Lisle and Hilton, 1992; Hilton and Lisle, 1993*).

$V^*$  was characterized with at least 100 sampling points per event. At each pool sampling location we measured the water depth, and then pushed the  $V^*$  rod into the bed until rod advancement was refused, subsequently recording the refusal depth (i.e. sedimentation depth) (*Lisle and Hilton, 1992*). Consistent with methodological guidance (*Hilton and Lisle, 1993*), all  $V^*$  measurements were made at relatively low discharges when streamflow was clear. Flow variability between  $V^*$  measurements over the 3-year study period was minor.  $V^*$  values were computed for each event according to:

$$V^* = \frac{\text{total sediment volume}}{\text{total residual pool volume}} \quad (2.5)$$

Note that the total residual pool volume is the sum of the total sediment and water volume situated below the downstream controlling riffle crest elevation (*Lisle and Hilton, 1992*).

A cross-section used to measure the controlling riffle crest elevation and track local bed change was located at the pool tail. The cross-section was surveyed with a laser level at ap-

proximately 60 cm intervals within the channel, and at slope breaks along the banks. All bed elevations were recorded to the nearest 2 mm, and the elevation surveys and data reduction were conducted in accordance with the methods described by *Harrelson et al.* (1994). It was not possible to establish more cross-sections due to time constraints during sampling events. Repeat longitudinal profiles were collected, but were of a resolution not useful to the present efforts.

### 2.4.3 Bedload transport measurements and modeling

#### Data collection

Bedload sediment transport was measured with a 76-mm Helley-Smith sampler that was fitted with a 0.25 mm mesh collection bag. Samples were collected according to the single equal width increment method (*Edwards and Glysson*, 1988). Bedload particles larger than 16 mm (and smaller than the opening) may be underrepresented by the Helley-Smith sampler due to an apparent trapping efficiency threshold (*Emmett*, 1980). We therefore consider our measurements representative for particles in the range of 0.5 to 16 mm. Bedload was sampled at four to ten locations across measurement transects for a duration of 30 to 60 seconds per vertical, dependent upon stage variability. Repeat bed load measurements were made for roughly one-quarter of the visits, and bed load samples were weighed, dried, weighed again and sieved at 1 phi intervals.

Flow measurements accompanied each bedload sediment measurement and were completed with bucket-wheel velocimeters and wading rod. Water level stage was recorded before and after each flow measurement. Bedload measurements began two years before the start of the present study in January 2008. Bedload measurements were restricted to flows less than  $2.5 \text{ m}^3/\text{s}$ , or close to one order of magnitude less than the peak flood of the study period. Bedload measurements primarily reflect Phase 1 (primarily sand-sized grains transported over a stable and coarser riffle surface), and to a lesser extent Phase 2 (Phase 1 transported substrate plus mobilization of some fraction of the coarser riffle surface substrate), transport conditions *Jackson and Beschta* (1982) (Figure 2.2), or Stage 1 and Stage 2 as detailed by *Hassan et al.* (2005). However, sediment transport modeling (discussed next) indicates that Phase 2 transport conditions occurred during most, if not all, of the floods observed through the study period. The flow related sampling limitation relative to the study goal of examining pool-riffle bed texture trends was addressed heuristically through construction of a sediment transport flux model for the gaging station location.

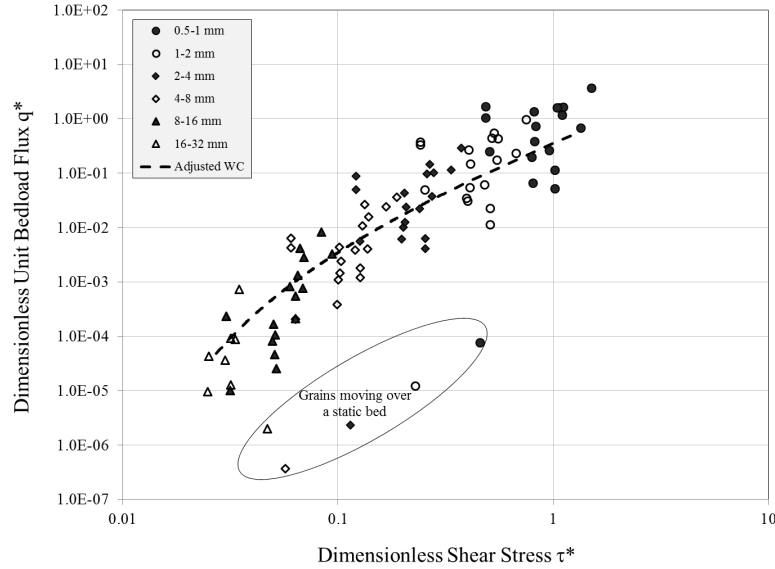


**Figure 2.6:** Dimensionless bed load transport rates for Majors Creek. The Adjusted W-C reflects sand and gravel component curves joined into one continuous curve, following the approach outlined by *Wilcock* (2001); each component curve was fit to the data using sum of squares minimization. Bedload samples collected immediately upstream of the subject riffle from December 2008 through April 2012.

### Sediment transport modeling

Fractional bedload flux modeling followed the approach developed by *Wilcock* (2001) whereby, in this case, the Wilcock-Crowe (W-C) function (*Wilcock and Crowe*, 2003) was calibrated to bedload measurements collected at the gage (Figure 2.6). The Wilcock-Crowe function was selected because the bulk bed samples indicate roughly 33% sand composition (Figure 2.2). The dimensionless W-C function for any grain class  $i$  is defined as:

$$W_i^* = \begin{cases} 0.002\phi^{7.5} & \phi < 1.35 \\ 14 \left( \frac{1-0.894}{\phi^{0.5}} \right)^{4.5} & \phi \geq 1.35 \end{cases} \quad (2.6)$$

The parameter  $\phi$  is a stress ratio ( $\tau/\tau_{ri}$ ) of which  $\tau$  is the average bed stress and  $\tau_{ri}$  is the average mobilizing reference stress for any size class  $i$  of the bed material. The average bed stress was computed as  $\gamma R_h S$  where  $\gamma$  is the unit weight of water,  $R_h$  is the hydraulic radius, computed with a field-measurement based empirical relationship, and  $S$  is the average bed slope in the downstream direction, assumed to approximate the water surface slope over many channel widths. The average mobilizing reference stress is dependent upon a hiding function ( $D_i/D_{50}$ ) and the average mobilizing reference stress for the mean grain size of the surface

material ( $\tau_{rs50}$ ) is defined as:

$$\frac{\tau_{ri}}{\tau_{rs50}} = \left( \frac{D_i}{D_{50}} \right)^{b_w}, \quad (2.7)$$

where  $D_i$  represents the mean diameter of each size class, and the exponent  $b_w$  is a fitting parameter dependent on  $D_i/D_{sm}$ :

$$b_w = \frac{0.67}{1 + \exp\left(1.5 - \frac{D_i}{D_{sm}}\right)}, \quad (2.8)$$

where  $D_{sm}$  is the mean grain size of the bed surface material. *Wilcock and Crowe* (2003) demonstrated that the average mobilizing reference stress for the mean size class of the surface material ( $\tau_{rm}$ ) is dependent upon the surface sand content:

$$\tau_{rm} = (\rho_s - \rho_w) g D_{sm} [0.021 + 0.015 \exp(-20F_s)], \quad (2.9)$$

where  $\rho_s$  is sediment density, here assumed to be 2.65 g/cm<sup>3</sup>,  $\rho_w$  is the density of fresh water,  $F_s$  is the percentage of sand in the surface material and  $g$  is gravitational acceleration. The dimensional transport rate for any grain size class  $i$  is computed following an Einstein-type flux:

$$q_{bi} = \frac{W_i^* F_i u_*^3}{[(\rho_s/\rho_w) - 1] g}, \quad (2.10)$$

where  $q_{bi}$  is the fractional sediment flux for grain size class  $i$ ,  $F_i$  is the percent of grain size class  $i$  present in the bed surface mixture,  $u_*^3$  is the shear velocity, computed as  $(\tau/\rho_w)^{0.5}$ . Calibration of the W-C function was achieved through adjustments to  $\tau_{ri}$  for the sand-sized and gravel-sized and coarser fractions, respectively (i.e. computed values of  $\tau_{ri}$  for sand-sized and gravel-sized and coarser fractions was multiplied by an adjustment factor). The  $\tau_{ri}$  adjustment factor for sand-sized fractions was 1.48 and for gravel-sized and coarser fractions was 2.10. The ultimate calibration fits were determined by sum of squares minimization. The calibrated, composite sediment rating curve shown in Figure 2.6 was developed after *Ashworth and Ferguson* (1989) and *Whiting and King* (2003) for comparative purposes. The dimensionless bed load transport rating curve shown in Figure 2.6 is defined by the dimensionless shear stress  $\tau^*$  (Shields stress) and the dimensionless Einstein bed load flux  $q^*$ . The Shields stress for grain fraction  $i$  can be defined as (*Shields*, 1936):

$$\tau_i^* = \frac{\tau}{(\rho_s - \rho_w) g D_i}. \quad (2.11)$$

The Einstein bed load flux for grain fraction  $i$  can be defined as [Parker, 2008]:

$$q_i^* = \frac{q_{bi} F_i^{-1}}{\{[(\rho_s/\rho_w) - 1] g D_i\}^{0.5} D_i} \quad (2.12)$$

The quantity  $q_{bi}$  was computed with Equation 2.10.

#### 2.4.4 Bed surface sampling

Two streambed samples were collected in June 2008 in close proximity to the pool-riffle pair in order to assess differences between bedload samples and general composition of the streambed surface. The two streambed samples were prepared from three separate sub-samples collected along two sampling transects, respectively. Sub-samples were collected using a 130 mm diameter sampler driven roughly 150 mm into the streambed. One-hundred and fifty mm approximates two times the active layer thickness (Hirano, 1971) according to:  $L_a = n_a D_{90}$  where  $L_a$  is the active layer thickness,  $n_a$  is a constant of order 1 to 2 (Parker, 2008) and  $D_{90}$  was measured to be 55 to 60 mm (Figure 2.2). The transect sub-samples were emptied onto a plastic tarp, thoroughly mixed, and sampled to produce the two streambed samples, respectively. The samples were then weighed, dried, weighed and sieved at one-phi intervals.

## 2.5 Results

### 2.5.1 Riffle texture adjustment

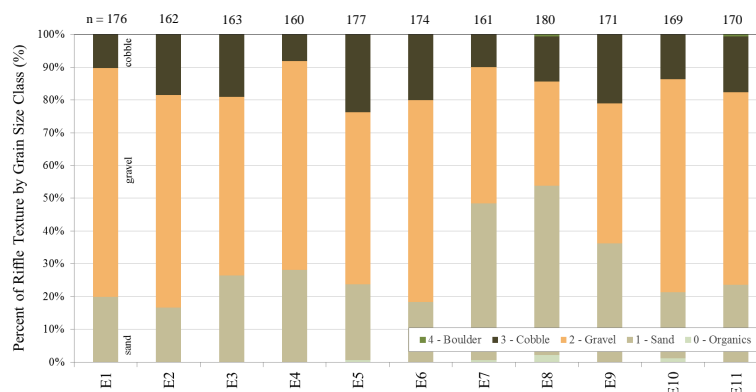
#### Cumulative point count based

Figure 2.7 provides summary results for the eleven riffle texture sampling events according to the grain size score 0 to 5. For E1 to E6 riffle texture exhibited a relatively consistent grain size composition of which a majority was gravel-sized substrate - gravel 61%, sand 22% and cobble 17% (Figure 2.7). Riffle texture shifted to a sand-sized substrate majority following the March 26, 2011 flood (E7: Figure 2.7) - sand 48%, gravel 42% and cobble 10% (Figure 2.7). The sandier riffle composition persisted through E8, after which texture began to trend back to a gravel dominated condition. The distribution of grain sizes for the last two sampling events is quite similar to the initial condition (E1: Figure 2.7)

#### Non-parametric statistics

Cochran's Q test results indicate that transect-based bed textures over the eleven bed-mobilizing events were different, and that the eleven floods did not result in effectively similar transect-based textures. Cochran's Q for Transect 1 yielded a p-value of  $2.17 \times 10^{-4}$  (n=31), for Transect 2 a p-value of  $8.97 \times 10^{-3}$  (n=32), for Transect 3 a p-value of  $1.36 \times 10^{-7}$  (n=30), for Transect 4 a p-value of  $4.59 \times 10^{-11}$  (n=32) and for Transect 5 a p-value of  $2.37 \times 10^{-9}$  (n=29), all well below  $\alpha = 0.01$ .

McNemar test results indicate that all transects exhibited at least one texture shift through the study period (Table 2: p-value < 0.05). A texture shift occurred at each transect from sampling event 6 to event 7, presumably due to a large flood that occurred between these



**Figure 2.7:** Riffle texture point count results for 11 sampling events from January 2010 through April 2012, expressed as percent stacked bars by grain size class.

two events (Table 2.1 and Figure 2.2). In addition, Transects 1 and 5 are characterized by one additional texture shift, Transect 2 and 4 by two additional shifts, and Transect 3 by three additional shifts (Table 2). Transect texture shifts along relatively finer or coarser texture trends varied in time (Table 2). For example, some transects exhibited trends from finer to coarser, and so on (Transects 2 and 3), whereas others exhibited only finer texture shifts (Transects 1 and 5), or a combination of both (Transect 4). On the other hand, spatial texture trends were similar when changes are considered with respect to event sequence (Table 2). For example, Transects 3 to 5 showed a fining texture trend from sampling event 2 to 3, all transects showed a fining trend from sampling event 6 to 7, and Transect 2 and 3 showed a coarsening trend from sampling event 9 to 10.

The McNemar test results can be compared qualitatively against spatial representations of the riffle texture point count data. Figure 2.8 illustrates the point count data spatially. The point count data have been classified as sand-sized or gravel-sized and coarser. Figure 2.9 illustrates riffle texture point count change spatially. Riffle texture change was specified as nodes which changed from sand-sized to gravel-sized and coarser, and vice versa. Figure 2.8 shows that with the exception of E7 to E9, riffle texture was generally coarse through the riffle center and fine along the riffle margins. Figure 2.9 highlights this point and is particularly useful because it provides a visual summary of how riffle texture changed from event to event.

### SOM method

After testing several different sizes of the 2-D grid (i.e. the number of patterns), we settle with a  $2 \times 3$  SOM that displays six temporal patterns across all sampling points and sampling events (Figure 2.10). The most common temporal patterns are 5 and 6 (each associated with 26% of the sampling points), whereas the least common is pattern 2 (associated with 6% of the sampling points). General interpretation of the six temporal patterns (Figure 2.10) based on their visual similarity and dissimilarity, results in grouping of patterns into three clusters (Figure 2.10). The first cluster is defined by patterns 1 and 2, the second cluster by pattern 3

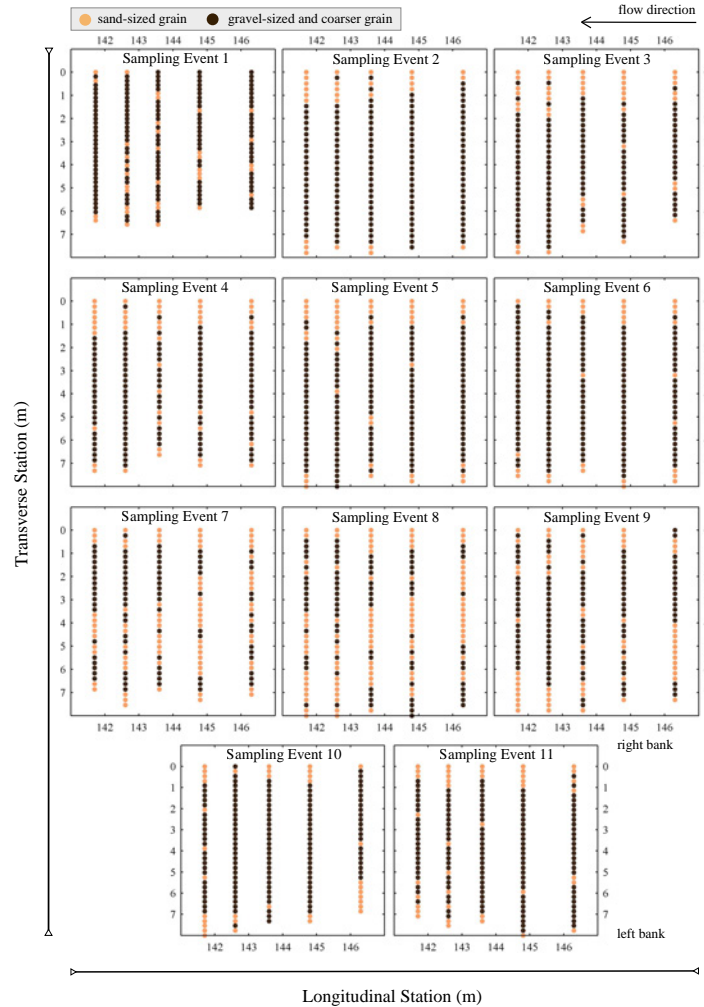


**Figure 2.8:** Spatial observations of riffle texture based on classifying the point counts shown in Figure 2.7 as either sand-sized or gravel-sized and coarser. Note that the sampling interval for E1 was slightly different from that used in all subsequent counts. As a result E1 data will not be used in additional non-parametric analyses.

and the third cluster by patterns 4-6 (Figure 2.10). We consider the second cluster to reflect transitional temporal conditions to those characterized by clusters one and three, because it contains some features of the first and third clusters. Specifically, the second cluster reflects the first cluster for E1:E5 and reflects the third cluster for E6:E11. All three clusters exhibit bed texture fining for E6 to E7, providing the only consistent response among the three clusters. The clusters exhibit differences at the beginning of the study period with clusters 1 and 2 characterized by fining through E4 and cluster 3 showing initial coarsening followed by little change through E6. All three clusters exhibit coarsening from E8 to E9 or E9 to E10, followed by slight to little fining between the last two sampling events.

We associate each temporal signal in the  $2 \times 3$  SOM with a pattern from each sampling point, based on the minimum root mean square distance between the observed temporal sig-

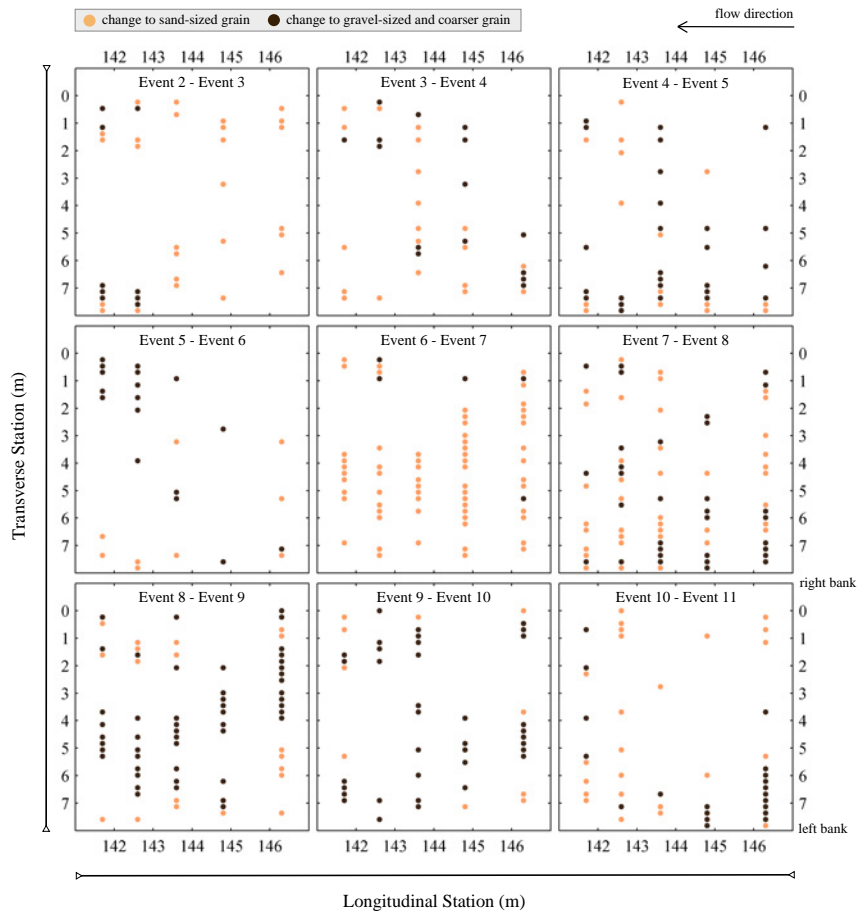


**Figure 2.9:** Observations of riffle texture change for sequential sampling events, computed with data shown in Figure 2.8 as a shift from either sand-sized to gravel-sized and coarser grains, or gravel-sized and coarser grains to sand-sized grains. Sampling sequence E1 to E2 has been omitted because the sampling stationing for E1 was slightly different for each subsequent event.

nal at the point, and the temporal signal in the SOM. To show which of the SOM patterns occurs for each sampling point, we plot the original grid of longitudinal and transverse sampling points and display the cluster number for each point (Figure 2.11). Notably, the third cluster plots as the dominant temporal response through the riffle core into the left bank, whereas cluster one prevails along the right bank riffle margin and cluster 2 shows spotty occurrence through the riffle core and along the left bank (Figure 2.11).

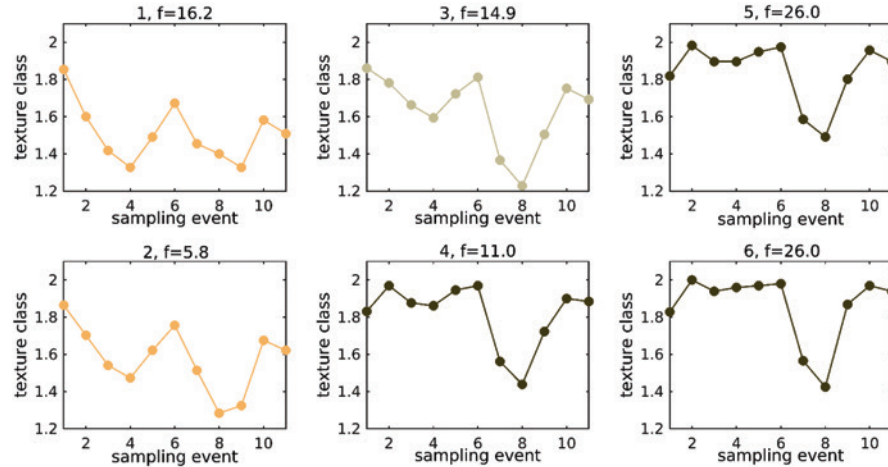


**Figure 2.10:** Final  $2 \times 3$  SOM (2-D grid) showing six characteristic temporal patterns of bed texture classes. The temporal pattern index number and number of points ( $f$ , in %) associated with the pattern are given above each plot. The patterns are grouped into three clusters, represented here by different colors: cluster one in gold (consisting of pattern index numbers 1 and 2), cluster 2 in light brown (pattern index number 3) and cluster three in dark brown (pattern index numbers 4, 5 and 6). The number of sampling points along each transect is set by the minimum number of sampling points  $n$  for each transect range provided in Table 2.

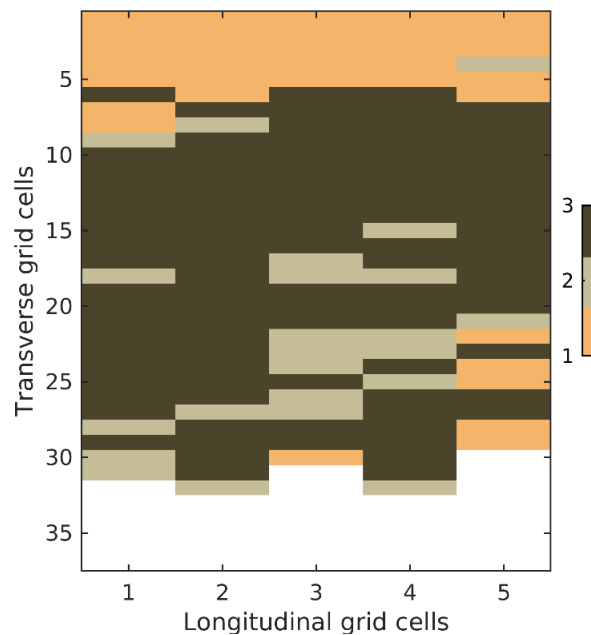


**Figure 2.11:** Spatial distribution of the three clustered bed texture temporal signals shown in Figure 2.10. The mapped color for each temporal signal is consistent with that used in Figure 2.10: gold (temporal patterns 1 and 2), light brown (pattern 3) and dark brown (patterns 4, 5 and 6). The top of the plot represents the right bank riffle margin. For clarity the results have been collapsed in space, i.e. the cluster indexes (1:3) are presented as a uniform grid of sampling points. No numerical interpolation has been performed between sampling points.

### 2.5.2 $V^*$ and cross-section surveys

$V^*$  conditions basically exhibit two states, those within the range of 0.55 to 0.70, punctuated by one event duration periods of lower sedimentation, within the range 0.36 to 0.40 (Figure 2.12A). The relatively lower  $V^*$  values of 0.36 and 0.40 were measured on E3 and E10, respectively (Figure 2.12A: Table 2.1). The median  $V^*$  value for the events is 0.61 (standard deviation is 0.12). Figure 2.13 shows results from repeat cross-sectional surveys completed at the tail of the pool, and head of the riffle (Figure 2.1). The data illustrate little net change to the bed or the banks at the section location, despite the occurrence of two relatively large flood events (Table 2.1).



**Figure 2.12:** (A) Pool  $V^*$  results for 11 sampling events from January 2010 through April 2012. (B) Sampling event to event normalized residual pool and sediment volume change. The residual pool and sediment volume change was computed by subtracting former normalized volume values from later volume values, e.g. E3 normalized volume values less E2 normalized volume values. Residual volumes have been normalized by the median residual pool and sediment volumes, respectively. See *Hilton and Lisle* [1992; Fig. 1 therein] for graphical depictions of the residual volumes. Errors bars in (A) represent the method repeatability as suggested by *Hilton and Lisle* (1993).

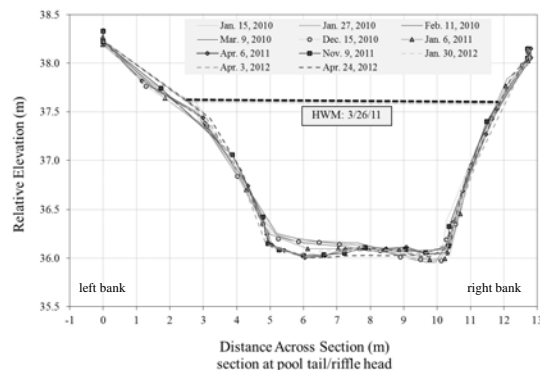


**Figure 2.13:** Repeat cross-sectional surveys completed at the transition from the pool to the riffle. High-water mark (HWM) for the flood of record during the study period is shown. Figure view is looking downstream. The stream banks are populated with mature redwood and California Bay-Laurel trees. Cross-section location noted in Figure 2.1.

### 2.5.3 Sediment transport and bed surface sampling

Sampled bedload consists predominately of sand-sized grains, and in a few cases, grains in the 16 to 32 mm and the 32 to 64 mm size classes were caught in the sampler (Figure 2.2). In all cases particles  $> 16$  mm represented less than 3-percent of the total sample mass. Grain size composition of bed load measurements was generally consistent through the study period (Figure 2.2) and noticeably finer than the bed surface composition. Bedload samples consisted of 80-percent or more sand-sized grains by mass, whereas the two surface samples consisted of 40- and 36-percent sand-sized grains by mass. The median grain diameter of bed load measurements ranged from 0.36 to 0.90 mm (medium to coarse sand-size fractions, respectively), whereas the median grain diameter of the surface samples ranged from 6.0 to 9.2 mm (fine to medium pebble-size fractions, respectively or gravels) (Figure 2.2). The relatively low capture of bedload particles  $> 16$  mm during the course of this study either indicates sampler performance consistency with the findings of Emmett [1980], or reflects little to no transport of these sizes at the time bedload measurements were made.

Dimensionless bedload flux by grain class predominately increases with the dimensionless stress (Figure 2.6). Exceptions to this overall trend include two bedload measurements made on December 30, 2010, following occurrence of an estimated 5-year flood (December 19<sup>th</sup>) and 11 days of continuous elevated streamflows, including a second significant peak on December 29<sup>th</sup>. The December 30<sup>th</sup> measurement points show as plotting to the left of the other measurements for any particular grain size class. The lowest fractional transport rates shown in Figure 2.6 were measured on April 5, 2010, which corresponds to the lowest measured water and bedload discharge during the study, 0.3 m<sup>3</sup>/s and 0.7 tons/day, respectively. Figure 2.14 provides a summary of fractional bedload transport modeling. Bedload transport computed over the three winter seasons was estimated as 204.09 tons in total (Table 2.1), and to have

occurred during just 11% of the study period, or due to 52% of the total water discharge (Figure 2.14). Appreciable sand-sized transport picked up at about 0.25 cms whereas appreciable gravel-size and coarser transport picked up at about 0.75 cms (Figure 2.14). Over the flows for which gravel and coarser transport was non-existent to quite minor, measurable volumes of sand-sized sediment (~20% of sand-sized total) was transported (Figure 2.14).

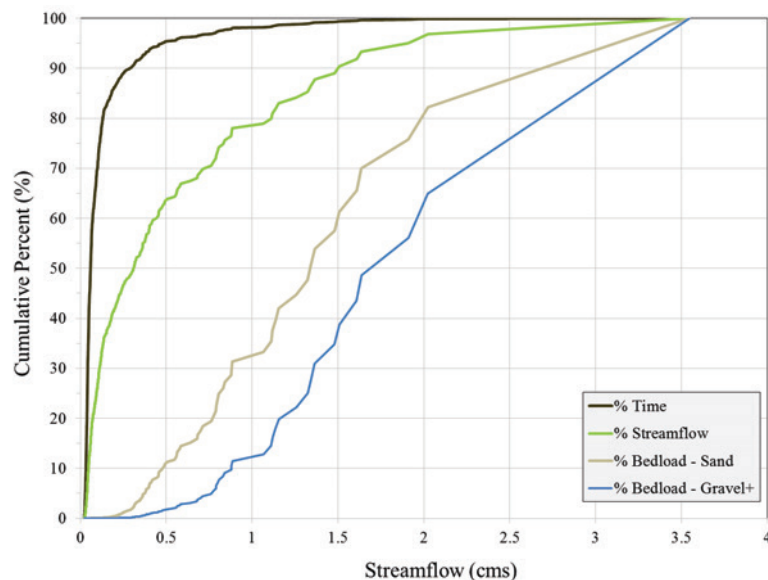


**Figure 2.14:** Accumulative percent of time, streamflow and bedload sediment, sand-sized and gravel-sized and coarser, for the 3-season study period. Bedload discharge for the 3-season period was computed with the adjusted WC curve shown in Figure 2.6. Analysis after *Emmett* [1999].

## 2.6 Discussion

### 2.6.1 Riffle texture dynamics and spatial organization

The McNemar and SOM clusters 1 and 2 provide for a generally consistent interpretation of riffle texture temporal responses during the study period. The temporal responses were cyclical and characterized by initial riffle texture fining, followed by coarsening, fining, coarsening, and then with slight fining between the last two events (Figures 2.8 and 2.9). The overall dominant texture response was a clear fining across much of the riffle surface, apparently due to the 20-year flood that occurred between sampling events 6 and 7 (Figures 2.8 and 2.9; Table 2:  $p < 0.05$ ). A fining response driven by relatively large reach-average bed stresses is consistent, at first order, with theory developed by *Buffington and Montgomery* (1999a) (Figure 2.15), noting that construction of Figure 2.15 and the discussion below reflects a general test of their theory, as we are limited by the lack of explicit grain size information for the point-count data.

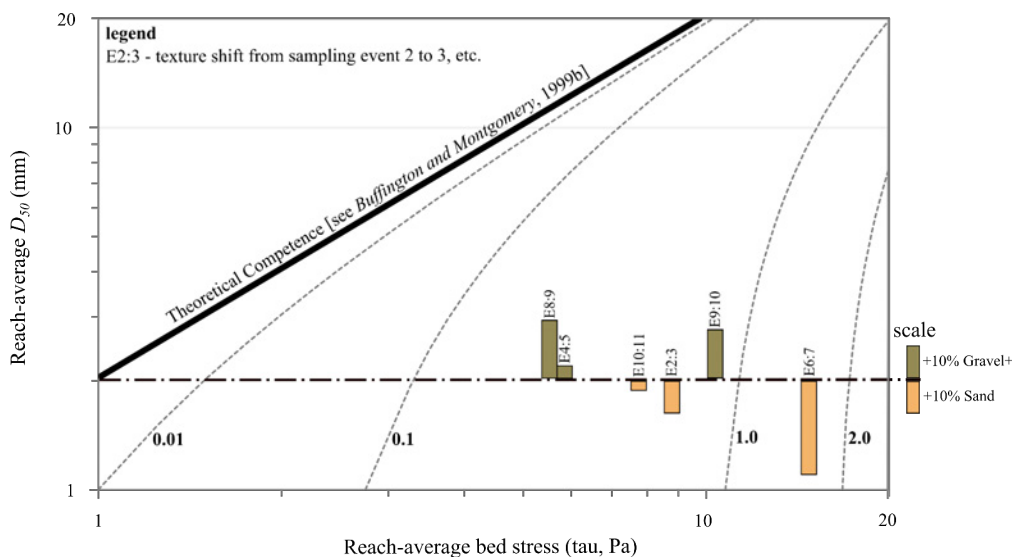


**Figure 2.15:** Predictions of reach-average median grain size vs. reach-average bed stress as developed by *Buffington and Montgomery (1999a)*. Median grain size predictions fall along the dashed light lines, which represent equilibrium unit bedload transport rates ( $\text{kg}\cdot\text{m}^{-1}\text{s}^{-1}$ ), and the bold black line which represents the estimated competent median grain size for a given average bed stress (i.e. Shields' condition). The dot-dashed black line reflects the transition from sand-sized grains to gravel-sized and coarser grains (denoted as gravel+). Bar labels reflect texture changes for sampling event sequences which exhibited significant riffle texture shifts (see Table 2). Texture shifts have been plotted as departures from sand-gravel and coarser transition line depending on whether the riffle in general fined or coarsened. The reach-average stress values reflect peak flood conditions in between each sampling event (see Table 2.1), and as computed with the sediment flux model using a gaging-derived empirical function for water depth. The maximum estimated mobile grain size for each intra-sampling event peak is provided in Table 2.1. Figure re-drawn from *Buffington and Montgomery (1999a)*

Figure 2.15 illustrates event sequence changes in percent sand-sized and gravel-sized and coarser substrate for event sequences which exhibited a significant change in texture (Table 2.2). Specifically, E6–E7 bracket the March 26, 2011 flood, which to some degree drove a 29-percent upward shift in measurement of sand-sized grains on the riffle bed surface. Sampling event 6 occurred on January 5, 2011 and sampling event 7 occurred on April 5, 2011, the first day post peak flood when conditions were suitable for measurements. Given the time spread from flood peak to E7, it is not possible to explicitly attribute the texture shift to conditions during the peak. Nonetheless, the overall fining response is consistent with *Buffington and Montgomery (1999a)*.

The fining response for E6–E7 (Figure 2.15) could also be attributed to a relatively high upstream supply of fine sediment (*Dietrich et al., 1989; Lisle et al., 1993; Paola and Seal, 1995; Nelson et al., 2009*), or due to conditions of high bed stress relative to the critical stress (*Paola and Seal, 1995*). The sediment transport flux model indicates that 95 tons of sand-sized grains were

transported in between E6–E7, as compared to 26 tons for gravel-sized and coarser grains. Though it is not clear if the relative upstream supply of fines was higher for the storm period between E6–E7, as compared to other sequential events, it is clear that the peak study period flood provided average bed stress conditions well above the critical sand and gravel and coarser stresses, respectively (Table 2.1). As a result, peak flood conditions of March 26, 2011 were likely an important aspect of the measured E6:E7 texture response.

The remaining texture responses of McNemar and SOM clusters 1 and 2 reflect a range of flood flows and sediment fluxes that vary by up to a factor four (Table 2.1), including floods of annual, bankfull and roughly twice-bankfull magnitude. The spatial responses for fining and coarsening were distributed across the riffle transects, and were not restricted to the channel margins or the channel center, suggesting widespread bedload movement during the floods (Figure 2.8). Figure 2.15 indicates that the texture responses of E8:9, E4:5, E10:11, E2:3 (sampling events; Table 2.1) are consistent with *Buffington and Montgomery* (1999a). The texture response of E9–E10 (Figure 2.15) on the other hand are not well described by the reach-average stress—average  $D_{50}$  model.

The coarsening response of E9–E10 is comparably strong amongst E2–E3, E4–E5, E8–E9 and E10–E11, as it is a consistent result for McNemar and SOM clusters 1-3. It seems possible that E9–E10 coarsening reflects riffle texture recovery from effects of the 20-year flood. Recovery could be explained by *Jackson and Beschta* (1982), who provide that of all the storage sites for sediments, riffles may respond most actively as a result of spatially non-uniform bedload transport under Phase 2 conditions (i.e. when coarse riffle surface sediments have been mobilized). Notably, peak flood conditions in between E9 and E10 were near to twice bankfull. This implies that bedload transport spatial non-uniformity can have a strong influence on riffle texture trends in streams with somewhat subdued bed topography, consistent in spirit with (*Nelson et al.*, 2010).

Despite the apparent variation of riffle texture temporal response given by McNemar and SOM clusters 1-3, Figure 2.11 indicates that the responses were spatially organized during the study period. Following from the preceding discussion, McNemar and SOM clusters 1 and 2 comprise one aspect of the spatial organization whereas SOM cluster 3 the other (Figure 2.11). This observation bridges the temporal and spatial, and indicates order in a set of results which at first pass appear to be disordered (*cf.* Figure 2.8). Furthermore, the full complement of results suggest that gravel-bed streams may characteristically respond to moderate and smaller sized floods through texture adjustment which is spatially and temporally variable. Large floods, however, appear to drive texture adjustments which are spatially and temporally consistent, for a period of time scaled by magnitude of disturbance generated by the flood. This time scale will vary from stream to stream.

### 2.6.2 Pool-riffle sedimentation coupling

We hypothesized sedimentation coupling between the pool-riffle pair for which coupling reflects similar temporal trends of pool filling or scouring and pool/riffle texture fining or coarsening, respectively. Figure 2.16 indicates two sequences of coupled sedimentation trends in the pool-riffle, perhaps one sequence of a partially coupled response and several sequences of decoupled responses. The E10–E9 change index shows coarsening of sediments in the pool and riffle, as well as a somewhat large evacuation of stored pool sediments (Figure 2.16). On the other hand the E11–E10 change index shows fining of sediments in the pool and riffle, as well as a swing back to increased storage of sediments in the pool (Figure 2.16). These results indicate coupling of sediment transport process between the pool and riffle, as pool depletion suggests general coarsening and pool filling general fining of pool sediments (*Lisle and Hilton, 1992*). Notably, E10–E9 pool depletion and the E11–E10 pool filling each occurred with a concurrent increase in the residual pool volume (Figures 2.12B). We are unaware of previous studies that reported sedimentation coupling for associated pool-riffle morphologic units.

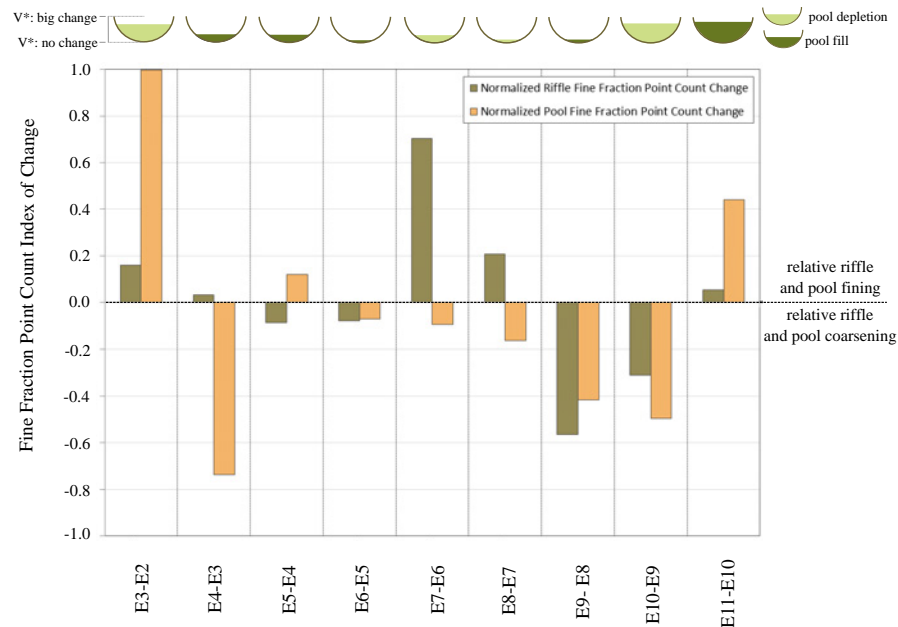


**Figure 2.16:** Sequential sampling period change of normalized riffle and pool fine fraction (sand-sized sediments) point count and  $V^*$  (top of plot). Riffle and pool fine fraction point count data were normalized by the sum of point counts for gravel- and coarser-sized substrate for each sampling event. The fine fraction index of change was computed by subtracting former normalized fine fraction point counts from later fine fraction point counts, e.g. E3 normalized fine fraction less E2 normalized fine fraction.  $V^*$  change plotted as relative change for illustration purposes only. Note that normalized riffle and pool fine fraction change for the first sequence of floods is lacking due to a pool fine fraction data gap for E1.

The E3–E2 change index illustrates fining of both the pool and riffle, yet a somewhat large

depletion of pool sediments (Figure 2.16). In this case pool sediment depletion was characterized by a large decrease in the residual pool volume (Figure 2.12B), indicating the pool had less storage volume. The E9–E8 change index shows pool and riffle texture coarsening (Figure 2.16), and little change in pool sediment volume storage (Figure 2.16). Residual pool volume remained generally unchanged during this period (Figure 2.12B). Lastly, the E6–E5 change index illustrates minor pool-riffle coarsening, with little change in pool sediment volume storage. These event sequences suggest partial sedimentation coupling as the texture responses trended similarly, yet the volume of pool sediment storage diverged or was unchanged.

Decoupled texture trends in the pool-riffle occurred for E4–E3, E5–E4, E7–E6 and E8–E7 (Figure 2.16). Decoupled sedimentation trends between pool-riffle pairs reflects spatially non-uniform sediment transport, as previously reported by *Jackson and Beschta* (1982). Furthermore, generally de-coupled sediment transport processes at the scale of a pool-riffle pair is consistent with that of *Sear* [1996], most of the pool-riffle maintenance theory (i.e. contrasting hydrodynamics from pool to riffle) and consistent in principle with the numerical results of *de Almeida and Rodríguez* (2011), who reported that pool-riffle pairs (and sequences) can exhibit maintenance coupling via sediment transport processes characterized by bedload rates and fractional content that differ from pool to riffle (*de Almeida and Rodríguez*, 2011): Figure 2.11 therein]. Whereas decoupled sedimentation trends appear to be related to processes of pool-riffle maintenance, it is unclear what role, if any, coupled sedimentation trends have for pool-riffles. Building from *Jackson and Beschta* (1982), periods of sedimentation coupling must reflect conditions of equal mobility (*Parker and Klingeman*, 1982) and uniformity of sediment transport process. As a result, our limited data set implies that periods of equal mobility, manifested over bedform pair length scales, is an important aspect of channel response to large floods.

## 2.7 Concluding remarks and next steps

The field-sampling approach permitted quantification of the spatial and temporal characteristics of riffle texture over the course of the study. In particular, SOM mapping of riffle texture trends to each riffle sampling node indicates a spatially and temporally organized process of riffle texture adjustment. Notably, the McNemar non-parametric test results were consistent with the EOF temporal trends of riffle texture. Riffle texture trends associated with significant change compare well with the reach-average bed stress - reach-average  $D_{50}$  model of *Buffington and Montgomery* (1999a). For all but one event sequence (E9–E10), the *Buffington and Montgomery* (1999a) response model captured both the direction and magnitude of texture adjustment in response to sediment mobilizing floods. The response trajectory of event sequence E9–E10 can be explained by *Jackson and Beschta* (1982)'s observations of spatially non-uniform sediment transport processes over a pool-riffle reach in the Oregon coast range. There may also, however, be other explanations.

Evaluation of local sedimentation trends for the pool-riffle pair with  $V^*$  and the riffle tex-

ture data suggest a period of coupling between the bedform units following the 20-year flood, consistent with previous work (Dietrich *et al.*, 1989; Lisle and Hilton, 1992). Demonstration of coupling for the present case was however tenuous, and would benefit from a more controlled environment. Therefore, we have used the present work to design flume experiments which we hypothesize will support a novel analysis of how sedimentation and surface sediment texture dynamics between pool and riffle factor for pool-riffle maintenance. Beyond the maintenance realm, these issues are particularly important for salmonids, because they rely on pool-riffles for habitat over a wide range of their life cycle.

We believe the riffle-texture aspects of the field-measurement strategy and analytical approach holds promise for identification and characterization of bed surface structures and sediment patches, as well as exploration of local sediment sorting processes. Further application of this program would benefit from a denser sampling of riffle sediments, including georeferenced photographs of sufficient resolution for more detailed analysis of surface sediments distribution.

## 2.8 Details of SOM methods

SOMs method, introduced by Kohonen (1982, 2001), approximates a dataset in multidimensional space by a flexible grid (typically of 1 or 2 dimensions) of cluster centers. For a 2-D rectangular grid, let the grid points or units be symbolized as  $\mathbf{i}_j = (l, m)$ , where  $l$  and  $m$  take on integer values, i.e.  $l = 1, \dots, L$ ;  $m = 1, \dots, M$ ; and  $j = 1, \dots, L \times M$ . To initialize the training process, an EOF method is usually performed on the dataset, and the grid  $\mathbf{i}_j$  is mapped to  $\mathbf{z}_j(0)$  (i.e. initial vectors in the data space) lying on the plane spanned by the two leading EOFs (or eigenvectors). As training proceeds, the initially flat 2-D surface of  $\mathbf{z}_j(0)$  is bent to fit the data. The original SOM is trained in a flow-through manner, i.e. observations (input vectors) are presented one at a time during training, though algorithms for batch training are also possible. In flow-through training, there are two steps to be iterated, starting with  $n = 1$ : (1) at the  $n$ -th iteration, select an observation (input vector)  $\mathbf{x}(n)$  from the data space, and find among the points  $\mathbf{z}_j(n - 1)$ , the one with the closest Euclidean distance to  $\mathbf{x}(n)$ . Call this closest neighbor  $\mathbf{z}_k(n)$ , and the corresponding unit  $\mathbf{i}_k(n)$  the best matching unit (BMU); (2) let

$$\mathbf{z}_j(n) = \mathbf{z}_j(n - 1) + \eta h \left( \|\mathbf{i}_j - \mathbf{i}_k(n)\|^2 \right) [\mathbf{x}(n) - \mathbf{z}_j(n - 1)] \quad (2.8A)$$

for which  $\eta$  is the learning rate parameter and  $h$  is a neighborhood or kernel function. The neighborhood function gives more weight to the grid points  $\mathbf{i}_j$  near  $\mathbf{i}_k(n)$ , than those far away, an example being a Gaussian drop-off with distance. Note that the distances between neighbors are computed for the fixed grid points ( $\mathbf{i}_j = (l, m)$ ), not for their corresponding positions  $\mathbf{z}_j(n)$  in the data space. Typically, as  $n$  increases, the learning rate is decreased gradually from the initial value of 1 towards 0, while the width of the neighborhood function is also gradually narrowed.

We use the MATLAB SOM Toolbox (*Vesanto et al., 2000*) where four types of neighborhood functions are available: ‘bubble’, ‘gaussian’, ‘cutgauss’ and ‘ep’ (or Epanechnikov function). Following the guidelines from *Liu et al. (2006)* we use the ‘bubble’ neighborhood function where  $h$  in 2.8A is:

$$h = F(\sigma_n - d_{jk}) \quad (2.8B)$$

The parameter  $\sigma_n$  is the neighborhood radius at  $n$ -th iteration,  $d_{jk}$  is the distance between the units  $\mathbf{i}_j$  and  $\mathbf{i}_k$  on the 2-D grid, and  $F$  is a step function:

$$F(x) = \begin{cases} 0 & \text{if } x < 0 \\ 1 & \text{if } x \geq 0 \end{cases} \quad (2.8C)$$

(see *Vesanto et al. (2000)* for the geometries of these neighborhood functions). The neighborhood radius  $\sigma_n$  is either constant or linearly decreasing between specified initial and final values.

Two quantitative measures (*Kohonen, 2001*) are used to help determine how many units one should use in SOMs, knowing that data underfitting will occur with too few units and overfitting with too many units. The first measure is the average quantization error (QE) which is the average distance between each data point (input vector)  $\mathbf{x}$  and  $\mathbf{z}_k$  of its BMU. The second measure is the topographic error (TE) which gives the percentage of data vectors for which the first BMU and the second BMU are not neighboring units. Smaller QE and TE values indicate better mapping quality. By increasing the number of units, QE can be further decreased; however, TE will eventually rise, indicating that an excessive number of units is used.

Our set of final parameters in MATLAB SOM Toolbox consists of the following: hexagonal lattice, sheet SOM shape, linearly initialized weights, bubble neighborhood radii of 2 and 1, and batch training performed over 200 iterations.

## Chapter 3

# Experimental setup and measurements

### 3.1 Introduction

A total of four experiments were conducted to complement the fieldwork focus of Chapter 2. In Chapter 2, we report that a pool-riffle pair was maintained across 11 sediment mobilizing floods, including an approximate 20-year flood. The pool-riffle pair exhibits minor amounts of net topographic adjustment across all floods, however, the riffle in particular responds to flood events through spatially organized bed sediment texture changes. This finding highlights that pool-riffles in topographic steady-state process flood supplies through changes in bed surface texture and roughness. We design our experiments to further examine sediment texture responses of pool-riffle structures to upstream supply forcing, and to develop enhanced data sets for use with our application of self-organizing maps to characterize sediment texture trends. However, we also specifically design our experiments to examine topographic responses of pool-riffle structures that are trending to a steady-state condition, as our field case of Chapter 2 exhibits statistically-steady behavior. This latter objective forms the main complementary part to the fieldwork focus of Chapter 2.

Here, we provide a summary of the experimental design for pool-riffle experiment 1 (PRE1), as well as details for data collection and processing. In general, we test how channel width variations and morphodynamics are coupled, defined by bed topography and sediment texture responses. Experimental water supply ranges from 1.2–2 times the threshold to mobilize bed sediments, on average, and sediment supply is at or near the theoretical capacity for each flow condition. Our experimental design addresses the following three guiding questions:

1. How does bed topography respond to non-uniform downstream changes in channel width, which introduces flow accelerations and corresponding variations in shear stress?
2. Do width induced topographic responses persist across mobility conditions which range from 2–4 times the threshold condition? Is there hysteresis in this response: will similar responses emerge for repeat experiments conducted with pre-conditioned bed topography and bed sediment texture?

3. What time-varying or steady features of bed topography and sediment texture indicate an equilibrium between upstream supplies of water and sediment and mountain streams?

In Chapters 4 and 5 we present results from PRE1, and use theory to frame and discuss implications of the results for pool-riffle formation, maintenance and equilibrium. Whereas we did use the characteristics of a field site to layout and calibrate the experiments (discussed in Section 3.2.1), the experiments, results and findings are generally applicable to mountain streams.

## 3.2 Laboratory experiment and methods

### 3.2.1 Setup and construction

PRE1 was conducted at the BioGeoMorphic eXperimental Laboratory (BGMX Lab) at the University of British Columbia, Vancouver, Canada (Figures 3.1a and 3.1b). The experimental flume measures 16 m in total length and 1 m in width, and we use 15 m to conduct the experiments. Water recirculates through the flume via a pump, but sediment does not (Figure 3.1). We introduce water to the upstream channel boundary through a series of stacked 5 cm  $\varnothing$  plastic pipes, collectively called the flow normalizer. The normalizer is 1000 mm in length, or roughly  $2w'$  in length, where  $w'$  is the average channel width, and we use it to establish an initially uniform flow. We introduce sediment to the flume via a speed-controlled conveyor, which dumps particles into a mixing chamber we call the randomizer. The randomizer consists of a vertical shaft with alternating cross-bars spanning the width of the shaft. As particles fall through the mixing chamber, their pathways are interrupted by the cross-bars, which flings the particles along random trajectories, providing a spatially-random distribution of sediment fall points on the inlet flume bed. The randomizer action provides a spatially and temporally uniform inlet boundary condition, which did not require manual adjustment during the experiments due to pile construction.

The flume outlet elevation is fixed, and the downstream-most 1.0 m of channel consists of straight channel walls. We chose this outlet configuration to provide controlled conditions for water and sediment leaving the flume, which pass through the particle imaging light box for flux measurement (discussed in Section 3.2.4). Figures 3.1a and 3.1b show that the experimental channel consists of downstream varying channel width, which for simplicity, reflects the average downstream width condition between inflection points along a field site (discussed next). We achieve the experimental width conditions by constructing a channel inside the flume with rough-faced veneer-grade D plywood, which has a surface roughness that varies from 1-4 mm, or roughly 0.15 to 0.60 times the geometric mean grain size of the experimental grain size mixture (discussed next).

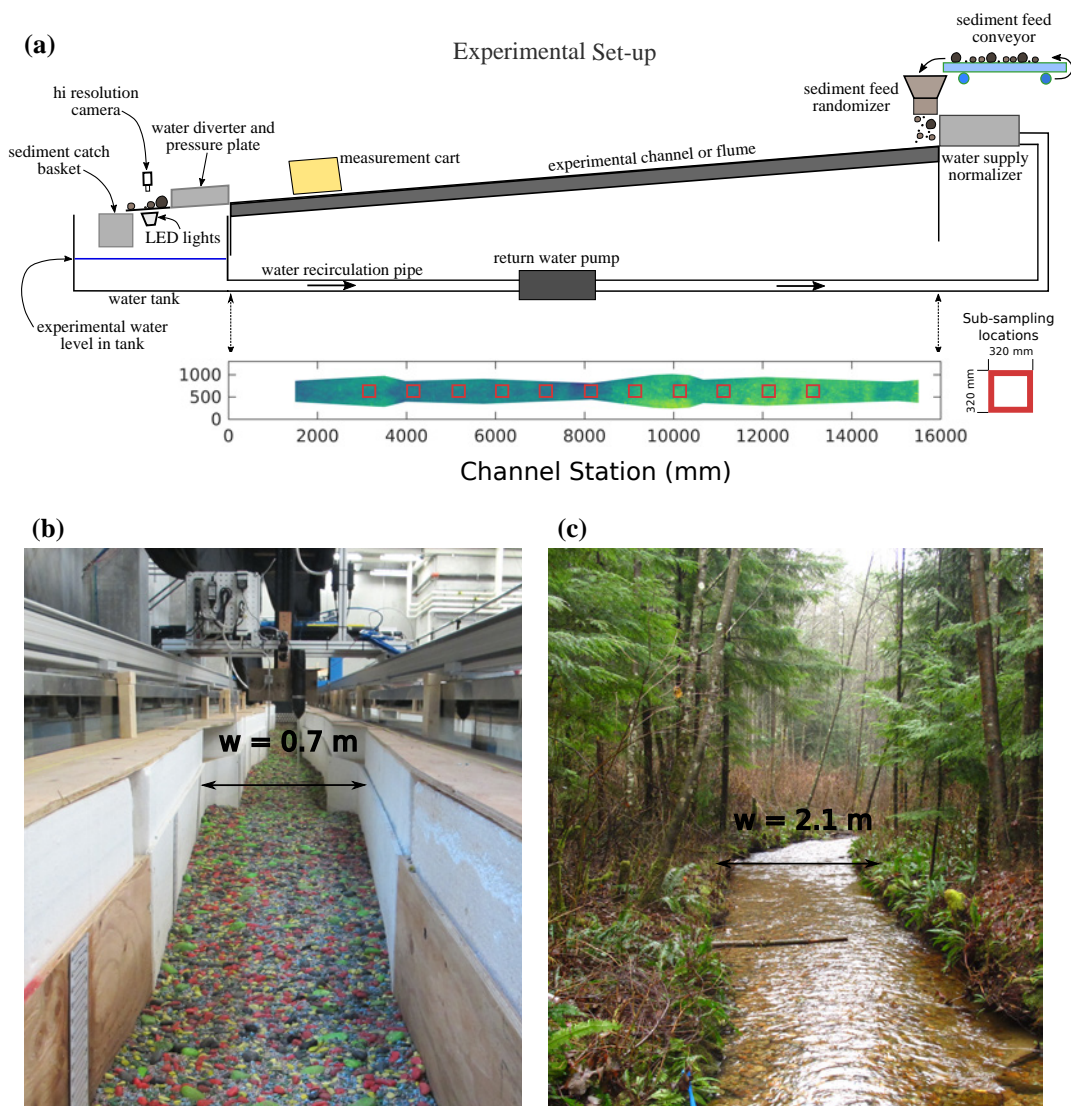


**Figure 3.1:** Overview and images of the experimental setup and field stream reach. (a) Schematic illustration of the experimental setup, including an overhead view of the experimental channel, showing the downstream width variation and subsampling locations indicated by red boxes. (b) Photograph of the experimental channel. The photograph view is looking upstream from station 1000 mm. Photograph taken at experimental time 2150 minutes. (c) Photograph of the field channel East Creek. The photograph view is looking downstream at the equivalent of experimental channel segment 7500 mm to 5000 mm.

### 3.2.2 Experimental design

Experimental scaling was guided by a 75-meter reach of East Creek, University of British Columbia Malcolm Knapp Research Forest, located 1.5 hours east of the University. East Creek is a small gravel-bedded mountain stream (Figure 3.1c). The field reach was chosen because it exhibits pool-riffles and roughened channel segments, with a reach-average bed slope ( $S$ ) of

0.015. Following *Henderson (1966)*, the geometric scale ratio for our 15 m experimental channel is  $L_r = 5$ , where the subscript r indicates the field:model length ratio (*Parker et al., 2003*). The experimental channel width and grain size distribution follows  $L_r$  (Figures 3.1 and 3.2), and the experimental channel slope equals that of the field site. The model grain size distribution ranges from 0.5–32 mm, with a geometric mean size of 7.3 mm ( $D_g$ ), a characteristic coarse grain size of 21.3 mm ( $D_{90}$ : for which 90% of all particles are smaller), and a geometric standard deviation of 2.5 ( $\sigma_g$ ) (Figure 3.2). We paint each grain size fraction a unique color to aid with analysis.

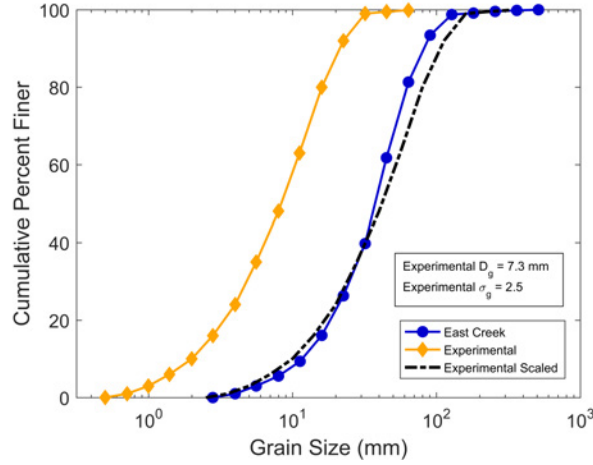


**Figure 3.2:** Cumulative grain size distribution for the experiment and the field reach along East Creek, with grain size in mm shown on the x-axis, and cumulative percent finer on the y-axis. The experimental distribution was scaled according to the geometric ratio  $L_r = 5$ .

The ratio of the maximum to minimum width along the experimental channel is  $\approx 2.1$ , and width variation provides a range of downstream width gradients from  $(-0.26)$ – $(+0.18)$ . As a result, experimental conditions are characterized by segments with minor width gradients, to segments with strong positive and negative gradients (Figure 3.1). The average channel width of the experimental channel is:  $w' = 547$  mm,  $(\sum w)/n$ , where  $w$  is the local width, and for context, the characteristic coarse grain size scales as 18 to  $36w$ . The minimum channel width along the channel is 370 mm (station 8150 mm), and maximum width is 785 mm (station 9960 mm).

We apply Froude scaling to determine the water supply flow rates for our experiments, which requires (*Henderson, 1966*):

$$Fr_r = 1 \quad (3.1)$$

where  $Fr_r$  is the Froude number field:model ratio, with ratio indicated by the subscript r, and  $Fr = \bar{U}_x / (gL_c)$ . We rearrange Equation 3.1 and solve for the field:model velocity ratio:

$$\bar{U}_{x,r} = (g_r L_r)^{0.5} \propto L_r^{0.5} \quad (3.2)$$

where  $\bar{U}_{x,r}$  is the downstream cross-sectionally averaged flow velocity field:model ratio, and  $g_r$  is the gravitational acceleration field:model ratio. Equation 3.2 provides a direct link with geometric scaling of the experiment, and provides the basis of experimental flow scaling:

$$Q_r = \bar{U}_{x,r} L_r^2 \propto L_r^{2.5} \quad (3.3)$$

Our field-estimate of the bankfull flow is 2.3 to 2.5 m<sup>3</sup>·s<sup>-1</sup>. Following Equation 3.3, the lowest experimental flow is 42 liters per second (l·s<sup>-1</sup>), and was supplemented with higher flows of 60 and 80 (l·s<sup>-1</sup>) (Table 3.1), which equate to flood magnitudes of roughly 5-, and 10-year recurrence intervals, respectively. The magnitude of flows used during PRE1 suggests mobile conditions for the entire experimental grain size distribution, reflected by ( $\tau / \tau_{ref}$ ) values which approach 2.0 (Table 4.1) (*Wilcock and McArdeell, 1997*). The variable  $\tau$  is the average bed stress, calculated as  $\tau = \rho_w C_d \bar{U}_{x,r}^2$ , and  $\tau_{ref}$  is the reference critical mobility stress for the bed surface median particle diameter  $D_{50}$ . The variable  $\rho_w$  is the density of water, taken as 1.0 g·cm<sup>-3</sup>, and  $C_d$  is a dimensionless drag coefficient, generally taken as a constant within open channel flows when  $Re > 10^{2-4}$ . The average Reynolds number for fully developed and hydrostatic flows is  $Re = (Q\bar{d}) / (\bar{A}\nu)$ , where  $\bar{d}$  is the cross-sectionally average water depth,  $\bar{A}$  is the average flow area, and  $\nu$  is the kinematic viscosity of water at 15°C (approximate temperature of water used in the experiments). Reynolds numbers for PRE1  $> 10^5$ . The Shields equation expresses the critical stress for the ( $D_{50}$ ) of all sediment particles on the bed surface (*Shields, 1936*):

$$\tau_{c50}^* = \frac{\tau_{c50}}{\rho' g D_{50}} \quad (3.4)$$

where  $\rho' = [(\rho_s / \rho_w) - 1]$ ,  $\rho_s$  is the density of sediment, taken as 2.65 g·cm<sup>3</sup>, and  $g$  is the acceleration due to gravity on Earth. To close Equation 3.4, the critical dimensional stress  $\tau_{c50}$  is calculated by assuming a reference dimensionless critical stress ( $\tau_{ref}^*$ ) for the  $D_{50}$ , which here we use a value of 0.030 for gravel mixtures (*Parker, 2007; Buffington and Montgomery, 1997*). In reality however, ( $\tau_{ref}^*$ ) is described by a probability distribution of possible values (e.g. *Wiberg and Smith, 1987; Kirchner et al., 1990; Buffington et al., 1992*) (Appendix B).

We chose sediment supply rates through iterative 1D numerical modeling of channel evolution, which facilitates examination of how theoretical capacity bedload transport varies along the length of the experimental channel due to changes in width and particle drag. We use two different transport functions for the simulations, in order to capture a larger range of possible experimental conditions:

1. The *Wong and Parker (2006)* corrected Meyer-Peter and Müller function (MPMf); and
2. The mixed grain size *Wilcock-Crowe (Wilcock and Crowe, 2003)* function (WCf).

The WCf, in particular, is suitable for our experimental grain size distribution, due to the 10% by mass, sand-sized composition of our mixture (*Wilcock and Crowe, 2003*) (Figure 3.2). We identify preliminary sediment supply rates by solving MPMf and WCf for

**Table 3.1:** Experimental details for PRE1

PRE1 Interval (-)	Elapsed Time (min)	Flow ( $l s^{-1}$ )	Sediment Feed ( $kg m^{-1}$ )	DEM/Photo (-)
0	0	-	-	yes
1	19	42	0.50	yes
2	50	42	0.50	yes
3	110	42	0.50	yes
4	230	42	0.50	yes
5	470	42	0.50	yes
6	710	42	0.50	yes
7	950	42	0.50	yes
8	1190	42	0.50	yes
9	1430	42	0.50	yes
10	1670	42	0.50	yes
11	1910	42	0.50	yes
12*	2150	42	0.50	yes
13	2225	60	0.80	yes
14*	2390	60	0.80	yes
15	2450	80	1.00	yes
16*	2570	80	1.00	yes
17	2630	80	1.00	yes
18	2870	42	0.50	yes
19	3110	42	0.50	yes
20	3350	42	0.50	yes
21	3590	42	0.50	yes
22	3830	42	0.50	yes
23	4070	42	0.50	yes
24*	4310	42	0.50	yes
25	4385	60	0.80	yes
26*	4550	60	0.80	yes
27	4610	80	1.00	yes
28	4730	80	1.00	yes
29	4790	80	1.00	yes

<sup>a</sup>Asterisk denotes achievement of mass equilibrium between feed and flux.

<sup>b</sup>The repeat phase of PRE1 began at elapse time 2630 minutes.

<sup>c</sup>The elapse time indicates the end time for the specified experimental interval.

<sup>c</sup>DEM stands for digital elevation model of the experimental channel.

- a. A uniform channel width, equivalent to  $w'$ ;
- b. A uniform longitudinal slope of 0.015;
- c. The three experimental flow rates 42, 60 and  $80 l \cdot s^{-1}$ ;
- d. A uniform longitudinal flow depth approximated as the normal depth; and

- e. Sediment textures based on the experimental grain size distribution (Figure 3.2).

We use the preliminary sediment supply rates for model simulations to assess topographic profile development. Preliminary sediment supply rates vary from 0.1 to 1.5 kilograms per minute ( $\text{kg}\cdot\text{m}^{-1}$ ). Model run durations are 20–40 simulation hours in total, which is sufficient to achieve steady-state conditions, which we define by the following two criteria (these criteria will be discussed further in Chapter 5):

1.  $\partial\eta/\partial t \rightarrow 0$ : Rate of changes in bed elevation goes to zero everywhere in the model domain; and
2.  $\partial D_{50}/\partial t \rightarrow 0$ : Rate of change of the median grain size on the bed surface goes to zero everywhere in the model domain.

Steady-state simulation results are necessary so we can evaluate whether projected bed profiles are compatible with the experimental setup, and specifically to avoid supply rates which cause profile lowering to the flume floor. These two points represent our evaluative criteria for the simulations. Interaction of the flow with the flume floor would introduce an additional forcing condition to bed profile and sediment texture development. Introduction of an additional forcing makes it difficult to understand whether width, or floor-related effects are responsible for experimental outcomes.

Simulations show that capacity bedload transport varies along the experimental channel by a factor of 2–100, for an initially uniform sloping bed surface ( $S = 0.015$ ), subject to the three experimental flow rates. After modeling several supply rates within the range of transport values for each flow, we simplified the problem, and chose the spatially-averaged capacity transport of the MPMf and WCf which met our evaluative criteria above. The selected sediment supply rates for each flow are: 0.5, 0.80 and 1.0 kilograms per minute ( $\text{kg}\cdot\text{m}^{-1}$ ), respectively (Table 3.1). One drawback to this approach is that the difference between the spatial average and true transport capacity increases with flow rate. As a result, sediment supply rates for 60 and 80 ( $\text{l}\cdot\text{s}^{-1}$ ) were less than capacity by some small fraction. We use each selected bedload supply rate for trial experiments to confirm the morphodynamic modeling. Here we use morphodynamics to refer specifically to bed topography and sediment texture adjustments. See Appendix A for model details and sample results for a simulation reflecting experimental conditions at  $42 \text{ l}\cdot\text{s}^{-1}$ .

### 3.2.3 Experimental procedure

We start PRE1 from a smoothed-bed, uniform slope condition (Figure 3.3). The profile in Figure 3.3 has the channel station in mm on the x-axis, and bed elevation in mm on the y-axis. We also provide a DEM (digital elevation model) at the top of Figure 3.3, for reference to the full channel topography, as well as the width layout. Prior to smoothing, the full thickness of sediment in the flume was thoroughly mixed to establish a random size distribution, and

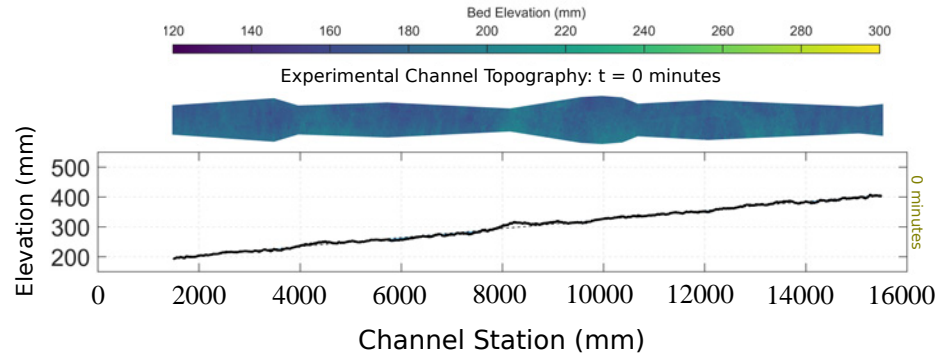


**Figure 3.3:** PRE1 initial bed topography shown as a longitudinal profile of the average elevation along the center 50 mm of the experimental channel from station 1500 to 15500 mm, and as a DEM (digital elevation model of the experimental channel) at the top. The perceptually uniform *Polarmap* colormap was used to map bed elevations in the DEM.

to remove textural heterogeneity related to previous trial runs (Figure 3.1b). Figure 3.4 shows the experimental water supply rate in  $\text{l}\cdot\text{s}^{-1}$  vs. time in minutes (a), and the sediment supply rate in  $\text{kg}\cdot\text{m}^{-1}$  (b). PRE1 consists of an initial and repeat phase (Figure 3.4b). The initial phase extends from  $t_e = 0$  minutes, where  $t_e$  is elapse time, to 2630 minutes, and the repeat phase extends from  $t_e = 2630$  minutes, to 4790 minutes (Table 3.1; Figure 3.4b). Flow and sediment supply continue at constant values until total sediment flux approximates the sediment supply rate, and in all cases the fractional flux was comparable to the fractional supply as determined by the Two-sample Kolmogorov-Smirnov test of continuous distribution similarity (Massey, 1951). Specifically, water and sediment supply varies over the course of PRE1 as follows (Table 3.1; Figure 3.4b):

1. For the initial phase:
  - (a) water supply was  $42 \text{ l}\cdot\text{s}^{-1}$ , and sediment supply was  $0.5 \text{ kg}\cdot\text{m}^{-1}$  from  $t_e = 0$  to 2150 minutes;
  - (b) water supply was  $60 \text{ l}\cdot\text{s}^{-1}$ , and sediment supply was  $0.8 \text{ kg}\cdot\text{m}^{-1}$  from  $t_e = 2150$  to 2390 minutes;
  - (c) water supply was  $80 \text{ l}\cdot\text{s}^{-1}$ , and sediment supply was  $1.0 \text{ kg}\cdot\text{m}^{-1}$  from  $t_e = 2390$  to 2630 minutes;
2. For the repeat phase:
  - (a) water supply was  $42 \text{ l}\cdot\text{s}^{-1}$ , and sediment supply was  $0.5 \text{ kg}\cdot\text{m}^{-1}$  from  $t_e = 2630$  to 4310 minutes;
  - (b) water supply was  $60 \text{ l}\cdot\text{s}^{-1}$ , and sediment supply was  $0.8 \text{ kg}\cdot\text{m}^{-1}$  from  $t_e = 4310$  to 4550 minutes;

- (c) water supply was  $80 \text{ l}\cdot\text{s}^{-1}$ , and sediment supply was  $1.0 \text{ kg}\cdot\text{m}^{-1}$  from  $t_e = 4550$  to 4790 minutes;

We use a ramping up and down period of 4-5 minutes each time the water supply is raised and lowered to and from the experimental flows of 42, 60 and  $80 \text{ l}\cdot\text{s}^{-1}$ . The repeat phase (Figure 3.4b) began from the prevailing channel topographic and bed surface sediment sorting conditions established by the end of the initial phase (Figure 3.4b).

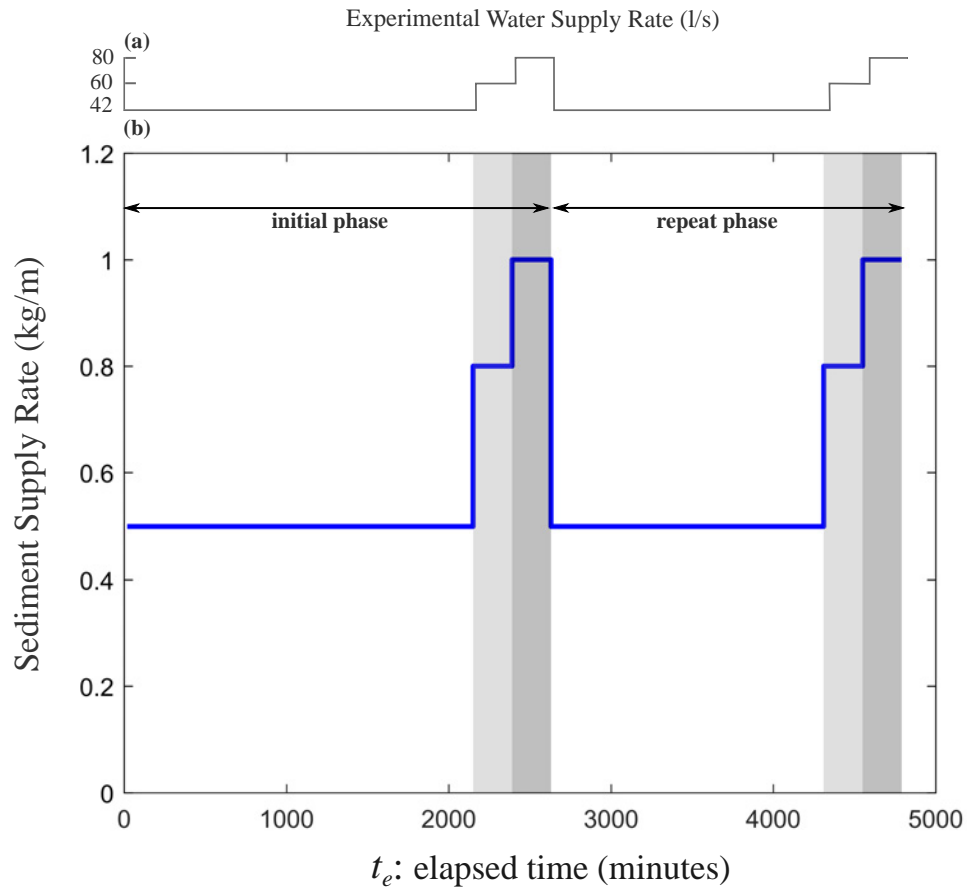


**Figure 3.4:** PRE1 details of water and sediment supply. (a) Timing and rate of flow during PRE1. (b) Timing and supply of sediment during PRE1. The first sequence of 42, 60 and  $80 \text{ l}\cdot\text{s}^{-1}$  water supply (and associated sediment feed) constitutes the initial experimental phase. The second flow and sediment feed sequence was the repeat phase. The vertical shaded areas reflect flow rates of 60 and  $80 \text{ l}\cdot\text{s}^{-1}$ , respectively.

### 3.2.4 Experimental measurements and processing

To address the general experimental questions presented in Section 3.1, we make direct measurements of bed topography, sediment flux from the channel, and water depth along the

channel, and we make indirect measurements of bed sediment texture. Measurements are made for data collection intervals that range from 19 to 240 minutes, with intervals during the first 240 minutes following a geometric progression starting from time 19 minutes (4 minute ramp up + 15 minute run interval) (Table 3.1). We use a geometric progression in order to better evaluate morphodynamic evolution during the first 2 hours of PRE1. The maximum data collection interval is 240 minutes. Practical considerations dictated that data collection intervals during the 60 and 80  $\text{l}\cdot\text{s}^{-1}$  flows were set by the time it took for substantial bed topography change to occur, ranging from 60 to 165 minutes.

### **Bedload flux**

We use a light table to measure bedload flux and enforce mass conservation (Zimmermann *et al.*, 2008). The light table system uses an overhead camera to measure particle positions in a water column 2 to 3 cm thick. The particles and water pass over a positively-sloping semi-transparent lexan base, which is back lit by a constant-voltage LED panel light measuring 610  $\text{mm}^2$ . Images of the silhouetted particles are captured at 15-20 Hz with an Allied Vision Technology GX2300 CCD camera. The camera uses a Kowa Optimed 16 mm 4/3" megapixel LM16XC lens, which was selected specifically for the GX2300 sensor resolution, and imaging distance of the setup. Images are processed with LabView<sup>TM</sup> code to compute the time-averaged flux for all grain size classes  $>2$  mm at a temporal resolution of 1Hz (Zimmermann *et al.*, 2008). The particle imaging setup went through extensive validation trials following Zimmermann *et al.* (2008). To independently evaluate PRE1 light table data, we hung a mesh basket at the downstream end of the light table to catch all flux from the experimental channel, which was weighed, then sub-sampled and sieved for comparison.

### **Bed surface topography**

We periodically stop flow to measure bed topography with a camera-laser setup mounted to an automated cart system. We subsequently use these data to produce DEMs with a spatial resolution of 1 mm. In total, we collected thirty DEMs during PRE1 (Table 3.1). The camera is an Allied Vision Technology Prosilica GC with a Kowa 15 mm 4/3" megapixel lens. We mount the camera at the downstream center of the measurement cart, looking upstream at an angle of roughly 15-degrees from horizontal. We mount a 5 mW 100 deg fan angle green line laser at the upstream center of the measurement cart, with the lens plane oriented parallel to the bed of the channel. As the cart moves upstream along the experimental channel, photographs of the laser illuminated bed are taken. We compare these photographs with a vertical elevation model of the flume to produce the DEMs. The vertical elevation is prepared by imaging a dot-matrix board placed in the vertical plane of the laser.

We use a 3-step algorithm to process each DEM:

1. We clip DEM margins to the experimental channel width;

2. We filter anomalously high elevation values; and
3. We fill DEM holes.

Anomalously high elevation values are caused by laser reflection off of boundaries. High values were iteratively identified by plotting the full distribution of elevations as a *cdf*, and subsequently removing values that occur at the extreme lower end of the *cdf*. We then visually inspect a draft DEM, and the filter threshold is adjusted if point elevations within the experimental channel were deleted, or if anomalously high values remain.

DEM holes occur due to camera view obstruction by large grains, and along short channel segments which exhibit strongly positive topographic gradients (from the reference frame of the camera view). We fill DEM holes assuming the local average elevation within immediately adjacent unaffected locations along the same longitudinal coordinate. After some trials, we set the lateral search neighborhood to be 30 grid points, which equates to a length scale of 15 mm. Our decision to correct DEM holes with lateral elevations, as opposed to a neighborhood of elevations, is consistent with the physical cause of the camera blind spots. After DEM processing was complete, we clip the DEM to longitudinal stations 1500 and 15500 mm, and 11 DEM locations are sub-sampled for further analysis. Sub-sampling locations are shown in Figure 3.1a, are located at 1000 mm increments ( $\approx 2w'$ ), and measure 320x320 mm<sup>2</sup>. We use one last processing step for each subsampled DEM, and discuss it next with the composite photograph.

### **Composite photographs of bed surface**

We produce a composite image of the experimental channel with a Canon D60 camera and Canon EF 17-40 mm f4.0 lens, fixed to 40 mm to minimize distortion and maximize image resolution. We mount the Canon camera at the upstream end of the cart, and upstream from the laser we use to collect the DEM. Individual photographs are captured at a sensor resolution of 1920Wx1280H  $\mu\text{m}^2$ . Based on lens construction and camera sensor size, we step the measurement cart at increments of 10-25 mm, depending on topographic relief, and we crop resultant images to the cart step distance and line each sub-image up edge to edge to produce the composite image. Composite image resolution is approximately 1–2 mm, with image information density ranging from 2.1–2.6 px/mm, or 4.4–27.0 px/sediment particle, depending on distance between channel bed surface and lens body, and lateral distance from image center. The upper end of the pixels per particle range exceeds the 20 pixels per particle goal put forth by *Zimmermann et al.* (2008). We use external LED overhead lights to provide consistent lighting conditions across all composite photographs.

We apply a 2-step process to the composite channel photographs to develop the final working image.

1. We line up each photograph to the same longitudinal coordinate system as the DEM. This was accomplished by applying a length scale offset based on the distance between

the first downstream row of photographic pixels and the first row of DEM data. The alignment operation has a resolution of roughly  $\pm 1$  mm at its best.

2. We clip the photograph to longitudinal stations 1500 and 15500 mm, which facilitates associated photographs and DEMs to be overlaid, within the resolution constraint just noted.

As with the DEMs, photographs are subsampled at 11 locations (Figure 3.1a), producing images with physical dimensions to match the subsampled DEMs. From visual inspection, the composite photographs show a minor amount of radial lens distortion at the image corners, and as a result, composite images were not corrected for distortion.

We apply one last post-processing step to produce subsampled composite images and DEMs which map to the same coordinates. The step involves use of two image mapping statements, assuming a coplanar perspective between the camera lens and the channel bed *Hugemann* (2010):

$$X - X_0 = [c_1(\hat{x} - x_0)]_z \quad (3.5)$$

$$Y - Y_0 = [c_2(\hat{y} - y_0)]_z \quad (3.6)$$

where real world coordinates are denoted by  $X$  and  $Y$ , and the origin defined by the position  $(X_0, Y_0)$ , which is co-located with the image center coordinates  $(x_0, y_0)$ . Image coordinates are denoted by  $\hat{x}$  and  $\hat{y}$ , which reflect estimates of position within the image. We use Equations 3.5 and 3.6 plus the image resolution (fixed for PRE1) to build image coordinate mapping databases of the channel bed for the full range of elevations observed during PRE1. This is analogous to the distortion-correction mapping database of *Hugemann* (2010).

We produce the image coordinate maps with photographs of a checkerboard (uniform check dimensions: 1x1 cm) placed horizontally within the widest flume location, and at three elevations beginning at the floor of the channel, and 30 and 60 cm above the floor. The total number of checks ( $C_n$ ) and pixels ( $Px_n$ ) from image center to edge were counted and recorded for each of the three photographs. The ratio  $Px_n/C_n$  provides a scaling of  $px/mm$  from image center to image edge for the photographed elevations, and linear regression provides a continuous scaling over elevations 0–60 cm (variable  $[c_2]_z$  of Equation 3.6. At each subsampling location and moving downstream to upstream through each row of image pixels, we produce a subsampled image with the following 2 steps:

1. We use the DEM to identify the elevation-specific image coordinate map to query; and
2. We locate the lateral image coordinates ( $\hat{x}$  and  $\hat{y}$ ) which measure  $\pm 180$  mm from image center by inverting each ratio  $Px_n/C_n$ , multiplying by 1  $px$  and summing.

We use the DEM resolution to prepare the subsampled DEM, and then numerically enhance it by linearly interpolating the DEM to match the resolution of each subsampled image. For

reference, we provide Figure 3.5, which illustrates a sub-sampled DEM and photograph pair for station 10000 mm, elapsed time 2150 minutes (Table 3.1).

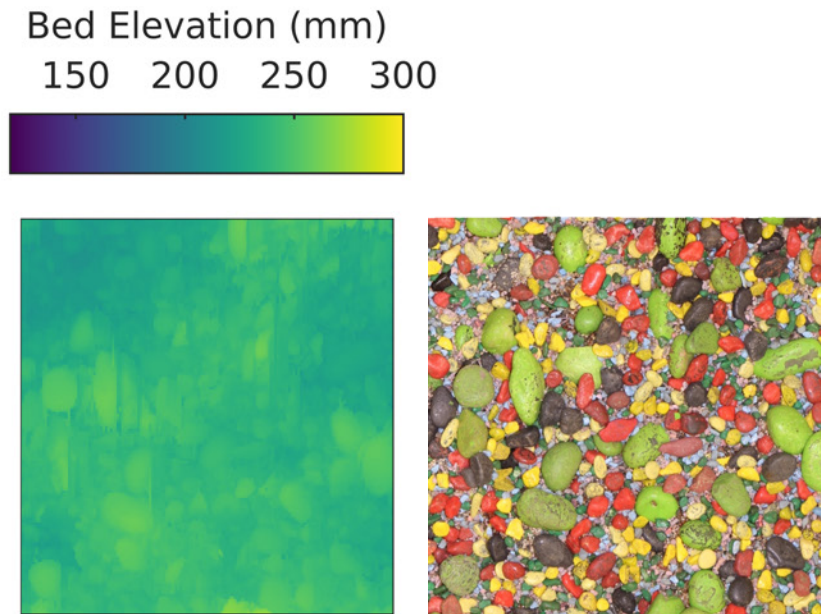


**Figure 3.5:** Example sub-sampled DEM and photograph pair for station 10000 mm, elapsed time 2150 minutes. The DEM is on the left hand side of the image, and the photograph on the right. The sub-sampled DEM and photograph measure  $320 \times 320$  mm<sup>2</sup>. Affects from the hole filling procedure are evident within the DEM, near the center left, and with respect to the larger, oblong sediment particle that has its major axis oriented in the vertical plane of the DEM.

### 3.2.5 Bed surface grain size distributions

We analyze subsampled images for grain size statistics using a semi-automated MATLAB<sup>®</sup> script. The script identifies grain sizes based on the painted color of each grain size class in the experimental mixture. The script begins by loading an RGB and HSV color database for each color used in the mixture. We build the color databases by randomly querying the respective color values of grains in several different subsampled images for grain size classes down to the Wentworth 2 mm gravel/sand threshold. Fifty grains from each grain size class were used to build the size-specific color databases. The script then proceeds to establish a fixed sampling grid of 100 points over the subsampled image, and moves point to point using built-in MATLAB<sup>®</sup> image analysis functions to identify the RGB and HSV color values in a  $3 \times 3$  px<sup>2</sup> area  $A_p$ .

A positive color detect was met if:

$$[A_p]_{RGB} = [A_p]_{HSV} \quad (3.7)$$

In the case of a positive color detect, the script increments the associated grain size class counter by 1, and uses the geometric mean grain size of the grain size class in the statistics calculations. If  $[A_p]_{RGB} \neq [A_p]_{HSV}$ , the user is prompted to identify the color of the sampled grain. All grains  $\leq 2$  mm were counted as 2 mm in diameter, effectively lumping these grains into the sand size classes. Validation of script results occurred by comparing the semi-automated results to manual counts for 5 different images. The only notable difference between the semi-automated and manual counts occurred for cases when the sampling node was located at the intersection of several grains.

The grain count procedure has an inherent error of approximately 5% due to sieve inaccuracies of the bulk sediments prior to painting. The sieve inaccuracies resulted in inclusion of smaller grains within the next larger grain size class. This error was constrained to grains  $< 16$  mm in diameter.

### 3.2.6 Manual water and bed surface profiles

We measure centerline longitudinal channel bed and water surface profiles with a point gauge. Profile measurement points were spaced 250 mm apart, providing 58 measurement locations for each profile. Profile collection took 12 minutes to complete, and in total, eighty-four manual profile measurements were completed in between the higher resolution automated DEM measurements. The tip of the point gauge was outfitted with a 3 cm  $\varnothing$  stainless steel washer so that it sat on the bed surface during bed measurements, and so that it was easier to sight along the water surface during those measurements. Water surface measurements made with the point gauge occurred over a period of about 10 seconds in order to capture a local quasi-average condition. Resolution of the bed and water surface measurements was  $\pm 1$  mm based on a visual estimate of reading variation of the point gauge scale.

All thirty DEMs were associated with a manual water surface profile, which was collected immediately prior to collecting the DEMs. Twenty-seven of the thirty DEMs were also associated with a manual bed surface profile. We use the manual bed surface profiles to align the water surface profiles within the same coordinate system of the DEM. We shift manually-collected channel bed profiles until alignment is achieved with a profile computed from an associated DEM. After some trials, the profile correction was determined to be 29 mm based on minimizing the sum of square differences between manual and DEM profiles. After vertical alignment, we smooth manual water surface profiles with an upstream/downstream moving average algorithm, and then interpolate the profiles to the DEM resolution. We use moving average window lengths of 2, 4 and 6 observation locations around the smoothing point. The final smoothing window length was chosen based on minimization of sum of squares differences between the non-smoothed and smoothed profiles, which was generally met with a window length of 2 or 4 observation locations. We smoothed the water surface profiles to remove the rapidly varying character of some segments of profiles.

### 3.2.7 Flow depth, flow area and average streamwise velocity

We use the DEMs and filtered and smoothed water surface profiles to determine the cross-sectionally averaged water depth ( $\bar{d}$ ), wetted flow area ( $A$ ), and the downstream-oriented flow velocity ( $\bar{U}_x$ ) at every longitudinal station  $j$  of the DEM:

$$\bar{d}_j = \frac{\sum_{k=1}^{k=n} (z_j - \eta_{j,k})}{n} \quad (3.8)$$

$$A_j = w_j \bar{d} \quad (3.9)$$

$$\bar{U}_j = \frac{Q_w}{A_j} \quad (3.10)$$

where  $z_j$  is the smoothed water surface elevation for longitudinal station  $j$ ,  $\eta_{j,k}$  is the DEM bed surface elevation for longitudinal station  $j$ , and transversal station  $k$ ,  $n$  is the total number of transversal stations,  $w$  is the experimental channel width at  $j$ , and  $Q_w$  is the flow rate. We calculate the local Froude number at location  $j$ :  $Fr_j = q_{w,j} / (g^{0.5} \bar{d}_j^{1.5})$ , where  $q_{w,j} = Q/w_j$ , and the local Reynolds number at  $j$ :  $Re_j = Q \bar{d}_j / A_j \nu$ . The local channel bed and water surface slopes,  $S_\eta$  and  $S_w$  respectively, were computed from the DEMs, and the smoothed water surface profiles. Side wall corrections were not made because the experimental channel walls provided some roughness, and because results presented here have focused on downstream differences in experimental conditions, as opposed to the magnitude of the values themselves.

## Chapter 4

# Morphodynamics of a width-variable gravel-bed stream: new insights on pool-riffle formation

### 4.1 Summary

Pool-riffles occur along gravel-bed mountain streams which exhibit downstream variations in channel width, such that pools are observed along segments of narrowing, and riffles at places of widening. Despite recognizing spatial correlations between channel width and bed topography, we lack a widely accepted mechanistic explanation of the correlation (See Section 1.2.2). We address this knowledge gap and build from existing work with systematic experimental evaluation of bed topography evolution and development within a channel that exhibits downstream width gradients ranging from  $-0.26$  (narrowing) to  $+0.18$  (widening). Our experiments reliably produce pools, riffles and roughened channel segments, which persist for sediment mobility conditions that varied on average by a factor 2–4 above the threshold value necessary to mobilize the experimental sediment mixture. Our results show that topographic responses are coupled to changes in channel width, which drives flows to accelerate or decelerate, for narrowing and widening, respectively. We characterize and understand theoretically this coupling in terms of a mathematical model which describes topography as directly dependent on spatial variations in the bulk flow speed, and inversely dependent on channel width and bed surface sediment mobility. The model suggests that a negative feedback between bulk flow speed variations and particle mobility drives channel evolution to states that tend to eliminate, or greatly diminish spatial differences in bedload transport. We show that among reaches of similar grain size, it is possible to project topographic responses knowing nothing more than how channel width changes downstream, regardless of mean channel slope.

## 4.2 Introduction

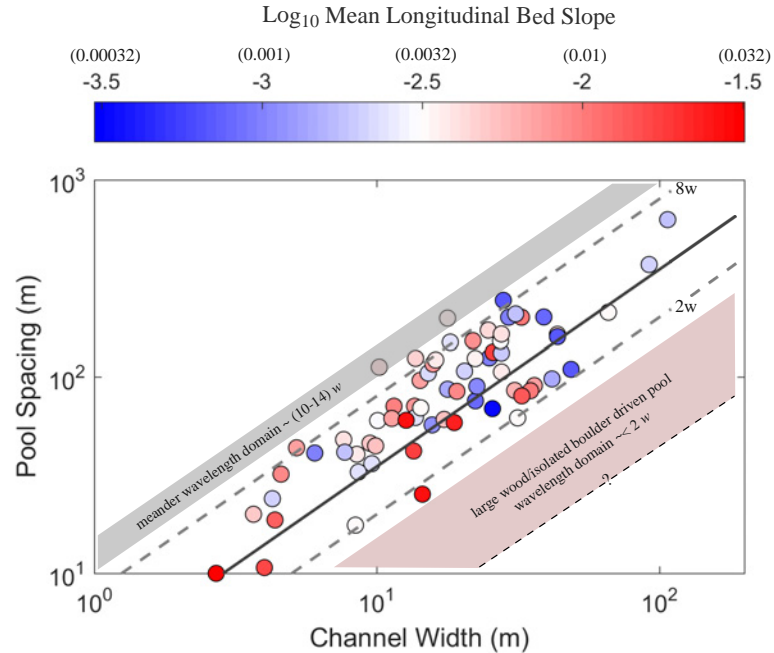
Pool-riffles are generic structures of river bed architecture within bedload dominated systems of gravel (2–64 mm) to cobble (64–256 mm) composition. Pools are topographic lows, related to a local tendency for net particle entrainment, where local is a length scale of 1 to 2 reach average channel widths ( $w'$ ). Riffles, by contrast, are topographic highs, reflecting the tendency for net particle deposition. Pool-riffles are observed across a broad range of natural conditions from mountain headwaters to valley lowland settings, straight to meandering river reaches (Leopold and Wolman, 1957), and for mean longitudinal bed slopes ranging from  $\approx 0.0001$  to 0.03 (Leopold and Wolman, 1957; Leopold et al., 1964; Church and Jones, 1982; Montgomery and Buffington, 1997; Chartrand and Whiting, 2000; Buffington et al., 2002; Hassan et al., 2008). The prevalence of pool-riffles throughout river systems highlights that the necessary formative conditions are common to many different parts of the fluvial landscape.

Figure 4.1 illustrates that pool spacing along relatively straight pool-riffle channels scales with the local channel width ( $w$ ), and is independent of channel steepness. Data from six previous studies suggest that mean pool spacing is  $2\text{--}8w'$  (Yalin, 1971; Richards, 1978; Keller and Melhorn, 1978; Carling and Orr, 2000), for mean bed slopes that vary by 2 orders of magnitude. Figure 4.1 also shows that pool spacing along channels with large roughness elements such as wood and boulders scales as  $0\text{--}2w'$  (Montgomery et al., 1995; Beechie and Sibley, 1997), and along meandering channel segments which commonly exhibit bars scales as  $10\text{--}14w'$  (Richards, 1976b). One expectation for the data in Figure 4.1 is that the spacing is related to eddies scaling in size with the water depth  $d$ , which deliver sufficient momentum flux to the bed to disaggregate it, entrain particles, and drive pool construction (Yang, 1971; Richards, 1976a; Carling and Orr, 2000). However, to our knowledge, no studies demonstrate any direct link between depth scaled eddies and pool-riffle formation. As a result, Figure 4.1 highlights key knowledge gaps:

1. Despite the evidence that pool-riffles collocate with narrow and wide channel segments along straight channel segments, respectively, it is not clear how or why channel width might enter into a mechanistic scaling for pool spacing.
2. We do not know why rivers with generally similar water depth conditions ( $\sim 1$  m) at formative discharge, exhibit such a wide range of pool spacings.
3. The distinctive pool spacing for roughness dominated, straight, and meandering river segments has not been explained.

The knowledge gaps motivate two critical questions, which are the focus of this Chapter:

- A. Figure 4.1 suggests that channel width exerts a strong control over pool spacing, but what in particular about channel width matters for pool spacing expression?
- B. Figure 4.1 includes data from many different river systems, each at differing stages of development in response to landscape construction and flood events. Do initial or inher-



**Figure 4.1:** Downstream pool spacing as a function of the local channel width ( $w$ ) for pool-riffles along relatively straight reaches. Data are colored according to the  $\log_{10}$  mean longitudinal bed slope. Two gray dashed lines suggest approximate limiting cases of  $2w$  and  $8w$ ; solid darker gray line is *MacVicar and Best* (2013)'s experimental result of  $(3-4)w$  for recovery of flow into and out of a fixed pool, implying a pool wavelength of  $(6-8)w$ . Values in parentheses above the slope colorbar are the equivalent fractional bed slope, defined as the change in bed elevation over some streamwise distance of many channel widths in length. Meander wavelength domain per *Richards* (1976b), and the large wood/boulder driven pool wavelength domain per *Montgomery et al.* (1995) and *Beechie and Sibley* (1997). Plotted data from *Leopold and Wolman* (1957); *Keller and Melhorn* (1978); *Montgomery et al.* (1995); *Sear* (1996); *Carling and Orr* (2000); *Thompson* (2001). Only  $S$  data used from *Leopold and Wolman* (1957), and only  $PR$  data used from *Montgomery and Buffington* (1997). The perceptually uniform *Polarmap* colormap was used for slope magnitude.

ited topographic and sediment texture conditions predetermine a particular outcome, and contribute to the variance illustrated in Figure 4.1?

We address these two questions with scaled laboratory experiments (PRE1: pool-riffle experiment 1) and theory, guided by three objectives. First, we examine how bed topography and bed sediment texture conditions (i.e. morphodynamics) evolve from initial to steady-state conditions along a variable width channel. In all cases initial conditions are far from steady-state. Second, we use experimental results to characterize the extent to which morphodynamic evolution depends on downstream changes in channel width. Third, we use repeat experiments to explore the potentially significant effects of hysteresis: does the history of bed evolution condition shape the character of its response in space and time?

We hypothesize that bed constitution and the potential for pool-riffle formation adjusts

to downstream flow accelerations and dynamic pressure variations related to changes in the cross-sectionally averaged velocity driven by channel width differences. We further hypothesize that the magnitude of these effects on the morphodynamic response, defined as a particular topographic and sediment texture outcome, will scale with the extent of width variation. A primary conclusion of our work is that the downstream channel width gradient is a general predictor of topographic response along stream reaches likely to exhibit pool-riffle architecture. We also identify restrictive conditions leading to pool digging and riffle construction, and show that bed history may not affect the general response pattern (i.e. the mean longitudinal bed slope), but that it does lead to unique responses.

## 4.3 Results

### 4.3.1 Identifying general response regimes with sediment flux, mean bed topography and bed sediment texture

In Figure 4.2 we show temporal variability of the PRE1 sediment flux ( $Q_{sf}$ ), normalized mean bed elevation ( $\bar{\eta}'$ ), normalized geometric mean bed surface grain size ( $D'_g = D_{gs}/D_{gf}$ ), and the normalized characteristic coarse bed surface grain size ( $D'_{90} = D_{90s}/D_{90f}$ ), expressed for the dimensionless time  $t_o$ , defined as the ratio of the elapsed time ( $t_e$ ) to the activation time ( $t_a$ : explained below). For  $D'_g$  and  $D'_{90}$ , the subscript  $s$  stands for the bed surface, and the subscript  $f$  stands for the upstream sediment supply. We also show the associated supplies of water ( $Q_w$ ) and sediment ( $Q_{ss}$ ) for context, and plotted quantities are given in Table 4.1. Figure 4.2 illustrates that ( $Q_{sf}$ ), ( $\bar{\eta}'$ ), and to a lesser extent mean  $D'_g$  and  $D'_{90}$ , vary systematically through PRE1, and we use these systematic trends to establish four characteristic response regimes for PRE1. The response regimes capture the morphodynamics of PRE1, and therefore help to explain how the variable-width experimental channel responds to upstream supplies of water and sediment. Overall, PRE1 has an initial, and a repeat phase (Figure 4.2a), which extend from  $t_o = 0-23.9$ , and  $t_o = 23.9-43.5$ , respectively. The characteristic response regimes are:

1. Bed response to the start of an experimental phase (Activation Time:  $t_a$ ): PRE1 has a start-up response we term the activation time  $t_a$ . The activation time represents the initial sediment redistribution along the experimental channel, which occurs due to the relatively high beginning sediment mobility. High sediment mobility provides a rapid increase in  $Q_{sf}$  during  $t_a$  to a peak, after which the rate of  $Q_{sf}$  change abruptly decreases. The bed evolution  $\bar{\eta}'$  during  $t_a$  exhibits a small positive rate of change. Average  $\bar{D}'_g$  and  $\bar{D}'_{90}$  follow the  $Q_{sf}$  trend, and each grain size show rapid increase in size to a peak before abruptly changing.  $t_a$  extends from  $t_o = 0$  to 1. As a result, the activation time only occurs during the initial phase.
2. Bed response to developing flow (Transient Time:  $t_t$ ): The transient period  $t_t$  has flow developing in response to topographic pattern construction along the experimental chan-

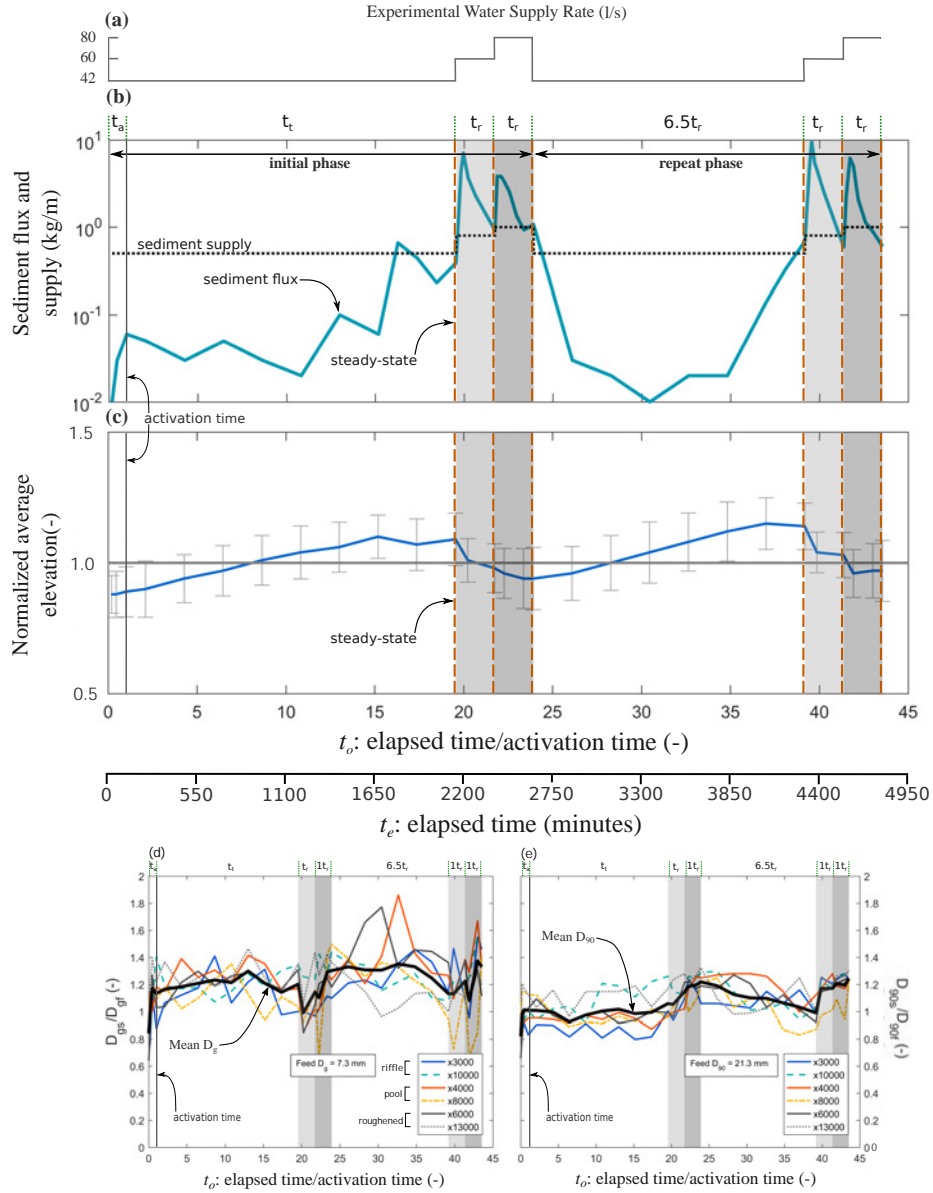


**Figure 4.2:** PRE1 morphodynamics summary: PRE1 morphodynamics summary: water and sediment supply, sediment flux, longitudinal mean bed topography, and geometric mean and characteristic coarse grain sizes vs. the dimensionless time  $t_o$ , defined as the ratio of elapse time  $t_e$  to activation time  $t_a$ . (a) Water supply rate ( $Q_w$ ) ( $\text{l}\cdot\text{s}^{-1}$ ). (b) Sediment supply rate and flux ( $Q_{ss}$  and  $Q_{sf}$ , respectively) ( $\text{kg}\cdot\text{m}^{-1}$ ). (c) Longitudinal normalized mean bed topography ( $\bar{\eta}'$ ), calculated as the ratio of the time-specific mean bed elevation for all subsampling locations, to the mean bed elevation across all subsampling locations and observation times. (d) Normalized geometric mean grain size ( $D_g$ ), calculated as the ratio of the bed surface  $D_g$  to the supply  $D_g$ . (e) Normalized characteristic coarse grain size ( $D_{90}$ ), calculated as the ratio of the bed surface  $D_{90}$  to the supply  $D_{90}$ . Activation ( $t_a$ ), transient ( $t_t$ ) and response ( $t_r$ ) periods indicated at the top of (b), (d) and (e).

nel. During the initial  $t_t$ ,  $Q_{sf}$  remains relatively consistent until  $t_o = 15.2$ , after which  $Q_{sf}$  rises rapidly to the supply rate, and remains consistent with the  $Q_{ss}$  through the end of the initial  $t_t$  ( $t_o = 19.5$ ).  $\bar{\eta}'$  rises at a uniform rate during the initial  $t_t$  until  $t_o = 15.2$ , after which topography is steady.  $\bar{D}'_g$  increases during  $t_t$  to a peak at  $t_o = 13.9$ , after which it drops through the end of the initial  $t_t$  ( $t_o = 19.5$ ).  $\bar{D}'_{90'}$ , on the other hand remains steady through the initial  $t_t$ . Following recovery from the initial period high flow sequence from  $t_o = 19.5$ – $23.9$ , the repeat phase transient responses are similar to those for the initial phase, with one exception.  $\bar{D}'_{90'}$  steadily decreases during the repeat phase  $t_t$ , recovering a value at  $t_o = 39.2$  which is roughly equivalent to the corresponding initial phase value at  $t_o = 19.5$ . The duration of the initial phase  $t_t$  is 18.2, and the repeat phase is 15.3.

3. Steady-state (SS): We define steady-state by two criteria, similar to that used for numerical simulations (Chapter 3.2.2). First, the extent to which mean topography is statistically stationary. Second,  $Q_{ss} \approx Q_{sf}$ . The second criteria holds for the total mass, and grain size specific (fractional) masses. Steady-state occurs at  $t_o = 19.5$  and 39.2, after extended time of topographic and flux steadiness (Table 4.1; Figure 4.2). Steady-state also occurs at the end of each response to steady-state ( $t_r$ ) periods (discussed next), at  $t_o = 21.7, 23.9, 41.4$  and 43.5.
4. Response of steady-state beds to supply regime changes (Bed Response Time:  $t_r$ ): The steady-state bed response period characterizes how a supply regime change is expressed by the channel from a SS. Step increases in supply during both the initial and repeat phases drives initially rapid increases in  $Q_{sf}$  and  $\bar{D}'_{90'}$ , and sharp decreases in  $\bar{\eta}'$  and  $\bar{D}'_g$ . After these early responses, and for both the initial and repeat phases,  $Q_{sf}$  abruptly changes and exhibits rapid rates of decrease,  $\bar{\eta}'$  continues to steadily decline,  $D'_{g'}$  also abruptly changes and exhibits increases, and  $\bar{D}'_{90'}$  steadily rises through the end of the  $t_r$  periods. At the end of the  $t_r$  periods, topographic and  $\bar{D}'_{90'}$  adjustments are quasi-steady,  $Q_{sf}$  settles to the supply rate, and  $\bar{D}'_{g'}$  is still responding. The first response to steady-state period is used as the characteristic  $t_r$  time for PRE1. Notably, the second, fourth and fifth  $t_r$  periods are roughly equivalent to the characteristic  $t_r$  time. The third  $t_r$  period, however, is equivalent to  $6.5t_r$ .

Across the response regimes,  $D'_{g'}$  displays varied adjustments for the pool, riffle and roughened channel structures, with no obvious feature-specific trends. However,  $D'_{g'}$  does exhibit a weak overall increasing trend through PRE1. By contrast,  $D'_{90'}$  responses are more consistent between pool, riffle and roughened channel structures. This suggests that  $D'_g$  is more responsive than  $D'_{90'}$  to the PRE1 conditions. Last, it is notable that across PRE1, the  $D_g$  measured along the channel is generally coarser than that of the supply, whereas the  $D_{90}$  is finer than the supply.

We now use the four characteristics response regimes to present results shown in Figures 4.3 to 4.4.

### 4.3.2 Topographic response: channel-wide and longitudinal profile development

Figure 4.3 illustrates channel bed topography for thirteen observation times during PRE1. Corresponding flow rate is indicated within each topographic map (DEM), and at the side of each DEM we provide the observation time as well as the response regime. We also show the subsampling locations in the DEM for  $t_e = 0$  minutes for reference. The top four DEMs show topographic development through the entirety of the  $t_a$ , the fifth through seventh DEMs show topographic development for different points within the initial  $t_t$ , and the bottom six DEMs illustrate topography for each SS condition:  $t=2150, 2390, 2630, 4310, 4550$  and  $4790$  minutes (Table 4.1).

Stations within segments of strong widening and narrowing (3600, 10000 and 8000 mm, respectively; Table 4.2) exhibit rapid topographic development during  $t_a$  (Figure 4.3), which in general has relatively high sediment mobility conditions (Table 4.1), demonstrated by the large rate of  $Q_{sf}$  increase to a peak value of  $0.064 \text{ kg}\cdot\text{m}^{-1}$  by the end of the  $t_a$  (Figure 4.2). At station 8000 mm, channel width has the strongest negative downstream width difference:  $\Delta w(x) = -0.25$  (Table 4.2), where we calculate fractional width change as the forward difference in a downstream moving reference frame:

$$\Delta w(x) = \frac{w(x+L) - w(x)}{\Delta L} \quad (4.1)$$

where  $w$  is the channel width at longitudinal station  $x$ , and  $\Delta L$  is the forward difference length scale between subsampling locations,  $\Delta L = 1000$  mm, or roughly  $2w'$  (Figure 4.3). The relatively large width reduction at 8000 mm correlates with a pool, and by the end of the  $t_a$  ( $t_e = 110$  minutes), this pool is well developed. The relatively large width increases at 10000 and 3600 mm correlates with riffles, and the initial style of topographic construction at these two stations differed during the  $t_a$  (Figure 4.3). At the downstream location, topography is built via progressive deposition of sediments over the entire riffle surface. At the upstream location, by contrast, topography is built by migrating fronts of bedload sediment. Each location corresponds to relatively large positive downstream width changes:  $\Delta w(x) = 0.19$  and  $0.17$ , respectively (Table 4.2). Channel segments for which  $\Delta w(x) = O(0)$  (Table 4.2) exhibit muted topographic responses during the  $t_a$ , relative to the narrow and wide zones.

Through the early part of the initial  $t_t$ , differences observed between stations 10000 and 3600 mm diminish, and topographic construction continues at stations 10000 and 3600 mm by incremental deposition of bedload. Subtle topographic development, relative to the narrow and wide zones, also continues during the  $t_t$  at channel segments for which  $\Delta w(x) = O(0)$ . However, periodic topographic waves are evident at  $t_e = 470$  minutes and 2150 minutes (end of the initial  $t_t$ ) from station 13000 to 11000 mm (Figure 4.3). These features occur with a

**Table 4.1:** Experimental details for PRE1

PRE1 Interval (-)	$t_o$ (-)	$t_e$ (minutes)	$Q_w$ (l·s <sup>-1</sup> )	$(Q_{ss})$ (kg·m <sup>-1</sup> )	$(Q_{sf})$ (kg·m <sup>-1</sup> )	$(\bar{\eta}')$ (-)	$\bar{D}_{g'}$ (-)	$\bar{D}_{90'}$ (-)	$\tau/\tau_{ref}$ (-)
0	0	0	-	-	-	0.90	0.675	0.820	-
1	0.2	19	42	0.50	0.009	0.88	0.849	0.983	1.49
2	0.5	50	42	0.50	0.027	0.88	1.014	1.013	1.47
3	1.0	110	42	0.50	0.064	0.89	0.977	1.009	1.48
4	2.1	230	42	0.50	0.048	0.90	1.007	1.008	1.44
5	4.3	470	42	0.50	0.027	0.94	1.024	0.996	1.53
6	6.5	710	42	0.50	0.050	0.97	1.047	0.925	1.59
7	8.6	950	42	0.50	0.030	0.97	1.074	0.974	1.54
8	10.8	1190	42	0.50	0.016	1.01	1.148	1.003	1.57
9	13.0	1430	42	0.50	0.099	1.06	1.299	1.012	1.54
10a	15.2	1670	42	0.50	0.058	1.10	1.209	0.985	1.63
10b	16.3	1790	42	0.50	0.660	-	-	-	-
11a	17.4	1910	42	0.50	0.437	1.07	1.149	0.994	1.56
11b	18.5	2030	42	0.50	0.226	-	-	-	-
12*	19.5	2150	42	0.50	0.393	1.09	1.202	1.059	1.56
13a	19.8	2180	60	0.80	4.284	-	-	-	-
13b	20	2195	60	0.80	7.113	-	-	-	-
13c	20.2	2225	60	0.80	3.670	1.01	0.991	1.052	1.75
14a	20.6	2270	60	0.80	2.296	-	-	-	-
14b*	21.7	2390	60	0.80	0.917	0.98	1.143	1.146	1.66
15a	21.9	2405	80	1.00	3.848	-	-	-	-
15b	22.1	2429	80	1.00	3.840	-	-	-	-
15c	22.3	2450	80	1.00	3.303	0.96	1.102	1.185	2.00
16a	22.5	2480	80	1.00	2.554	-	-	-	-
16b	23	2525	80	1.00	1.336	-	-	-	-
16c*	23.4	2570	80	1.00	0.927	0.94	1.294	1.198	1.78
17	23.9	2630	80	1.00	1.067	0.94	1.302	1.219	1.77
18	26.1	2870	42	0.50	0.033	0.96	1.330	1.190	1.26
19	28.3	3110	42	0.50	0.016	1.00	1.309	1.126	1.45
20	30.5	3350	42	0.50	0.013	1.04	1.306	1.101	1.52
21	32.6	3590	42	0.50	0.018	1.08	1.352	1.100	1.50
22	34.8	3830	42	0.50	0.022	1.12	1.330	1.063	1.64
23	37	4070	42	0.50	0.143	1.15	1.248	1.032	1.66
24*	39.2	4310	42	0.50	0.509	1.14	1.132	0.999	1.68
25a	39.4	4336	60	0.80	4.488	-	-	-	-
25b	39.6	4351	60	0.80	9.622	-	-	-	-
25c	39.7	4370	60	0.80	5.479	-	-	-	-
25d	39.9	4385	60	0.80	4.527	1.04	1.131	1.170	1.71
26a	40.3	4430	60	0.80	2.436	-	-	-	-
26b*	41.4	4550	60	0.80	0.595	1.03	1.225	1.171	1.62
27a	41.5	4565	80	1.00	2.231	-	-	-	-
27b	41.7	4589	80	1.00	6.212	-	-	-	-
27c	41.9	4610	80	1.00	5.062	0.96	1.082	1.210	1.75
28a	42.2	4640	80	1.00	2.069	-	-	-	-
28b	42.6	4685	80	1.00	1.132	-	-	-	-
28c	43	4730	80	1.00	0.892	0.97	1.374	1.195	1.91
29	43.5	4790	80	1.00	0.600	0.97	1.158	1.242	1.74

1. Asterisk denotes achievement of mass equilibrium between feed and flux.
2. The elapse time indicates the end time for the specified experimental interval.
3.  $t_o$  defined as ratio  $t_e/t_a$ , where  $t_e$  is the elapse time and  $t_a$  is the activation time.
4. Sediment flux is the mean flux for the observational interval.
5.  $\bar{\eta}'$  is the normalized mean bed elevation for the 11 subsampling locations.
6.  $\tau/\tau_{ref}$  is the mean for the 11 subsampling locations.
7.  $\tau_{ref}$  is the reference stress associated with  $\tau_{ref}^* = 0.030 = \tau/[(\rho_s - \rho_w)gD_i]$ .
7. The repeat phase of PRE1 began at elapse time 2630 minutes.

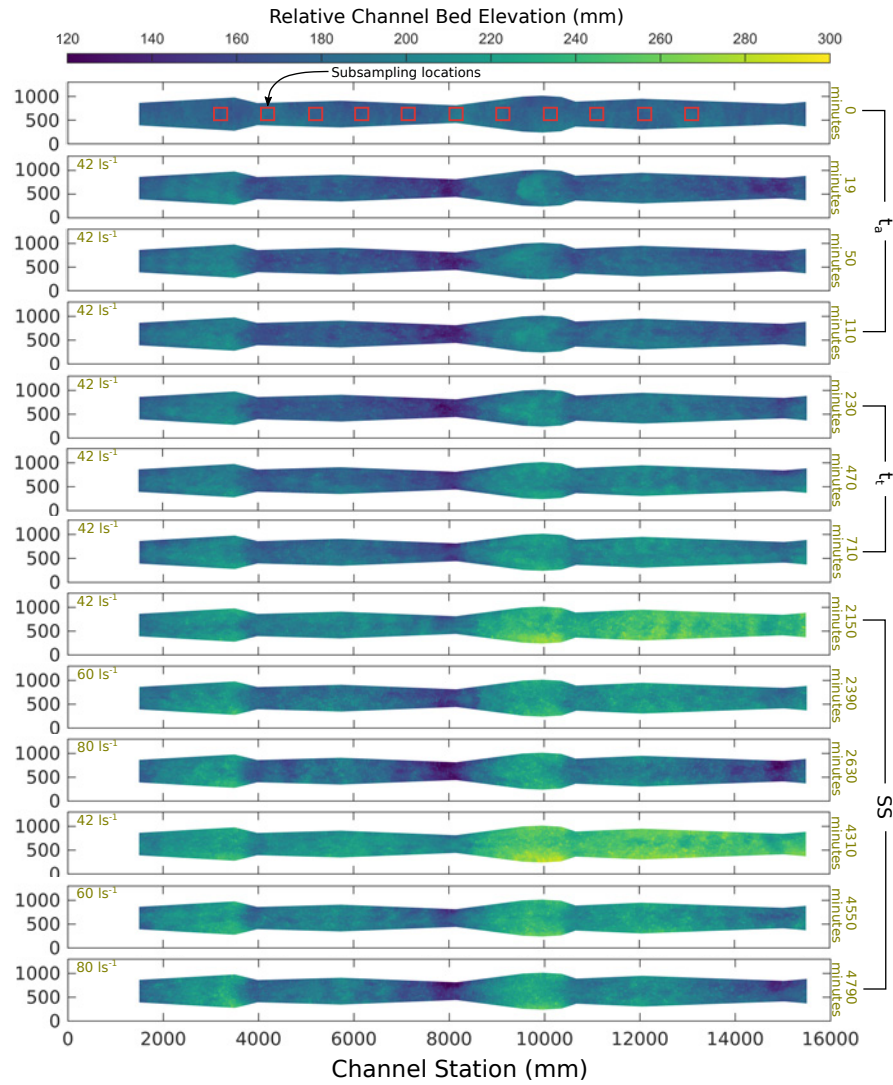


**Figure 4.3:** Summary panel of topographic responses observed during PRE1. Topographic responses provided for elapsed time 0, 19, 50, 110, 230, 470, 710, 2150, 2390, 2630, 4310, 4550 and 4790 minutes; steady-state topography at times 2150, 2390, 2630, 4310, 4550 and 4790 minutes (Table 4.1). At the side of each DEM we provide the elapse time, and within each DEM we indicate the flow rate for the preceding experimental interval. We show the subsampling locations for reference with the red boxes in the  $t_e = 0$  min. DEM. DEM coloring based on the perceptually uniform *Virdis* colormap.

spacing  $\approx w'$ , and are comparable to  $D_{90}$  high, where  $D_{90}$  is the 90th percentile grain size of the experimental distribution (Figure 3.2). By the end of the initial phase  $t_t$ , the overall spatial pattern of topography evident by  $t_e = 110$  minutes remains.

Steady-state topography has a few characteristic patterns, depending on flow and sediment supply rates (Figure 4.3). SS at  $t_e = 2150$  and 4310 minutes ( $42 \text{ l}\cdot\text{s}^{-1}$ ) has riffles centered

**Table 4.2:** Values of downstream width change between subsampling locations

Bounding Subsampling Locations									
3000:4000	4000:5000	5000:6000	6000:7000	7000:8000	8000:9000	9000:10000	10000:11000	11000:12000	12000:13000
0.187	-0.056	0.0051	0.089	0.059	-0.252	-0.107	0.178	-0.065	0.072

1. Downstream width change calculated with Equation 4.1 for length scale  $h = 1000$  mm

at stations 9800 and 3600 mm, a pool centered at 8000 mm, and roughened channel segments elsewhere. Upstream of the pool, topographic magnitude is high relative to downstream of the pool, and generally ranges from 200 to 300 mm. Downstream of the pool, topographic magnitude is relatively low, and generally ranges from 140 to 240 mm. At each subsequent SS, riffles and pools persist at the same stations, albeit at increasingly lower relative elevations, and an additional pool emerges at station 15000 mm. This pool is most evident in SS at  $t_e = 2630$  and 4790 minutes.

In order to better characterize the statistically steady conditions just described, we supplement the SS DEMs with corresponding longitudinal profiles shown in Figure 4.47. We also provide the initial condition profile and DEM for context, and the elapse time and associated flow rate is given to the right of each profile (Table 4.1). We determine SS profile residuals with the zero-crossing method (*Melton, 1962; Richards, 1976a*), which provides one way to qualitatively distinguish pools, riffles and roughened channel segments (cf. *Carling and Orr, 2000*). Furthermore, we project the residuals back onto the SS slopes, to show the scale of bed structures relative to the overall relief. We distinguish pools as negative residual departures from the detrended profile for length scales of  $\sim w'$ , and denote these with the letter  $P$ . We distinguish riffles as positive residual departures, again for  $\sim w'$ , and denote these with the letter  $R$ . Roughened channel segments have minor residual departures that fluctuate around the detrended profile, and we denote these with the letters  $Ro$ .

Figure 4.4 highlights that pools are collocated at points of narrowing, riffles at points of widening, and roughened channel segments where width changes are negligible. In general, the prevalence of pools at SS increases with increasing flow and sediment supply rates, indicated by the magnitude and downstream extent of the pool depth shown for SS at 42 vs. 60 and vs.  $80 \text{ l}\cdot\text{s}^{-1}$ , at stations 8000 and 15000 mm. The growth of a pool at station 4000 mm for increasing supply rates further demonstrates the dependence of pool prevalence on external supply conditions. The SS profiles reveal that topographic relief increases with flow and sediment supply rates, but that channel-average longitudinal bed slopes decrease (Table 4.3). PRE1 began from an initial slope of 0.015, steepened to 0.0191 at SS 2150 minutes, decreased to 0.0162 at SS 2390 minutes, and decreased yet more so to 0.0138 at SS 2630 minutes (Table 4.3). We observe a similar progression of steepening and relaxing for the repeat phase. Comparison of the profiles shown in Figure 4.4 with results of Figure 4.2 reveals that  $Q_{sf}$  remains at relatively low values for long durations during profile construction ( $t_t$ ), and rises significantly

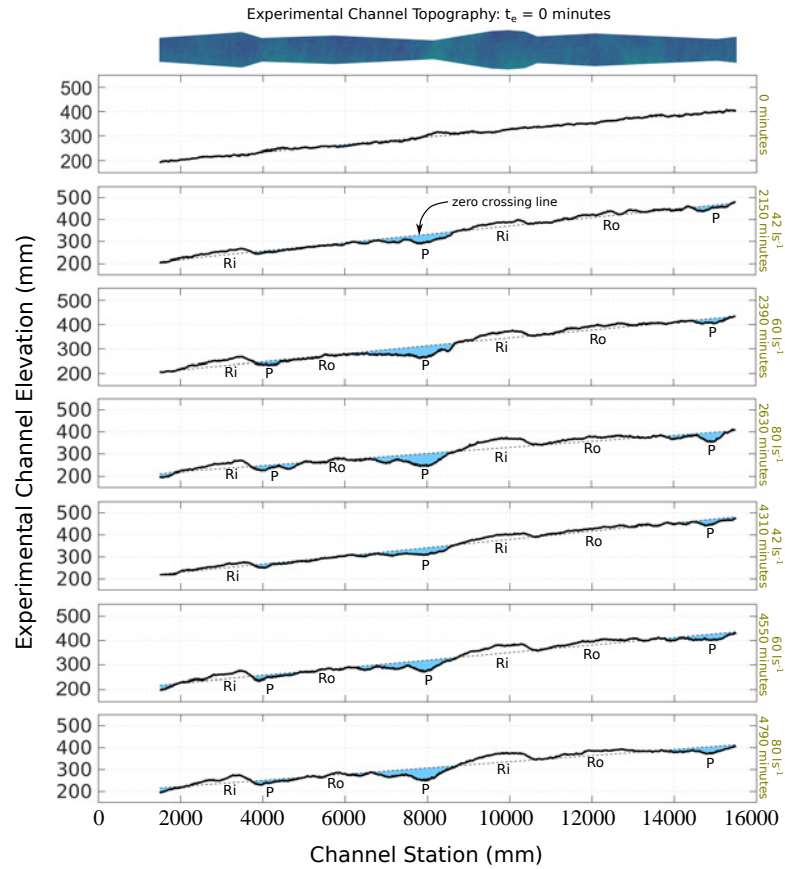


**Figure 4.4:** Identification of pool-riffle structures with the zero-crossing method. DEM of the channel at  $t_o = 0$  shown at top for reference. Zero-crossing profiles ((Richards, 1976a)) projected onto the experimental channel slope at  $t=0$ , 2150, 2390, 2630, 4310, 4550 and 4790 minutes elapsed time. These times reflect steady-state conditions for the PRE1 flow and sediment supply rates (see Table 4.1). Profiles are computed for the center 100 mm of each corresponding DEM. We indicate the general topographic response for each steady-state case with the abbreviations P (pool), Ri (riffle), and Ro (roughened channel).  $t_e$  and  $Q_w$  for the preceding experimental interval is given to the right of each profile. The zero-crossing line is represented by the light dashed line, specifically called out for  $t=2150$  minutes.

and then peaks during profile relaxation ( $t_r$ ). A peak  $Q_{sf}$  response occurs for each SS supply change, except following the third SS at  $t_e = 23.9$ , after which  $Q_{sf}$  drops continuously before leveling off, and the eventually rising, as the topographic profile is restored.

**Table 4.3:** Values of average channel bed slope for initial and steady-state conditions

$t_e = 0$ min.	2150 min.	2390 min.	2630 min.	4310 min.	4550 min.	4790 min.
0.015	0.0191	0.0162	0.0138	0.0186	0.0156	0.0141

1. Average channel slopes calculated with profiles shown in Figure 4.4.

To characterize how SS topographic conditions are organized by downstream changes in channel width, we augment the SS profiles shown in Figure 4.4 with box-and-whiskers plots of SS normalized local mean bed elevation ( $\eta/\bar{\eta}$ ) vs. normalized local width ( $w/w'$ ) provided in Figure 4.5. Local refers to the specific value of  $\eta$  or  $w$  at longitudinal station  $x$ , and  $\bar{\eta}$  is the associated channel average SS bed elevation. We use the results of Figure 4.5 to characterize the width-specific conditions which give rise to topographic expression at the SSs, and cast topographic development tendencies in terms of a balance between the entrainment and depositional responses, expressed through  $w_o = w/w'$ .

The entrainment response governs SS at  $w_o \lesssim 0.90$ . These relative widths are narrow, and associated with topographic responses  $\eta/\bar{\eta}$  which tend to values of 0.80 or less, indicating that the entrainment response is larger than the depositional one. These conditions lead to pools. On the other hand, the depositional response governs SS at  $w_o \gtrsim 1.10$ . These relative widths are large, and associated with topographic responses  $\eta/\bar{\eta}$  which tend to values of 1.20 or more, indicating that the depositional response is larger than the entrainment one. These conditions lead to riffles. Last, the tendency for entrainment and deposition to balance is captured qualitatively across all SSs for  $0.90 \gtrsim w_o \lesssim 1.10$ . These relative widths are similar to the mean width, and are associated with topographic responses  $\eta/\bar{\eta}$  which tend to range between 0.90 to 1.10. These conditions lead to roughened channel segments.

The magnitude of topographic diversity for any given value of  $w_o$  is relatively large for smaller values of the mobility conditions  $\tau/\tau_{ref}$ , where  $\tau$  is the shear stress and  $\tau_{ref}$  is a reference stress for threshold of motion conditions, and diminishes with increasing mobility (Table 4.1; Figure 4.5). This result is shown Figure 4.5 by the increasing range of values between the lower and upper quartiles, and the increasing magnitude of associated whisker lengths for decreasing mobility conditions, and especially for intermediate responses. On the other hand, topographic relief is relatively large for increasing values of  $\tau/\tau_{ref}$ , and diminishes with decreasing mobility (Table 4.1). This result is reflected by the range of  $\eta/\bar{\eta}$  values shown in the box plots (Figure 4.5), as well as the departure of the distribution of  $\eta/\bar{\eta}$  values from the 1:1 line, which diminishes for increasing values of  $\tau/\tau_{ref}$ .

We use topographic profiles to explore the response trends shown in Figure 4.5 in more detail, and in particular to emphasize the spatial character of the data through the normalized axes. Figure 4.6 illustrates profile traces for SS at  $t_e = 2150$  and 2630 minutes. The x- and y-axes of Figure 4.6 are the same as those for Figure 4.5, but in Figure 4.6 we show the mean relative elevation of each longitudinal position along the experimental channel, expressed according

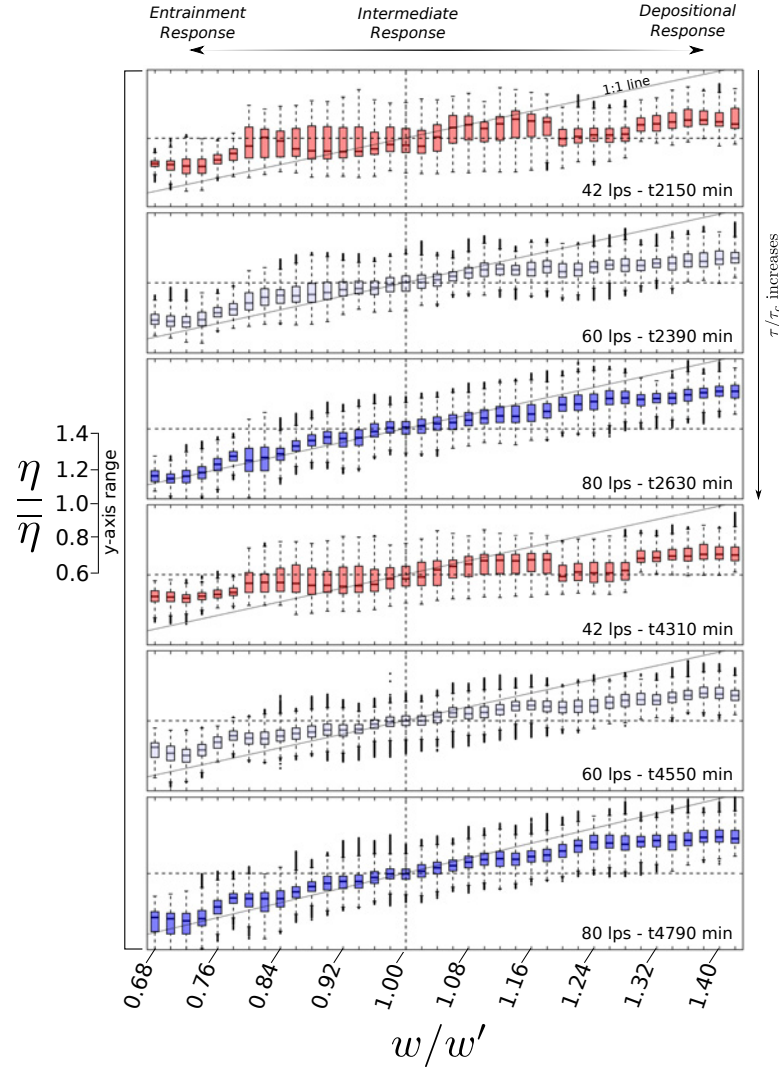


**Figure 4.5:** Summary panel of SS topographic responses observed during PRE1 illustrated with box-and-whiskers plots. The physical nature of responses is provided at the top of the panel, and mobility condition  $\tau/\tau_{ref}$  is provided to the right. The term  $w$  is the local channel width;  $w' = 547$  mm and is the mean channel width of the experimental channel,  $\eta$  is the local elevation provided by the DEM, and  $\bar{\eta}$  is the mean elevation of the experimental channel for each SS condition. The y-axis range is consistent for all six subplots.

to the specified range of colors.

The two SS profiles indicate that similar values of  $w_0$  can generate differing topographic responses. The magnitude of dissimilarity between the  $w_0$  associated responses depends on the mobility condition  $\tau/\tau_{ref}$ , with lower mobilities driving more accentuated differences (Table 4.1). The lines and station call outs shown along topographic trace segments correspond to specific pool, riffle and roughened channel structures within the experimental channel (Figure

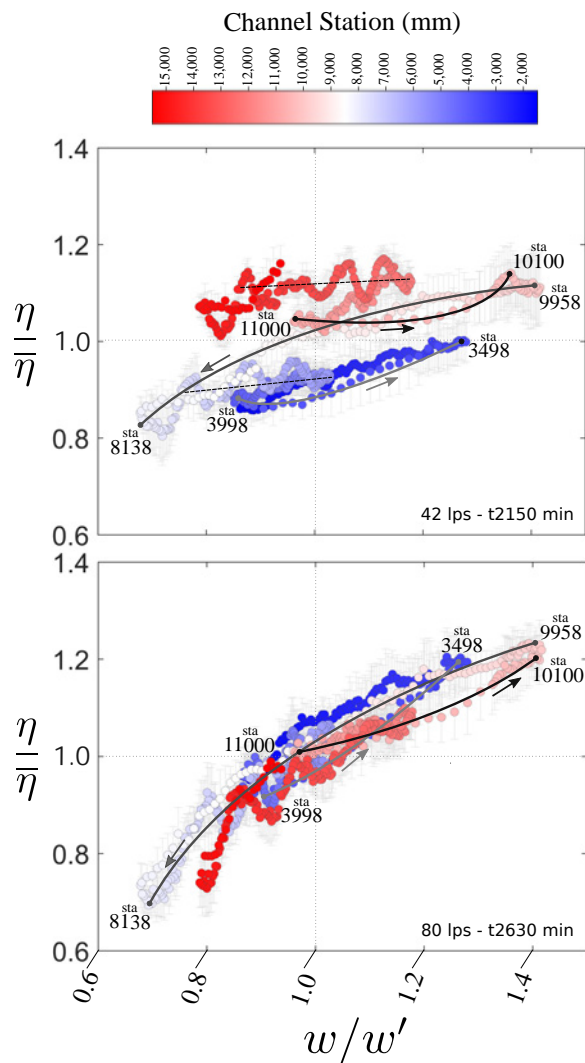


**Figure 4.6:** Profile traces of topographic response for steady-state conditions at  $t=2150$  and  $2630$  minutes. Same axes as used in Figure 4.5. Colorbar denotes location along experimental channel (see Figures 4.3 and 4.4). The individual elevation points along the profile trace reflect the data represented by each corresponding box from Figure 4.5. The arrows indicate the downstream direction along the profile traces. The perceptually uniform *Polarmap* colormap was used for location mapping.

4.4). Comparison of Figures 4.3 and 4.6 indicates that the traces exhibit a topographic hysteresis type response for both SS cases. Pool-riffle type structures can develop in a way that yields riffle-pool (station 9958 to 8138 mm: widening to narrowing), or pool-riffle (station 3998 to 3498 mm: narrowing to widening), in an upstream/downstream moving reference frame, regardless of  $\tau/\tau_{ref}$ . The profile traces also illustrate that on average, the local bed slope departs from the mean longitudinal slope for lower mobility conditions  $\tau/\tau_{ref}$ , and tends to the mean longitudinal slope as the mobility condition  $\tau/\tau_{ref}$  increases. Local here refers to bed slopes over length scales of  $1-5w'$ .

### 4.3.3 Effects of initial conditions on topographic responses

We use the same data for SS conditions shown in Figures 4.5 and 4.6 to examine the effects of initial conditions on longitudinal topographic response. Figure 4.7 shows normalized local mean bed elevation ( $\eta/\bar{\eta}$ ) vs. normalized channel station ( $x/w'$ ), where  $x$  is channel station. We provide the dimensional channel station at the top of the plot for reference, a DEM for context on how width changes, and the profiles were filtered using a moving average window length  $l = 100$  nodes, or 200 mm.

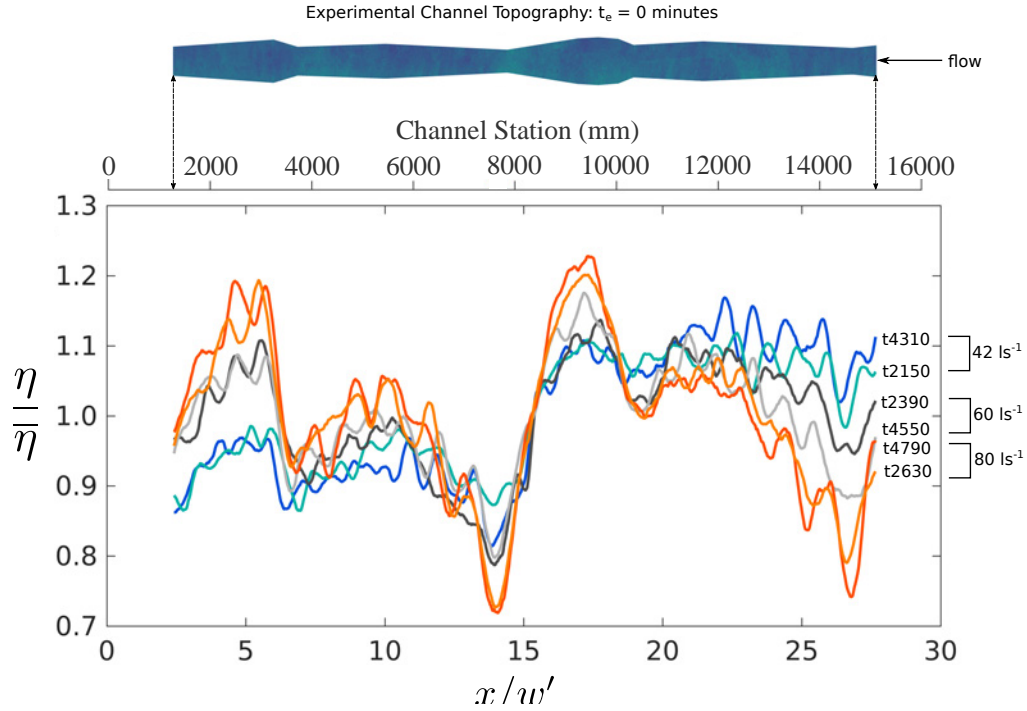


**Figure 4.7:** Steady-state normalized topographic profiles for PRE1.  $x$  is the channel station in mm, and  $x/\bar{w}$  is the normalized channel station. As with Figures 4.5 and 4.6, local mean elevation  $\eta$  has been normalized by the associated profile mean elevation  $\bar{\eta}$ . Average, filtered profiles computed for center 50 mm of the experimental channel at  $t = 2150, 2390, 2630, 4310, 4550$  and  $4790$  minutes, and were filtered with a moving average window length  $l = 100$  nodes, or 200 mm. Periodic bedload or sediment waves discussed in Section 4.3.2 are evident in several of the profiles, and in particular for  $t_e = 4310$  minutes, between stations 22–26.

The SS profiles are organized into three populations, and the nature of profile organization changes from upstream to downstream, and generally reflects topographic relief. For example, from  $x/\bar{w} = 16$ – $20$ , the  $80 \text{ l}\cdot\text{s}^{-1}$  conditions exhibit the largest  $\eta/\bar{\eta}$  values, and the  $42 \text{ l}\cdot\text{s}^{-1}$  conditions exhibit the smallest. In contrast, from  $x/\bar{w} = 13$ – $16$  this organization is flipped, and the  $42 \text{ l}\cdot\text{s}^{-1}$  conditions exhibit the largest  $\eta/\bar{\eta}$  values, and the  $80 \text{ l}\cdot\text{s}^{-1}$  conditions exhibit the smallest. Normalized profiles for the  $60 \text{ l}\cdot\text{s}^{-1}$  conditions are consistently in between those of the  $42$  and  $80 \text{ l}\cdot\text{s}^{-1}$  cases. Comparison of the profiles with the DEM suggests that the topo-

graphic responses are shifted slightly downstream from the widest and narrowest points, by a length scale of roughly  $5D_{90}$ .

The SS profiles are visually comparable in shape and pattern from stations 3–20, as suggested by consistent riffle occurrence from  $x/w' = 3$ –6 and 16–20, and pool occurrence from  $x/w' = 13$ –16. In contrast to pattern similarity, each SS profile reflects a qualitatively unique morphodynamic response to the external supply conditions, as paired profiles for the 42, 60 and  $80 \text{ l}\cdot\text{s}^{-1}$  cases are visually different, and profiles across all supply conditions are different. The primary visual difference is magnitude of response for any given station  $x/w'$ , characterized by the vertical offset between associated SS profiles.

#### 4.3.4 Summary of main results

PRE1 produced pool-riffle and roughened channel structures that were persistent across mobility conditions ( $\tau/\tau_{ref}$ ), which on average were greater than 2. Pools were colocated with points of width narrowing, where  $w_o \lesssim 0.90$ , riffles with points of widening, where  $w_o \gtrsim 1.10$ , and roughened channel beds were expressed along segments where width change was constrained to the range  $0.90 \gtrsim w_o \lesssim 1.10$ . The characteristic coarse grain size  $D_{90}$  was notably similar between morphologic structures, regardless of width condition. The topographic and sediment texture of pools, riffles and roughened channel beds develop rapidly during the start-up, or activation time  $t_a$ , and evolve more slowly thereafter during the transient period  $t_t$ , as a SS condition is approached. Topographic and sediment texture perturbations away from steady-state ( $t_r$ ) are of short duration, roughly  $2 - 2.5t_o$  under increased supplies of water and sediment. The effect of inherited bed states does not precondition the outcome, as initial and repeat SS bed morphologies exhibit consistent spatial patterns of topography and bed slope. However, all six SS bed profiles are unique, exhibiting different absolute topographic responses, and different  $D_{50}$  and  $D_{90}$  characteristic bed surface grain sizes. The combined results suggest that SS bed topography is coupled to downstream changes in channel width, but sediment texture for PRE1 does not show a clear spatial correlation with width, such as pools with finer sediment textures than riffles (cf. Lisle, 1979; Hodge *et al.*, 2013). In the next section we present and develop a physical explanation for our observations of bed topography-channel width coupling.

## 4.4 Physically linking channel width changes to topographic response

### 4.4.1 Downstream changes in flow speed and mobility

Pools, riffles and roughened channel structures are reliably produced by PRE1, and there is a spatial association between pools and riffles, and segments of channel narrowing and widening. But how does narrowing and widening mechanically lead to pools and riffles? We expect

from flow continuity that mean flow velocity, and hence particle mobility will increase for channel narrowing, and decrease for widening. We demonstrate this expectation in Figure 4.8, where we show the average DEM (i.e. topographic response) for all six SS conditions, along with the normalized mean downstream change in (a) flow speed ( $\widetilde{U}_x$ ) and (b) particle mobility ( $\hat{\tau}^*$ ). We determine downstream changes in flow speed and mobility with Equation 4.1, and normalize by the mean speed for all subsampling locations and observation times (Table 4.1), and by the reference mobility value  $\tau_{ref}^* = 0.030$ , respectively. We use Equation 3.10 to determine the mean flow speed, and the Manning-Strickler formulation of the Shields equation (Parker, 2007, 2008) to determine particle mobility ( $\tau^*$ ), expressed for the uniform flow condition as (Parker, 2007):

$$\hat{\tau}^* = \left[ \left( \frac{k_s^{0.33} q_w^2}{\alpha_r^2 g} \right)^{0.30} \left( \frac{S^{0.70}}{\rho' D_{90}} \right) \left( \tau_{ref}^* \right)^{-1} \right]_{x,t_0:t_n}, \quad (4.2)$$

where  $k_s = n_k D_{90}$  is a measure of local bed roughness in absence of bedforms,  $n_k = 2$  (Parker, 2008),  $q_w = Q_w / w_s$ , where  $w_s$  is the mean width for each subsampling location, the constant  $\alpha_r = 8.1$  (Parker, 1991), and  $S$  is the local channel bed surface slope, and local here is the distance between subsampling locations. Values of  $S < 0$  were set to  $S = 0.001$ .

Figure 4.8a shows that flow speed declines in segments of channel widening (warmer colors), increases along segments of narrowing (colder colors), and has negligible variation in straight segments where downstream width changes are small (neutral colors). The spatial pattern of flow speed change correlates with the spatial pattern of SS bed topography, suggesting a mechanistic link. We observe pools where flows accelerate, reflecting net particle entrainment, riffles where flows decelerate, reflecting net particle deposition, and roughened channel segments where flow speed change is negligible (Figure 4.8a; cf. Figure 4.4). However, flow speed change shown at station 4500 mm is declining, yet the bed topography has a relatively low elevation (cf. Figure 4.4).

Figure 4.8b shows that particle mobility declines in segments of channel widening (warmer colors), increases along segments of narrowing (colder colors), and has negligible variation in straight segments where downstream width change is minor (neutral colors). However, there is one notable departure from these general spatial correlations. Station 7500 mm shows relatively low topography, but a strong depositional prediction (bright red circle). The primary factor driving this discrepancy in Equation 4.2 is the relatively large decrease in bed slope  $S$ , moving from station 8500 mm to station 7500 mm. Figure 4.8a also shows that flow speed changes very little from station 8500 to 7500 mm. So, whereas the momentum flux decreases between stations 8500 and 7500 mm, the flow speed remains relatively high, thus favoring particle entrainment conditions, as captured by the DEM.

The relationship between spatial patterns of flow speed change and particle mobility, to SS bed topography is consistent with field measurements of riffles located at points of widening, where flow decelerates, and pools located at points narrowing, where flow accelerates, within

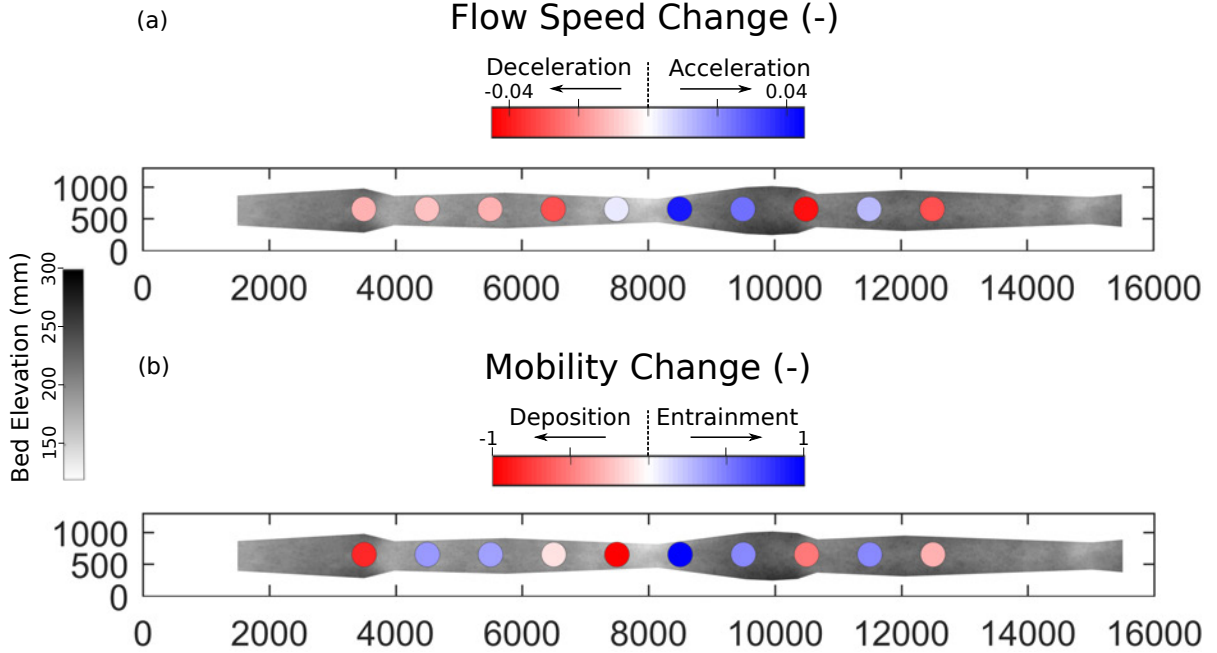


**Figure 4.8:** Average steady-state topography related to downstream changes in (a) normalized cross-sectionally averaged flow speed, and (b) normalized sediment mobility. Average topography determined from the six SS conditions (Table 4.1). Change in downstream flow speed and mobility determined with Equation 4.1 for all subsampling locations, averaged across observational times 1-29 (Table 4.1). Changes are plotted mid-way between subsampling locations. Flow speed normalized by the mean flow speed for all subsampling locations and PRE1 observation times, and mobility normalized by a  $\tau_{ref}^*$  value of 0.030. The perceptually uniform *Polarmap* colormap was used to show flow speed and particle mobility change

alluvial (MacVicar and Roy, 2007) and bedrock river reaches (Venditti et al., 2014). Furthermore, the coupling of downstream changes in channel width, flow speed change, particle mobility and bed topography shown in Figure 4.8, is consistent with theory and field measurements (Furbish, 1998; Furbish et al., 1998). As a result, Figure 4.8 motivates the hypothesis that local changes in the longitudinal bed slope correlates with downstream changes of channel width  $w$  and mean flow velocity  $\bar{U}_x$ .

#### 4.4.2 Downstream changes in channel width and bed slope

In Figure 4.9a we plot the mean channel bed slope  $\bar{S}_{local}$  versus the associated downstream change in width:  $\Delta w(x) \cdot \Delta L^{-1}$ . We determine local bed slope as the difference in mean bed elevation between subsampling locations using the same form of Equation 4.1, where we average the bed topography within each subsampling location. We determine mean bed slopes from the associated values for observations 1–29 (Table 3.1), and the bed slope error bars are the sample standard deviation across all observations. As with Figure 4.8a, we show the downstream change in  $\bar{U}_x$  with the circle colors: warm colors for decelerating flow, cold colors for

**Table 4.4:** Mean values of  $U_x/\bar{U}_x$  and  $\tau^*/\tau_{ref}^*$  for subsampling locations

Subsampling Locations										
3000	4000	5000	6000	7000	8000	9000	10000	11000	12000	13000
0.939	0.980	0.990	1.010	1.056	1.064	0.979	0.951	1.004	0.988	1.040
0.150	1.674	0.962	0.321	0.546	3.892	1.120	0.367	1.315	0.476	0.990

1.  $U_x$  calculated from continuity, and is the cross-sectional average velocity.
2.  $U_x$  averaged across all times.
3.  $\bar{U}_x$  is the mean for all subsampling locations for all times.
4.  $\tau^*$  calculated with Equation 4.2.
5.  $\tau_{ref}^*$  set to 0.030 (*Buffington and Montgomery, 1997*).
6. Mean values determined from 30 values for each subsampling location.

accelerating flow, and neutral colors for negligible flow speed change. Last, the circle size for PRE1 data reflects the average mobility condition  $\tau^*/\tau_{ref}^*$  for observations 1–29 (Table 4.4). In Figure 4.9b we supplement our experimental data with appropriate steady-state results reported by *de Almeida and Rodríguez (2012)* and *Nelson et al. (2015)*. *de Almeida and Rodríguez (2012)* provides numerical simulations of the Bear River, AK, U.S. (star symbol; data source is Figure 2 of *de Almeida and Rodríguez (2012)*), and *Nelson et al. (2015)* provides experiments guided by the physical characteristics of the middle reach of the Elwha River, WA, U.S. (diamond symbol; data source is Run 1, Figure 6 of (*Nelson et al., 2015*)). For *de Almeida and Nelson’s* data points, we use *P* to indicate pool and *R* for riffle.

Figure 4.9a indicates that as channel segments increasingly narrow, local bed slope steepens in the downstream direction (positive values of  $\bar{S}_{local}$ ), as channel segments increasingly widen, slopes steepen in the upstream direction (negative values of  $\bar{S}_{local}$ ), and for segments which exhibit little change in width, local bed slopes respond with negligible downstream or upstream topographic gradients (values close to zero). In a downstream moving reference frame, Figure 4.9 highlights that pools are favored for relatively large, negative changes in downstream width, for which the bulk flow is accelerating, and  $\tau^* \gg \tau_{ref}^*$ . Riffle type deposits are more likely for relatively large, positive changes in downstream width, for which the bulk flow is decelerating, and  $\tau^* \ll \tau_{ref}^*$ . Grain roughness dominated beds for negligible changes in width, positive or negative, for which the downstream bulk flow speed change is minor, and  $\tau^* \approx \tau_{ref}^*$  (Table 4.4; Figure 4.8).

Figure 4.9b illustrates that local bed slopes from PRE1, *de Almeida and Rodríguez (2012)* and *Nelson et al. (2015)* exhibit a systematic response across the full range of downstream width change, from (-0.30)–(+0.30). This result is particularly important because the overall reach-average bed slope of *de Almeida and Rodríguez (2011, 2012)*’s simulation (and field site) is 0.002, and the reach-average bed slope of *Nelson et al. (2015)*’s experimental channel Run 1 (and field

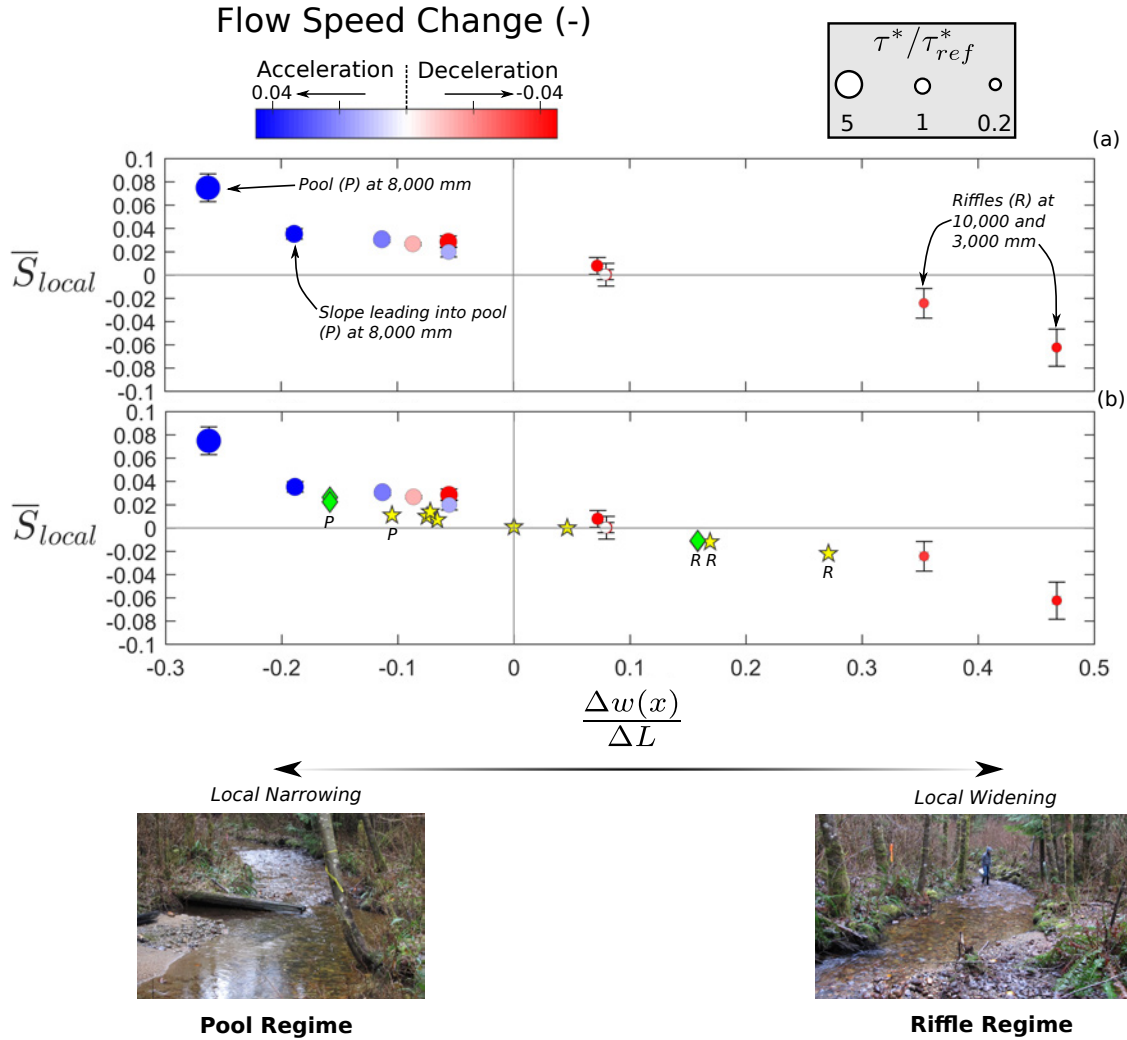


**Figure 4.9:** (a) Average channel bed slope as a function of the downstream change in channel width and flow speed. We determine bed slope as the forward difference using Equation 4.1 and then take the mean and sample standard deviation (error bars) for observations 1–29 (Table 3.1). Flow speed change is depicted by color, and the mean mobility condition  $\tau^*/\tau_{ref}^*$  is indicated by circle size (Table 4.4). (b) Same plot as (a), but we add corresponding data from *de Almeida and Rodríguez* (2012) (stars: Figure 2 therein), and *Nelson et al.* (2015) (diamonds: mean of data from Run 1 in Figure 6 therein). For deAlmeida and Nelson’s data, we use *P* to indicate pool, and *R* to indicate riffle.

site) is 0.007. These bed slopes stand in contrast to the range of our SS experimental channel bed slopes of 0.014 to 0.019 (Table 4.3), highlighting consistency between bed slope response and width change across almost one order of magnitude of overall reach-average bed slope. The ordered expression of  $\bar{S}_{local}$  across the width change domain of Figure 4.9 motivates the hypothesis that the local bed slope can be predicted with information about nearby changes in width and/or flow speed.

### 4.4.3 Theory for the local channel profile

Our results show a two-way coupling between the flow, the bed and general particle mobility, which is driven by downstream changes in channel width (Figures 4.8a and b). Changes in width lead to conditions whereby the flow loses speed at segments of channel widening, favoring particle deposition, gains speed at segments of narrowing, favoring particle entrainment, and remains relatively uniform where width change is minor, for which particle deposition and entrainment are roughly balanced. Therefore, the results of Figures 4.8a and 4.8b motivates development of a mathematical model which predicts the local channel profile, and which is dependent upon how flow speed changes, because particle mobility is dependent upon the fluid drag. We build from *Snow and Slingerland (1987)*; *Duró et al. (2016)*; *Bolla Pittaluga et al. (2014)* and *Ferrer-Boix et al. (2016)*, and begin our analysis with four assumptions: (1) statistical steady-state conditions, as defined in Chapter 3.2.2 by the requirements that the rates of bed elevation, and bed surface sediment texture change of the median grain size each approach zero; (2) characteristic grain sizes are spatially uniform,  $\partial D_i / \partial x = 0$ , (3) channel banks change position at rates much less than those of bed elevation and bed surface sediment texture; and (4) a channel reach of at least  $10\text{--}20w'$  in length has a well-defined average bed surface slope.

With these assumptions, channel profile construction is governed by bed sediment mass conservation. Accordingly, the Exner equation (*Exner, 1925*) in one-dimension is:

$$\frac{\partial \eta}{\partial t} = -\frac{1}{\varepsilon} \frac{\partial q_b}{\partial x}, \quad (4.3)$$

where  $\eta$  is the channel bed elevation,  $t$  is time, the solid fraction in the bed is  $\varepsilon = (1 - \phi)$ , where  $\phi = 0.4$  is the volume-averaged streambed porosity of the active layer  $L_a = kD_c$  (*Hirano, 1971*), where  $k$  is constant between 1 and 2 (*Parker, 2008*), and  $D_c$  is a characteristic grain size, generally taken as  $D_{90}$ ,  $q_b$  is the total bedload transport rate per unit channel width, and  $x$  is spatial location in the streamwise orientation. We write Equation 4.3 in expanded form with the dimensionless Einstein bedload number (*Einstein, 1950*), expressed for the sum of all bedload fractions following *Parker (2007)*:

$$q_b^* = \frac{q_b}{(Rg)^{0.5} D_c^{1.5}}, \quad (4.4)$$

where  $q_b^*$  is the dimensionless unit bedload transport rate,  $R$  is the relative density of sediment:  $[(\rho_s / \rho_w) - 1]$ , for which  $\rho_s = 2.65 \text{ g}\cdot\text{cm}^{-3}$  is the density of sediment,  $\rho_w = 1.0 \text{ g}\cdot\text{cm}^{-3}$  is the density of water, and  $D_c$  is a characteristic grain size. Combining Equations 4.3 and 4.4, and nondimensionalizing with  $x \approx L_c$ ,  $T = \Delta\eta / (\partial\eta / \partial t)$  and  $X = \Delta\eta / (\partial\eta / \partial x)$ , where the scale  $L_c$  is defined below, we obtain a dimensionless form of the Exner equation, written in terms of the topographic gradient:

$$\frac{\partial \eta}{\partial x} \approx -\Lambda \frac{\partial q_b^*}{\partial x^*}, \quad (4.5)$$

where  $g' = Rg$  and

$$\Lambda = \frac{(g')^{0.5} D_c^{1.5}}{\varepsilon U_c L_c}. \quad (4.6)$$

$\Lambda$  characterizes development of the local channel profile in terms of a competition between two time scales: (1) the time scale for topographic spreading, or relaxation over the length  $L_c$ , and (2) the time scale for eddy overturning (Yalin, 1971; Carling and Orr, 2000), or bed forcing, which scales the dynamic pressure force imparted at  $D_c$ , expressed as:

$$\Lambda \equiv \frac{t_{\text{spreading}}}{t_{\text{forcing}}} = \underbrace{\left( \frac{(g' D_c)^{0.5}}{\varepsilon L_c} \right)}_{\text{spreading}} \underbrace{\left( \frac{D_c}{U_c} \right)}_{\text{forcing}}. \quad (4.7)$$

The spreading time scale changes considerably depending on channel bed packing  $\varepsilon$ , and for loosely packed beds this time scale is relatively small, and for tightly packed beds, the time scale is relatively large. This suggests that as the solid fraction of the bed becomes increasingly small, the bed material is more responsive to the flow. As a result, the spreading time scale is a measure of bed resistance. More generally though, the spreading time scale is conceptually understood as similar to how honey spreads when poured onto a flat surface, for which spreading is driven by gravity acting on the height of the initial honey pile, and resisted by honey's viscosity. In the present case, Equation 4.7 indicates that the driving gravitational force is resisted by the degree of bed packing  $\varepsilon$ , and that the magnitude of the spreading time scale is a function of how  $D_c$  scales relative to  $L_c$ . On this last point it is useful to recognize that increases or decreases in bed topography magnitude scale as the characteristic grain sizes  $D_c$  that are locally participating in the adjustment response.

The characteristic velocity  $U_c$  could be taken to be the rate at which a disturbance or response propagates downstream along a stream bed (e.g. Stecca *et al.*, 2014; Juez *et al.*, 2016, and citations therein), or the speed with which the bed changes vertical position. Here we assume  $U_c$  is governed by the mechanical coupling of the flow to the bed, and thus specify that  $U_c \approx u_*$  ( $u_*$  is the shear velocity), and use the Manning-Strickler resistance formulation of the shear velocity:

$$u_* = \sqrt{\left( \frac{k_s^{0.33} q_w^2}{\alpha_r^2} \right)^{0.30} (gS)^{0.70}} \quad (4.8)$$

Shear velocity is a reasonable choice for  $U_c$  because it captures the rate at which shear and momentum flux are delivered to the top of the bed, which, in turn governs the transport magnitude. Equation 4.8 is particularly appropriate because it reflects how flow intensity ( $q_w$ ) changes in the downstream direction, which scales the flow speed change, and hence the mobility condition. We take the characteristic length scale  $L_c$  to be the channel width, because width inversely scales the cross-sectionally average flow velocity. Figures 4.8 and 4.9 show that this sets up a spatial variation in flow speed and particle mobility, which correlates with

spatial patterns of bed topography. With  $U_c$  and  $L_c$  defined, Equation 4.5 becomes:

$$\frac{\partial \eta}{\partial x} \approx -\Lambda \frac{\partial q_b^*}{\partial x^*} \approx -\frac{(g')^{0.5} D_c^{1.5}}{\epsilon u_* w} \frac{\partial q_b^*}{\partial x^*}, \quad (4.9)$$

which has two unknowns,  $D_c$  and  $q_b^*$ . We specify  $D_c$  as the sediment supply  $D_{90}$  grain size, which means  $D$  is treated as spatially uniform and therefore constant. This choice underscores the earlier noted assumption of morphodynamic equilibrium, and recognition that the  $D_{90}$  has a strong influence on rates of particle mobilization and transport (Schneider *et al.*, 2016; MacKenzie and Eaton, 2017; Masteller and Finnegan, 2017).

The dimensionless bedload transport  $q_b^*$  requires discussion. This parameter can be determined, for example, with the Wong and Parker (2006) corrected form of the Meyer-Peter and Müller bedload transport relation (Meyer-Peter and Muller, 1948):  $q_b^* = 3.97(\tau^* - \tau_{ref}^*)^{1.5}$ , which states that transport intensity is a non-linear function of the excess Shields stress (Shields, 1936). However, Figure 4.8b illustrates that anomalous Shields stress conditions relative to bed topography exist for locations 7000, 5000 and 4000 mm for PRE1. We therefore propose a scaling of  $q_b^*$  based on Figure 4.8a:

$$q_b^* \approx \bar{U}_x^* \approx -\frac{\bar{U}_x}{(g'\bar{d})^{0.5}}, \quad (4.10)$$

where Equation 4.10 is a form of Froude number, the square of which expresses a balance between the kinetic energy available in the velocity field, and the potential energy stored in the bed topography, which is a measure of the relative bed strength. Here  $g' = g[(\rho_s/\rho_w) - 1]$ , and  $\bar{d}$  is cross-sectionally averaged water depth. Use of  $g'$  in the nondimensionalization requires that the bed be viewed as a granular gravity current, rather than a solid boundary. We assume that changes in the relative strength occur over distances which scale as  $\bar{d}$ , which complements the assertion of a flow timescale that scales as  $t \approx L_c/U_c$ .

Our choice of  $\bar{U}_x$  nondimensionalization is motivated by the way in which the bed responds to water flow down a channel characterized by downstream changes in width (Figures 4.8 and 4.9). The bed responds by either building topography and storing potential energy (PE), or destroying topography to a magnitude commensurate with the kinetic energy (KE) extracted from the velocity field to do the work of mobilizing the bed.

Normalization of  $\bar{U}_x$  by  $(g'\bar{d})^{0.5}$  yields  $\bar{U}_x^*$  values that are 0(1), ranging from 0.70–1.06. Multiplying  $\bar{U}_x^*$  by -1 is necessary because the relative magnitude of  $\bar{U}_x^*$  is reversed to that of  $\bar{U}_x$ , because of the effect of water depth. Introducing -1, however, preserves the spatial character of  $\bar{U}_x$  as observed during PRE1 (Figure 4.8). Furthermore, scaling of  $q_b^*$  in terms of  $\bar{U}_x$  is supported by Figure 4.10, which illustrates that downstream changes in the cross-sectionally averaged velocity are inversely correlated with variations in width, which relates to the relative mobility condition. There is scatter amongst the data, but the trend is clear and expected (Thompson *et al.*, 1998; MacVicar and Roy, 2007; Thompson and McCarrick, 2010; de Almeida and Rodríguez, 2012; MacVicar and Rennie, 2012).

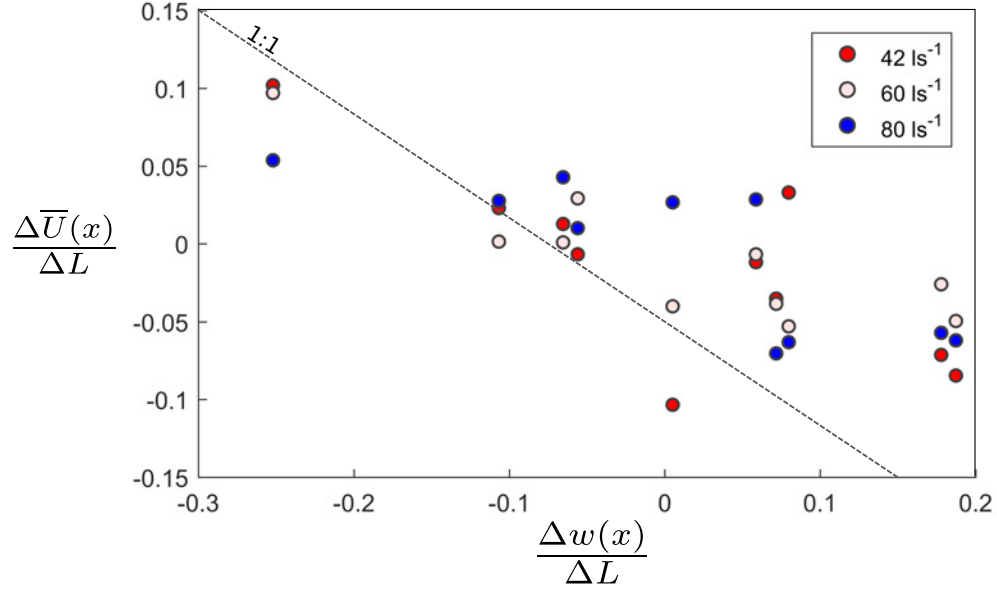


**Figure 4.10:** Downstream changes in local mean flow speed for associated changes in channel width. Changes computed as forward differences with Equation 4.1. PRE1 observations indicate that mean downstream changes in flow speed for 42, 60 and 80  $\text{l}\cdot\text{s}^{-1}$  were inversely correlated with downstream changes in width.

With our proposed scaling of  $q_b^*$ , Equation 4.9 is written in the final form used herein:

$$\frac{\partial \eta}{\partial x} \approx \Lambda \frac{\partial \bar{U}_x^*}{\partial x^*} \approx \frac{(g')^{0.5} D_{90}^{1.5}}{\varepsilon u_* w} \frac{\partial \bar{U}_x^*}{\partial x^*} \equiv \bar{S}_{local} \quad (4.11)$$

To calculate  $S_{local}$  from experimental data, and over the range of local width changes, we assume steady flow and steady-state topographic profile conditions (Figures 4.3 and 4.4), for which bed sediments have sorted to an approximately consistent spatial grain size distribution, defined by the sediment supply. Figure 4.10 permits us to constrain the calculation of  $S_{local}$  based on the range of observed  $\bar{U}_x$  for the steady-state conditions, and associate the resulting values of  $S_{local}$  with the range of experimental changes in local channel width. Furthermore,  $w$  and computed values of  $u_*$  used in Equation 4.11 are averaged between the subsampling locations (Figure 4.2), and  $S$  in the shear velocity calculation was specified as the initial mean flume slope of 0.015. Use of the initial mean flume slope is appropriate because we are interested in how spatial variations in particle mobility, set by the initial slope, unit discharge, local mean fluid velocity and bed roughness, gives rise to a local slope response.

## 4.5 Discussion

The combined results of Sections 4.3 and 4.4 raise several questions which require further discussion. First, Figure 4.8 illustrates that local topographic gradients from PRE1, *de Almeida and Rodríguez* (2012) and *Nelson et al.* (2015) are systematically expressed across the range of

downstream width change  $-0.3 : +0.3$ . For PRE1 results, we further observe that flow speed and particle mobility changes inversely with variations of channel width. Therefore, we revisit a more focused Question 1 presented within the Introduction: How specifically does channel width matter for pool-riffle development? Second, Figure 4.4 illustrates that longitudinal topographic gradients are similar across a range of water and sediment supply conditions that vary by a factor 2, with the lowest experimental flows simulating the bankfull flow. In particular, what does persistence of pool, riffle and roughened channel bed structures at the largest flow and sediment supply rates suggest for pool-riffle maintenance with respect to these conditions? Third, results presented in Figures 4.3 and 4.4 indicate that pool-riffles are created by at least two different processes along variable width channels. What are these processes and why is it important to identify them? Last, the six SS topographic profiles of Figures 4.4 and 4.7 exhibit overall consistent patterns, indicating that pools, riffles and roughened bed structures are spatially anchored by changes in width. However, Figure 4.7 reveals that each SS profile is unique. We address Question 2 presented in the Introduction, and ask how this finding is important for that sediment transport theory which is built from a probabilistic perspective, versus a deterministic one?.

#### 4.5.1 Predicting local channel slope along variable-width channels

We developed Figures 4.8 and 4.9 to help explain how and why channel width matters for pool-riffle development. Results from these figures motivated development of our mathematical model for the local topographic gradient  $S_{local}$  (Equation 4.11), which we plot in Figure 4.11 with our experimental observations of  $S_{local}$ , plus those of *de Almeida and Rodríguez* (2012) and *Nelson et al.* (2015). As before, we plot these quantities vs. the downstream change in channel width, which to simplify discussion we define as  $\Gamma$ . We indicate flow speed change as before, based on the specified colors, and the size of circles for the PRE1 results indicates the mobility condition magnitude  $\tau^* / \tau_{ref}^*$  (Table 4.4).

On the secondary axis we show the downstream change in the average local width to depth ratio:  $\Delta\bar{\alpha}(x)$  (square symbols). The dashed light gray line is a linear best fit to  $\Delta\bar{\alpha}(x)$ , as we know of no theory which describes how the width to depth ratio changes along variable width channel segments. The linear best fit has a coefficient value of 22. We determine  $\Delta\bar{\alpha}(x)$  as the difference between subsampling locations, and we take averages of  $\Delta\bar{\alpha}(x)$  from the associated values for observations 1–29 (Table 3.1). The error bars are the sample standard deviation across all observations.

We frame the results shown in Figure 4.11 by identifying regimes in terms of  $\Gamma$ – $S_{local}$ – $\Delta\bar{\alpha}$  parameter space, building from our previous explanations. Figure 4.11 suggests that relatively straight channel segments of variable downstream width exhibit three regime spaces for  $\Gamma$  and  $S_{local}$ , which based on the combined results of PRE1, *de Almeida and Rodríguez* (2012) and *Nelson*

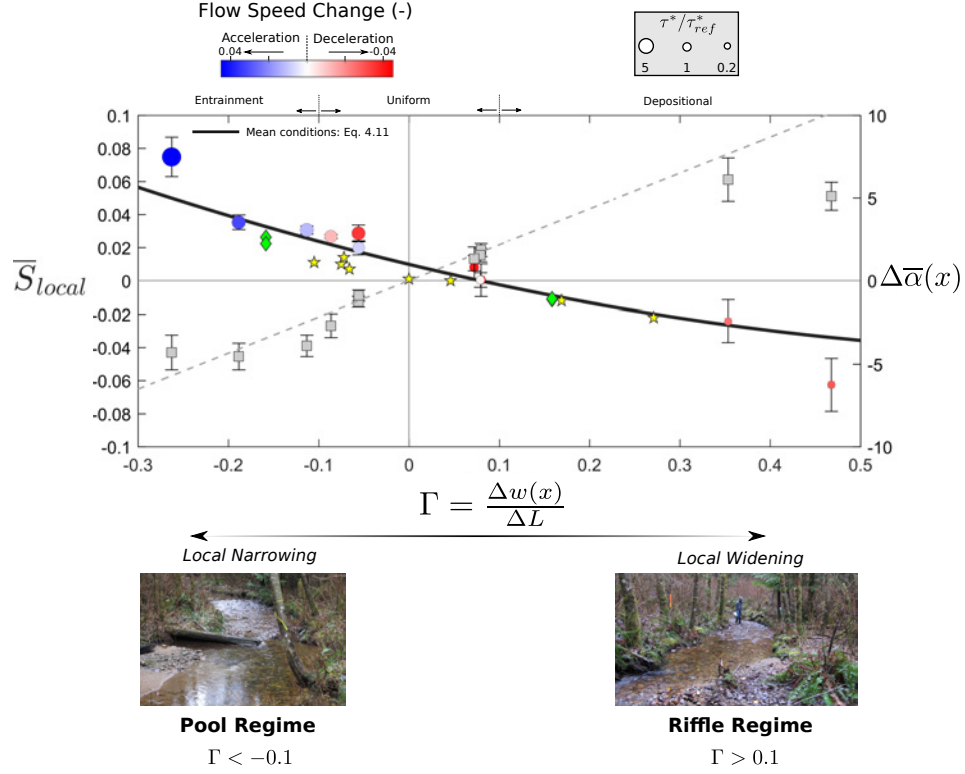


**Figure 4.11:** Prediction of local SS channel slope across the range of channel width conditions using Equation 4.11, plotted with  $\bar{S}_{local}$  for PRE1, *de Almeida and Rodríguez* (2012), and *Nelson et al.* (2015) (circles, stars and diamonds as in Figure 4.9, respectively). The predicted  $\bar{S}_{local}$  curve reflects the mean of PRE1 water supply conditions, and is shown with the dark, solid curve. On the secondary axis we show the average downstream change in the width to depth ratio  $\bar{a}$ . The average of  $\Delta\bar{a}(x)$  is taken for the associated values of observations 1–29, and error bars are the standard deviation over the observation range. The light gray dashed line is a linear best fit to  $\Delta\bar{a}(x)$  with a coefficient value of 22.

*et al.* (2015), we define as:

$$\text{Slope Regimes} = \begin{cases} \text{Entrainment Regime:} & \Gamma < -0.1 \text{ and } S_{local} > 0.2 \\ \text{Uniform Regime:} & -0.1 < \Gamma < 0.1 \\ & 0.02 > S_{local} > -0.1 \\ \text{Depositional Regime:} & \Gamma > 0.1 \text{ and } S_{local} < -0.1 \end{cases}$$

Pool development defines the entrainment regime along relatively straight channel reaches, driven by downstream flow speed changes  $\Delta\bar{U}_x \cdot \Delta L^{-1}$  that are increasing, and mobility conditions  $\tau^*/\tau_{ref}^*$  which are well above threshold conditions. The uniform regime defines roughened channel development, driven by downstream flow speed changes that are relatively minor, and mobility conditions that are near the threshold condition. Riffle construction defines

the depositional regime, driven by downstream flow speed changes that are decreasing, and mobility conditions that are well below the threshold condition (cf. Table 4.4).

The datasets of Figure 4.11 indicate that the spaces defined by  $(\Gamma < 0, S_{local} < 0)$ , as well as  $(\Gamma > 0, S_{local} > 0)$  may not be physically possible at the local scale, for relatively straight channel segments of gravel composition. However, at the basin scale, the  $(+\Gamma, +S_{local})$  regime gives rise to the upward-concave river profile of graded channel conditions, whereby the channel slope evolves to transport the prevailing basin sediment supply, given the associated water supply conditions (Sternberg, 1875; Gilbert, 1877; Leopold and Maddock, 1953; Langbein and Leopold, 1964). Last, the  $(-\Gamma, -S_{local})$  regime is driven by geologic controls that are relatively decoupled from the flow-bed coupling conditions described here, with one example being a bedrock-controlled channel segment due to normal faulting, which exhibits narrowing (Ouchi, 1985; Schumm et al., 2002).

Associated with the  $\Gamma-S_{local}$  regimes,  $\Gamma$  and  $\Delta\alpha$  exhibit two regimes, we define as:

$$\text{Width/Depth Regimes} = \begin{cases} \text{Depth Regime:} & \Gamma < -0.1 \text{ and } \alpha < -2 \\ \text{Uniform Regime:} & -0.1 < \Gamma < 0.1 \\ & 2 > \alpha > -2 \\ \text{Width Regime:} & \Gamma > 0.1 \text{ and } \alpha > 2 \end{cases}$$

The depth regime is characterized by water depths that are increasing relative to channel width. As a result, flows are comparatively deep and increasing in speed, delivering more momentum flux to the bed, and it is for such conditions that pools develop. The uniform regime is characterized by comparable changes in width and depth. As a result, flows are approximately uniform, and it is for such conditions that roughened channel segments develop. The width regime is characterized by channel widths that are increasing relative to water depth. As a result, flow are comparatively shallow and decreasing in speed, and it is for such conditions that riffles develop.

Equation 4.11 indicates that local slope construction depends on the magnitude of  $\Lambda$ , and the sign and magnitude of  $\partial\bar{U}_x^*/\partial x^*$ . The influence of  $\Lambda$  is governed by how the magnitude of  $t_{spreading}$  compares to  $t_{forcing}$ , noting that local channel width drives the magnitude of  $t_{spreading}$ , and local shear velocity drives  $t_{forcing}$ . In Figure 4.12 we show  $\Lambda$  vs.  $\Gamma$ . We observe that  $\Lambda$  varies inversely with  $\Gamma$ , and decreases monotonically from 0.30 to 0.25 as  $\Gamma$  increases from 0 to 0.20. As a result,  $\Lambda$  has a particularly strong affect on  $S_{local}$  under narrowing width conditions, compared to cases for which width is widening (cf. Figures 4.11 and 4.12).

Additionally, Figure 4.11 shows that for the narrowest and widest width conditions,  $S_{local}$  is roughly twice as steep leading into pools, as it is for riffles. Figure 4.12 explains that the steeper pool entrance slopes are due to how  $\Lambda$  varies against  $\Gamma$ , with values in the pool regime that are roughly twice as large as values in the riffle regime. From our definition of  $\Lambda$  in Equation 4.7, we therefore understand that pools develop when  $t_{spreading}$  is characteristically

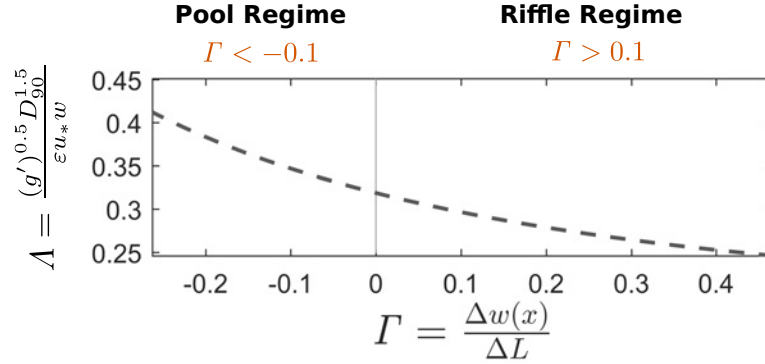


**Figure 4.12:** Summary of  $\Lambda$  of Equation 4.11 vs.  $\Gamma$  for PRE1.  $\Lambda$  varies inversely with  $\Gamma$ , and ranges by roughly a factor 2 across the PRE1 width conditions.

large relative to  $t_{forcing}$ , indicating that pool development is governed by momentum flux delivery to the bed, which drives particle entrainment. On the other hand, we understand that riffles develop when  $t_{spreading}$  is characteristically small relative to  $t_{forcing}$ , indicating that riffle development is governed by topographic spreading and growth as a result of reduced momentum flux delivery to the bed.

But why, specifically, are pool entrance slopes roughly twice as steep as those of riffles, for  $(-0.30 < \Gamma < -0.10)$  and  $(0.10 < \Gamma < 0.30)$ , respectively? From our choice of physical scales, Equation 4.11 shows that the value of  $\Lambda$  depends on the local shear velocity  $u^*$  and width  $w$ , owing to our choice of  $D_c = D_{90_{us}}$ , where  $D_{90_{us}}$  is a constant and is the 90th percentile size class of the upstream supply. For increasing values of  $\Gamma$ , the shear velocity decreases, and as  $\Gamma \rightarrow 0.30$ , the product  $(u^*w)$  tends to a constant value, and  $\partial \bar{U}_x^* / \partial x^*$  approaches a negative limiting value. It follows then that the magnitude of these values, expressed through Equation 4.11, yield riffle entrance slopes between  $(-0.02)$ – $(-0.03)$ , or about half that of pools, and for the associated ranges of  $\Gamma$  noted at the beginning of the paragraph.

As a closing remark, the dynamics of slope construction just discussed suggest that the conversion and storage of kinetic as potential energy at locations of sediment deposition and channel widening, has an upper limiting condition near  $\Gamma = 0.30$  (Figure 4.11) and for channel reaches that exhibit SS bed profiles. This makes sense because SS profiles ultimately provide the conditions necessary to transport the upstream supply of sediment through segments of positive and adverse bed slopes, where adverse slopes are the limiting transport cases. By contrast though, Figure 4.11 suggests that a limiting condition for pools occurs for some value of  $\Gamma < -0.30$ , indicating that the release and conversion of potential to kinetic energy from wide to narrow segments is not as readily limited, as the reverse case. Which taken together, implies that river flows dig holes that are comparatively deeper than deposits are tall. Last, it is important to recognize that the mobility conditions for pool vs. riffle of are similar magnitude

relative to the threshold condition, 5 vs. 0.2 (Figures 4.11 and 4.12), yet yield the disparate  $S_{local}$  responses just discussed.

Figure 4.11 illustrates that  $\Delta\bar{\alpha}(x)$  varies linearly over the range of PRE1 width conditions, such that:

$$\Delta\alpha(x) \propto \frac{\Delta w(x)}{\Delta L} \quad (4.12)$$

Because of a coupling between the flow and the bed,  $\Delta\bar{\alpha}(x)$  is a summary of the morphodynamic processes that led to net adjustment of bed topography across the range of imposed width changes. Net adjustment of bed topography to external conditions is known to converge toward states for which the local divergence of bedload flux goes to zero (Equation 4.3; (Bolla Pittaluga *et al.*, 2014)). It follows then that  $\Delta\bar{\alpha}(x)$  reflects the tendency to balance local fluid momentum and resulting solid fluxes. The balancing occurs over a characteristic length scale reflected in the  $\Delta\alpha(x) \propto -\Delta w(x)$  proportionality, Equation 4.12, which, noting that  $\Delta\alpha = \Delta w / \Delta\bar{d}$ , we find the length scale is of order:

$$\Delta x \approx \chi \Delta\bar{d}, \quad (4.13)$$

where  $\bar{d}$  is the local cross-sectionally averaged flow depth, and  $\chi$  is a constant, which for PRE1 has a value of 22. For the pool at station 8000 mm,  $\Delta\bar{d}$  has an average value of 4.0 cm across observations 1–29, whereas for the riffles at stations 4000 and 10000 mm, the average values are -2.5 and -1.6 cm, respectively. This suggests that channel width narrowing drives a mean flow response which manifests over length scales that are roughly twice as long compared to that for riffles, from  $\sim 2w'$  for pools vs.  $\sim w'$  for riffles. These mean flow relaxation length scales are reflected in both  $t_{spreading}$  and  $t_{forcing}$ , because as the relaxation length gets bigger, as in the case of pools, we expect  $t_{spreading}$  to get bigger, and we expect  $t_{forcing}$  to get smaller, and vice versa for riffles, as shown in Figure 4.12. Therefore, Equation 4.13 provides the basic information needed to understand how water depth responds to downstream changes in channel width, for a range of upstream water and sediment supply conditions.

#### 4.5.2 Maintenance of bed topography along variable-width channels: support for an emerging view

We suggest that the combined results of Figures 4.3 through 4.11 provide evidence that the combination of PRE1 flows are important for topographic expression, and by extension morphodynamics in natural streams. Experimental support for our proposal consists of two parts. First, pool-riffle and roughened channel persistence across all experimental water and sediment supply conditions suggests that morphologic response is reinforced across the range of supply conditions. Second, increasing topographic relief for lower overall longitudinal gradients, and vice versa suggests that different supply magnitudes maintain channel form in different, but equally important ways (Figures 4.4 and Table 4.3).

Our perspective is consistent with *Pickup and Rieger (1979)*; *Parker et al. (2003)*; *Bolla Pit-*

*taluga et al.* (2014) and *Brown and Pasternack* (2017)'s interpretation that the full distribution of flows under the present day hydrology is important for channel morphology, as raised by (*Ferrer-Boix et al.*, 2016). More importantly, however, recognizing the importance of the full hydrologic regime in channel form maintenance builds immediate bridges with ecology, and in particular with the field of environmental flows, and the natural flow paradigm (NFP) concept (e.g. *Poff et al.*, 1997; *Acreman et al.*, 2014b). The NFP reflects the view that the entire flow regime consisting of droughts, floods of all size, annual low flows, etc. are critical to the support of riverine processes and ecological communities. NFP may seem at odds with the perspective that bankfull, or the effective flood is the most important flow for mountain stream morphologic maintenance (*Wolman and Miller*, 1960; *Emmett*, 1999; *Whiting et al.*, 1999). The bankfull or effective flow perspective is based on quantifying the flood magnitude that moves the most bedload sediment over long periods of time. Since alluvial channels are built by sediment transport, it follows that the bankfull or equivalent flow maintains river form or shape. Despite hydroclimatological variation in the frequency of bankfull or effective flows (*Williams*, 1978), the morphologic basis of bankfull is a critical aspect of geomorphology (*Phillips and Jerolmack*, 2016).

To bridge the apparent gap between concepts underpinning views of environmental and bankfull flows, we suggest that results presented here coupled with supporting work by *Pickup and Rieger* (1979); *Parker et al.* (2003); *Bolla Pittaluga et al.* (2014) and *Brown and Pasternack* (2017) highlights that larger floods build the framework, or foundation skeleton of gravel-bed mountain streams, and that smaller, more frequent floods fill out the skeleton (Figure 4.4), while retaining the shape or morphology of the skeleton (Figure 4.7). The filling out process evolves according to the sequence and magnitude of floods, which work collectively to enhance morphologic diversity (Figures 4.5 and 4.6), and build the riverine palette from which measurable ecosystem services are realized (*Acreman et al.*, 2014a, Figure 1 therein). Accordingly and over long periods of time, the bankfull or effective flow would be the most important element of the flows which fill out the skeleton.

### 4.5.3 Development of pool-riffles along variable width channels

Figures 4.3 and 4.4 illustrate that two types of pool-riffle structures formed within the experimental channel. The first type, referred to as entrainment-driven pool-riffles, occur along channel segments with downstream width variations that proceed from relatively wide segments to narrower ones. The riffle-pool from station 10000 to 6000 mm of the experimental channel reflects an entrainment-driven feature (Figures 4.3 and 4.4). The second type, referred to as depositional-driven pool-riffles, is the sequential inverse of the entrainment-driven type, whereby width is organized to proceed from relatively narrow segments to wider ones. The pool-riffle from station 12000 to 10000, and 5000 to 3000 mm reflects a depositional-driven feature (Figure 4.3).

The names of each pool-riffle type convey the processes responsible for formation. In the

first case, entrainment-driven riffle-pools form due to the downstream release of KE stored within the upstream riffle, which drives net particle entrainment downstream of the riffle, and pool formation. Depositional-driven pool-riffles form due to downstream storage of KE, which manifests as locally elevated water surface elevations. Channel segments immediately upstream of the points of widening, and locally high water surface elevations, are affected by this downstream condition, leading to increased water depths, and passive pool formation. Figure 4.4, in particular, illustrates this condition, and also shows that the upstream pool bed slopes are similar, or slightly steeper than the overall longitudinal bed slope. Indicating that net particle entrainment has a minor role in pool-riffle formation under depositionally-driven processes. *de Almeida and Rodríguez* (2011) also reports the prevalence of backwater-controlled pool-riffles for their Bear River, AR, U.S. simulation reach.

It is important to identify the different processes which give rise to pool-riffles for at least two reasons. First, formative hypotheses must account for the development mechanisms required to explain the observations in Figures 4.3, 4.4 and 4.9. The second practical reason is that river restoration practitioners should be aware that different design approaches will yield pool-riffles, but that the associated structures will exhibit differing characteristics.

#### 4.5.4 General implications of unique profiles for sediment transport theory

The paired topographic profiles for 42, 60 and 80  $\text{l}\cdot\text{s}^{-1}$  shown in Figure 4.7 probably reflects just a few of the many possible SS topographic states that would otherwise result from the same external conditions. This reality means that the emergence of bed topography within the PRE1 experimental channel is best described by a probability distribution of  $n$  possible states (steady-state shapes), conceptually reflecting the idea of microstates as discussed by *Furbish et al.* (2016), and in line with the probabilistic nature of sediment mobility (*Wiberg and Smith, 1987; Kirchner et al., 1990; Hassan et al., 1991, e.g.*), sediment transport (e.g. *Einstein, 1950; Furbish et al., 2012; Ancey and Heyman, 2014*), and turbulence. This outcome is not consistent, however, with expectations built from Equations 4.3 and 4.4, which imply a uniform outcome for the same supplies of water and sediment. So, is it possible to reconcile the probabilistic behavior shown in Figure 4.7 with the uniform basis of Equations 4.3 and 4.4? We suggest that the emergence of non-unique topographic profiles for similar upstream supply conditions offers a potential link between particle scale probabilistic transport theory (*Furbish et al., 2012; Ancey and Heyman, 2014; Furbish et al., 2016*), and manifestation of these processes at larger scales.

To motivate future work, we provide the following example to illustrate a possible link. The assumptions underpinning Equation 4.11 preclude a probabilistic perspective, but that does not constrain solutions to unique outcomes. The dimensionless downstream mean velocity gradient  $\partial\bar{U}_x^*/\partial x^*$  responds to the local topographic and surface texture conditions, over length scales of  $1-2w'$ . If SS topography is described by a probability distribution of possible states,  $\partial\bar{U}_x^*/\partial x^*$  will correspondingly vary, and drive non-unique outcomes for the same upstream supply conditions. Furthermore, relaxing the assumption of a spatially fixed  $D_{90}$  of

Equation 4.11, would introduce more local variability into the problem, which would reinforce the tendency for non-unique topographic responses, and would better reflect grain size variability as shown in Figures 4.2d and 4.2e. The particle effect would diminish, however, for cases where natural channels have time periods of likely  $10^1 - 10^3$  years, or more to respond and evolve to uniform upstream conditions, depending on initial conditions relative to those of SS (Howard, 1982).

## 4.6 Conclusions and next steps

Motivated by previous observations that pool-riffles are colocated with segments of channel narrowing and widening, respectively, we use scaled laboratory experiments and theory to examine how and why downstream channel width variations give rise to these bed structures, and under conditions common to natural streams. Our experiments produce pool-riffle, and roughened channel morphologic structures across flow and sediment supply rates that vary by a factor 2. Pools occur where the downstream change in width  $\Delta w(x) \cdot \Delta L^{-1} < -0.10$ , riffles occur where  $\Delta w(x) \cdot \Delta L^{-1} > +0.10$ , and roughened channel beds where  $-0.10 < \Delta w(x) \cdot \Delta L^{-1} < +0.10$ . These general threshold conditions are consistent with data from numerical simulations (de Almeida and Rodríguez, 2012) and experiments (Nelson *et al.*, 2015), and also highlight that relatively straight channel segments constrained by  $-0.10 < \Delta_h w(x) h^{-1} < +0.10$  are unlikely to develop pool-riffle pairs, unless they are driven by some other external condition which leads to relatively large spatial differences in sediment transport. Furthermore, pool-riffle formation is the result of at least two different processes: entrainment-driven and depositional driven. Which one ultimately governs local conditions depends on the spatial organization of channel width. Therefore, along relatively straight channel segments, the spatial organization of channel width drives the general topographic response.

We show that local topographic gradients  $S_{local}$  are systematically expressed across the range of downstream width change  $(-0.30)$ – $(+0.30)$ , and for reach-average bed slopes that vary by one order of magnitude. This finding points out that we can determine the general behavior of  $S_{local}$  by knowing nothing more than how channel width changes in the downstream direction, and over length scales of 1–2 average widths. We examine specific controls on  $S_{local}$  organization with a 1D mathematical model developed from statements of mass conservation, bedload transport, and scaling arguments supported by our experimental measurements. Our model is motivated by the observation that bed topography and width change are coupled through downstream variations of mean flow speed, but the model indicates that the physics governing this coupling outcome is expressed through the parameter  $\Lambda$ .  $\Lambda$  expresses the relative importance of a relaxation vs. the forcing times scale. Pools emerge when the forcing time scale is characteristically small relative to the relaxation time scale, and riffles emerge when the difference between the two time scales decreases by a factor 2 or more. Furthermore, the expression of  $S_{local}$  over the range of  $\Delta w(x) \cdot \Delta L^{-1}$  presented in Figures 4.9 and 4.11 is conditioned by the spreading timescale, as it is a measure of bed resistance for alluvial channels.

Our experiments idealize natural gravel-bed streams as ones with fixed banks, high enough to contain relatively large floods. Whereas the height of channel walls in PRE1 were high enough to contain all flows, so that the width conditions were controlled across all upstream supplies, we do not suggest that our work or results reflect bedrock canyon reaches. As such, it is helpful to contextualize our work as framing an end member case where local width is the dominant driving mechanism of bed topography expression. Notably, *de Almeida and Rodríguez (2011)* and *Brown and Pasternack (2017)* offer numerical and field-case results for the opposite end member case where the nature of channel width control relaxes to give way to other driving mechanisms, which are discharge dependent. Fruitful next steps include examination of topographic responses under variable upstream sediment supply conditions, with pulses of differing texture, and hydrographs, with an emphasis on whether it is possible to break the width control and evolve toward a completely different topographic response, including the occurrence of lateral bars. We also suggest that our results can frame the basis for a unified pool-riffle formative hypothesis within mountain stream settings.

## Chapter 5

# Morphodynamic evolution of a width-variable gravel-bed stream: a battle between local topography and grain size texture

### 5.1 Summary

Statistical steady-state is commonly defined as mass continuity of bedload sediment over channel reaches of many channel widths in length, or longer. Proposals for equilibrium conditions commonly carry on from this steady-state definition by stating that under conditions of mass continuity, rivers express a longitudinal bed profile which varies around some long-term stable pattern. But this larger-scale view of equilibrium neglects the local physical processes that give rise to the stationary profiles, and we lack a formal definition of equilibrium based on these processes. We address this need and use mass conservation statements for the bulk riverbed, and the sediment particles which comprise the riverbed to define two new dimensionless numbers which quantify the rates of bed topography and bed sediment texture adjustment to upstream water and sediment supplies, for which sediment texture is defined by the local spatial distribution of grain sizes for areas that scale as  $(w')^2$ . We hypothesize that a local equivalence of these rates defines fluvial equilibrium, which can be scaled up to reaches of many channel widths with supporting information on the spatial distribution of these rates. Our equilibrium definition depends on only three quantities: a topographic adjustment velocity, a particle composition adjustment velocity, and a term which quantifies the degree of difference between the fractional composition of the local bedload supply and the sediments stored in the bed substrate, in relation to the fractional composition of the long-term average sediment supply. We apply our new view to experimental data from pool-riffle experiment 1, and find that equilibrium conditions are achieved for relatively high bed sediment mobilities.

## 5.2 Introduction

Mountainous rivers flow through channels that are remarkable for their spatial complexity. Water moves over steps of various size, accelerates through narrowings, slows at deep pools and becomes complex at bends. Depositing and mobilizing sediments along the way. Over relatively long times, the inherent richness of river systems can give way to some measure of order, typified by river longitudinal profiles that settle to a statistically steady-state condition (SS) (*Howard, 1982; Ahnert, 1994*), which we define by two criteria. First, steadiness of average topography, and second, that the upstream sediment supply  $Q_{ss}$  is approximately equal to the downstream sediment flux at the outlet  $Q_{sf}$  (see Figure 4.2). The second criteria holds for both the total mass of the sediment mixture, and the fractional mass of each grain size.

Statistically steady profiles are characterized by a natural downstream progression of channel bedform geometry and topography, and associated bed sediment grain size distributions or textures (*Montgomery and Buffington, 1997*). Closer to the headwaters, channels are steep, and exhibit boulder ( $> 256$  mm) bed stepped reaches of many channel widths in length. As drainage area increases, channels are more moderately sloped, with undulating cobble and gravel (2–256 mm) bed reaches. Closer to the terminus, or out into the lowland plains, channels are gently sloped, and exhibit meandering forms composed of sand ( $> 2$  mm) covered beds (e.g. *Leopold and Wolman, 1957; Montgomery and Buffington, 1997; Church, 2006*).

In Chapter 4 we demonstrate that adjustments of channel bed topography and grain size distribution are coupled to local variations of channel size via changes in flow speed and particle mobility condition, expressed through the parameter  $\Lambda$ . Local width variations, which we define by length scales of a few average widths, are important because they modulate the total mass and fractional composition of sediments transported to downstream reaches, principally due to sediment storage within relatively wide channel segments, and depending on the extent to which sediment is mobilized (cf. Chapter 4) (*Furbish et al., 1998; Bolla Pittaluga et al., 2014; Ferrer-Boix et al., 2016*). As a result, SS at the reach and larger scale is conditioned by the cumulative time scales necessary for channel profiles to develop in response to local width variations (*Howard, 1982; Paola et al., 1992; Ahnert, 1994; Bolla Pittaluga et al., 2014*). Here, we build from our findings of Chapter 4, and suggest that the coupling between channel bedform geometry, surface texture, and channel width is also important for SS conditions, and provides a way to define “fluvial equilibrium”.

Fluvial equilibrium is a useful, but often times confusing concept with a long history. *Howard (1982)* defines equilibrium as a temporally invariant functional relationship between system inputs and outputs, which in the present case includes the total and fractional masses of all sediment sizes within  $Q_{ss}$  and  $Q_{sf}$ . *Ahnert (1994)* elaborates on *Howard’s* proposal, and states that equilibrium is an equivalence of the rates of processes acting on sediment supply, which drives erosion and deposition, and ultimately gives rise to sediment mass continuity. *Ahnert’s* proposal builds directly from *Domenico Guglielmini (Guglielmini, 1697; Chorley et al., 2009)*, who postulated in 1697 that “streams erode or build up their beds until an equilibrium

is reached between force and resistance” (Chorley *et al.*, 2009, page 84). Du Buat (*du Buat*, 1786), and then Gilbert (*Gilbert*, 1877) continued with this view, and Gilbert surmised that equilibrium is tied to an equality of action, which can be understood as comparability between the capacity to do work to the streambed, and the resistance offered by the bulk bed. Despite the frequent use of equilibrium within fluvial studies, we are unaware of a formalized definition built from *Gilbert (1877)’s*, *Howard (1982)’s*, or *Ahnert (1994)’s* proposals.

Here we use *Ahnert (1994)’s* general proposal, and define equilibrium as an equivalence between the rates of constructing local mean bed topography and slope, and bed surface sediment texture or roughness, as determined by the bed surface local grain size distribution, for areas that scale as  $(w')^2$  (*Venditti et al.*, 2012; *Chartrand et al.*, 2015). Disequilibrium occurs when these rates are not equivalent. We assume that the topographic and texture rates are much larger than those of channel bank, or channel position change, and we further assume on the basis of results presented in Chapter 4, that equilibrium reflects a balance between momentum flux delivery to the bed, and the strength of the bed itself. We are therefore focused on mechanical equilibrium, and we quantify the rates of topographic and texture change, at maximum spatial scales of roughly  $w'$ , because this is the approximate minimum scale at which channel width change drives a morphologic response, absent external forcing by wood or boulders (see Figure 4.1). Our definition of fluvial equilibrium is distinct from conventional views of statistical steady-state in two ways:

- a. Statistical steady-state is defined by mean bed elevation steadiness, and sediment mass balance. Equilibrium is defined by local rates of constructing topography and bed surface roughness
- b. Statistical steady-state is usually evaluated over length scales of many average channel widths, whereas equilibrium is determined at scales that measure of maximum of  $w'$ .

We build our statement of fluvial equilibrium from mass balance expressions and scaling arguments, and our work was motivated by three important questions:

1. Can we build a definition of equilibrium that captures the physics discussed in Chapter 4, and which is easily tested with experimental, or field data?
2. Can equilibrium conditions be determined, or reliably inferred from the appropriate mass balance statements?
3. For a given set of water and sediment supplies, will the same balance of forces be expressed by 1 profile/grain size bed pattern (*Parker and Wilcock*, 1993; *Church and Ferguson*, 2015), or a suite of possible patterns as suggested by Figure 4.7? This question also addresses the related issue of whether equilibrium is achieved in generally the same manner for a set of supply conditions?

We hypothesize that riverbed response to imposed flow and sediment supply conditions at the local scale of  $w'$  is governed by two filters which either drive the tendency to build topography, or the tendency to entrain sediment particles resting on the bed surface (Figure 5.1–discussed in detail within Section 5.3.1). The proposed filters conceptually reflect the physical processes which drive sediment deposition and entrainment. Consequently, at equilibrium these filters have equivalent gains and local sediment continuity is achieved. Accordingly, we also hypothesize that equilibrium is expressed through statements of total and fractional mass conservation of the riverbed, consistent in principle with *Ahnert* (1994).

We test our hypotheses with flume experiments conducted within a variable-width channel, the details of which are reviewed in Chapter 3. A principal finding of this chapter is that equilibrium condition is dependent upon comparability of topographic and grain size adjustment rates, and similarity between three populations of sediment particles that set local responses: the local bed subsurface, the local sediment supply, and the long-term average upstream sediment supply. The grain sizes term is rate limiting, and ultimately governs equilibrium time scales, which expands upon existing topographic-focused ideas (*Howard*, 1982; *Ahnert*, 1994), and basin-scale theory (*Paola et al.*, 1992).

## 5.3 Morphodynamic evolution metrics at the scale of a channel width

### 5.3.1 Problem set-up

At the local scale of a few channel widths, rivers respond to supply fluctuations of water or sediment through adjustments of channel size, streamwise topographic profile, and bed surface texture. Along relatively straight mountain streams, adjustments of channel size are neglected, because topographic profile and texture adjustment rates are relatively much larger, and changes in size are intermittent. Our focus therefore is with adjustments of the streamwise topographic profile, and bed surface texture, which force disequilibrium conditions by altering local rates of sediment transport for time scales of at least a few flood events (cf. Chapter 2). We conceptualize this view in Figure 5.1a, where we illustrate the physical processes of sediment supply modification in terms of depositional and entrainment filters. As we will show, the action of these filters modulates channel evolution toward fluvial equilibrium.

Figure 5.1a shows that local sediment supply  $Q_{ss}$  has a magnitude and composition, which for disequilibrium conditions, are modified by deposition and/or entrainment. The degree of modification sets the properties of the local sediment flux  $Q_{sf}$ . For a control volume covering a unit area of the bed, incoming sediment grains transported along the streambed can either settle to the bed, or remain in motion and continue downstream, and additional grains can be entrained, or not. The tendency for any of these outcomes depends on the local profile and bed texture conditions, which in turn reflects departure from the associated equilibrium.

The depositional filter (Figure 5.1a) is a result of feedbacks between the local bed topogra-

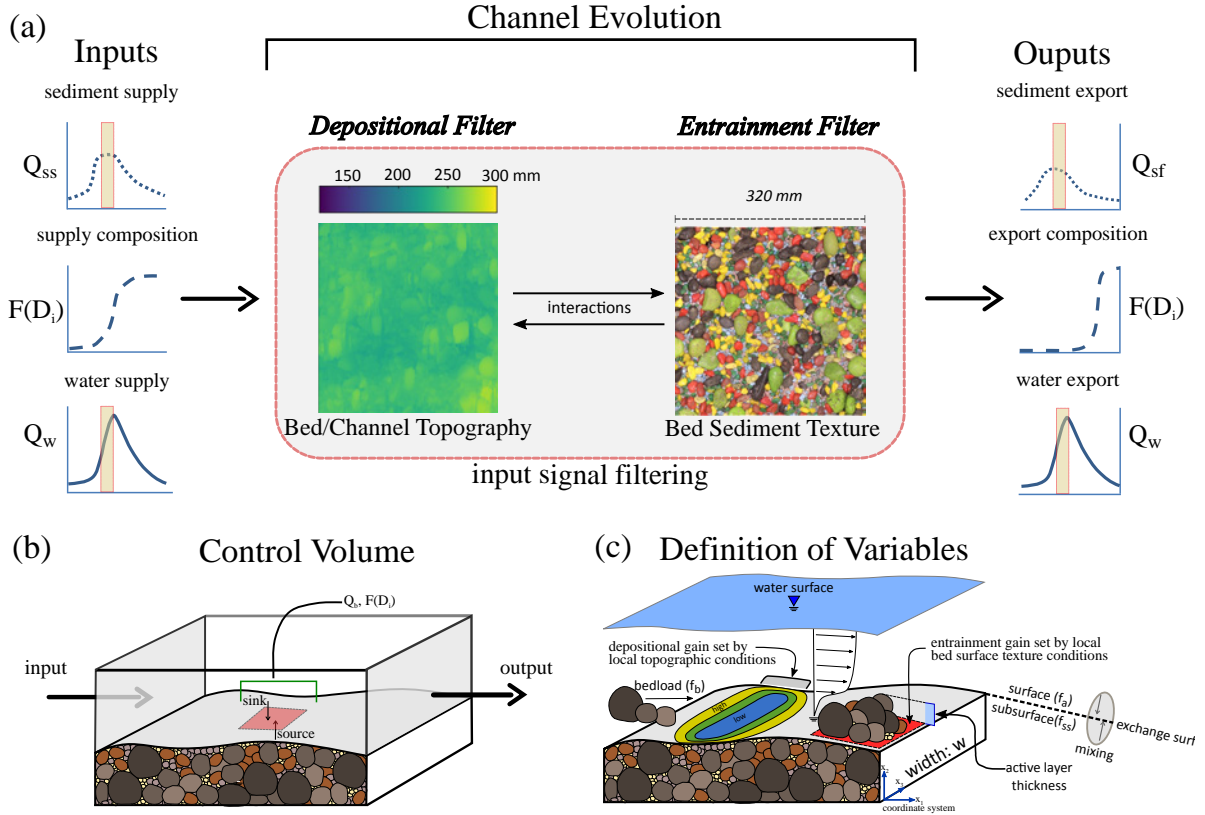


**Figure 5.1:** Conceptual illustration of how topographic and sediment texture filters work to drive channel evolution. (a) The top panel illustrates that incoming sediment supply  $Q_{ss}$ , transported by some supply of water  $Q_w$ , is acted upon by topographic and sediment texture filters to give rise to the outgoing sediment flux  $Q_{sf}$ . Both the magnitude and composition of the incoming supply can change. Images of the DEM and photograph of the bed surface provided for illustration of the concepts. (b) The control volume for the problem illustrates that the filter actions lead to the channel bed being a sink or source of sediment particles. Filtering the  $Q_{ss}$  by deposition means the channel bed is a sink for particles, and filtering by entrainment means it is a particle source. (c) Definition of variables used for derivation of the local topographic and particle response numbers,  $N_t$  and  $N_p$  respectively.

phy and the flow. Over bed areas of roughly  $(w')^2$ , bed topography scales the average downstream flow velocity  $\bar{U}_x$ , due to flow continuity and coupling with the local channel width condition (see Chapter 4).  $\bar{U}_x$ , and in particular the downstream change in  $\bar{U}_x$  in turn scales the average momentum flux imparted to the bed, and therefore the tendency to deposit sediment in motion or not. As we show in Chapter 4, under conditions where local flow speed decreases, the tendency for deposition is relatively high, where flow speed increases, the tendency for sediment grains in motion to continue downstream is relatively high, and where flow speed change is negligible, either outcome is possible (e.g. *Hoey and Ferguson, 1994; Parker, 2008*).

The entrainment filter (Figure 5.1a) is a function of the local sediment texture, which sets

the average mobility condition for any grain resting on the bed surface. Mobility is commonly expressed (1) as a function of relative grain size, which captures the degree to which smaller grain sizes are sheltered from the flow by larger grains (e.g. *Ashida and Michiue, 1972; Parker, 1990*), (2) based on the content of sand sized grains in the bed surface, which reflects near-bed velocity structure (*Wilcock and McArdell, 1993; Wilcock and Crowe, 2003*), and (3) based on how grains rest on the bed surface, which captures the relative difficulty of pivoting a grain out of a pocket (*Wiberg and Smith, 1987; Kirchner et al., 1990; Buffington et al., 1992*). As one example, bed surfaces that are relatively rough, with many grain sizes present, will preferentially entrain larger grains, or grains which sit relatively high in the flow, above the bed surface (*Wiberg and Smith, 1987; Kirchner et al., 1990; Buffington et al., 1992*) (also see Appendix B). Furthermore, the depositional and entrainment filters also interact, because filtering by each occurs at different rates, and this triggers additional possible responses.

Figure 5.1b shows the local control volume for our filtering problem, and Figure 5.1c provides definition of variables which will be used below when we derive our statement of fluvial equilibrium. In the problem definition of Figure 5.1b, the upstream water supply  $Q_w$  is unaffected by filtering, and the channel bed is either a sink, or source of sediment. The channel bed acts as a sink due to affects of the depositional filter, and acts as a source due to affects of the entrainment filter.

We have set up the local equilibrium problem in terms of depositional and entrainment filters, which we link to the local bed topography, and bed surface texture, respectively. These links offer a natural basis from which to derive our equilibrium statement, which we complete with mass conservation statements for the bulk riverbed, and the particles which make up the bed. We make these choices because these conservation statements can quantify the respective filtering responses over relatively short time scales, ideally that are less than the duration of a flood event. Furthermore, the mass conservation statements embody information concerning the dynamics of how each process responds to upstream water and sediment supply forcing (e.g., *Hoey and Ferguson, 1994; Paola and Voller, 2005; Parker, 2008; Stecca et al., 2014*), and this is the information needed to examine equilibrium conditions. To build understanding in the next section, we characterize bed and particle related dynamics with new dimensionless quantities we term the topographic, particle and channel response numbers ( $N_t$ ,  $N_p$  and  $N_e$ ), respectively.  $N_t$  and  $N_p$  are derived by nondimensionalizing the respective mass conservation statements, with choice of specific length, time, velocity and flux scales.  $N_e$  is defined as the ratio  $N_t/N_p$ . The next section presents our derivation of each number.

### 5.3.2 Mass conservation

#### Exner equation: mass conservation of the riverbed

The general statement of riverbed mass conservation in one dimension is written (*Exner, 1925; Paola and Voller, 2005*):

$$\frac{\partial \eta}{\partial t} = -\frac{1}{\varepsilon} \frac{\partial q_b}{\partial x}, \quad (5.1)$$

where  $\eta$  is channel bed elevation at position  $x$ ,  $t$  is time,  $\varepsilon = (1 - \phi)$ , where  $\phi$  is the volume-averaged streambed porosity (assumed to be spatially uniform and set as 0.40) of the active layer  $L_a = kD_c$  (*Hirano, 1971*), where  $k$  is constant between 1 and 2 (*Parker, 2008*), and  $D_c$  is a characteristic grain size, generally taken as  $D_{90}$ , which is the local grain size for which 90% of bed material within the active layer is smaller, and  $q_b$  is streamwise bedload flux per unit  $w$ . Equation 5.1 expresses mass conservation for riverbeds as a balance between temporal changes of local bed topography and the net flux of bedload  $Q_{sf}$ .

#### Hirano equation: mass conservation of riverbed grain sizes

The particle mass conservation statement in one dimension (*Hirano, 1971*), is written following the derivation by *Juez et al. (2016)*:

$$f_{es} \frac{\partial}{\partial t} (\eta - L_a) + \frac{\partial}{\partial t} (f_a L_a) = -\frac{1}{\varepsilon} \frac{\partial q_\psi}{\partial x}, \quad (5.2)$$

where  $q_\psi$  is streamwise sediment flux per unit  $w$  for grain size  $\psi = \log_2 D$  and  $D$  is a grain size in mm,  $f_{es}$  is the volume probability density of  $\psi$  at the exchange surface (*Viparelli et al., 2010*) (Figure 5.1c), and  $f_a$  is volume probability density of  $\psi$  within  $L_a$ , or as expressed at the bed surface (Figure 5.1c), assuming a constant particle density. Based on the two-layer model of the bed subsurface (Figure 5.1c) (*Hirano, 1971*), the active layer composition defines which particle size classes  $\psi$  can be entrained into bedload. Consequently, the probability distribution of  $f_a$  defines the composition or roughness of the bed surface. Equation 5.2 expresses mass conservation of particles comprising the bed as a balance between temporal changes to the exchange surface position and the  $L_a$  thickness (Figure 5.1c), to the net fractional flux of bedload (i.e. flux of each grain size fraction  $\psi$ ).

Equations 5.1 and 5.2 are linked via the definition of  $q_b$  (*Parker et al., 2000*):

$$f_b = q_\psi / q_b, \quad (5.3)$$

where  $f_b$  is the volume probability of  $\psi$  within the local bedload (Figure 5.1c), and  $q_b = \sum q_\psi$  across all grain size classes. The exchange surface composition  $f_{es}$  regulates solid fractional fluxes between the local bed substrate ( $f_s$ ) and active layer ( $f_a$ ) (Figure 5.1c), and  $f_{es}$  depends

on whether the local bed surface builds or lowers, determined as (Hoey and Ferguson, 1994):

$$f_{es} = \begin{cases} f_s & \text{if } \partial\bar{\eta}/\partial t < 0 \\ \beta f_a + (1 - \beta)f_b & \text{if } \partial\bar{\eta}/\partial t > 0, \end{cases} \quad (5.4)$$

where  $\beta$  is a partitioning coefficient that ranges in value from 0 to 1. During phases of bed surface lowering, or net particle entrainment,  $f_{es}$  is composed of the bed substrate. During phases of bed surface heightening, or net particle deposition,  $f_{es}$  is a linear combination of the bed substrate and active layer compositions, assuming  $\alpha \neq 0$ . It is important to recognize that Equation 5.2 simplifies to Equation 5.1 for a uniform mixture of bed sediment.

Our goal is to express Equation 5.2 in a form where  $q_b$  is a function of  $f_{es}$ ,  $f_a$ ,  $f_b$ , and  $L_a$ . We therefore apply Equations 5.1 and 5.3 to Equation 5.2, and rearrange to obtain:

$$\frac{\partial}{\partial t}(f_a L_a) - f_{es} \frac{\partial L_a}{\partial t} = -\frac{1}{\varepsilon} \left[ \frac{\partial}{\partial x}(f_b q_b) - f_{es} \frac{\partial q_b}{\partial x} \right] \quad (5.5)$$

The last term of Equation 5.5 can be simplified by assuming  $f_b$  is constant, and moreover that  $f_b$  sets the rate at which the bedload transport gradient  $\partial f_b / \partial x$  changes in  $x$ , because  $f_b$  sets the fractional composition of  $q_b$ , and the fractional composition changes based on the makeup of the bed surface  $f_a$ . Therefore,  $f_b$  acts on the bedload flux gradient (Tritton, 1988), and Equation 5.5 becomes:

$$\frac{\partial}{\partial t}(f_a L_a) - f_{es} \frac{\partial L_a}{\partial t} = - \left[ \frac{(f_b - f_{es})}{\varepsilon} \frac{\partial q_b}{\partial x} \right] \quad (5.6)$$

The first term of Equation 5.6 can be expanded with the product rule, and Equation 5.6 can be restated, grouping like terms and defining  $\delta_1 = (f_b - f_{es})/\varepsilon$ :

$$L_a \frac{\partial f_a}{\partial t} + (f_a - f_{es}) \frac{\partial L_a}{\partial t} = -\delta_1 \frac{\partial q_b}{\partial x} \quad (5.7)$$

Because  $|L_a| \gg |(f_a - f_{es})|$ , and defining  $\sigma_v = \delta_1 / L_a$  [ $1/L$ ], Equation 5.7 is simplified to:

$$\frac{\partial f_a}{\partial t} \approx -\sigma_v \frac{\partial q_b}{\partial x} \quad (5.8)$$

Equation 5.8 is a kinematic wave equation, and states that the time rate of change of  $f_a$  depends on the flux of  $q_b$ , which is modulated by  $\sigma_v$ . The inverse of  $\sigma_v$  is a sorting length scale (Folk, 1966) for a given  $\delta_1$ . Depending on the magnitude of  $L_a$ , the length scale is characteristically small for comparable bedload and substrate compositions, and large for dissimilar compositions. Small sorting length scales implies that evolution of the local bed surface composition will occur relatively rapidly, as compared to longer length scales.

### 5.3.3 Nondimensional Exner and Hirano equations

#### Nondimensional Exner

We nondimensionalize Equation 4.3 assuming  $\eta \sim L_c$ ,  $t \sim (L_c/U_c)$ ,  $q_b \sim q_{b_c}$ , and  $x \sim L_c$ :

$$U_c \frac{\partial \eta^*}{\partial t^*} \approx - \frac{q_{b_c}}{\varepsilon L_c} \frac{\partial q_b^*}{\partial x^*}, \quad (5.9)$$

where  $q_{b_c}$  is a characteristic bedload flux per unit  $w$ , and  $L_c$ , and  $U_c$  are a characteristic length scale, and velocity or speed. We next multiply Equation 5.9 by  $1/U_c$  to obtain:

$$\frac{\partial \eta^*}{\partial t^*} \approx - \underbrace{\frac{q_{b_c}}{\varepsilon L_c U_c}}_{1/N_t} \frac{\partial q_b^*}{\partial x^*} \approx - \frac{1}{N_t} \frac{\partial q_b^*}{\partial x^*}. \quad (5.10)$$

Here,  $N_t$  is the dimensionless topographic response number and is a ratio of two velocities:  $U_c \cdot (L_c/q_{b_c})$ . Or based on the parameter  $\Lambda$  from Chapter 4, a ratio of two time scales:  $(U_c/L_c \cdot (L_c^2/q_{b_c}))$ . To further characterize  $N_t$ , we must specify reasonable choices for  $q_{b_c}$ ,  $L_c$ , and  $U_c$ . We set  $q_{b_c}$  as the local sediment supply  $Q_{ss}$ , determined at maximum spatial scales of  $w'$ . Sediment transport theory commonly uses  $L_a$  to approximate the bed depth which participates in sediment transport, and thus  $L_a$  is a measure of a local channel bed response length scale. Consequently,  $L_c = L_a$ . Since  $N_t$  describes the time rate of change of bed topography, the characteristic velocity  $U_c$  is defined as the rate at which the local bed surface changes its vertical position,  $U_b$ , because this defines the responsiveness of the bed to upstream supplies. With these definitions, we state  $N_t$  as:

$$N_t(t) \approx \frac{\varepsilon L_a U_b}{q_{b_c}}. \quad (5.11)$$

Physically,  $N_t(t)$  expresses the tendency to build or consume local bed topography over some time period  $t$ , which depends on the magnitude and sign of  $U_b$  and  $q_{b_c}$ . The magnitude of  $N_t(t)$  depends on how the two velocities  $U_b$  and  $(L_a/q_{b_c})$  compare, noting in particular that the bed speed  $U_b$  is governed by the degree of local topographic departure from an equilibrium, as will be shown below. When the velocity ratio is relatively large and positive,  $U_b$  drives the local bed elevation to increase through deposition, and when it is negative,  $U_b$  drives the local bed elevation to decrease through entrainment. When the velocity ratio is relatively small, positive or negative, bed elevation change is negligible, and the local sediment flux  $Q_{sf}$  total mass is close to, or equivalent with the upstream sediment supply  $Q_{ss}$ . Last, based on our assumption that  $q_b \sim q_{b_c}$ , the term  $\partial q_b^*/\partial x^* <$  will have a value that generally ranges from 0–2 or 3. Here, however, we are not concerned with this term.

### Nondimensional Hirano

We determine the particle response number  $N_p$  in an analogous way to  $N_t$ , and nondimensionalize Equation 5.8 with the assumptions stated above, plus our assumption that  $f_a \sim f_c$ :

$$\frac{f_c U_c}{L_c} \frac{\partial f_a^*}{\partial t^*} \approx - \frac{\sigma_v q_{b_c}}{L_c} \frac{\partial q_b^*}{\partial x^*}, \quad (5.12)$$

where  $f_c$  is a characteristic volume probability density of grain size class  $\psi$ . Whereas  $f_a$  is dimensionless, defining  $f_a^*$  in terms of a characteristic fractional content  $f_c$  is useful because it ultimately permits incorporation of a third grain size population into the problem, which is necessary in order to represent all grain size sources that drive sediment texture adjustment at the local scale, as we will discuss below. We next multiply Equation 5.12 by  $L_c / (f_c U_c)$ , and obtain:

$$\frac{\partial f_a^*}{\partial t^*} \approx - \underbrace{\frac{\sigma_v q_{b_c}}{f_c U_c}}_{1/N_p} \frac{\partial q_b^*}{\partial x^*} \approx - \frac{1}{N_p} \frac{\partial q_b^*}{\partial x^*}. \quad (5.13)$$

Here,  $N_p$  is the dimensionless particle response number, which is a ratio of two velocities:  $U_c \cdot (L_c / q_{b_c})$ , modified by the degree of similarity between the fractional content of the local bedload, and the exchange surface at the base of the active layer (Figure 5.1c). In order to further characterize  $N_t$ , must specify reasonable choices for  $q_{b_c}$ ,  $f_c$ , and  $U_c$ . As above, we set  $q_{b_c}$  as the local sediment supply  $Q_{ss}$ , determined at maximum spatial scales of  $w'$ . For the characteristic fractional content  $f_c$  we step away from the local scale, and define it as the basin-scale average upstream bedload supply composition  $f_{us}$ . Use of a non-local quantity here is reasonable because over long periods of time ( $\approx > 10^1 - 10^2$  years),  $f_{us}$  sets the composition of channel reaches many  $w$  in length. As a result, local bed areas are ultimately adjusting to the upstream supply compositions over relatively long times.

The characteristic speed  $U_c$  is defined in the context of streambed texture, which we specify as the rate at which a characteristic grain size changes:  $U_p$ . The characteristic grain size could be the  $D_{50}$ ,  $D_{90}$ , or some combination of grain sizes, but here we quantify  $U_p$  in terms of the  $D_{90}$  because of the earlier noted role it has for sediment mobility and transport. With these definitions, and recalling that  $\sigma_v = \delta_1 / L_a$  and  $\delta_1 = (f_a - f_{es}) / \varepsilon$ , we recast  $N_p$  as:

$$N_p(t) \approx \left( \frac{f_{us}}{f_b - f_{es}} \right) \frac{\varepsilon L_a U_p}{q_{b_c}} \approx \delta_2 \frac{\varepsilon L_a U_p}{q_{b_c}}, \quad (5.14)$$

where  $\delta_2 = f_{us} / (f_b - f_{es})$ , which expresses the tendency for the local fractional composition to fine or coarsen, depending on the sign of  $(f_b - f_{es})$ .

Physically,  $N_p(t)$  expresses the tendency for bed surface texture to change over some time period  $t$ , which depends on the sign of  $U_p$  and  $q_{b_c}$ . The relative magnitude of  $N_p(t)$  depends on how the two velocities  $\delta_2 \varepsilon U_p$  and  $(L_a / q_{b_c})$  compare, noting that the particle speed  $U_p$  is governed by the degree of local texture departure from an equilibrium, which is quantified

by  $\delta_2$ . When the velocity ratio is relatively large and positive,  $U_p$  drives the local bed surface fractional composition of a given size class  $\psi$  to increase through deposition, and when it is negative,  $U_p$  drives the local bed surface fractional composition of a given size class  $\psi$  to decrease through entrainment. When the velocity ratio is relatively small, positive or negative, fractional composition change is negligible, and the local sediment flux  $Q_{sf}$  fractional mass is close to, or equivalent with the upstream sediment supply  $Q_{ss}$  fractional mass.

Last, we highlight that  $\delta_2$  has a strong affect on the value of the particle velocity  $\delta_2 \varepsilon U_p$ . As an example, Figures 5.2a–5.2c show that  $\delta_2$  generally ranges from (-20:+20) for a steady upstream supply composition value  $f_{us} = 0.3$ , and  $f_b = 0, 0.5$  and  $1.0$ , and  $f_{es} \in [0.05, 0.95]$ . Notably, the largest values of  $\delta_2$  occur when  $f_b$  and  $f_{es}$  approach equivalence (Figures 5.2b and 5.2c). This is important because when  $f_b$  and  $f_{es}$  are near equivalence for an extended duration of time, local fractional composition conditions are likely approaching an equilibrium.

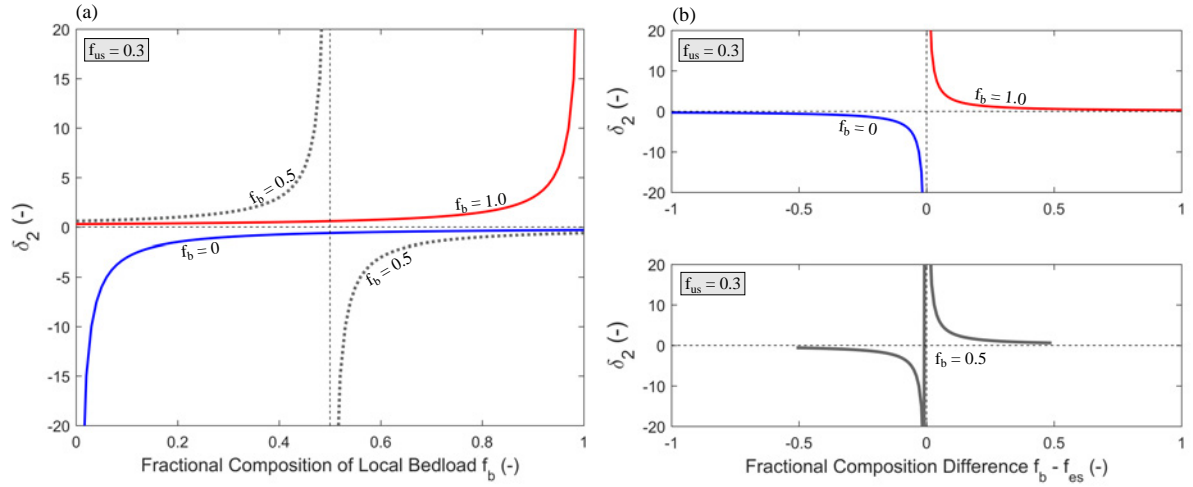


**Figure 5.2:** Example values of  $\delta_2$  of Equation 5.14 vs. (a)  $f_b$  and (b)  $f_b - f_{es}$ , for parameter values  $f_{us}=0.3$ ,  $f_b=0, 0.5$  and  $1.0$ , and  $f_{es} \in [0.01, 0.99]$ .  $\delta_2$  is asymptotic across the entire range of plausible values for the fractional variables  $f_{us}$ ,  $f_b$  and  $f_{es}$ .

### 5.3.4 Dimensionless channel response number: $N_e$

The hypotheses we presented within Section 5.2 suggests that equilibrium occurs where:

$$\partial \eta^* / \partial t^* \approx \partial f_a^* / \partial t^* \quad (5.15)$$

Therefore, we combine Equations 5.11 and 5.14 to introduce a channel response number:

$$N_e(t) = \left( \frac{N_t}{N_p} \right) = \left( \frac{1}{\delta_2} \right) \frac{U_b}{U_p} \quad (5.16)$$

$N_e$  expresses a balance between the bed and particle velocities,  $U_b$  and  $\delta_2 U_p$ , respectively, and builds directly from *Ahnert* (1994)'s equilibrium proposal, for which we view  $U_b$  as the rate

of topographic adjustment, and  $\delta_2 U_p$  as the rate of texture adjustment. More specifically,  $U_b$  quantifies the time rate of change of the local bed elevation, and  $\delta_2 U_p$  quantifies the time rate of change of a local bed surface grain size fraction. Therefore,  $N_e(t)$  is a ratio of the two adjustment rates which determine how local river segments change in response to upstream supplies of water and sediment.

Since we are specifically interested in whether the time rate of change of topography, or texture governs the local  $N_e$  condition, and given that both velocities can take positive or negative values, we write Equation 5.16 as an absolute value:

$$N_e \approx \left| \left( \frac{1}{\delta_2} \right) \frac{U_b}{U_p} \right|. \quad (5.17)$$

Equation 5.17 highlights that we expect equilibrium conditions where  $N_e \approx O(1)$ , which, importantly, is a function of the choices we made to assign scales to  $U_c$  and  $L_c$ .

### 5.3.5 Calculations of $\delta_2$ , $U_b$ , $U_p$ and $N_e$

To determine  $N_e$ , we calculate  $\delta_2$ ,  $U_b$  and  $U_p$  for all subsampling locations  $x_j \in [4000:1000:13,000]$ , and all observation times  $t_n$  1–29 (see Table 3.1), with data from pool-riffle experiment 1 (PRE1). Development of the data we use in the calculations is presented in Chapter 3. The specific data sets we use are local bed topography derived from the digital elevation models, the local grain size distributions derived from the composite photographs, and the upstream bedload sediment boundary conditions. We now step through calculation of each quantity.

#### Calculation of $\delta_2$

Instead of focusing on a particular size class, such as the  $D_{50}$ , or a combination of size classes, we determine  $\delta_2$  by assuming that changes in the fractional composition of each grain size population  $f_{us}$ ,  $f_b$  and  $f_{es}$ , scales according to changes in the standard deviation of each population distribution, which contributes to  $\partial f_a^* / \partial t^*$ . Therefore, we calculate  $\delta_2$  at a given location  $x_j$  and observation time  $t_n$  as:

$$\delta_{2,x_j,t_n} \approx \frac{s_{us}}{(s_b - s_{es})}, \quad (5.18)$$

where  $s$  is the sample standard deviation for grain size fractions of the experimental sediment supply ( $s_{us}$ ), the local bedload supply ( $s_b$ ) and the local exchange surface ( $s_{es}$ ), for subsampling location  $x_j$  and for observational time  $t_n$ . Note that because  $s_b$  is the local bedload supply, it is determined from subsampling location  $x_{j-1}$ , in a downstream moving reference frame. We calculate the sample standard deviation of the grain size fractions as:

$$s_{x_j,t_n} = \sqrt{\frac{1}{K} \sum_{i=1}^K (f_{i,\psi} - \bar{f})_{x_j,t_n}^2}, \quad (5.19)$$

where  $s_{x_j, t_n}$  is the weighted sample standard deviation at subsampling location  $x_j$  and time  $t_n$ ,  $K$  is the number of grain size fractions,  $f_{i, \psi}$  is the fractional content for the experimental supply, near-local bedload supply or the local exchange surface for grain size class  $\psi$ , and  $\bar{f}$  is the average fractional content across all grain size classes. We choose to calculate  $\delta_2$  with standard deviations of the grain size populations, as opposed to a characteristic grain size (e.g.  $D_{50}$  or  $D_{90}$ ), because  $s$  reflects how the grain size population for the local bedload and exchange surface varies in time, as opposed to an explicit size class, which may change independently from the population. As a result, use of  $s$  to evaluate  $\delta_2$  provides a complete and straightforward test of dissimilarity between the three grain size populations.  $s_{us}$  was constant in the calculations.

We do not have a direct measure of  $s_b$  from PRE1 experimental data. We can however estimate  $s_b$  based on quantifying the local bedload supply distribution  $f_b$  at  $x_{j-1}$  and  $t_n$ , which depends on how the composition changes from  $t_{n-1}$  to  $t_n$ :

$$f_{b, \psi, x_j, t_n} = \begin{cases} 0 & \text{if } f_{b, \psi, x_{j-1}, t_n} > f_{b, \psi, x_{j-1}, t_{n-1}} \\ f_{b, \psi, x_{j-1}, t_{n-1}} + (f_{b, \psi, x_{j-1}, t_{n-1}} - f_{b, \psi, x_{j-1}, t_n}) & \text{if } f_{b, \psi, x_{j-1}, t_n} < f_{b, \psi, x_{j-1}, t_{n-1}} \end{cases} \quad (5.20)$$

Equation 5.20 states that the local bedload fractions for any size class  $\psi$ , at subsampling location  $j$ , and for time  $t_n$ :

1. Goes to zero if the fractional composition of any size class  $\psi$  is enriched at  $x_{j-1}$  between  $t_{n-1}$  and  $t_n$ ; and
2. Is a linear combination of (a) the composition at  $x_{j-1}$  at  $t_{n-1}$  plus (b) the difference between compositions from  $t_{n-1}$  to  $t_n$  if the fractional composition is depleted.

In the latter case, we assume that the bed surface supplies the additional fractional composition, consistent with how we define the control volume (Figure 5.1b). After  $f_{b, \psi, x_j, t_n}$  is calculated for all grain size classes with Equation 5.20, the sum of  $f_{b, \psi, x_j, t_n}$  may have a fractional value less than 1, because of loss of fractional content. It is therefore necessary to renormalize the fractions such that for  $N$  total grain size classes:

$$\sum_{i=1}^N f_b = 1. \quad (5.21)$$

We then use Equations 5.19 and 5.21 with the values for  $f_b$  to calculate  $s_b$ .

We do not have a direct measure of  $s_{es}$  from PRE1 experimental data, but we can estimate it using the times series of bed surface sample standard deviations,  $s_a$ , which permits us to construct a basic stratigraphic column at each subsampling location  $x_j$  (Figure 5.3). The stratigraphic columns are time dependent, and account for cycles of deposition and entrainment, which means our approach is consistent with theory (Viparelli *et al.*, 2010), given the resolution of our data.

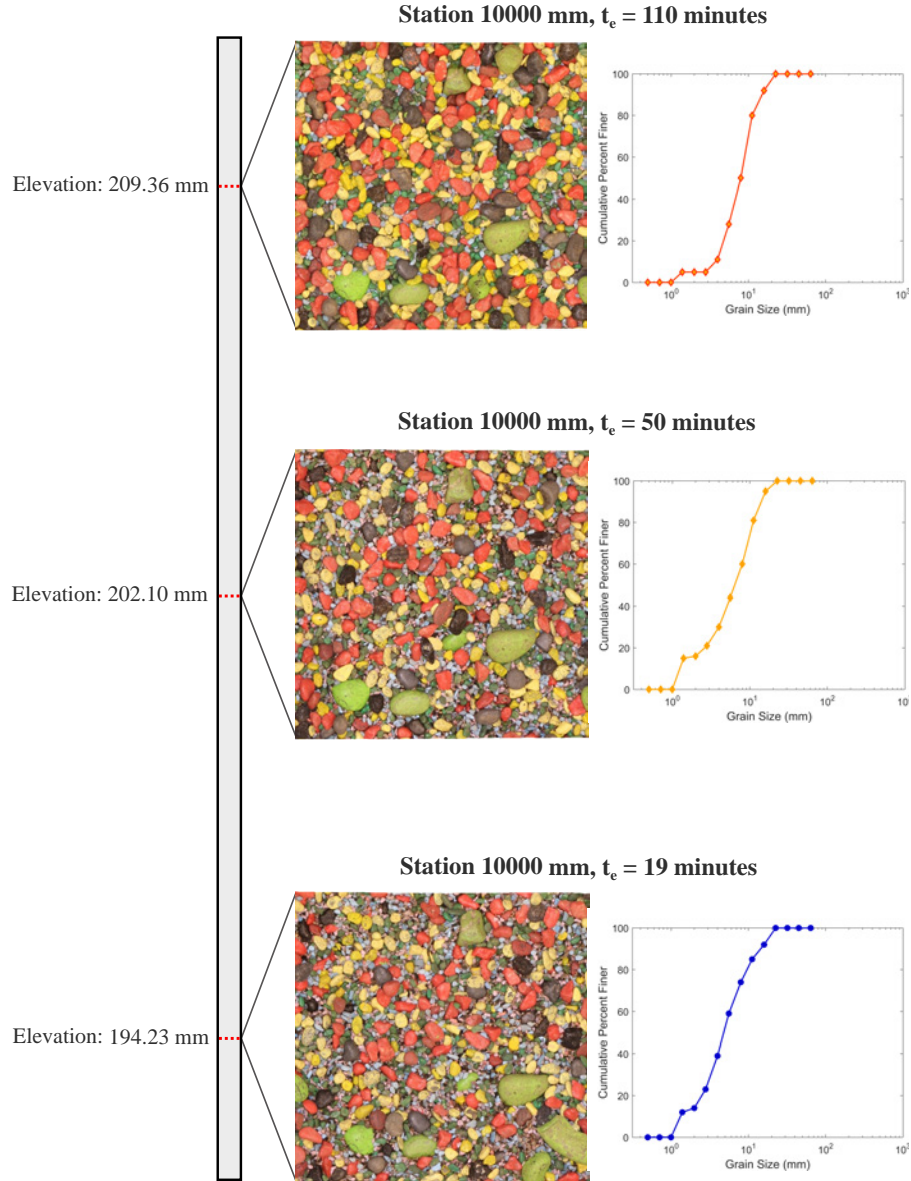


**Figure 5.3:** Example bed sediment texture data used to build stratigraphic column at station 10000 mm for  $t_e = 19, 50$  and 110 minutes. Note that these three times correspond to sequential periods of sediment deposition, and hence bed elevation increases. This temporal behavior corresponds to rule 1 discussed on page 102.

We begin determination of  $s_{es}$  by associating each value of  $s_n$  with its corresponding relative average bed elevation  $\bar{\eta}$ , resulting in pairs of values at each subsampling location  $x_j$ , and for each time  $t_n$ :  $(s_n, \bar{\eta})_{x_j, t_n}$ . At the end of this process we have 29 value pairs for each subsampling location, and are ready to determine  $s_{es}$ . Figure 5.1c indicates that the exchange surface lies at the interface between the subsurface and the active layer. Therefore, we use four different rules to assign a value to  $s_{es}$  at each subsampling location  $x_j$  and for each observation time  $t_n$ :

1. For sequential observations of deposition during the initial experimental phase (see Fig-

ures 3.4 and 4.2) at any  $x_j$ , the value of  $s_{es}$  for time  $t_n$  is assigned the value of  $s_a$  for time  $t_{n-1}$ . This means that the exchange surface distribution at  $t_n$  is assumed to reflect the recently buried active layer distribution. An example of this rule is subsampling location 10000 mm, which is shown as an example in Figure 5.3.

2. For sequential observations of entrainment during the initial experimental phase at any  $x_j$ , the value of  $s_{es}$  for time  $t_n$  is assigned the value of  $s_{us}$ , as long as the average bed elevation at time  $t_n$  is lower than it was at time  $t_{n-1}$ . This means that the exchange surface distribution at  $t_n$  is assumed to reflect the bed subsurface material that has not been reworked by the flow. This distribution matches the upstream supply distribution. An example of this rule is subsampling location 8000 mm
3. For cycles of deposition and entrainment during the initial experimental phase at any  $x_j$ , the value of  $s_{es}$  is assigned the value of  $s_a$  for the nearest, preceding elevation that is higher than the elevation at  $t_n$ . This assumes that during the best matching preceding time, the bed was built by a distribution that was uniform in time over the depositional time interval.
4. For the repeat experimental phase (see Figures 3.4 and 4.2), stratigraphy constructed during the initial phase is replaced by newly constructed stratigraphy as the bed subsurface is reworked. Otherwise, we apply the previous 3  $s_{es}$  assignment rules depending on average bed elevations dynamics.

We then determine  $\delta_2$  with the values for  $s_{us}$ ,  $s_b$  and  $s_{es}$  using Equation 5.18.

#### Calculation of $U_b$

We determine the rate of topographic adjustment  $U_b$  for each subsampling location and observational time as:

$$U_b \approx \frac{\bar{\eta}_{x_j,t_n} - \bar{\eta}_{x_j,t_{n-1}}}{t_n - t_{n-1}} \approx \left. \frac{\Delta \bar{\eta}}{\Delta t} \right|_{t_n:t_{n-1}}, \quad (5.22)$$

where  $\bar{\eta}$  is the local average bed elevation at  $t = n$  and  $t = n - 1$ .

#### Calculation of $U_p$

We determine the corresponding grain size adjustment rate  $U_p$  as:

$$U_p \approx \frac{D_{90_{us}} - D_{90_{x_j},t_n}}{t_n - t_{init}} \approx \left. \frac{\Delta D_{90}}{\Delta t} \right|_{t_n:t_r}, \quad (5.23)$$

where  $D_{90_{us}}$  is drawn from the experimental sediment supply, and  $t_{init}$  is the starting time for each flow sequence of PRE1 (Table 3.1; Figure 5.4b). Therefore,  $t_n - t_{init}$  is a cumulative time for each flow sequence. Equation 5.23 reflects the fact that the local bed surface texture ultimately adjusts to the composition of the upstream sediment supply as equilibrium is approached.

### Calculation of $N_e$

With Equations 5.18, 5.22 and 5.23, we approximate the channel response number for PRE1 as:

$$N_e \approx \left| \left( \frac{s_b - s_{es}}{s_{us}} \right)_{t_n} \frac{\Delta \bar{\eta}_{t_n:t_{n-1}}}{\Delta D_{90,t_n:t_{init}}} \frac{\Delta t_{t_n-t_{init}}}{\Delta t_{t_n-t_{n-1}}} \right| \quad (5.24)$$

As applied here, Equation 5.24 states that the local channel response is the product of three ratios:

1. The first ratio quantifies the magnitude of difference between local grain size distributions and the upstream supply distribution;
2. The second ratio quantifies the magnitude of difference between the speed of topographic and surface roughness adjustment; and
3. The third ratio quantifies the difference between the surface roughness adjustment time scale, and the time increment of observation.

From the three ratios, it is evident that as equilibrium is approached, the grain size and speed ratios decline in magnitude, and the time scale ratio increases.

## 5.4 Results

Figure 5.4 illustrates evolution of the sediment flux  $Q_{sf}$  (b),  $N_t$  (c),  $N_p$  (d),  $\delta_2$  (e) and  $N_e$  (f) for PRE1. Each quantity is plotted against the dimensionless time  $t_o$ , defined as the ratio of the elapsed time  $t_e$  to the activation time  $t_a$ . In the top panel (a) we show the supply of water ( $Q_w$ ), and the light and darker gray vertical fill areas in panels (b)–(f) indicate when supplies change. Within panel (b), we show the times associated with the initial and a repeat experimental phases, which extend from  $t_o = 0$ –23.9, and  $t_o = 23.9$ –43.5, respectively; at the top of panel (b), we indicate the associated response regimes as either the start-up ( $t_a$ ), transient ( $t_t$ ), steady-state or response to steady-state ( $t_r$ ) periods. The character of each regime was presented in Section 4.3.1, and here we provide a summary recap of each regime, and follow that with description according to  $N_t$ ,  $N_p$ ,  $\delta_2$  and  $N_e$ . For  $N_t$  (c),  $N_p$  (d),  $\delta_2$  (e) and  $N_e$  (f), we show the mean as well as 10th and 90th percentile value trends; for  $N_e$  (f) we also provide the median and geometric mean value trends.

The start-up period defines the beginning of PRE1, running from  $t_o = 0$  to  $t_o = 1$ , termed the activation time ( $t_a$ ) (Figure 5.4b).  $t_a$  characterizes initial redistribution of sediment along the experimental channel in response to coupling between downstream changes in (1) width and (2) average flow speed. The transient regime ( $t_t$ ) reflects the adjustment of bed topography and sediment texture to the upstream supplies, leading to the first steady-state, defined above in Section 5.2 as average topographic steadiness, and mass balance. The initial phase ( $t_t$ ) extends from  $t_o = 1$ –19.5. A total of six SSs occur during PRE1, at  $t_o = 19.5, 21.7, 23.9, 39.2, 41.4$  and 43.5. The response to steady-state  $t_r$  captures how the channel responds to changes

in upstream water and sediment supplies from a SS condition. A total of five  $t_r$  periods occur during PRE1 (Figure 5.4b).

#### 5.4.1 Topographic and sediment texture response numbers: $N_t$ and $N_p$

$N_t$  drops one-order of magnitude during the activation time from a high of  $\approx 10^{-2}$ , and by the end settles into an approximately steady, to a slight decreasing condition through the initial phase transient period (Figure 5.4c). Just before steady-state at  $t_o = 19.5$ ,  $N_t$  drops to a low of roughly  $10^{-3.2}$  (mean response).  $N_t$  rises abruptly to a peak during the first response to a SS period, and then drops almost as rapidly to the second steady-state condition. Again,  $N_t$  rises during the second response to SS period, but not as rapidly as during the first, reaches a peak, and then drops to a value similar in magnitude to that at the end of the first response period, marking the third steady-state. The 10th and 90th percentile responses are consistent with the mean response during the initial phase, and bound a response range that spans roughly one-order of magnitude. The repeat phase behavior of  $N_t$  is similar to that of the initial phase, excluding the start-up period, including the strong narrowing of overall response about half-way through, similar SS values, and within a comparable value range. The difference is that 10th percentile response departs from the mean at  $t_o = 28$  (Figure 5.4c).

$N_p$  drops more than one-order of magnitude during the activation time from a high of order  $10^{-2}$ , and continues to steadily drop during the initial phase transient period to a low of  $10^{-3.2}$  (Figure 5.4d), marking conditions at the first SS (mean response).  $N_p$  rises strongly to a peak during the first response to SS period, and then drops to the second steady-state condition. Again,  $N_p$  rises during the second response to SS period, reaches a peak, and then drops to the third steady-state, and to a value almost one-order of magnitude higher compared to that of the first SS. The 10th and 90th percentile responses are consistent with the mean response during the initial phase, and reflect a tight variational range of 1.5 to  $2N_p$ . The repeat phase behavior of  $N_p$  is similar to that of the initial phase, excluding the start-up period, including comparable SS values. A key difference is that the repeat phase first response to SS period ends ( $t_o = 39.2$ ) at a value about  $2N_p$  higher than the value at the first SS (Figure 5.4d).

#### 5.4.2 Sediment texture $\delta_2$

$\delta_2$  mean is unresponsive during the activation period, maintaining a value of roughly  $10^0$  (Figure 5.4e). The 10th and 90th percentile values drop and increase, however.  $\delta_2$  rises quickly at the beginning of the initial phase transient period, reaching a peak of  $10^{0.8}$  at  $t_o=2.2$  (mean value). Following this peak  $\delta_2$  drops to a value of  $10^0$ , where it remains until the first SS. Relatively small increases occur after the first and second SSs, with equally minor decreases to the next SS conditions. The repeat phase behavior is similar to the initial phase during the first response to SS, but exhibits larger responses during subsequent response to SS periods, comparatively After the fourth SS,  $\delta_2$  rises rapidly to a value of  $10^{0.7}$ , then falls to a value at the fifth SS consistent with the second SS. After the fifth SS,  $\delta_2$  rises rapidly to a value of  $10^1$ ,

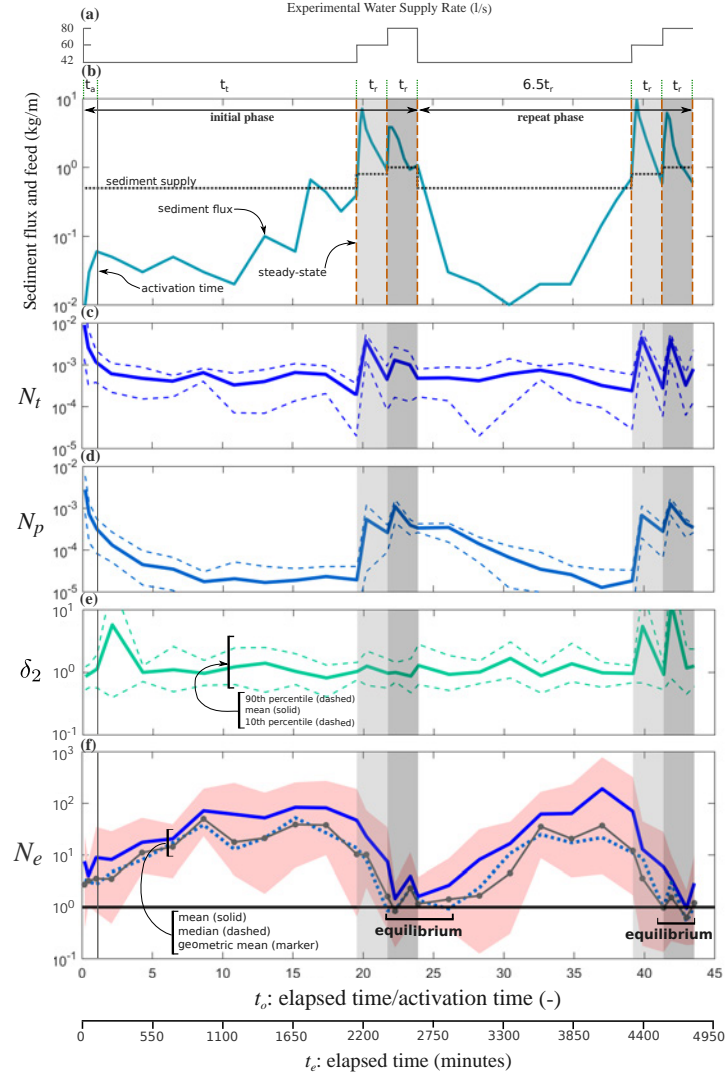


**Figure 5.4:** Summary of  $Q_{sf}$ ,  $N_t$ ,  $N_p$ ,  $\delta_2$  and  $N_e$  for PRE1, vs. the dimensionless time  $t_o$ , defined as the ratio of elapsed time  $t_e$  to the activation time  $t_a$ .  $N_t$  determined with 5.11,  $N_p$  and  $\delta_2$  with 5.14, and  $N_e$  with Equation 5.24. (a) Water supply rate. (b) Sediment supply rate and flux. The initial experimental phase occurred from dimensionless time 0 to roughly 24, and the repeat phase from 24 to 43. Activation ( $t_a$ ) and transient ( $t_t$ ) periods indicated at the top of (b). Steady-state occurred on six separate occasions during PRE1, as indicated by the position of the vertical dashed lines. Evolution of (c)  $N_t$ , (d)  $N_p$ , (e)  $\delta_2$  and (f)  $N_e$  during PRE1. Evolution consisted of start-up, transient, steady-state and response to steady-state phases. See text for explanation of each phase. The solid lines in (c), (d) and (e) are the means for 29 observational times across PRE1. The dashed lines below and above the solid lines shown in (c), (d) and (e) illustrate the 10th and 90th percentile responses, respectively. The mean (solid line), median (dashed line) and geometric mean (line with marker) responses of  $N_e$ . The range of  $N_e$  responses between the 10th and 90th percentile values is also provided as the red shaded region.

one order of magnitude higher than that following the second SS, and then falls again to a value similar to the third SS. The 10<sup>th</sup> and 90<sup>th</sup> percentiles generally cover a value of range of one-half order of magnitude during the initial and repeat phases (Figure 5.4e).

### 5.4.3 Channel response number: $N_e$

Behavior of the channel response number  $N_e$  is generally in contrast to  $N_t$  and  $N_p$ , and is sensitive to  $\delta_2$ , when it is large relative to the ratio ( $N_t/N_p$ ).  $N_e$  begins the activation period with a mean value of  $10^0.3$ , and ends with a mean value of approximately  $10^0.1$ . From the start of the initial phase transient period,  $N_e$  rises steadily until  $t_o=8.6$ , drops somewhat until  $t_o=10.8$ , and then increases to a peak mean value of 23.0 at  $t_o=17.4$ , with a corresponding median value of 21.9, and geometric mean of 20. Following this peak,  $N_e$  declines steadily to the end of the initial phase transient period, and occurrence of the first SS at  $t_o = 19.2$ , achieving a mean value of 5.3, a median of 6.7 and geometric mean of 3.6.

$N_e$  continues to decline through the first response to SS period, and has a mean value of 2.4 at the second steady-state, a median of 1.6 and a geometric mean of 1.5. The declining trend continues to  $t_o=22.3$ , achieving a low during the initial phase with a mean value of 1.7, and a median and geometric mean of 1.0.  $N_e$  then rises thereafter through most of the second response to SS period of the initial phase, with a mean value of 2.5 at the third SS, a median of 2.0 and a geometric mean of 2.0. The repeat phase exhibits generally similar behavior compared to the initial phase, rising to the middle of the first response to SS at  $t_o = 32.6$ , and falling thereafter to a repeat phase low at the fifth SS, with values of  $O(1)$ . The channel response number at the last SS achieves a slightly higher value to that for the 3<sup>rd</sup> SS, 4.5 vs. 2.5, respectively. More specifically though, there are a few differences between the initial and repeat phases.  $N_e$  peaks earlier during the first response to SS period of the repeat phase, as compared to the initial phase transient period, and  $N_e$  responds during the last response to SS of the repeat phase with an up–down–up cycle, which is not exhibited during the second response to SS.

The 10<sup>th</sup> and 90<sup>th</sup> percentile value range generally approaches or slightly exceeds one-order of magnitude during most of PRE1, and rises and falls with the mean values (Figure 5.4f). Two episodes of greater than one order of magnitude value range occurs during PRE1, one each during the initial and repeat phases:  $t_o = 10.8$ –13.0 and  $t_o = 28.3$ –30.5. We suggest that equilibrium conditions occur around the second, and fifth and sixth SSs, during which time  $N_e \approx O(1)$ . Furthermore, steadily declining  $N_e$  values leading up to both equilibrium cases indicates conditions throughout the experimental channel were evolving toward equivalence between the topographic and texture velocities,  $U_b$  and  $\delta_2 U_p$ , respectively.

### 5.4.4 Results summary

In summary, results show that  $N_t$  and  $N_p$  respond in a consistent way during PRE1, evolving from highs at  $t_o = 0$ , to lows at the first steady-state.  $N_t$  and  $N_p$  are responsive to flow and sed-

iment supply increases, generally showing rapid rises to peaks immediately following supply changes, with steady decline thereafter to the next steady-state.  $N_t$  and  $N_p$  show overall consistency between the initial and repeat phases.  $\delta_2$  on the other hand responds along generally different trajectories compared to  $N_t$  and  $N_p$ . Immediately following the activation period,  $\delta_2$  peaks, falls rapidly, and then maintains basically a uniform response until the fourth SS, at which point it exhibits an up–down–up–down cycle that ranges over one order of magnitude.

$N_e$  integrates these three signals into a generally predictable response pattern, rising to highs during the relatively long first transient and third SS response periods, and thereafter trending toward  $O(1)$  values, which suggests equilibrium conditions during the subsequent SS response periods.

## 5.5 Discussion

The combined results of Figure 5.4 indicates that our mass balance derived topographic, particle and channel response numbers for river segments of approximate length  $w'$ , Equations 5.11, 5.14 and 5.24, respectively, provide reasonable results and may be of use in a broader context. Specifically, the results highlight two questions: First, how do the bed and particle velocities,  $U_b$  and  $\delta_2 U_p$ , respectively, contribute to equilibrium conditions during development of the pool-riffle and roughened channel structures discussed in Chapter 4? And second, how does our view of fluvial equilibrium in terms of  $N_e$  help clarify equilibrium and distinguish it from SS?

### 5.5.1 Local contributions to equilibrium conditions during pool-riffle and roughened channel development and maintenance

Figure 5.4f shows that the time rate of change of topography governs pool-riffle and roughened channel development for PRE1 during the initial phase transient period  $t_t$ , and the repeat phase first response to steady-state period  $6.5t_r$ . During these times, the average mobility condition  $\tau/\tau_{ref}$  is characteristically low, ranging from 1.20–1.60 (Table 4.1), where  $\tau$  is the average bed stress, calculated as  $\tau = \rho_w C_d \bar{U}_x^2$ , and  $\tau_{ref}$  is the reference critical mobility stress for the bed surface median particle diameter  $D_{50}$  (see Chapter 3.2.2 for complete description). When topography governs the equilibrium condition  $N_e$ ,  $U_b$  ranges from a factor 2–10 times larger than  $U_p$ , given that  $\delta_2$  is generally uniform with an approximate value of 1 throughout (Figures 5.4c, 5.4d and 5.4e). Hence, at lower relative mobility conditions, the primary adjustment response to pool-riffle and roughened channel development is through the construction of topography, and bed surface texture, or roughness, plays a less important role.

A different dynamic, however, is evident at higher relative mobility conditions  $\tau/\tau_{ref}$  (Table 4.1), following the SSs that result from the initial phase transient period  $t_t$ , and the repeat phase first response period  $6.5t_r$  (Figure 5.4). During the first and second SS response periods, the bed and particle velocities approach equivalence, and maintain a ratio of roughly 3.0. At  $t_0 = 22.3$ , however, a mean value of 1.7 is observed, which from the mean trend of the

preceding data, suggests that conditions are evolving to equilibrium. The mean trend of  $\delta_2$  throughout this time generally fluctuates around a value of 1.0, highlighting that adjustments of the grain size fractions which contribute to the bed surface texture  $f_a$  remains uniform, and does not affect  $N_e$ .

During the fourth and fifth SS response periods, the bed and particle velocities again approach equivalence, but for these times  $\delta_2$  has a large effect on the equilibrium conditions  $N_e$ . Figures 5.4c, 5.4d and 5.4e show that when topographic and particle velocities spike,  $\delta_2$  also spikes, because the local bedload supply and exchange surface standard deviations are comparable. When the topographic and particle velocities drop,  $\delta_2$  does as well, and tends to values of 1.0. It is during these relaxations that  $N_e$  also approaches a value of 1.0, indicating that equilibrium is achieved for the mean trend.

These findings are important, because in contrast to the lower mobility conditions, at higher mobility the adjustment response to pool-riffle and roughened channel maintenance is shared equally between topography and bed surface texture. Specifically, texture adjustment occurs primarily through bed surface coarsening, with an increase in the  $D_{90}$  grain size throughout much of the experimental channel for the higher mobility periods (see Figure 4.2). This response is expected within channels of gravel and cobble composition, due to preferential entrainment of finer grain sizes to balance mobility over the entire distribution (e.g. *Parker and Klingeman, 1982*), or when the upstream supply of sediment is reduced (e.g. *Dietrich et al., 1989*). In the present case, both of these effects play a role.

### 5.5.2 Local and channel response numbers: a new view of fluvial equilibrium

We conceptualize the local processes that contribute to equilibrium conditions along relatively straight mountain streams as depositional and entrainment filters, which alter the upstream sediment supply by driving local storage or depletion of sediment particles, until flow and mobility conditions support mass continuity (Figure 5.1). Because the depositional filter relates to the local bed topography, and the entrainment filter to the local bed surface texture, we constructed our view of fluvial equilibrium from mass conservation considerations for the bulk riverbed, and the particle fractions making up the riverbed. Our construct is consistent with *Ahnert (1994)*'s focus on mass budgets, and also builds from *Howard (1982)*'s emphasis on equilibrium, or grade, reflected in mutual adjustments of the channel gradient and flow characteristics.

From scaling  $\eta$ ,  $t$ ,  $q_b$ ,  $x$  and  $f_a$ , we propose that local equilibrium and disequilibrium is described by the ratio of the bed and particle velocities,  $U_b$  and  $\delta_2 U_p$ , respectively. Our proposal builds on the existing view that equilibrium is a problem of sediment continuity, expressed by longitudinal profiles that are just capable of transporting the upstream sediment supply, known as the graded river profile (*Gilbert, 1877; Mackin, 1948*). Whereas we use this view to build Equation 5.24, we augment it to account for textural adjustments, or sorting processes, which matter at the local scale. Recognizing the importance of texture and sorting to fluvial

equilibrium complements the analogous emphasis detailed by *Paola and Seal (1995)* for the problem of downstream sediment fining.

Taken together, the results presented in Figures 4.8, 4.11 and 5.4 show that the occurrence of equilibrium defined by Equation 5.24 is characterized by channel width conditions that varies by a factor 2, a grain size distribution that spans 0.5–32 mm, and for local bed slopes  $S_{local}$  that range on average from adverse downstream values of 3%, to positive downstream values of almost 6%. These varied morphodynamic conditions are a solid test of our formal equilibrium statement, defined as  $N_e = U_b / \delta_2 U_p$ . More importantly, our new view may offer a link to help bridge established work on equilibrium at larger spatial scales *Sternberg (1875)*; *Gilbert (1877)*; *Mackin (1948)*; *Langbein and Leopold (1964)*; *Snow and Slingerland (1987)*; *Paola et al. (1992)*; *Bolla Pittaluga et al. (2014)*; *Blom et al. (2016)*, with that focused on local conditions (*Ferrer-Boix et al., 2016*). First, our framework can be incorporated into numerical models to evaluate equilibrium at a wide range of spatial and temporal scales, and for an equally broad set of driving conditions. Second, it is possible that our approach can yield estimates of the time scale needed for a river reach of many channel widths to reach equilibrium. Although, specifying this time scale may require different choices for the characteristic scales, the exercise would yield an outcome that augments the basin-scale equilibrium times presented by *Howard (1982)*; *Paola et al. (1992)*.

## 5.6 Conclusions

We use theory and scaling arguments to demonstrate that the ratio of the bed and sediment particle velocities,  $U_b$  and  $\delta_2 U_p$ , defines fluvial (dis)equilibrium conditions, and that equilibrium, specifically, is achieved when the velocity ratio is  $O(1)$ . For PRE1, this occurs for relatively high sediment mobility conditions, when the rate of bed surface coarsening is comparable to the rate of topographic adjustment, and notably does not include a significant affect from the local sediment sorting state  $\delta_2$ . This finding suggests an important point which connects with findings from Chapter 4: equilibrium along channel reaches of variable width can occur under conditions of spatially non-uniform bed surface sediment texture. This highlights the intrinsic link between local bed topography and surface roughness, which adjusts and emerges in response to locally-driven flow velocity conditions. Hence, equilibrium is not restricted to spatially uniform bed surface sediment distributions.

Our results further indicate that for lower sediment mobilities, local adjustments of bed topography govern the (dis)equilibrium condition, and that this affect continues after mass continuity is achieved. Notably, the post-continuity period of topographic influence on (dis)equilibrium occurs for time scales that are at least 30% of the time necessary for continuity to emerge. This finding motivates an important expectation: watersheds with rainfall dominated hydrology will process water and/or sediment supply perturbations relatively quickly, vs. watersheds of snow-melt driven hydrology, for which equilibrium time scales are comparatively long. The lag between mass continuity and equilibrium also highlights a key characteristic of fluvial

processes, which is obscured by defining statistical steady-state in terms of continuity. After continuity is achieved, processes that build bed shapes and topography, as well as bed sediment textures, are still at work, further adjusting to local conditions, albeit, at smaller and smaller rates, as (dis)equilibrium conditions trend toward a velocity ratio of  $O(1)$ .

Last, PRE1 sediment flux  $Q_{sf}$  exhibits consistent rates of relaxation toward continuity following four separate episodes of water and sediment supply increases. General rate consistency suggests an  $e$ -fold time of  $t_o \approx 0.5$  or less, or approximately 1 hour under experimental conditions. Using that the  $e$ -fold time is the time necessary for a perturbation to diminish by  $\sim 37\%$  of its initial value (*Slingerland and Kump, 2011*), the supply perturbations of PRE1 are completely processed within  $t_o \approx 2.0$ – $2.5$ , or 6 to 8 hours under high mobility experimental conditions. With a time scaling of  $L_r/U_r \approx 2.5$ , which is based on Froude scaling discussed in Chapter 3, we obtain an approximate perturbation relaxation time scale of order 20 hours for high mobility conditions, and natural cases of comparable dimension and character to the East Creek field site. In Chapter 2 we found that bed sediment texture conditions of a pool-riffle pair along a small mountain stream in the Santa Cruz Mountains, CA, U.S., required three floods to recover from a sediment texture disturbance driven by an approximate 20-year flood (Table 2.4). Sediment mobilization durations for typical rainfall hydrographs along this small mountain stream are less than 24 hours, highlighting reasonable consistency between experimental and field conditions.

## Chapter 6

# Concluding remarks

The aim of my thesis was to build understanding of how pool-riffles form and are maintained along channel segments of variable width. I was specifically interested in characterizing the mechanical coupling between width conditions, local bed topography and bed surface texture. Accordingly, one of my main goals was to build a physical explanation for the widely reported spatial correlations between channel width and pools at points of narrowing, and riffles at points of widening. In this chapter I provide a summary of the main findings from my work, and I discuss future directions motivated by these findings.

### 6.1 Summary

Chapter 3 presents the use of non-parametric statistics and self-organizing maps (SOM) to examine and characterize riffle texture trends across 11 sediment mobilizing floods. The subject pool-riffle has occurred in its present form and location for at least 14 years, and therefore the work provides insight on pool-riffle maintenance through riffle texture adjustment. I show that net riffle head elevation is stationary during the study period, and that riffle texture responds to each flood, but generally maintains a coarse riffle center of gravels (2–64 mm) and cobbles (64–256 mm), and finer lateral margins of sand (<2 mm), with one exception. The largest flood drove fining of much of the riffle surface, as demonstrated by the McNemar contingency test completed for each sampling transect, and the SOMs. Riffle fining persisted for two subsequent floods, and the third event saw texture conditions recover to those measured at the beginning of the field study. I also show that pool sediment storage responds to each flood, exhibiting a range of conditions. The major result and finding of this study is that non-parametric statistics and SOM can be used to characterize the role of riffle texture adjustment for pool-riffle maintenance. Topographically stationary pool-riffles are maintained, in part, through riffle textural adjustments which occur at a frequency equal to that of sediment mobilizing floods. Furthermore, textural adjustments are spatially and temporally organized, suggesting that sediment transport patterns are conditioned at the scale of a pool-riffle pair.

In Chapter 4, I build from the Chapter 3 field study and present experimental and theoret-

ical results on pool-riffle formation along a variable width channel. The experiments produce pool, riffle and roughened channel bed structures, which I show to collocate with channel segments which are narrowing and widening, and which exhibit negligible width change, respectively. Continuity shows that flows accelerate to construct pools, decelerate to construct riffles, and generally uniform flows yield roughened channels. I demonstrate that local channel bed slopes for my experiments, one additional experiment and a numerical study are organized along a systematic trend across the range of width gradients from  $(-0.30)$ – $(+0.30)$ . Notably, the reach-average bed slopes for the three data sets vary by one order of magnitude. These results motivated development of a mathematical model which indicates that slope construction is controlled by the ratio of two velocities. The velocity ratio  $\Lambda$  represents two characteristic time scales: the time scale for bed surface sediments to spread a length scale  $L$  under gravity, vs. the time scale of momentum flux delivery to the bed surface. Application of the model to the local bed slope data sets reveals that pools form when the spreading time scale is characteristically large, and riffles form when it is small. Each formative condition is associated with a suggested threshold width gradient.

In Chapter 5, I present a new definition of fluvial equilibrium based on mass conservation statements for the bulk riverbed, and the particle size fractions which comprise the riverbed. The final equilibrium statement is obtained by nondimensionalizing the conservation statements and specifying scales for elevation, time, length, bedload transport and bed surface grain size fractions. Similar to Chapter 4, I find that fluvial equilibrium conditions are described by a ratio of two velocities. The velocity ratio  $N_e$ , or equilibrium condition, represents the speed at which the bed surface increases or decreases in height, and the speed at which bed surface grain sizes change fractional composition, through grain size population fining or coarsening. Application of  $N_e$  to my experimental data shows that these two speeds more readily exhibit comparable values, and hence the local channel is in equilibrium, when sediment mobility conditions are relatively high. This result is consistent with findings from Chapter 3, which highlights the importance of riffle texture adjustment for pool-riffle maintenance. Last,  $N_e$  permits variable bed surface grain sizes between pools, riffles and roughened channel segments at equilibrium, which, foregoing the equilibrium aspect, is consistent with many observational data sets of natural streams *Lisle (1979)*; *de Almeida and Rodríguez (2011)*; *Caamaño et al. (2012)*; *Hodge et al. (2013)*; *Papangelakis and Hassan (2016)*.

## 6.2 Future directions

### Application to river restoration design

The results of Chapter 4 have implications for river restoration design strategies and approaches. Specifically, Figure 4.11 suggests that it is possible to determine the average residual length scale of pools, riffles and roughened channel segments for variable width channels, relative to the reach-average longitudinal bed slope. Having a simple method to predict the aver-

age residual length scale will benefit restoration design, because it helps to reduce uncertainty involving the average bed profile conditions of a particular design concept. The common way to achieve this presently is through numerical simulations, which are costly and time intensive to perform. Furthermore, a simulation is restricted to a particular design concept, as opposed to a range of possible conditions.

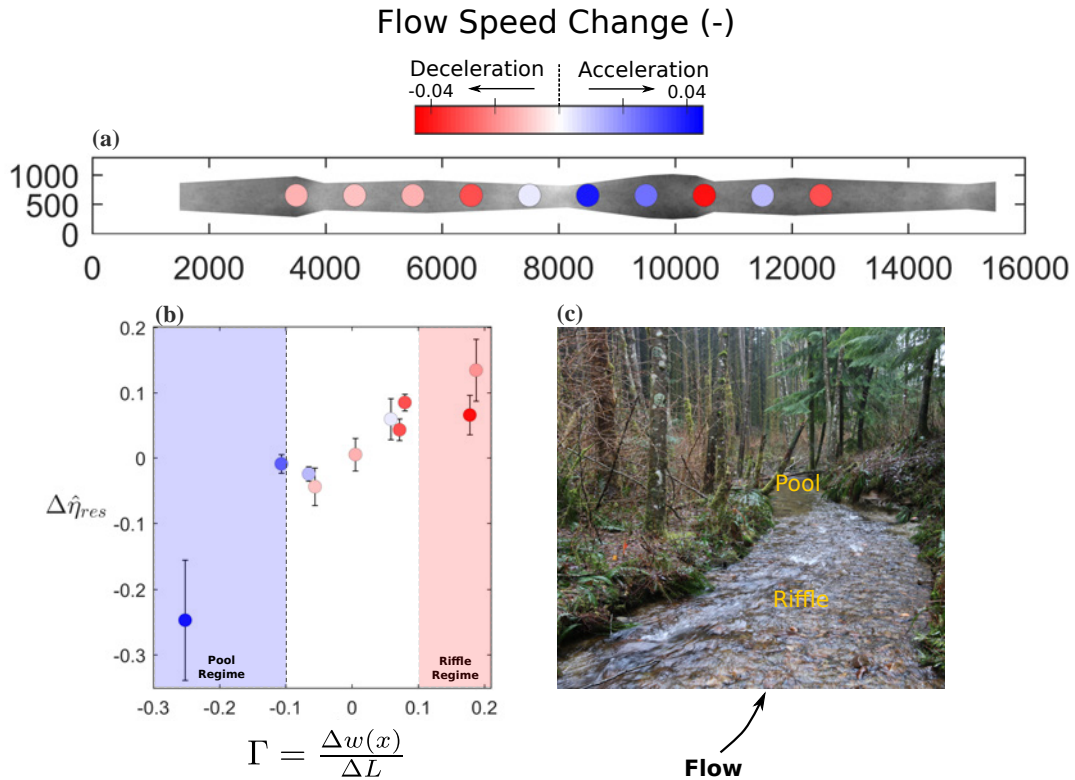


**Figure 6.1:** Observations of residual depths for PRE1 determined from zero-crossing profiles. (a) Average bed topography for the six PRE1 steady-state conditions with the average change in downstream flow speed, depicted by the circle colors. Flow speed change plotted half-way between bounding differencing stations. (b) Residual depth for 10 locations shown in (a), determined from the zero-crossing profiles computed for observations 1–29 (Table 3.1). Error bars are the sample standard deviation for the observations. (c) Photography of a pool-riffle along East Creek, near Maple Ridge, BC. Pool-riffle location spatially correlated with narrow and wide channel segments, respectively.

In Figure 6.1, I show the average downstream change in the residual length scale  $\Delta \bar{\eta}$  vs. the downstream change in width, determined for subsampling locations of PRE1. The residual length scale was determined from the average zero-crossing trend line for PRE1, and residual lengths are normalized by the average total elevation loss across the PRE1 experimental channel. In Table 6.1 I provide the normalized residual lengths for each subsampling location of PRE1. Figure 6.1 shows that the normalized downstream change in residual length varies directly with the downstream change in channel width, suggesting the residual lengths can be

**Table 6.1:** Mean values of normalized residual depth  $\bar{\eta}_x$  for subsampling locations

Subsampling Locations										
3000	4000	5000	6000	7000	8000	9000	10000	11000	12000	13000
0.1047	-0.0298	0.0140	0.0086	-0.0765	-0.1361	0.1108	0.1197	0.0537	0.0780	0.0347

1.  $\bar{\eta}_x$  calculated from observations 1–29 for PRE1
2.  $\bar{\eta}_x$  normalized by the average total elevation loss across the PRE1 experimental channel.
4.  $\bar{\eta}_x$  calculated from the associated average zero-crossing trend line for PRE1.

projected for a given width condition. The normalized change in residual length scales ranges from -25% within the pool at station 8000 mm, to roughly +10% in the riffles at station 10000 and 3000 mm. My goal is to use the theory presented in Chapter 4 to develop a straightforward design methodology for pool-riffles of variable width channels.

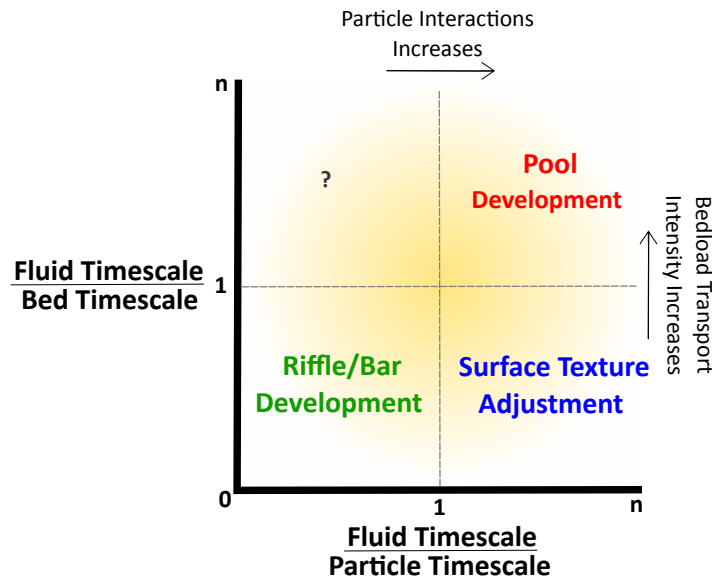


**Figure 6.2:** Concept mountain streambed architecture regime diagram. The x-axis is the ratio of the flow to the particle time scales and the y-axis is the ratio of the flow to the bed time scales.

### Identifying a mountain streambed architecture regime diagram

Equations 4.7 and 5.16 highlight that the dynamics of pool-riffle formation, and equilibrium condition are expressed through characteristic time scales, which describe how the bed, particles and the flow participate in development of channel bed architecture. Furthermore, from Figures 4.11, 4.12 and 5.4 we understand that pools, riffles and roughened channel structures exhibit a likely range of time scales that are particular to each channel bed response. As a

result, we hypothesize that the channel bed, particles and flow time scales can be used to develop of mountain stream bed architecture regime diagram. A concept of the diagram is shown in Figure 6.2, where I plot the ratio of the flow to the particle time scales on the x-axis, and the ratio of the flow to the bed time scales on the y-axis. My hypothesis proposes that:

1. Riffles occur when the flow time scale is small relative to the particle or bed time scales. This regime is characterized by minor net bedload transport intensities of partial mobility, or Stage II or Phase II transport conditions per *Ashworth and Ferguson (1989)* and *Hassan et al. (2005)*, respectively.
2. Roughened channel segments with patches, clusters and surface structuring occur when the flow and particle time scales are comparable, but the flow time scale remains small relative to the bed time scale. Therefore, particle-particle interactions are relatively large, but bedload intensity remains in the partial-mobility condition.
3. Pools occur when the flow, particle and bed time scales are comparable, providing relatively high particle-particle interactions, and high rates of bedload transports, or Stage III or Phase III transport conditions per *Ashworth and Ferguson (1989)* and *Hassan et al. (2005)*, respectively.

I have developed flow time scales from the Navier-Stokes Equation, with the next step to determine particle and bed time scales from the work of Chapters 4 and 5.



**Figure 6.3:** Photograph of an inverted pool-riffle channel segment along the Bridge River, near Camoo Creek Road, BC, Canada. A landslide during the summer 2015 delivered coarse sediment and willow trees to the channel, narrowing the channel at the delivery point by 60%, and resulting in an upstream backwatered pool, and riffle through the landslide deposit.

### Identifying a unified pool-riffle formation hypothesis

The work of Chapter 4 lays the groundwork to develop a unified pool-riffle formation hypothesis, and on which accounts for both the entrainment- and depositionally-driven formative mechanisms. Furthermore, the formative hypothesis would need to account for the not

uncommon observation of pools at points of widening, and riffles at points of narrowing, as shown in Figure 6.3, which I call inverted pool-riffle topography. I hypothesize that inverted cases can be explained using morphodynamic simulations, and can be shown to have a tendency to evolve to cases where pools collocate with points of narrowing, and riffles with points of widening, as discussed and examined here.

# Bibliography

- Aberle, J., and V. Nikora (2006), Statistical properties of armored gravel bed surfaces, *Water Resources Research*, 42(11), doi : 10.1029/2005WR004674.
- Acreman, M., A. H. Arthington, M. J. Colloff, C. Couch, N. D. Crossman, F. Dyer, I. Overton, C. A. Pollino, M. J. Stewardson, and W. Young (2014a), Environmental flows for natural, hybrid, and novel riverine ecosystems in a changing world, *Frontiers in Ecology and the Environment*, 12(8), 466–473, doi : 10.1890/130134.
- Acreman, M. C., I. C. Overton, J. King, P. J. Wood, I. G. Cowx, M. J. Dunbar, E. Kendy, and W. J. Young (2014b), The changing role of ecohydrological science in guiding environmental flows, *Hydrological Sciences Journal*, 59(3-4), 433–450, doi : 10.1080/02626667.2014.886019.
- Ahnert, F. (1994), Equilibrium, scale and inheritance in geomorphology, *Geomorphology*, 11(2), 125–140, doi : [http://dx.doi.org/10.1016/0169-555X\(94\)90077-9](http://dx.doi.org/10.1016/0169-555X(94)90077-9).
- Ancey, C., and J. Heyman (2014), A microstructural approach to bed load transport: mean behaviour and fluctuations of particle transport rates, *Journal of Fluid Mechanics*, 744, doi : 10.1017/jfm.2014.74.
- Ashida, K., and M. Michiue (1972), Study on hydraulic resistance and bedload transport rate in alluvial streams, *Transactions of the Japan Society of Civil Engineers*, 206, 59–69.
- Ashworth, P. J., and R. I. Ferguson (1989), Size-selective entrainment of bed load in gravel bed streams, *Water Resources Research*, 25(4), 627–634, doi : 10.1029/WR025i004p00627.
- Beechie, T. J., and T. H. Sibley (1997), Relationships between channel characteristics, woody debris, and fish habitat in northwestern Washington streams, *Transactions of the American Fisheries Society*, 126(2), 217–229, doi : 10.1577/1548-8659(1997)126<0217:RBCCWD>2.3.CO;2.
- Bishop, C. (2006), *Pattern Recognition and Machine Learning*, Springer, New York, NY, USA.
- Blom, A., E. Viparelli, and V. Chavarrías (2016), The graded alluvial river: Profile concavity and downstream fining, *Geophysical Research Letters*, 43(12), 6285–6293, doi : 10.1002/2016GL068898.
- Bolla Pittaluga, M., R. Luchi, and G. Seminara (2014), On the equilibrium profile of river beds, *Journal of Geophysical Research: Earth Surface*, 119(2), doi : 10.1002/2013JF002806.
- Booker, D., D. Sear, and A. Payne (2001), Modelling three-dimensional flow structures and patterns of boundary shear stress in a natural pool-riffle sequence, *Earth Surface Processes and Landforms*, 26(5), 553–576, doi : 10.1002/esp.210.

- Brabb, E. E. (1989), Geologic Map of Santa Cruz County, California: A digital database, *Tech. rep.*, United States Geological Survey.
- Brown, R. A., and G. B. Pasternack (2017), Bed and width oscillations form coherent patterns in a partially confined, regulated gravel–cobble-bedded river adjusting to anthropogenic disturbances, *Earth Surface Dynamics*, 5(1), 1–20, doi:10.5194/esurf-5-1-2017.
- Buffington, J. M., and D. R. Montgomery (1997), A systematic analysis of eight decades of incipient motion studies, with special reference to gravel-bedded rivers, *Water Resources Research*, 33(8), 1993–2029, doi:10.1029/96WR03190.
- Buffington, J. M., and D. R. Montgomery (1999a), Effects of sediment supply on surface textures of gravel-bed rivers, *Water Resources Research*, 35(11), P. 3523, doi:199910.1029/1999WR900232.
- Buffington, J. M., and D. R. Montgomery (1999b), Effects of hydraulic roughness on surface textures of gravel-bed rivers, *Water Resources Research*, 35(11), 3507, doi:10.1029/1999WR900138.
- Buffington, J. M., W. E. Dietrich, and J. W. Kirchner (1992), Friction angle measurements on a naturally formed gravel streambed: Implications for critical boundary shear stress, *Water Resources Research*, 28(2), P. 411, doi:199210.1029/91WR02529.
- Buffington, J. M., T. E. Lisle, R. D. Woodsmith, and S. Hilton (2002), Controls on the size and occurrence of pools in coarse-grained forest rivers, *River Research and Applications*, 18(6), 507–531, doi:10.1002/rra.693.
- Bunte, K., S. R. Abt, J. P. Potyondy, and K. W. Swingle (2009), Comparison of three pebble count protocols (EMAP, PIBO, and SFT) in two mountain gravel-bed streams, *JAWRA Journal of the American Water Resources Association*, 45(5), 1209–1227, doi:10.1111/j.1752-1688.2009.00355.x.
- Caamaño, D., P. Goodwin, and J. M. Buffington (2012), Flow structure through pool-riffle sequences and a conceptual model for their sustainability in gravel-bed rivers, *River Research and Applications*, 28(3), 377–389, doi:10.1002/rra.1463.
- Cao, Z., P. Carling, and R. Oakey (2003), Flow reversal over a natural pool-riffle sequence: a computational study, *Earth Surface Processes and Landforms*, 28(7), 689–705, doi:10.1002/esp.466.
- Carling, P. (1991), An appraisal of the velocity-reversal hypothesis for stable pool-riffle sequences in the river severn, England, *Earth Surface Processes and Landforms*, 16(1), 19–31, doi:10.1002/esp.3290160104.
- Carling, P., and H. Orr (2000), Morphology of riffle-pool sequences in the River Severn, England, *Earth Surface Processes and Landforms*, 25(4), 369–384.
- Carling, P., and N. Wood (1994), Simulation of flow over pool-riffle topography: A consideration of the velocity reversal hypothesis, *Earth Surface Processes and Landforms*, 19(4), 319–332, doi:10.1002/esp.3290190404.
- Chartrand, S. M., and P. J. Whiting (2000), Alluvial architecture in headwater streams with special emphasis on step-pool topography, *Earth Surface Processes and Landforms*, 25(5), 583–600.

- Chartrand, S. M., M. Jellinek, P. J. Whiting, and J. Stamm (2011), Geometric scaling of step-pools in mountain streams: Observations and implications, *Geomorphology*, 129(1-2), 141–151, doi:10.1016/j.geomorph.2011.01.020.
- Chartrand, S. M., M. A. Hassan, and V. Radić (2015), Pool-riffle sedimentation and surface texture trends in a gravel bed stream, *Water Resources Research*, 51(11), doi:10.1002/2014WR016259.
- Cherkassky, V., and F. Mulier (1998), *Learning from Data*, Wiley, New York, NY, USA.
- Chin, A. (2002), The periodic nature of step-pool mountain streams, *American Journal of Science*, 302(2), 144–167, doi:10.2475/ajs.302.2.144.
- Chorley, R. J., R. P. Beckinsale, and A. J. Dunn (2009), *The History of the Study of Landforms Or the Development of Geomorphology: Geomorphology Before Davis Vol. 1*, Routledge Revivals: the History of the Study of Landforms Series, 678 pp., Routledge.
- Church, M. (2006), Bed material transport and the morphology of alluvial river channels, *Annual Review of Earth and Planetary Sciences*, 34(1), 325–354, doi:10.1146/annurev.earth.33.092203.122721.
- Church, M., and R. I. Ferguson (2015), Morphodynamics: Rivers beyond steady state, *Water Resources Research*, 51(4), doi:10.1002/2014WR016862.
- Church, M., and D. Jones (1982), Channel bars in gravel-bed rivers. In: Hey, R.D., Bathurst, J.C. and Thorne, C.R., Gravel-bed Rivers, *Gravel-bed rivers*, pp. 291–338.
- Church, M., and A. Zimmermann (2007), Form and stability of step-pool channels: Research progress, *Water Resources Research*, 43(3), doi:10.1029/2006WR005037.
- Church, M., D. McLean, and J. Walcott (1987), River bed gravels: sampling and analysis, in *Sediment Transport in Gravel-Bed Rivers*, edited by C. R. Thorne, J. Bathurst, and R. D. Hey, pp. 43–87, John Wiley and Sons, Chichester.
- Church, M., M. A. Hassan, and J. F. Wolcott (1998), Stabilizing self-organized structures in gravel-bed stream channels: Field and experimental observations, *Water Resources Research*, 34(11), 3169–3179, doi:10.1029/98WR00484.
- Clark, J. C. (1966), *Tertiary stratigraphy of the Felton-Santa Cruz area, Santa Cruz Mountains, California*, 184 pp., Dept. of Geology, Stanford University.
- Clayton, J., and J. Pitlick (2007), Spatial and temporal variations in bed load transport intensity in a gravel bed river bend, *Water Resources Research*, 43(2), WO2426, doi:10.1029/2006WR005253.
- Clifford, N. (1993a), Formation of rifflepool sequences: field evidence for an autogenetic process, *Sedimentary Geology*, 85(1-4), 39–51.
- Clifford, N. (1993b), Differential bed sedimentology and the maintenance of riffle-pool sequences, *CATENA*, 20(5), 447–468.
- Clifford, N., and K. Richards (1992), The reversal hypothesis and the maintenance of riffle-pool sequences: a review and field appraisal, in *Lowland Floodplain Rivers: Geomorphological Perspectives*, edited by P. A. Carling and G. E. Petts, pp. 43–70, Wiley, Chichester.

- Conover, W. J. (1980), *Practical Nonparametric Statistics*, 2nd ed ed., 493 pp., Wiley, New York.
- Cui, Y., and G. Parker (1997), A quasi-normal simulation of aggradation and downstream fining with shock fitting, *Int. J. Sediment Res*, 12(2), 68–82.
- de Almeida, G. A. M., and J. F. Rodríguez (2011), Understanding pool-riffle dynamics through continuous morphological simulations, *Water Resources Research*, 47(1), W01,502, doi:10.1029/2010WR009170.
- de Almeida, G. A. M., and J. F. Rodríguez (2012), Spontaneous formation and degradation of pool-riffle morphology and sediment sorting using a simple fractional transport model, *Geophysical Research Letters*, 39(6), L06,407, doi:10.1029/2012GL051059.
- Dietrich, W. E., and J. D. Smith (1984), Bedload transport in a river meander, *Water Resources Research*, 20(10), 1355–1380.
- Dietrich, W. E., and P. J. Whiting (1989), Boundary shear stress and sediment transport in river meanders of sand and gravel, in *River Meandering. Water Resources Monograph 12.*, pp. 1–50, American Geophysical Union, Washington.
- Dietrich, W. E., J. W. Kirchner, H. Ikeda, and F. Iseya (1989), Sediment supply and the development of the coarse surface layer in gravel-bedded rivers, *Nature*, 340(6230), 215–217, doi:10.1038/340215a0.
- Dietrich, W. E., P. Nelson, E. Yager, J. G. Venditti, M. P. Lamb, and L. Collins (2005), Sediment patches, sediment supply, and channel morphology, in *4th Conference on River, Estuarine, and Coastal Morphodynamics, A.A. Balkema Publishers, Rotterdam*, edited by G. Parker and M. Garcia, pp. 79–90, Taylor and Francis, London.
- Dolan, R., A. Howard, and D. Trimble (1978), Structural control of the rapids and pools of the colorado river in the grand canyon., *Science (New York, N.Y.)*, 202(4368), 629–31, doi:10.1126/science.202.4368.629.
- du Buat, L. (1786), *Principles D'hydraulique et de Pyrodynamique Verifies Par un Grand Nombre D'experiences Faites par Ordre du Gouvernement*, 2nd, vol. ed., Firmin Didot, Paris.
- Duró, G., A. Crosato, and P. Tassi (2016), Numerical study on river bar response to spatial variations of channel width, *Advances in Water Resources*, 93, Part A, 21–38, doi:http://dx.doi.org/10.1016/j.advwatres.2015.10.003.
- Edwards, T. K., and G. D. Glysson (1988), *Field Methods for Measurement of Fluvial Sediment: Techniques of Water-Resources Investigations Series 03-C2*, 89 pp., Department of the Interior, US Geological Survey.
- Einstein, H. A. (1950), *The Bed-load Function for Sediment Transportation in Open Channel Flows (Google eBook)*, 71 pp., U.S. Department of Agriculture.
- Emmett, W. W. (1980), *Field Calibration of the Sediment-trapping Characteristics of the Helley-Smith Bedload Sampler*, geological ed., 44 pp., Washington: US Government Printing Office.
- Emmett, W. W. (1999), Quantification of channel-maintenance flows for gravel-bed rivers, in *Wildland Hydrology*, edited by D. Olsen and J. P. Potyondy, tps-99-3 ed., pp. 77–84, American Water Resources Association, Herndon, VA.

- Emmett, W. W., and M. G. Wolman (2001), Effective discharge and gravel-bed rivers, *Earth Surface Processes and Landforms*, 26(13), 1369–1380, doi : 10.1002/esp.303.
- Exner, F. (1925), Über die Wechselwirkung zwischen Wasser und Geschiebe in ussen, *Sitzungsbericht Akad. Wiss. Wien*, (Abt. 2a), 165–203.
- Ferrer-Boix, C., S. M. Chartrand, M. A. Hassan, J. P. Martín-Vide, and G. Parker (2016), On how spatial variations of channel width influence river profile curvature, *Geophysical Research Letters*, 43(12), 6313–6323, doi : 10.1002/2016GL069824.
- Folk, R. L. (1966), A Review of grain-size parameters, *Sedimentology*, 6(2), 73–93, doi : 10.1111/j.1365-3091.1966.tb01572.x.
- Furbish, D. J. (1998), Irregular bed forms in steep, rough channels: 1. Stability analysis, *Water Resources Research*, 34(12), 3635–3648, doi : 10.1029/98WR02339.
- Furbish, D. J., S. D. Thorne, T. C. Byrd, J. Warburton, J. J. Cudney, and R. W. Handel (1998), Irregular bed forms in steep, rough channels: 2. Field observations, *Water Resources Research*, 34(12), 3649–3659, doi : 10.1029/98WR02338.
- Furbish, D. J., P. K. Haff, J. C. Roseberry, and M. W. Schmeeckle (2012), A probabilistic description of the bed load sediment flux: 1. Theory, *Journal of Geophysical Research: Earth Surface*, 117(F3), doi : 10.1029/2012JF002352.
- Furbish, D. J., M. W. Schmeeckle, R. Schumer, and S. L. Fathel (2016), Probability distributions of bed load particle velocities, accelerations, hop distances, and travel times informed by Jaynes’s principle of maximum entropy, *Journal of Geophysical Research: Earth Surface*, 121(7), 1373–1390, doi : 10.1002/2016JF003833.
- Gilbert, G. (1877), *Geology of the Henry Mountains*, 160 pp., Government Printing Office, Washington, D.C.
- Gill, M. (1983a), Diffusion model for aggrading channels, *Journal of Hydraulic Research*, 21(5), 355–367, doi : 10.1080/00221688309499457.
- Gill, M. (1983b), Diffusion model for degrading channels, *Journal of Hydraulic Research*, 21(5), 369–378, doi : 10.1080/00221688309499458.
- Guglielmini, G. (1697), *Della Natura de Fiumi, Trattato Fisico-Mathematica*, Bologna.
- Harrelson, C. C., C. L. Rawlins, and J. P. Potyondy (1994), *Stream Channel Reference Sites: an Illustrated Guide to Field Technique*, 67 pp., Department of Agriculture Rocky Mountain Research Station.
- Harrison, L., and E. Keller (2007), Modeling forced poolriffle hydraulics in a boulder-bed stream, southern California, *Geomorphology*, 83(3-4), 232–248, doi : 10.1016/j.geomorph.2006.02.024.
- Hassan, M. A., and M. Church (2000), Experiments on surface structure and partial sediment transport on a gravel bed, *Water Resources Research*, 36(7), 1885–1895, doi : 10.1029/2000WR900055.
- Hassan, M. A., M. Church, and A. P. Schick (1991), Distance of movement of coarse particles in gravel bed streams, *Water Resources Research*, 27(4), 503–511, doi : 10.1029/90WR02762.

- Hassan, M. A., M. Church, T. E. Lisle, F. Brardinoni, L. Benda, and G. E. Grant (2005), Sediment transport and channel morphology of small, forested streams, *JAWRA Journal of the American Water Resources Association*, 41(4), 853–876, doi:10.1111/j.1752-1688.2005.tb03774.x.
- Hassan, M. A., B. J. Smith, D. L. Hogan, S. Luzi, David, A. E. Zimmerman, and B. C. Eaton (2008), Sediment storage and transport in coarse bed streams: scale considerations, in *Gravel-Bed Rivers VI: From Process Understanding to River Restoration*, edited by H. Habersack, H. Piegay, and M. Rinaldi, chap. 18, pp. 473–496, Elsevier B.V., doi:10.1016/S0928-2025(07)11137-8.
- Henderson, F. M. (1966), *Open Channel Flow*, Macmillan series in civil engineering, 522 pp., Macmillan.
- Hilton, S., and T. E. Lisle (1993), Measuring the fraction of pool volume filled with fine sediment, *Res. Note PSW-RN-414, USDA For.*, 11p.
- Hirano, M. (1971), River-bed degradation with armoring, *Proceedings of the Japan Society of Civil Engineers*, 1971(3), 55–65.
- Hodge, R., D. Sear, and J. Leyland (2013), Spatial variations in surface sediment structure in riffle-pool sequences: a preliminary test of the Differential Sediment Entrainment Hypothesis (DSEH), *Earth Surface Processes and Landforms*, 38(5), 449–465, doi:10.1002/esp3290.
- Hoey, T. B., and R. Ferguson (1994), Numerical simulation of downstream fining by selective transport in gravel bed rivers: Model development and illustration, *Water Resources Research*, 30(7), 2251–2260, doi:10.1029/94WR00556.
- Howard, A. D. (1982), Equilibrium and time scales in geomorphology: Application to sand-bed alluvial streams, *Earth Surface Processes and Landforms*, 7(4), 303–325, doi:10.1002/esp.3290070403.
- Hugemann, W. (2010), Correcting lens distortions in digital photographs, *Ingenieurbüro Morawski+ Hugemann: Leverkusen, Germany*, p. 12.
- Jackson, W. L., and R. L. Beschta (1982), A model of two-phase bedload transport in an Oregon coast range stream, *Earth Surface Processes and Landforms*, 7(6), 517–527, doi:10.1002/esp.3290070602.
- Juez, C., C. Ferrer-Boix, J. Murillo, M. A. Hassan, and P. García-Navarro (2016), A model based on Hirano-Exner equations for two-dimensional transient flows over heterogeneous erodible beds, *Advances in Water Resources*, 87, 1–18, doi:http://dx.doi.org/10.1016/j.advwatres.2015.10.013.
- Kaski, S., J. Kangas, and T. Kohonen (1998), Bibliography of self-organizing map (SOM) papers: 1981–1997, *Neural Comput. Surv.*, 1, 102–350.
- Keller, E. A. (1971), Areal Sorting of Bed-Load Material: The Hypothesis of Velocity Reversal, *Geological Society of America Bulletin*, 82(3), 753.
- Keller, E. A., and W. N. Melhorn (1978), Rhythmic spacing and origin of pools and riffles, *Geological Society of America Bulletin*, 89(5), 723.

- Kirchner, J. W., W. E. Dietrich, F. Iseya, and H. Ikeda (1990), The variability of critical shear stress, friction angle, and grain protrusion in water-worked sediments, *Sedimentology*, 37(4), 647–672, doi:10.1111/j.1365-3091.1990.tb00627.x.
- Kohonen, T. (1982), Self-organising formation of topologically correct feature maps, *Biological Cybernetics*, 43, 59–69.
- Kohonen, T. (2001), *Self-Organizing Maps*, 528 pp. pp., Springer, New York.
- Kondolf, G. M. (2000), Assessing salmonid spawning gravel quality, *Transactions of the American Fisheries Society*, 129(1), 262–281, doi:10.1577/1548-8659(2000)129<0262:ASSGQ>2.0.CO;2.
- Kondolf, G. M., and M. G. Wolman (1993), The sizes of salmonid spawning gravels, *Water Resources Research*, 29(7), 2275–2285, doi:10.1029/93WR00402.
- Langbein, W. B., and L. B. Leopold (1964), Quasi-equilibrium states in channel morphology, *American Journal of Science. Journal Science*, 262(6), 782–794.
- Leo, G. W. (1961), The plutonic and metamorphic rocks of Ben Lomond Mountain, Santa Cruz County, Ph.D. thesis.
- Leopold, L., and T. Maddock (1953), *The hydraulic geometry of stream channels and some physiographic implications*, 64 pp., U.S. Govt. Print. Off., Washington.
- Leopold, L., and M. G. Wolman (1957), *River Channel Patterns: Braided, Meandering, and Straight*, 85 pp.
- Leopold, L. B., M. G. Wolman, and J. P. Miller (1964), *Fluvial Processes in Geomorphology*.
- Lisle, T. E. (1979), A sorting mechanism for a riffle-pool sequence, *Geological Society of America Bulletin*, 90(7), 1142–1157.
- Lisle, T. E. (1986), Stabilization of a gravel channel by large streamside obstructions and bedrock bends, Jacoby Creek, northwestern California, *Geological Society of America Bulletin*, 97(8), 999–1011.
- Lisle, T. E., and S. Hilton (1992), The volume of fine sediment in pools: an index of sediment supply in gravel-bed streams, *Journal of the American Water Resources Association*, 28(2), 371–383.
- Lisle, T. E., and S. Hilton (1999), Fine bed material in pools of natural gravel bed channels, *Water Resources Research*, 35(4), 1291–1304, doi:10.1029/1998WR900088.
- Lisle, T. E., and M. A. Madej (1992), Spatial Variation in Armouring in a Channel with High Sediment Supply, in *Dynamics of Gravel Bed Rivers*, edited by C. R. T. & P. T. P. Billi, R. D. Hey, pp. 277–293, John Wiley & Sons, Ltd.
- Lisle, T. E., F. Iseya, and H. Ikeda (1993), Response of a channel with alternate bars to a decrease in supply of mixed-size bed load: A Flume Experiment, *Water Resources Research*, 29(11), 3623–3629, doi:10.1029/93WR01673.
- Liu, Y., R. Weisberg, and C. Mooers (2006), Performance evaluation of the Self-Organizing Map for feature extraction, *J. Geophys. Res.*, 111, C05,018, doi:10.1029/2005jc003117.

- MacKenzie, L. G., and B. C. Eaton (2017), Large grains matter: contrasting bed stability and morphodynamics during two nearly identical experiments, *Earth Surface Processes and Landforms*, pp. n/a—n/a, doi:10.1002/esp.4122.
- Mackin, J. (1948), Concept of the graded river, *Geological Society of America Bulletin*, 59(5), 463–512, doi:10.1130/0016-7606(1948)59[463:COTGR]2.0.CO;2.
- MacVicar, B., and J. Best (2013), A flume experiment on the effect of channel width on the perturbation and recovery of flow in straight pools and riffles with smooth boundaries, *Journal of Geophysical Research: Earth Surface*, 118(3), 1850–1863, doi:10.1002/jgrf.20133.
- MacVicar, B., and C. Rennie (2012), Flow and turbulence redistribution in a straight artificial pool, *Water Resources Research*, 48(2), doi:10.1029/2010WR009374.
- MacVicar, B., and A. Roy (2011), Sediment mobility in a forced riffle-pool, *Geomorphology*, 125(3), 445–456, doi:10.1016/j.geomorph.2010.10.031.
- MacVicar, B., and A. G. Roy (2007), Hydrodynamics of a forced riffle pool in a gravel bed river: 1. Mean velocity and turbulence intensity, *Water Resources Research*, 43(12), doi:10.1029/2006WR005272.
- MacWilliams, M., J. Wheaton, G. Pasternack, R. Street, and P. Kitanidis (2006), Flow convergence routing hypothesis for pool-riffle maintenance in alluvial rivers, *Water Resources Research*, 42(10), doi:10.1029/2005WR004391.
- Massey, F. (1951), The Kolmogorov-Smirnov test for goodness of fit, *Journal of the American Statistical Association*, 46(253), 68–78, doi:10.1080/01621459.1951.10500769.
- Masteller, C. C., and N. J. Finnegan (2017), Interplay between grain protrusion and sediment entrainment in an experimental flume, *Journal of Geophysical Research: Earth Surface*, 122, doi:10.1002/2016JF003943.
- Melton, M. A. (1962), Methods for measuring the effect of environmental factors on channel properties, *Journal of Geophysical Research*, 67(4), 1485–1490, doi:10.1029/JZ067i004p01485.
- Meyer-Peter, E., and R. Muller (1948), Formulas for bed-load transport, in *2nd Congress International Association of Hydraulic Research (I.A.H.R.)*, Stockholm.
- Montgomery, D. R., and J. M. Buffington (1997), Channel-reach morphology in mountain drainage basins, *Geological Society of America Bulletin*, 109(5), 596–611, doi:10.1130/0016-7606(1997)109.
- Montgomery, D. R., J. M. Buffington, R. D. Smith, K. M. Schmidt, and G. Pess (1995), Pool spacing in forest channels, *Water Resources Research*, 31(4), 1097–1105, doi:10.1029/94WR03285.
- Nelson, P., J. G. Venditti, W. E. Dietrich, J. W. Kirchner, H. Ikeda, F. Iseya, and L. S. Sklar (2009), Response of bed surface patchiness to reductions in sediment supply, *Journal of Geophysical Research*, 114(F2), doi:10.1029/2008JF001144.
- Nelson, P., W. E. Dietrich, and J. G. Venditti (2010), Bed topography and the development of forced bed surface patches, *Journal of Geophysical Research: Earth Surface*, 115(F4), doi:10.1029/2010JF001747.

- Nelson, P., D. Bellugi, and W. E. Dietrich (2012), Delineation of river bed-surface patches by clustering high-resolution spatial grain size data, *Geomorphology*, doi:10.1016/j.geomorph.2012.06.008.
- Nelson, P., A. K. Brew, and J. A. Morgan (2015), Morphodynamic response of a variable-width channel to changes in sediment supply, *Water Resources Research*, 51(7), 5717–5734, doi:10.1002/2014WR016806.
- Oja, M., S. Kaski, and T. Kohonen (2002), Bibliography of Self-Organizing Map (SOM) papers: 19982001 addendum, *Neural Comput. Surv.*, 3, 1–156, doi:10.1093/ml/71.2.257.
- Ouchi, S. (1985), Response of alluvial rivers to slow active tectonic movement, *Geological Society of America Bulletin*, 96(4), 504–515, doi:10.1130/0016-7606(1985)96<504:ROARTS>2.0.CO;2.
- Paola, C., and R. Seal (1995), Grain size patchiness as a cause of selective deposition and downstream fining.pdf, doi:94WR02975.
- Paola, C., and V. R. Voller (2005), A generalized Exner equation for sediment mass balance, *Journal of Geophysical Research*, 110(F4), F04,014, doi:10.1029/2004JF000274.
- Paola, C., P. L. Heller, and C. L. Angevine (1992), The large-scale dynamics of grain-size variation in alluvial basins, 1: Theory, *Basin Research*, 4(2), 73–90, doi:10.1111/j.1365-2117.1992.tb00145.x.
- Papangelakis, E., and M. A. Hassan (2016), The role of channel morphology on the mobility and dispersion of bed sediment in a small gravel-bed stream, *Earth Surface Processes and Landforms*, 41(15), 2191–2206, doi:10.1002/esp.3980.
- Parker, G. (1990), Surface-based bedload transport relation for gravel rivers, *Journal of Hydraulic Research*, 28(4), 417–436, doi:10.1080/00221689009499058.
- Parker, G. (1991), Selective sorting and abrasion of river gravel. II: Applications, *Journal of Hydraulic Engineering*, 117(2), 150–171, doi:10.1061/(ASCE)0733-9429(1991)117:2(150).
- Parker, G. (2007), *1D Sediment Transport Morphodynamics with Applications to Rivers and Turbidity Currents*.
- Parker, G. (2008), Transport of gravel and sediment mixtures, in *Sedimentation Engineering: Theory, Measurements, Modeling and Practice (ASCE Manuals and Reports on Engineering Practice No. 110)*, edited by M. Garcia, chap. 3, pp. 165–251, ASCE, Reston, VA.
- Parker, G., and P. C. Klingeman (1982), On why gravel bed streams are paved, *Water Resources Research*, 18(5), 1409, doi:10.1029/WR018i005p01409.
- Parker, G., and P. R. Wilcock (1993), Sediment feed and recirculating flumes: fundamental difference, *Journal of Hydraulic Engineering*, 119(11), 1192–1204, doi:10.1061/(ASCE)0733-9429(1993)119:11(1192).
- Parker, G., C. Paola, and S. Leclair (2000), Probabilistic Exner sediment continuity equation for mixtures with no active layer, *Journal of Hydraulic Engineering*, 126(11), 818–826, doi:10.1061/(ASCE)0733-9429(2000)126:11(818).

- Parker, G., C. M. Toro-Escobar, M. Ramey, and S. Beck (2003), Effect of Floodwater Extraction on Mountain Stream Morphology, *Journal of Hydraulic Engineering*, 129(11), 885–895, doi: 10.1061/(ASCE)0733-9429(2003)129:11(885).
- Pasternack, G. B., M. K. Bounrisavong, and K. K. Parikh (2008), Backwater control on rifflepool hydraulics, fish habitat quality, and sediment transport regime in gravel-bed rivers, *Journal of Hydrology*, 357(1-2), 125–139, doi:10.1016/j.jhydrol.2008.05.014.
- Phillips, C. B., and D. J. Jerolmack (2016), Self-organization of river channels as a critical filter on climate signals, *Science*, 352(6286), 694–697, doi:10.1126/science.aad3348.
- Pickup, G., and W. A. Rieger (1979), A conceptual model of the relationship between channel characteristics and discharge, *Earth Surface Processes*, 4(1), 37–42, doi:10.1002/esp.3290040104.
- Poff, N. N., J. D. Allan, M. B. Bain, J. R. Karr, K. L. Prestegard, B. D. Richter, R. E. Sparks, and J. C. Stromberg (1997), The natural flow regime, *BioScience*, 47(11), 769–784, doi:10.2307/1313099.
- Radić, V., and G. Clarke (2011), Evaluation of IPCC models performance in simulating late 20th century climatologies and weather patterns over North America, *J. Clim.*, 24, 5257–5274, doi:10.1175/JCLI-D-11-00011.
- Rantz, S. E. (1971), Precipitation depth-duration-frequency relations for the San Francisco Bay region, California, *United States Geological Survey research*, pp. C237–C241.
- Repetto, R., M. Tubino, and C. Paola (2002), Planimetric instability of channels with variable width, *Journal of Fluid Mechanics*, 457, 79–109, doi:10.1017/S0022112001007595.
- Richards, K. S. (1976a), Channel width and the riffle-pool sequence, *Geological Society of America Bulletin*, 87(6), 883.
- Richards, K. S. (1976b), The morphology of riffle-pool sequences, *Earth Surface Processes and Landforms*, 1(1), 71–88, doi:10.1002/esp.3290010108.
- Richards, K. S. (1978), Channel geometry in the riffle-pool sequence, *Geografiska Annaler*, 60(12), 23–27, doi:10.2307/520962.
- Sawyer, A. M., G. B. Pasternack, H. J. Moir, and A. a. Fulton (2010), Riffle-pool maintenance and flow convergence routing observed on a large gravel-bed river, *Geomorphology*, 114(3), 143–160, doi:10.1016/j.geomorph.2009.06.021.
- Schmeeckle, M. W., and J. M. Nelson (2003), Direct numerical simulation of bedload transport using a local, dynamic boundary condition, *Sedimentology*, 50(2), 279–301.
- Schneider, J. M., D. Rickenmann, J. M. Turowski, B. Schmid, and J. W. Kirchner (2016), Bed load transport in a very steep mountain stream (Riedbach, Switzerland): Measurement and prediction, *Water Resources Research*, 52(12), 9522–9541, doi:10.1002/2016WR019308.
- Schumm, S. A., S. A. Schumm, J. F. Dumont, and J. M. Holbrook (2002), *Active Tectonics and Alluvial Rivers*, Cambridge University Press, Cambridge, UK.

- Sear, D. (1996), Sediment transport processes in pool-riffle sequences, *Earth Surface Processes and Landforms*, 21(3), 241–262, doi:10.1002/(SICI)1096-9837(199603)21:3<241::AID-ESP623>3.0.CO;2-1.
- Shields, A. (1936), Anwendung der Ähnlichkeits-Mechanik und der Turbulenz-forschung auf die Geschiebebewegung, *Preussische Versuchsanstalt für Wasserbau und Schiffbau*, 26, 524 – 526.
- Slingerland, R., and L. Kump (2011), *Mathematical Modeling of Earth's Dynamical Systems: A Primer*, stu - stud ed., 231 pp., Princeton University Press, Princeton, NJ.
- Snow, R. S., and R. L. Slingerland (1987), Mathematical Modeling of Graded River Profiles, *The Journal of Geology*, 95(1), 15–33.
- Soni, J. P., K. G. Ranga Raju, and R. J. Garde (1980), Aggradation in streams due to overloading, *Journal of the Hydraulics Division*, 106(No. HY1), 117–132.
- Stecca, G., A. Siviglia, and A. Blom (2014), Mathematical analysis of the Saint-Venant-Hirano model for mixed-sediment morphodynamics, *Water Resources Research*, 50(10), 7563–7589, doi:10.1002/2014WR015251.
- Sternberg, H. (1875), Untersuchungen Über Langen-und Querprofil geschiebeführender Flüsse, *Zeitschrift für Bauwesen*, XXV, 483–506.
- Thompson, D. (2001), Random controls on semi-rhythmic spacing of pools and riffles in constriction-dominated rivers, *Earth Surface Processes and Landforms*, 26(11), 1195–1212, doi:10.1002/esp.265.
- Thompson, D. (2010), The velocity-reversal hypothesis revisited, *Progress in Physical Geography*, 35(1), 123–132.
- Thompson, D., and C. McCarrick (2010), A flume experiment on the effect of constriction shape on the formation of forced pools, *Hydrology and Earth System Sciences*, 14, 1321–1330, doi:10.5194/hess-14-1321-2010.
- Thompson, D., J. M. Nelson, and E. Wohl (1998), Interactions between pool geometry and hydraulics, *Water Resources Research*, 34(12), 3673–3681, doi:10.1029/1998WR900004.
- Thompson, D., E. Wohl, and R. Jarrett (1999), Velocity reversals and sediment sorting in pools and riffles controlled by channel constrictions, *Geomorphology*, 27(3-4), 229–241.
- Tritton, D. (1988), *Physical Fluid Dynamics*, 2nd ed., 519 pp., Oxford University Press, Oxford.
- Trujillo-Ortiz, A., R. Hernandez-Walls, and A. Castro-Perez (2004), McNemarextest: McNemar's exact probability test. A MATLAB file.
- Venditti, J., P. Nelson, J. Minear, J. Wooster, and W. Dietrich (2012), Alternate bar response to sediment supply termination, *Journal of Geophysical Research*, 117(F2), F02,039, doi:10.1029/2011JF002254.
- Venditti, J. G., C. D. Rennie, J. Bomhof, R. W. Bradley, M. Little, and M. Church (2014), Flow in bedrock canyons, *Nature*, 513(7519), 534–537.

- Vesanto, J., J. Himberg, E. Alhoniemi, and J. Parhankangas (2000), SOM toolbox for Matlab 5, Helsinki University of Technology, Helsinki, Finland, Rep. A57, *Tech. rep.*
- Viparelli, E., O. Sequeiros, A. Cantelli, P. Wilcock, and G. Parker (2010), River morphodynamics with creation/consumption of grain size stratigraphy 2: numerical model, *Journal of Hydraulic Research*, 48(6), 727–741, doi:10.1080/00221686.2010.526759.
- White, J. Q., G. B. Pasternack, and H. J. Moir (2010), Valley width variation influences rifflepool location and persistence on a rapidly incising gravel-bed river, *Geomorphology*, 121(3-4), 206–221, doi:10.1016/j.geomorph.2010.04.012.
- Whiting, P., J. Stamm, D. Moog, and R. Orndorff (1999), Sediment-transporting flows in headwater streams, *Geological Society of America Bulletin*, 111(3), 450–466, doi:10.1130/0016-7606(1999)111<0450:STFIHS>2.3.CO;2.
- Whiting, P. J., and J. G. King (2003), Surface particle sizes on armoured gravel streambeds: effects of supply and hydraulics, *Earth Surface Processes and Landforms*, 28(13), 1459–1471, doi:10.1002/esp.1049.
- Wiberg, P. L., and J. D. Smith (1985), A theoretical model for saltating grains in water, *Journal of Geophysical Research*, 90(C4), 7341, doi:10.1029/JC090iC04p07341.
- Wiberg, P. L., and J. D. Smith (1987), Calculations of the critical shear stress for motion of uniform and heterogeneous sediments, *Water Resources Research*, 23(8), P. 1471, doi:198710.1029/WR023i008p01471.
- Wilcock, P. R. (2001), Toward a practical method for estimating sediment-transport rates in gravel-bed rivers, *Earth Surface Processes and Landforms*, 26(13), 1395–1408, doi:10.1002/esp.301.
- Wilcock, P. R., and J. C. Crowe (2003), Surface-based transport model for mixed-size sediment, *Journal of Hydraulic Engineering*, 129(2), 120–128, doi:10.1061/(ASCE)0733-9429(2003)129:2(120).
- Wilcock, P. R., and B. W. McArdell (1993), Surface-based fractional transport rates: Mobilization thresholds and partial transport of a sand-gravel sediment, *Water Resources Research*, 29(4), 1297–1312, doi:10.1029/92WR02748.
- Wilcock, P. R., and B. W. McArdell (1997), Partial transport of a sand/gravel sediment, *Water Resources Research*, 33(1), 235–245, doi:10.1029/96WR02672.
- Wilkinson, S. N., I. D. Rutherford, and R. J. Keller (2008), An experimental test of whether bar instability contributes to the formation, periodicity and maintenance of pool-riffle sequences, *Earth Surface Processes and Landforms*, 33(11), 1742–1756, doi:10.1002/esp.1645.
- Williams, G. P. (1978), Bank-full discharge of rivers, *Water Resources Research*, 14(6), 1141–1154, doi:10.1029/WR014i006p01141.
- Wolman, M. G. (1954), A method of sampling coarse river-bed material, *American Geophysical Union Transactions* 35, pp. 951–956, doi:10.1029/TR035i006p00951.
- Wolman, M. G., and J. P. Miller (1960), Magnitude and frequency of forces in geomorphic processes, *The Journal of Geology*, 68(1), 54–74, doi:10.1086/626637.

- Wong, M., and G. Parker (2006), One-dimensional modeling of bed evolution in a gravel bed river subject to a cycled flood hydrograph, *Journal of Geophysical Research: Earth Surface*, 111(F3), n/a–n/a, doi:10.1029/2006JF000478.
- Yalin, M. (1971), On the formation of dunes and meanders, in *Proceedings of the 14th Congress of the International Association for Hydraulic Research*, chap. 3, pp. C101–108, IAHR, Paris.
- Yang, C. T. (1971), Formation of riffles and pools, *Water Resources Research*, 7(6), 1567, doi:10.1029/WR007i006p01567.
- Zimmermann, A. E., M. Church, and M. A. Hassan (2008), Video-based gravel transport measurements with a flume mounted light table, *Earth Surface Processes and Landforms*, 33(14), 2285–2296.

# Appendix A

## Numerical channel evolution model description

### A.1 Summary

A de-coupled numerical model of channel bed evolution was developed following Parker (2007) and Wu (2008). The model consists of four components, which together describe the basic physical processes governing channel evolution:

Step 1: 1D non-uniform hydrodynamics (GVF Solution to Saint Venant Equations);

Step 2: Mixed grain sediment transport (Wilcock-Crowe, 2003);

Step 3: Diffusive bed evolution (Exner Equation);

Step 4: Bed sediment sorting and properties (Hirano Type Exner Equation).

The model uses a finite differences scheme and bed evolution is solved sequentially over a 1D domain in the order presented above, with each step completed prior to moving to the next step. At the end of the four steps the model advances to the next time step and the calculations are completed again. Step 1 determines the shear velocity  $u_*$  and the sediment particle mobility conditions  $\tau^*$ . Step 2 determines the sediment transport rate using  $u_*$  and  $\tau^*$ . Step 3 determines the change in bed elevation over the 1D domain based on the sediment flux gradient in  $x$ . Step 4 determines the fractional composition of the bed surface and flux at each node based on the mass balance of each size fraction, and from this information the bed roughness is determined. Steps 1 through 4 provide the conditions for the next time step. The model is considered an approximate formulation of channel evolution, useful to explore and simulate the problem in a manner consistent with the assumptions used to develop the governing equations for each of the four model components. Principal aspects of channel evolution not addressed by the model include:

1. Flow patterns characterized by lateral and/or vertical motions;
2. Flow properties associated with time independent turbulent motions;
3. Bedload sediment transport patterns defined by lateral motions;
4. Interactions of flow with a rough channel bank;
5. Bed stratigraphy for cycles of erosion and deposition;

## A.2 1D nonuniform hydrodynamic model

Following *Parker (2007)*, the hydrodynamic model solves the 1D mass conservation and steady, nonuniform Saint-Venant equations for incompressible flow of constant density. The 1D water mass conservation statement is:

$$\frac{\partial U_x \bar{d}}{\partial x} = 0, \quad (\text{A.1})$$

where  $U_x$  is the downstream average flow velocity,  $\bar{d}$  is the average water depth and  $x$  is distance along the channel. The 1D momentum conservation statement is:

$$\frac{\partial U_x^2 \bar{d}}{\partial x} = -0.5g \frac{\partial \bar{d}^2}{\partial x} - g \bar{d} \frac{\partial \eta}{\partial x} - C_f U_x^2, \quad (\text{A.2})$$

where  $g$  is the acceleration of gravity on Earth,  $\eta$  is the channel bed elevation and  $C_f$  is a dimensionless bed resistance coefficient. Equation A.2 is simplified with Equation A.1, and by integrating Equation A.1, which yields  $U \bar{d} = q_w = \text{constant}$  (unit flow rate), and:

$$\frac{\partial U}{\partial x} = \frac{q_w}{\bar{d}} \frac{\partial \bar{d}}{\partial x} \quad (\text{A.3})$$

Applying Equation A.1 to A.2 provides:

$$U_x \frac{\partial U_x}{\partial x} = -0.5g \frac{\partial \bar{d}}{\partial x} - g \bar{d} \frac{\partial \eta}{\partial x} - C_f \frac{U_x^2}{\bar{d}} \quad (\text{A.4})$$

Applying Equation A.3 to A.4 and rearranging provides the backwater solution to the Saint-Venant Equations:

$$\frac{\partial \bar{d}}{\partial x} = \frac{S - S_f}{1 - Fr^2}, \quad (\text{A.5})$$

where  $S = -\partial \eta / \partial x$  (channel bed slope),  $S_f = C_f Fr^2$  (friction slope or slope of the total energy line) and  $Fr^2 = (q_w^2 / g \bar{d}^3) = (U_x^2 / g \bar{d})$  ( $Fr$  is the Froude number). For uniform flows,  $S = S_f$ . Equation A.5 is a first-order differential equation requiring one boundary condition in  $\bar{d}$ . Use of the backwater solution assumes that (1) the flow is gradually varying in  $x$  (i.e. the length scale of the pressure term ( $L_x$ ) is therefore assumed to satisfy  $H/L_x \ll 1$ ), and hence the pressure force can be approximated as hydrostatic, with the channel bed surface defining the

local datum; and (2) the viscous stress is negligible, but that a friction force acts at the bed–water interface on the overlying fluid through a drag relation:  $C_f U_x^2$ .

Equation A.5 is solved numerically using the Standard Step Method (STM), with a convergence tolerance of 0.0008 m. The backwater solution does not adequately simulate water depth along pool segments with adverse channel bed slopes. I address this issue with a simple numerical approximation that I call the reduced complexity adverse slope algorithm (RCASA). RCASA locates segments along the numerical domain which exhibit adverse bed slopes, and then it identifies the downstream bed elevation for each segment where the bed slope changes sign. This location is the controlling location, and the bed elevation here determines the residual water depth in the upstream pool until the controlling bed elevation is exceeded at some upstream location  $x$ . The water depth through the pool is approximated as the normal depth ( $h_o$ ) at the controlling location plus an incremental depth based on an estimated pool water surface slope. The normal depth is determined with the Manning-Strickler formulation:

$$h_o = \left( \frac{k_s^{\frac{1}{3}} q_w^2}{\alpha_r^2 g S} \right)^{\frac{3}{10}}, \quad (\text{A.6})$$

where  $\alpha_r$  is a dimensionless quantity assigned a value of 8.1 (*Parker, 2008*),  $k_s = n_k D_{90}$  is a measure of bed roughness using the 90th percentile grain size class, and  $n_k = 2$  (*Parker, 2008*). The pool water surface slope is set by observed associated slopes from pool-riffle experiment 1 (PRE1), which for  $42 \text{ ls}^{-1}$  ranged from 0.5–1%. Lastly, Equation A.5 is limited by cases when the Froude number  $\geq 1$ . To address this shortcoming, water depths for Froude numbers higher than  $\sim 0.9995$  are approximated by the quasi-normal momentum balance (*Cui and Parker, 1997*), for which  $S = S_f$ .

### A.3 Mixed grain sediment transport model

The model uses the *Wilcock and Crowe (2003)* sediment transport function to determine fractional rates of bedload transport for the PRE1 bed surface sediment mixture. The dimensionless W-C function for any grain class  $i$  is defined as:

$$W_i^* = \begin{cases} 0.002\phi^{7.5} & \phi < 1.35 \\ 14 \left( \frac{1-0.894}{\phi^{0.5}} \right)^{4.5} & \phi \geq 1.35, \end{cases} \quad (\text{A.7})$$

where  $\phi$  is a stress ratio ( $\tau/\tau_{r\psi}$ ) of which  $\tau$  is the average bed stress and  $\tau_{r\psi}$  is the average mobilizing reference stress for any size class  $\psi$  of the bed material, where  $\psi = \log_2(D_i)$  and  $D_i$  represents the mean diameter of each grain size class according to the Wentworth scale for half- $\psi$  increments. The average bed stress was determined with the drag equation given

above, and  $C_f$  was determined using the Manning-Strickler formulation:

$$C_f = \frac{1}{\alpha_r^2} \left( \frac{\bar{d}}{k_s} \right)^{-\frac{1}{3}}, \quad (\text{A.8})$$

where  $\alpha_r$  is a dimensionless quantity assigned a value of 8.1 (Parker, 2008),  $\bar{d}$  is the average flow depth determined with the backwater solution discussed above,  $k_s = n_k D_{90}$  is a measure of bed roughness using the 90th percentile grain size class, and  $n_k = 2$  (Parker, 2008). The average mobilizing reference stress is dependent upon a hiding function ( $D_i/D_{50}$ ) and the average mobilizing reference stress for the mean grain size of the surface material ( $\tau_{rs50}$ ) is defined as:

$$\frac{\tau_{ri}}{\tau_{rs50}} = \left( \frac{D_i}{D_{50}} \right)^{b_w}, \quad (\text{A.9})$$

where the exponent  $b_w$  is a fitting parameter dependent on  $D_i/D_{sm}$ :

$$b_w = \frac{0.67}{1 + \exp\left(1.5 - \frac{D_i}{D_{sm}}\right)}, \quad (\text{A.10})$$

and  $D_{sm}$  is the mean grain size of the bed surface material. Wilcock and Crowe (2003) [2003] demonstrated that the average mobilizing reference stress for the mean size class of the surface material ( $\tau_{rm}$ ) is dependent upon the surface sand content:

$$\tau_{rm} = (\rho_s - \rho_w) g D_{sm} [0.021 + 0.015 \exp(-20F_s)], \quad (\text{A.11})$$

where  $\rho_s$  is sediment density, here assumed to be 2.65 g/cm<sup>3</sup>,  $\rho_w$  is the density of fresh water, here assumed to be 1.00 g/cm<sup>3</sup> and  $F_s$  is the percentage of sand in the surface material. The dimensional transport rate for any grain size class  $i$  is computed following an Einstein-type flux:

$$q_{b\psi} = \frac{W_i^* f_a u_*^3}{Rg}, \quad (\text{A.12})$$

where  $q_{b\psi}$  is the fractional sediment flux for grain size class  $\psi$ ,  $f_a$  is the volume probability of  $\psi$  within in the bed surface mixture,  $u_*^3$  is the shear velocity, computed with the Manning-Strickler formulation:

$$u_*^2 = \left( \frac{k_s^{0.33} q_w^2}{\alpha_r^2} \right)^{0.30} (gS)^{0.70}, \quad (\text{A.13})$$

$R$  is the relative density of sediment  $(\rho_s/\rho_w) - 1$ .

## A.4 Channel evolution model

Channel bed evolution is solved with the 1D Exner equation of mass conservation (*Exner, 1925*):

$$\frac{\partial \eta}{\partial t} = -\frac{1}{\varepsilon} \frac{\partial q_b}{\partial x}, \quad (\text{A.14})$$

where  $t$  is time,  $\varepsilon$  is the solid fraction of the bed, and  $q_b$  is the total sediment transport flux. The total sediment fluxes needed to compute the change in bed elevation at each spatial node comes from the previous step, and for all but the upstream and downstream nodes, spatial gradients of sediment flux in  $x$  are determined as central differences. Equation A.14 has, for example, a diffusion type analytical solution which can be found by assuming (1) steady, uniform flow and (2) that sediment transport can be approximated as a simple power law function of average flow velocity, yielding (*Soni et al., 1980; Gill, 1983a,b*):

$$\frac{\partial \eta}{\partial t} = \frac{b q_b}{3\varepsilon} \frac{\partial^2 \eta}{\partial x^2}, \quad (\text{A.15})$$

Provided that the simulations seek projections of channel bed longitudinal profiles, we specify the starting channel bed profile as an appropriate initial condition, and since Equation A.15 is second order, we need two boundary conditions: (1) sediment supply rate at the upstream model boundary and (2) a channel bed elevation at the downstream model outlet.

## A.5 Grain sorting model

The grain sorting model is based on the active layer concept developed by *Hirano (1971)*, as applied by *Parker (1991)*, and as further developed by *Viparelli et al. (2010)*, to the problem of bed surface sediment sorting and mass conservation of the various grain sizes present on the bed surface along a channel profile. The active layer is a relatively thin layer of surficial sediments that are conceptualized to participate in bedload transport, as well as bed evolution. Notably, the active layer concept is applicable only for Stage 1 and 2 transport conditions (*Hassan et al., 2005*). As noted above, the active layer length scale is commonly estimated as the 90<sup>th</sup> percentile grain class of the bed surface times a constant, which ranges from a value of 1 to 2 (*Parker, 2008*). The active layer grain size distribution changes due to erosion and deposition based on fractional bedload transport capacity. The model presently tracks the changing composition of active layer sediments due to erosion and subsequent deposition. Cycles of erosion and deposition can be handled, but presently are not.

The grain sorting model for a unit width of stream bed is computed as:

$$\varepsilon \left[ L_a \frac{\partial f_a}{\partial t} + (f_a - f_{es}) \frac{\delta L_a}{\delta t} \right] = -\frac{\partial q_{b\psi}}{\partial x} + f_{es} \frac{\delta q_b}{\delta x}, \quad (\text{A.16})$$

where  $L_a$  is the active layer thickness and  $f_{es}$  is the volume probability of  $\psi$  within the active layer/bed substrate interface. The left hand side of Equation A.16 represents the mass of bed

sediments within a control volume, and the right hand side reflects the net mass inflow rate of sediment. Exchange of sediments between the active layer and sediments below is controlled by the exchange fraction parameter:

$$f_{es} = \begin{cases} f_{ss}|_{z=\eta-L_a} & \text{for bed erosion} \\ \beta f_a + (1 - \beta)p_{bi} & \text{for bed deposition,} \end{cases} \quad (\text{A.17})$$

where  $f_{ss}$  is the volume probability of  $\psi$  within the bed substrate and  $\beta$  is a partitioning coefficient assigned a value of 0.5.

## A.6 Model set-up and boundary conditions

The channel bed evolution model is computed following a finite difference numerical scheme. Determination of the spatial and time steps is subject to the Courant stability parameter ( $C_n$ ) where an estimated mean flow velocity, and the model spatial and temporal differences are used to compute the projected model stability:

$$C_n = \frac{\bar{u}\Delta t}{\Delta x} \quad (\text{A.18})$$

Courant stability values less than 1 are sought for finite difference numerical models. The estimated mean flow velocity used in Equation A.18 is computed with the normal flow depth approximation.

As described above, the model requires three boundary conditions in total. One at the upstream end and two at the downstream end of the model domain. The upstream boundary condition is set as the sediment supply rate for all times  $t$ :

$$q_b(x_o, t) = q_{b_o}, \quad (\text{A.19})$$

where  $x_o$  is the upstream most node in the model domain. The fractional flux  $q_{b\psi}$  is determined from  $q_b$  based on the fractional proportion of each grain size class  $\psi$  in the supply mixture. The two downstream boundary conditions for the flume simulations are set as (1) the water surface elevation at the downstream most computational node for all times  $t$ , determined with the normal depth approximation ( $h_o$ ):

$$h(x_L, t) = h_o, \quad (\text{A.20})$$

and, (2) the channel bed elevation at the downstream most computational node for all times  $t$ , determined by the elevation at the initial time ( $\eta_o$ ):

$$\eta(x_L, t) = \eta_o, \quad (\text{A.21})$$

where  $L$  is the length of the computational domain from upstream to downstream.

## A.7 Model application to experiment PRE1

Figure A.1 compares steady-state longitudinal profiles for PRE1, and channel evolution model application to PRE1, at  $t_e = 2150$  minutes. We also show the initial profiles, and the initial experimental DEM for reference. The experimental and simulation profiles exhibit similar morphologic responses to the upstream supplies of water and sediment, with pool, riffle and roughened channel features located in a consistent manner along the channel. The depths of pools, heights of riffles, and topographic magnitudes of roughened channel segments are also similar. Notably, the simulation profile informed design of PRE1, as discussed in Section 3.2.2. The simulation was run for a spatial step of 10 cm, a time step of 0.1 seconds, and with a RCASA pool water surface slope of 1.0%.

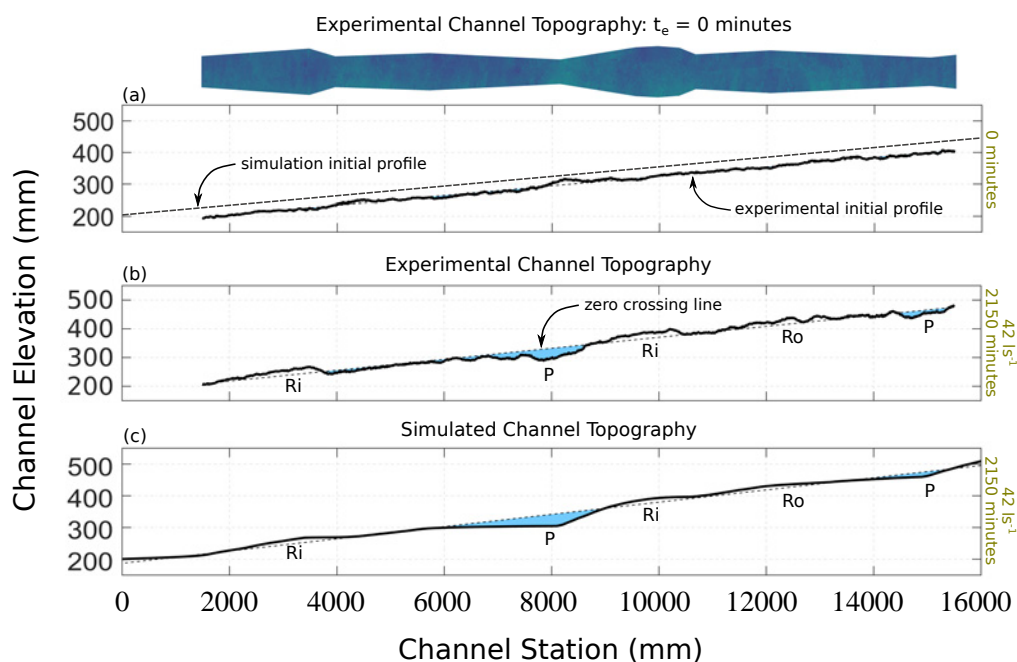


**Figure A.1:** Profile comparison of experimental and simulation outcomes for  $t_e = 2150$  minutes. At the top we show the channel layout and experimental DEM at  $t_e = 0$  minutes for reference. (a) The initial simulation (dashed line) and experimental profiles (solid lines). (b) Experimental profile at steady-state  $t_e = 2150$  minutes, with zero-crossing negative residuals colored for reference. (c) Simulation profile at steady-state  $t_e = 2150$  minutes (simulation duration), with zero-crossing negative residuals colored for reference. See Section 4.3.2 for information concerning the zero-crossing method.

## Appendix B

# Probabilistic friction angle model of particle mobility

### B.1 Motivation

Mobilization of a grain resting on or within the channel bed surface will occur when the downstream and upward directed forces acting on the grain exceed the forces acting to keep the grain at rest. The resisting forces acting to keep the grain at rest are  $F_g$  and  $F_f$ , the gravitational and resisting frictional forces, respectively (Wiberg and Smith, 1987). The driving forces acting to mobilize the grain are  $F_d$ ,  $F_l$  and  $F_b$ , the drag, lift and buoyancy forces, respectively (Wiberg and Smith, 1987). From this context, grain mobilization is generally approximated with the Shields stress criterion ( $\tau_c^*$ ) (Shields, 1936), which reflects the ratio of driving to resisting forces for uniform or non-uniform flow conditions, formulated in the most simplified form possible:

$$\tau_c^* = \frac{\tau}{(\rho_s - \rho_w)gD_i'} \quad (\text{B.1})$$

where  $\tau$  is the dimensional shear stress,  $\rho_s$  is sediment density, here assumed to be 2.65 g/cm<sup>3</sup>,  $\rho_w$  is the density of fresh water, here assumed to be 1.00 g/cm<sup>3</sup>,  $D_i$  represents the mean diameter of each grain size class according to the Wentworth scale for half- $\psi$  increments, and  $\psi = \log_2(D_i)$ . The driving force  $\tau$  is commonly taken to be equivalent to  $\rho_w g \bar{d} S$ , where  $g$  is the acceleration of gravity on Earth,  $\bar{d}$  is the average water depth and  $S$  is the channel bed slope. The resisting force is taken to be the gravitational force acting on the submerged weight of a sediment grain.

Application of Equation B.1 yields singular values of the Shields stress for any grain size  $D_i$ , or a range of values if the driving force is assumed to vary, achieved by varying the mean flow depth by some specified amount. Either approach will provide Shields stress conditions that are constrained over a narrow range. This stands in contrast to the view that sediment transport is a probabilistic phenomenon (Hassan *et al.*, 1991; Furbish *et al.*, 2012; Ancey and Hey-

man, 2014; Furbish et al., 2016), for which sediment particles on the bed surface have mobility conditions described by a distribution of possible values (Wiberg and Smith, 1987; Kirchner et al., 1990; Buffington et al., 1992).

We address these differences with a numerical model of the particle mobility problem as presented by Wiberg and Smith (1987); Kirchner et al. (1990) and Buffington et al. (1992). The model builds a randomly constructed virtual 1D river bed from a specified grain size distribution. Sediment particles from the same distribution are randomly placed along the virtual riverbed, but grain placement is restricted to known locations of grain–grain intersection on the virtual riverbed. The geometric characteristics of each placed grain are determined, providing measurement of the grain friction angle, which determines the relative mobility of all placed grains and which is used to determine  $\tau_c^*$  of Equation B.1. The goal of the model is to use a simple mechanics-based approach to examine particle mobility probability distributions for poorly sorted gravel-bed rivers. The specific goal is to examine how/if morphodynamic predictions are affected by the distributions of possible mobility states, as opposed to deterministic mobility approximations, such as those associated with Equation B.1. Here I describe the details of the model, and provide some results to demonstrate the model capabilities, and characteristics of simulated  $\tau_c^*$  distributions.

## B.2 Simplifying assumption of the present model

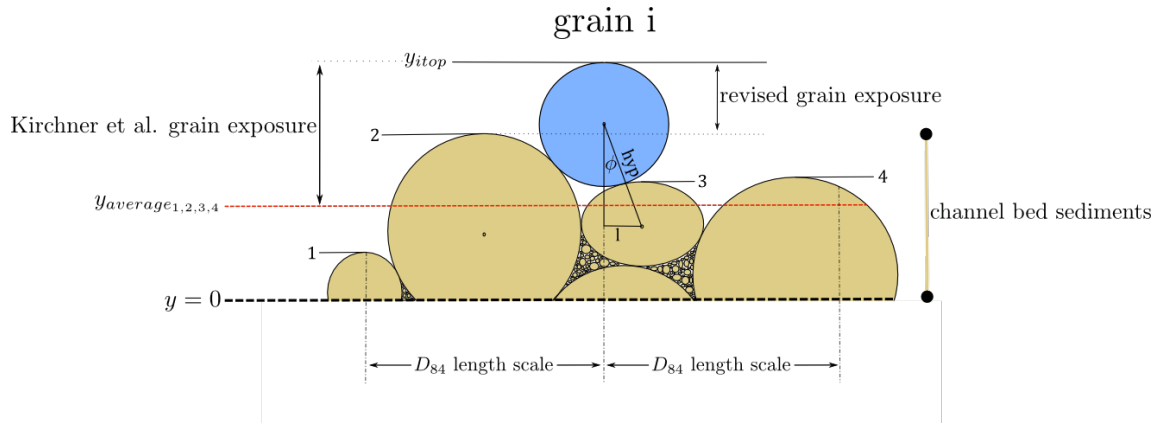


**Figure B.1:** Schematic view of friction angle based mobilization problem as defined by Kirchner et al. (1990). Grain projection ( $e$ ) is determined by the local average bed elevation, where local is defined by a length scale equivalent to the  $D_{84}$  percentile grain size. Grain exposure ( $e$ ) defines the upstream face length scale exposed to the oncoming fluid flow, determined as the distance from the top of the upstream neighboring grain to the top of the grain of interest.  $e$  can have a value of 0 if the grain of interest is sheltered by the upstream neighboring grain. The friction angle  $\phi$  is determined by how the grain of interest sits on the supporting grains.

Kirchner et al. (1990) derived a particle force balance solution by expanding Equation B.1 into a form for which  $\tau_c^*$  of any particular grain on the bed surface is a function of grain

projection ( $p$ ), grain exposure ( $e$ ) and the grain friction angle  $\phi$  (Figure B.1). Grain projection scales the magnitude of the drag force:  $F_d = 0.5\rho_w C_d (0.5A_s) \overline{U}_{xz}^2$ , because  $p$  sets the datum from which the vertical velocity profile is computed, where  $C_d$  is the drag coefficient,  $\overline{U}_{xz}$  is the vertically-averaged velocity impinging on the upstream exposed face of the grain and  $A_s$  is the total exposed area of the grain to the surrounding fluid. *Kirchner et al.* (1990) specifies the datum for calculation of the vertical velocity as the nearby upstream/downstream average bed elevation ( $y_{average_{1,2,3,4}}$ : Figure B.1), where the averaging length scale in both directions is equivalent to the  $D_{84}$  percentile grain size on the bed surface. *Buffington et al.* (1992) used this set-up to calculate  $\tau_c$  values for frozen bed surface samples from Wildcat Creek, Berkeley, CA, U.S. Inclusion of  $p$  by *Kirchner et al.* (1990) in  $F_d$  assumes that the flow field feels the riverbed at the specified datum, which requires the flow to be attached and developing from the datum elevation. I simplify the problem by assuming that grain exposure adequately approximates the vertical length scale over which the upstream flow field develops to a relatively rough bed surface. This simplification reduces the fluid mechanical assertions implied by use of the projection length scale.

### B.3 Solution for $\tau_c$ with the $p$ simplification

*Kirchner et al.* (1990) expands Equation B.1 by accounting for  $F_d$ ,  $F_l$  and the grain friction angle  $\phi$ :

$$\frac{1}{6}(\rho_s - \rho_w)g\pi D^3 = F_w = \frac{F_d}{\tan \phi} + F_l, \quad (\text{B.2})$$

where  $F_w$  is the weight force, or the immersed weight of a sediment particle of diameter  $D$ . As indicated above,  $F_d$  is (*Wiberg and Smith, 1987*):

$$F_d = 0.5\rho_w C_d (0.5A_s) \langle u^2(z) \rangle, \quad (\text{B.3})$$

where  $\overline{U}_{xz}^2$  is rewritten as  $\langle u^2(z) \rangle$ . The vertical velocity profile is a logarithmic function of the distance above the reference datum (*Kirchner et al.*, 1990):

$$u(z) = \left( \frac{\tau}{\rho_w} \right)^{0.5} \kappa^{-1} \ln \left( \frac{z + z_o}{z_o} \right), \quad (\text{B.4})$$

where  $\kappa$  is van Karmen's constant, here assumed to have a value of 0.407,  $z$  is the elevation of the grain top exposed to the flow field ( $y_{top}$ : Figure B.1) and  $z_o$  is the lowest elevation of the grain exposed to the oncoming flow. The distance  $z - z_o$  defines the grain exposure  $e$  (Figure B.1). The logarithmic term is abbreviated as  $f(z)$ , and combining Equations B.3 and B.4 gives:

$$F_d = 0.5C_d (0.5A_s) (\tau \kappa^{-2}) f(z)^2 \quad (\text{B.5})$$

$F_l$  is a function of the scaled velocity difference (scaled by the lift coefficient) acting over the exposed surface area of a grain from the grain top to the lowest elevation of the grain exposed

to the oncoming flow (Wiberg and Smith, 1987):

$$F_l = 0.5\rho_w C_l A_s (u_t^2 - u_b^2), \quad (\text{B.6})$$

where  $u_t^2$  is the velocity at the grain top and  $u_b^2$  is the velocity at the lowest elevation of the grain exposed to oncoming flow. Similar to  $F_d$ , the  $F_l$  velocity difference term is a function of the velocity profile, also assumed to be logarithmic in form, providing  $F_l$  as:

$$F_l = 0.5C_l A_s (\tau\kappa^{-2}) [f(z_t)^2 - f(z_b)^2] \quad (\text{B.7})$$

The drag coefficient  $C_d$  is taken to have a value 0.40, and the lift coefficient  $C_l$  a value of 0.20 (Wiberg and Smith, 1985). The grain friction angle  $\phi$  is calculated as:

$$\phi = \sin^{-1} \frac{d_1}{d_2}, \quad (\text{B.8})$$

where  $d_1$  is the horizontal distance between the overlying grain center, and the downstream neighboring grain center, and  $d_2$  is the straight line distance between the overlying grain center coordinates, and the downstream neighboring grain center coordinates (Figure B.1). As a note, the downstream neighboring grain lies partially beneath the overlying grain, for which the mobility condition is sought. With values for  $C_d$  and  $C_l$ , a method to determine  $\phi$ , and Equations B.5 and B.7, all that remains is to specify how to determine  $A_s$ . The surface area of a grain resting on particles beneath is determined through revolution about the axis parallel to the bed surface (Figure B.1):

$$A_s = \int_a^b 2\pi(r^2 - x^2) \sqrt{\left(\frac{r^2}{r^2 - x^2}\right)} dx, \quad (\text{B.9})$$

where the limits of integration are taken as  $a$  = the lowest grain elevation exposed to oncoming flow (point 2 of Figure B.1), which is taken to have a relative elevation of 0 (equivalent to  $z_0$ ), and  $b$  = the grain top elevation ( $y_{itop}$  of Figure B.1). With the integration limits specified, Equation B.9 simplifies to:

$$A_s = \int_0^{y_{itop}} 2\pi r dx, \quad (\text{B.10})$$

and integrating with respect to  $x$  and applying the limits yields:

$$, A_s = 2\pi r e \quad (\text{B.11})$$

where  $e$  is taken as the grain exposure, defined above as the difference between the grain top elevation and the lowest elevation of the grain exposed to the oncoming flow, defined by the elevation of the neighboring upstream grain top (Figure B.1). As indicated in Equation B.5, the drag force is a function of  $A_s$  normal to the flow, so  $A_s$  is multiplied by 0.5. The lift force on

the other hand is a function of the entire exposed surface area  $A_s$ .

Combining Equations B.2, B.5, B.7 and B.11, rearranging, and solving for  $\tau = \tau_c$  yields a revised form of the force balance describing a spherical grain resting on the channel bed:

$$\tau_{cr} = (\rho_s - \rho_w)g \frac{\pi D^3}{6} \cdot \left[ 0.5C_d \tan^{-1} \theta \kappa^{-2} \pi r e \cdot f(z)^2 + C_l \kappa^{-2} \pi r e \cdot (f(z_t)^2 - f(z_b)^2) \right]^{-1} \quad (\text{B.12})$$

With the definition of  $z_o$ , the velocity difference quantity on the right hand side of Equation B.12 simplifies to  $f(z)^2$ . Finally, results from Equation B.12 are used in Equation B.1 to determine the Shields stress  $\tau_c^*$ , provided that  $e > 0$ . If  $e \leq 0$ ,  $\tau_c^*$  is not computed.

## B.4 Sample simulation inputs and results

The model begins by the user specifying the grain size distribution, which is assumed to be normally distributed grain size sample, described by a mean size and standard deviation (Figure B.2). The model uses the specified distribution to construct the virtual riverbed, which

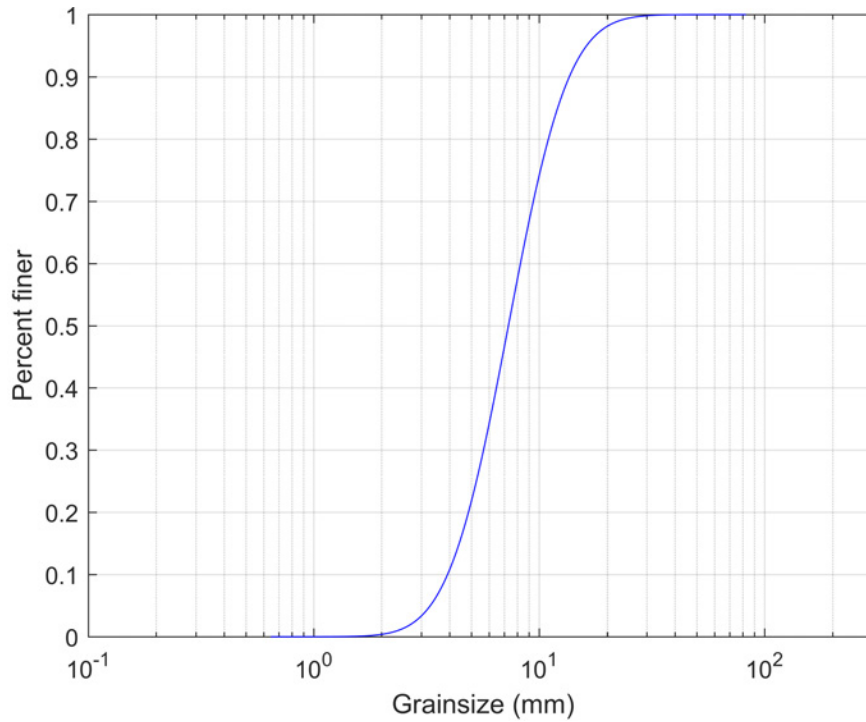


**Figure B.2:** Sample grain size distribution for the friction angle model. The illustrated distribution matches the PRE1 grain size mixture.

generally consists of 5000–10000 grains. Grain sizes are randomly chosen from the distribution, and placed sequentially along the riverbed. Grains from the same distribution are then randomly placed along the riverbed, and the grain friction  $\phi$  is determined with Equation B.8, as the center coordinates of every grain on the virtual riverbed, and those placed on the

riverbed are stored by the model. Typically, 10–20% of all placed grains are discarded for every 5000 placed grains because  $e \leq 0$ . Figure B.3 illustrates sample results from applying Equation B.12 to the grain size distribution shown in Figure B.2, for the steps just discussed. Figure B.3

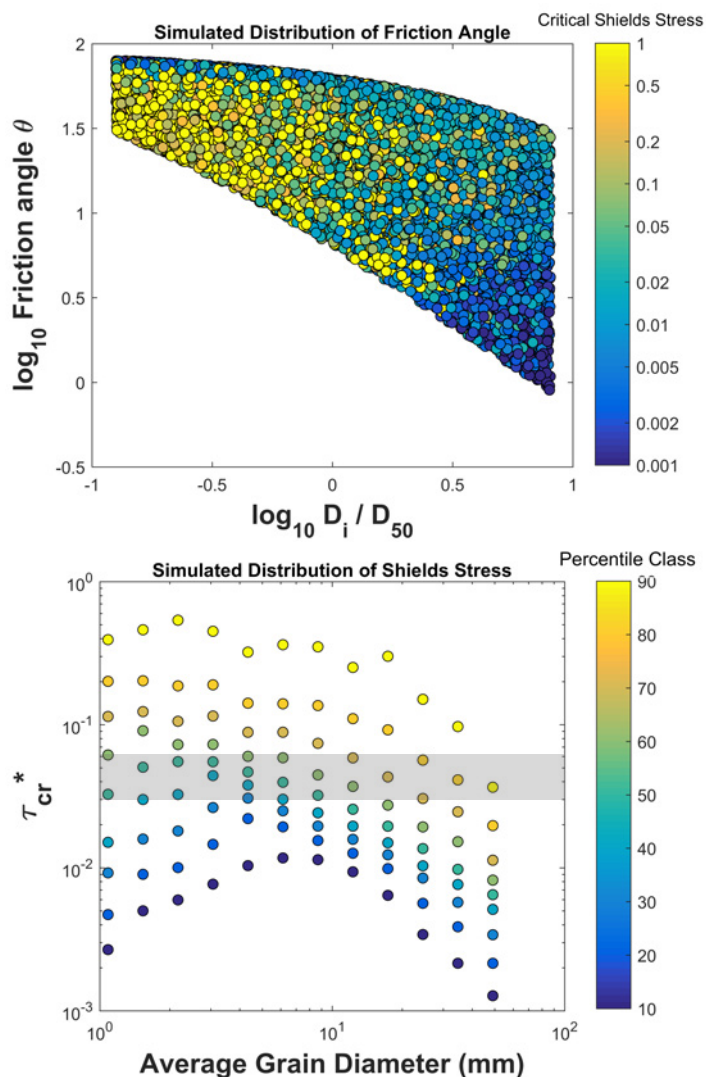


**Figure B.3:** Simulated grain mobility conditions using the friction angle model. The top plot illustrates measured friction angle  $\phi$  vs. the relative grain diameter  $D_i/D_{50}$ , colored based on the critical Shields stress value  $\tau_{cr}^*$ . The bottom plot shows the 10th–90th percentile values for the critical Shields stress value  $\tau_{cr}^*$  vs. the average grain diameter for each grain size class of the simulated distribution. The gray shaded region highlights the typical value range of 0.03–0.06 for  $\tau_{cr}^*$  (cf. Buffington and Montgomery, 1997). Results shown with the perceptually uniform *Viridis* colormap.

shows that simulated grain mobility is systematically distributed according to grain size for poorly sorted gravel mixtures, like that of PRE1 (Figure B.2). Smaller grains tend to exhibit higher critical mobility conditions, as shown with the yellow colors of the top panel in Figure B.3, and the magnitude of associated values for the 10th–90th percentile results of the lower

panel. On the other hand, larger grains tend to exhibit lower critical mobility conditions, as shown with the blue colors of the top panel in Figure B.3, and the magnitude of associated values for the 10<sup>th</sup>–90<sup>th</sup> percentile results of the lower panel. For the simulated grain size distribution, the lower panel of results also indicates that grain size classes within the center of the distribution are characteristically less mobile than the grain size classes on either end of the distribution. This result is common to simulation outcomes for mixtures with geometric mean sizes greater than roughly 5–6 mm, with standard deviations greater than roughly 0.5 mm, and normal distribution limits of five times the standard deviation. The result indicates that there is some optimal hiding or packing problem, particular to grain size classes that lie near the mode of the distribution.

## **B.5 Friction angle model availability and citation**

The model was coded in MATLAB<sup>®</sup>, and has been partially translated to Python. The model is freely available on my GitHub site: [https://github.com/smchartrand/ParticleMobility\\_FA](https://github.com/smchartrand/ParticleMobility_FA). The model is licensed with a MIT license, and is citable with the following digital object identifier: doi: 10.5281/zenodo.250114, which can be found here: <https://doi.org/10.5281/zenodo.250114>.

## Appendix C

# Sediment transport as a rarefied phenomenon

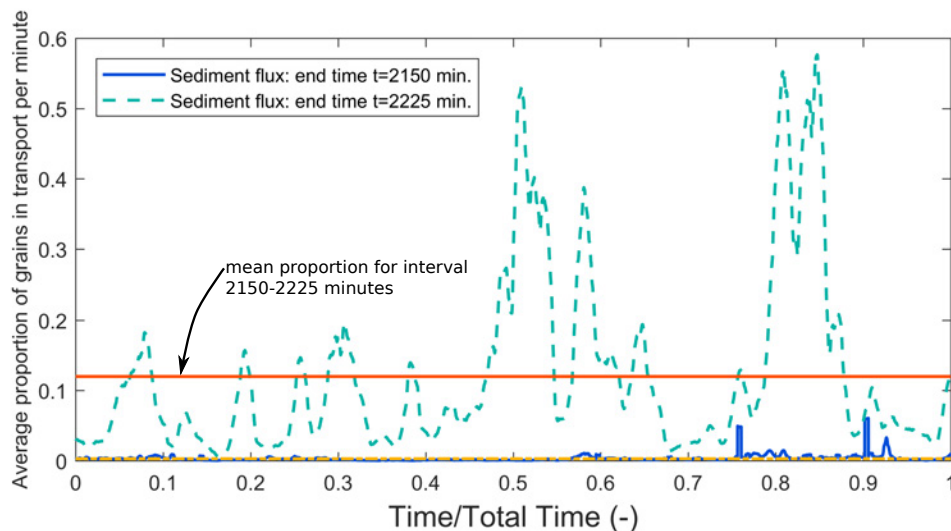


**Figure C.1:** Measured sediment flux from the flume. The plot illustrates sediment flux as an approximate proportion of the total grains on the bed surface participating in transport, for a bed area measuring 547x547 mm<sup>2</sup> and assuming the bed is composed of 8 mm diameter grains (the average channel width of experiment pool-riffle 1 (PRE1) and the grain size mixture D<sub>50</sub>, respectively). Sediment flux at end time 2150 minutes reflects steady-state conditions for an approximate bankfull flow, and sediment flux at end time 2225 minutes reflects adjustment of the 2150 minutes steady-state conditions to an increase in flow and sediment feed such that average sediment mobility was 2x the threshold condition of  $\tau_c^* \approx 0.030$ . Sediment flux during the interval 2150-2225 minutes was the highest measured during PRE1, yet with on average only 12% of the sediment particles on the bed surface participating in transport. For the prior interval the average proportion participating in transport was well below 1% (yellow line at bottom of plot).

Figure C.1 shows that the approximate proportion of sediment particles on the bed surface

---

that participate in sediment transport ranges, on average, from less than 1% to roughly 12% for experiment pool-riffle 1 (PRE1). This range reflects steady-state topographic conditions (end time  $t=2150$  min.), and a significant perturbation to the upstream boundary conditions that gave rise to the  $t=2150$  min. steady-state (end time  $t=2225$  min.). This set of results is one demonstration that sediment transport is a rarefied phenomenon (*Furbish et al., 2016*). See Chapters 3 and 4 for more details regarding the experimental conditions.